Inelastic Scattering of Magnetically Trapped Atomic Chromium

A thesis presented

by

Robert deCarvalho

to

The Department of Physics

in partial fulfillment of the requirements

for the degree of

Doctor of Philosophy

in the subject of

Physics

Harvard University

Cambridge, Massachusetts

May 2003

Thesis Advisor | Author

John Doyle | **Robert deCarvalho**

Inelastic Scattering of Magnetically Trapped Atomic Chromium

Abstract

Cold collisions of atomc chromium in a magnetic trap are studied. A cryogenic buffer gas is employed to load 10^{12} chromium atoms into a magnetic trap at an initial temperature of $\sim 1\ K$. The trap depth is then lowered to cool the atoms to temperatures as low as $2\ mK$. After cooling, the steady state temperature and the number of remaining atoms are measured and the chromium collisional properties extracted. Elastic and inelastic scattering rates for ^{52}Cr-^{52}Cr are measured at temperatures ranging from $2\ mK$ to $1\ K$. The inelastic scattering rate coefficient shows a dramatic variation with temperature. At $1\ K$ it is roughly $10^{-13} cm^3 s^{-1}$. However, at temperatures just above the ultra-cold limit, the scattering rate sharply increases to values as high as $2 \times 10^{-9} cm^3 s^{-1}$.

Contents

List of figures

Acknowledgments

Throughout graduate school I have had the privilege of working with an outstanding group of people to whom I feel a deep sense of gratitude.

First of all, I want to thank my advisor, John Doyle for being an excellent mentor and for fostering a stimulating and pleasant research environment. My approach to physics and research has been molded not only by his intuitive understanding of physical principals and his clear-sighted approach to problem solving, but also his effective style for managing people and making critical decisions. It has been a pleasure working in his group.

The graduate students I have worked with the past several years have been truly exceptional. It has been a real pleasure working with each of them. There are a few I would like to especially acknowledge. I'm not sure how I would have made it through the late nights of grinding through problem sets in the basement without the camaraderie of Carlo and Dan, the loyal comradeship of Sergei, and, of course, his Russian copy of Landau. I am especially grateful for having worked so closely with Jonathan Weinstein. In addition to his outstanding technical competence and insight into physics, his quick sense of humor was a welcome addition to life in the lab. It has been a pleasure working with Cindy Hancox. She played a vital role in obtaining and analyzing the new experimental results of this thesis. I would also like to thank Robert Michniak for many fruitful discussions on modeling physical systems.

I would especially like to acknowledge my family who has been so incredibly supportive. I thank my father for his sterling example of resolve, commitment and perseverance. I thank my mother for her dedication in giving me a solid education through home school. I thank my brother and sister for their listening ear and helpful advice.

There are two people to whom I owe an enormous debt of gratitude, Howard Shattuck and Dr. J. G. Jacobson. Without their encouragement and support, my current career path would not have been possible. Thank you.

Finally I would like to acknowledge the hand of providence to whom I owe the balance, peace of mind, and overall contentment in my life.

Chapter 1
Introduction

The purpose of this thesis is to describe work done in our lab on buffer-gas loading and evaporative cooling of magnetically confined chromium. The emphasis will be on new measurements we have taken that determine important collisional properties of magnetically confined chromium. These measurements explore a previously uninvestigated energy regime and have culminated in surprising results.

This thesis is written with the hope that it will serve as a useful resource to the student who is beginning to work in the field of magnetic trapping and evaporative cooling. With this in mind, much of the foundational groundwork for understanding both the experimental procedures and the theoretical models for systems of magnetically trapped atoms is laid out in detail.

1.1 Importance of Magnetic Trapping

Magnetic trapping and evaporative cooling techniques [1, 2] have enabled the achievement of very low temperatures and high phase-space densities, leading to a revolution in atomic physics. These techniques provided the enabling technologies for such important areas of research as Bose-Einstein condensation, atom interferometry, atom

lithography and the study of ultra-cold atomic collisions [3, 4, 5, 6, 7]. The new horizons brought into view by magnetic trapping and evaporative cooling have, by no means, been fully explored.

As an example, one area of new physics awaiting investigation is the study of dipolar gases. In these systems, the dipole-dipole interactions (either magnetic or electric) can dominate the dynamics. It has been pointed out by several authors that new and interesting effects can occur in dipolar gases, including "self-assembled" complex wavefunction structure [8], robust quantum computation [9], single component superfluidity [10] and new quantum phases of matter, including the supersolid [11].

To date, most trapping and cooling experiments have been performed with a relatively small number of atomic and molecular species, and with samples containing small numbers of particles. The full potential of trapping and cooling can only be fully realized by developing techniques that extend the possibility of magnetic trapping to as many different species as possible.

1.2 Buffer-Gas Loading

Buffer-gas loading is a technique invented and developed in our laboratory [12] as a general method for loading virtually any paramagnetic species into a magnetic trap. Because it relies only on elastic collisions, buffer gas loading is essentially independent of the internal structure of the species to be trapped. This independence is

maintained as long as the internal structure is such that elastic scattering with the buffer gas dominates any inelastic collisional processes that may exist.

Our implementation of buffer-gas loading is discussed at length in Chapter 2. Using buffer gas loading, we find it straightforward to magnetically trap up to 10^{12} atoms at densities approaching $10^{13}\ cm^{-3}$ and temperatures of $\sim 1K$.

1.3 Collisions and Evaporative Cooling

Without evaporative cooling, the production of degenerate quantum gases would not be a reality. This incredibly powerful technique is the method of choice for achieving the enormous gains in phase space density required to obtain quantum degenerate gases. Evaporative cooling is implemented in our experiment by ramping the depth of the magnetic trap to increasingly smaller values thereby selectively removing the more energetic atoms confined in the trap.

The efficiency of evaporative cooling in terms of atom loss, as well as in terms of the lowest temperatures attainable, is a function of the elastic and inelastic scattering rates between trapped atoms. Elastic collisions drive the evaporative cooling process. Inelastic collisions drive a heating process which competes with the evaporative cooling to establish a steady state temperature. Additionally, in our experiment, inelastic collisions provide the dominant mechanism for losing atoms from the trap. The ratio of elastic to inelastic collision rates is the single most important para-

meter in determining the success or failure of achieving quantum degeneracy using evaporative cooling in a magnetic trap.

Because of this, the scattering properties are an extremely important consideration when selecting an atom to study in the quantum degenerate regime. The scattering properties of all but the simplest atoms are quite difficult to calculate from first principals. This means that a big part of determining the viability of a given atom for producing a quantum degenerate gas involves an experimental determination of its scattering properties.

1.4 Why Atomic Chromium

Although chromium's scattering characteristics were unknown prior to our experiments, it has many properties which make it an ideal atom not only for buffer-gas cooling and magnetic trapping, but also for studying in the quantum degenerate regime. The large ground state magnetic moment of chromium, $6\ \mu_B$, makes for a relatively strong interaction with a magnetic trapping field. This allows experiments to be run with trapping magnets that are technically easy to construct. The large magnetic moment of chromium also makes it a promising candidate for the study of dipolar gases, as mentioned above.

Chromium has four naturally occurring isotopes: three Bosons, ^{50}Cr, ^{52}Cr, ^{54}Cr and one Fermion, ^{53}Cr. Each of the Bosonic isotopes has nuclear spin equal to zero. The resulting absence of hyperfine structure greatly simplifies their spec-

troscopy. Although the nuclear spin of the fermion isotope ($I = 3/2$) complicates its observed spectrum, a simultaneous confinement of the Fermion with it's Bosonic siblings would make an interesting system for the observation of quantum degeneracy.

In its ground state, chromium has a $^7S_3$ configuration. This means all the angular momentum of the chromium atom is contained in the spin of its electrons. The spherically symmetric electron distribution in the $^7S_3$ configuration could avoid certain inelastic processes present in the buffer-gas cooling of non s-state atoms. If the atom were not spherically symmetric, one can imagine it would be more susceptible to undergoing inelastic collisions while thermalizing with the cold atoms of a buffer gas. Even though we are unaware of any experimental evidence supporting this hypothesis, working with an S state atom eliminates concern over this issue.

The spectroscopy of chromium is well understood. A group of lines around $430\ nm$ ($a^7S_3 \rightarrow^7 P_{2,3,\text{ and, }4}$) can be probed to provide excellent diagnostic tools for measuring the properties of magnetically confined chromium. This group of transitions is virtually closed, which alleviates concerns of optical pumping to undetectable ground states. Furthermore, the different Zeeman shifts of the ground and excited states for these transition result in spectral shifts that match perfectly with the scanning range of the laser we use for detection. A detailed description of the spectroscopy we perform on the $a^7S_3 \rightarrow^7 P_4$ transition is given in Chapters 2 and 7.

Finally, chromium is a metal. We find that the laser ablation technique used as an atom source in our experiments is particularly well suited for use with metals. This production technique, combined with the efficiency of buffer gas cooling, is responsible for the extremely large number ($\sim 10^{12}$) of atoms we are able to magnetically trap.

1.5 Thesis Overview

The research prospects associated with magnetic trapping and evaporative cooling warrant a detailed study of the collisional processes that play such a prominant role in determining the dynamics of evaporative cooling. The bulk of this thesis focuses on measurements of the inelastic collision rates for magnetically trapped atoms of the Bosonic ^{52}Cr.

Although the apparatus used in these measurements has been detailed elsewhere [13], a brief description is given in Chapter 2. However, the main focus of Chapter 2 is to provide the reader with an in-depth understanding of the procedure used in our experiment to produce reliable data for our measurements.

The analysis of our data is thoroughly described in Chapter 3. To the casual reader, the most relevant portion of this chapter is perhaps the section on the foundations of our analysis. This section presents the assumptions and approximations we make in obtaining our measured values. At the writing of this thesis, theory has not been able to account for the scattering rates we observe. In working to match the

results of theory with experiment, it is important to understand the assumptions and approximations we make in obtaining our values.

A good sense for the effects of these approximations is obtained by studying the supporting data presented in Chapter 4. These data support our understanding of the inelastic scattering rates for the ^{52}Cr-^{52}Cr system. We see scattering rate coefficients as large as $\sim 10^{-9}\ cm^3 s^{-1}$. This rate is truly enormous when compared to the typical inelastic rates for other atoms in the ultra cold limit [14, 15], $\sim 10^{-15}$ to $10^{-12} cm^3 s^{-1}$. Although we see evidence that this huge inelastic rate is decreasing at the lowest temperatures we are able to obtain (due to technical limitations in our apparatus), the general behavior involves the rate blowing up with reducing temperature.

This surprising behavior of the inelastic rate motivated us to develop a model of the behavior of trapped gases. Although the dynamics of evaporative cooling and atoms confined in traps has been treated quite extensively in the literature, we were unable to find a treatment that would adequately describe the conditions observed in our trap (i.e. low ratio of trap depth to temperature). This resulted in our developing a model of trapped gases which is described at length in Chapter 5. This model provides a self-consistency check on our data and increases the confidence level in our measurements.

At the writing of this thesis, a group of theorists is making rapid progress in developing a theoretical understanding of our results. The challenges involved in this

work are largely due to two factors. First, the inter-atomic potentials for chromium, with its six unpaired electrons, are quite formidable to obtain from ab-initio calculations. Since these potential are needed to accurately predict the scattering behavior of chromium, knowing them is essential in understanding our results. Secondly, the energy regime over which we conduct our measurements is in the cross-over region between classical and quantum scattering behavior. In the lingo of quantum scattering physics, most of our measurements are taken in the "few partial wave regime." This intermediate energy regime precludes the use of either the classical or the ultracold approximations usually employed in describing scattering behavior. Because of this, a full quantum calculation is necessary for understanding the system. Although a full description of the required scattering theory is beyond the scope of this thesis, Chapter 6 presents a qualitative description of our shape-resonance hypothesis for explaining the behavior of the inelastic scattering rate. The interactions responsible for inelastic processes are also briefly discussed and a theoretical "laundry list" of unanswered questions is presented.

In addition to their impact on both evaporative cooling and the understanding of the classical to quantum transition in scattering theory, our measurements may have some relevance to the field of ab-initio molecular potential calculations. Chromium's six unpaired electrons push the limits of these ab-initio calculations. The special challenge this presents has generated quite some interest in calculating the chromium-chromium interaction potentials [16, 17, 18, 19, 20, 21, 22, 23, 24].

Unfortunately, most of this work has concentrated on the singlet potential. Very little work has been done in calculating the interaction potential between two spin polarized chromium atoms. Accurate values for these potentials are essential in scattering rate calculations. It will be interesting to see if the ab-initio calculations for the complete set of chromium interaction potentials produces scattering rates consistent with our experimental observations.

Finally, the tantalizing downturn we observe in the measured inelastic scattering rate gave birth to the hope that perhaps we could employ laser cooling to lower the temperature of our atoms to a regime with smaller inelastic rates. Chapter 7 presents an analysis of laser cooling in the presence of inelastic losses. This chapter also describes how our implementation of laser cooling met with disappointment due to technical problems. The cryogenic environment of our trapping cell does not allow illumination of our atom cloud with the laser intensity required for laser cooling. Introducing the cooling laser resulted a degradation of the vacuum inside our cryogenic trapping cell thereby leading to increased atom loss.

Chapter 2
Experimental Overview

This chapter gives a brief description of our experimental apparatus. A detailed discussion of the apparatus has been laid out in the thesis of Jonathan Weinstein [13]. This chapter is intended to compliment that discussion. As such, some components of our system will be described in detail whereas others will only be summarized. Additionally, Appendix B of this thesis contains machine drawings for the various components that make up our experiment.

This chapter also contains a detailed description, not only of the experimental procedure we use to measure the Cr-Cr inelastic scattering rates, but also a description of how we process our data to obtain the signals used in our analysis.

2.1 Introduction to Experiment

Our experiment uses buffer-gas cooling to load a gas of atomic chromium into a magnetic trap. Laser ablation is used to inject a hot plume of Cr atoms into a cryogenically cooled ^{4}He buffer gas. Collisions with the buffer gas provide translational thermalization which rapidly cools the the Cr atoms to the temperature of the buffer gas.

This buffer-gas cooling process takes place inside a thermally conductive cell, held at cryogenic temperatures by a dilution refrigerator. The buffer gas density in

the cell is controlled by varying the temperature of the cell walls. An anti-Helmoltz magnetic trap surrounds the cell. As the cell walls are cooled to remove the non-magnetic buffer gas, the field of the trapping magnet confines the Cr atoms and prevents them from reaching the cell walls where they would stick and be lost.

This results in a cloud of magnetically trapped chromium atoms at temperatures on the order of $1\ K$. The cloud can then be cooled by simply ramping down the depth of the magnetic trap.

Throughout this process, the behavior of the trapped cloud is monitored using optical absorption spectroscopy.

2.2 Cryogenic Apparatus

Trapping takes place inside a cryogenic cell surrounded by an anti-Helmholtz magnet, see Figure 2.1. The magnet is a superconducting spherical quadrupole with depth that can be varied from 0 to 3 T. The cryogenic cell is constructed of two concentric plastic tubes with superfluid liquid helium filling the space between to form a thermally conductive jacket. This superfluid jacket is thermally anchored to the mixing chamber of a dilution refrigerator. Buffer-gas cooling is implemented by filling the inner volume of the cell with a fixed quantity of ^{4}He vapor. The quantity of vapor is chosen such that varying the cell temperature from $\sim 1\ K$ to $\sim 140\ mK$ causes the ^{4}He density to vary from a maximum of roughly $10^{17}\ cm^{-3}$ down to the theoretically estimiated very low densities ($<1\ cm^{-3}$), indicated from extrapolations of the

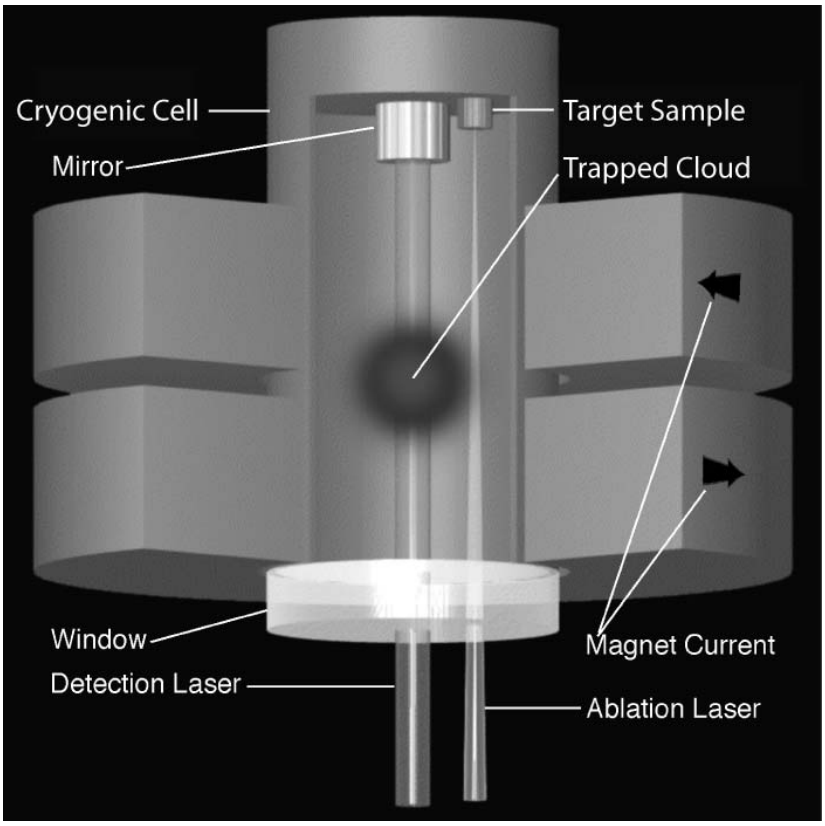

Figure 2.1: Cut-away view of cryogenic trapping apparratus. Atomic Cr is produced by laser ablating a solid sample affixed to the ceiling of the cell. Varying the temperature of the double-walled plastic cell controls the density of ^{4}He used for buffer gas loading. Confinement is provided by flowing current through two superconducting coils arranged in the anti-helmholtz configuration.

vapor pressure curve [25] of liquid ^{4}He. Our atomic source is a small lump of natural metallic chromium attached to the inside of the top lid of the cell. The reader is referred to the thesis of Jonathan Weinstein [13] for a complete description of our cryogenic apparatus.

2.3 Optical Detection Setup

Figure 2.2 shows a typical configuration for our detection setup. A *Coherent 899* titanium sapphire laser is pumped by a *Coherent Verdi* solid state pump laser to produce about $1\ watt$ of $850\ nm$ laser light. The frequency of the laser is monitored with a wavemeter. A commercial doubling cavity doubles the output of the Ti:Saph to the required $425\ nm$ wavelength for detecting chromium. The detection beam passes through an intensity stabilizer, affectionately known as the "noise eater," before passing through a $50\ \mu m$ diameter pin hole to clean up the beam profile. After passing through a variable attenuator, the beam is sent to a small optical breadboard mounted on the bottom of our dewar. A beam splitter sends a portion of the beam to a reference photomultiplier tube which is used to monitor the intensity fluctuations of the detection light. The remaining portion of the beam is sent into the cryostat, passed through the cloud of trapped atoms and reflected back out to the signal photomultiplier. Each photomultiplier is mounted behind an iris and spectral filter to limit the amount of background light reaching the photocathodes.

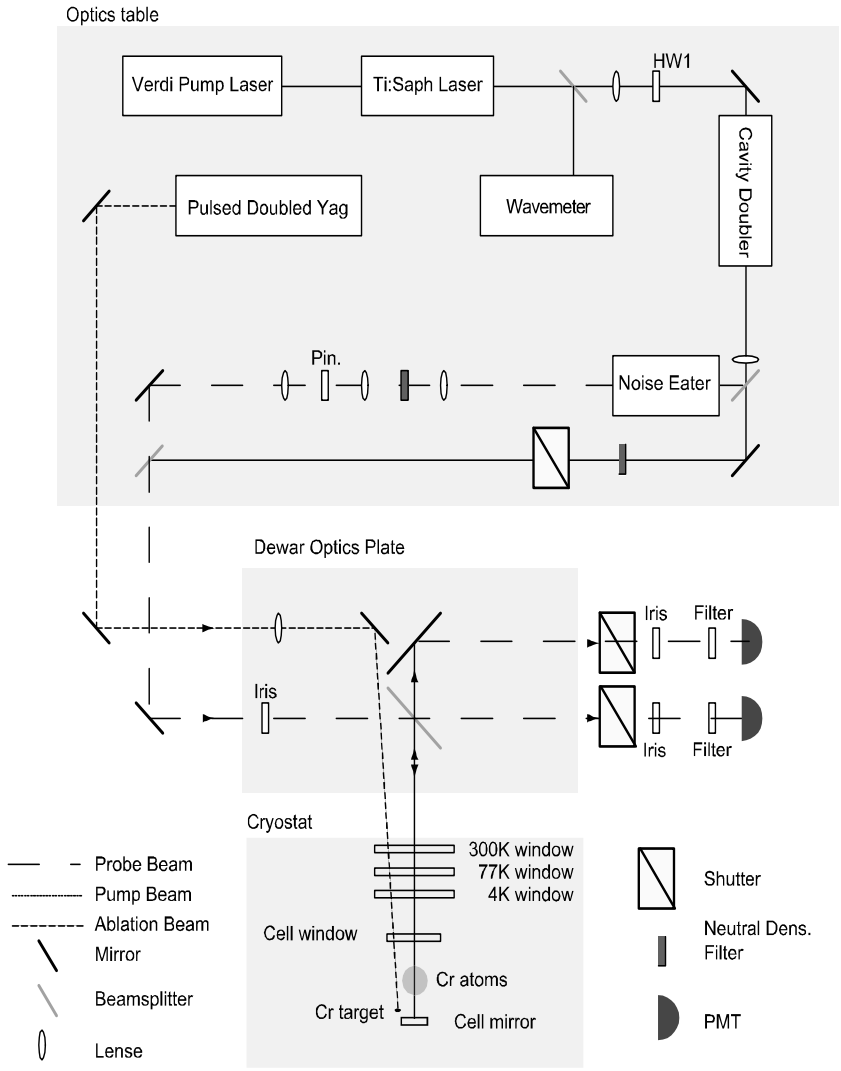

Figure 2.2: The laser ablation beam is generatated by a pulsed doubled YAG. It is focused and steered onto the solid lump of chromium in the cryo-cell. The pump and probe beams are both produced by doubling the output of a Ti:Saph laser. A shutter is used to pass the pump beam only during the times it is needed. The probe beam goes through a series of conditioning optics before passing through the trapped atoms. The shutters in front of the PMTs are used to protect them against the bright pump beam. The band-pass filters in front of the PMTs discriminate against non-resonant light.

A second beam, the pump beam, bypasses the conditioning optics and is used to illuminate the atoms with intense laser light in the hopes of observing laser cooling. This beam is passed through a variable attenuator to control its intensity. A shutter is used to turn the pump beam on and off. When the pump beam is introduced into the cryostat, its high intensity would damage the photomultiplier tubes. To prevent this, shutters are introduced in front of the photomultipliers.

The current produced by the photomultiplier tubes (PMTs) is passed through transimpedance amplifiers (HP SR570 current preamps from Hewlett Packard) to produce the voltages read by our data acquisition system. We employ the built-in low pass filters on the amplifiers to reduce the noise on our signals.

2.4 Data Acquisition System

We use Lab Windows CVI for the Solaris 2.5 operating system to provide a user interface for sending GPIB commands to control a CAMAC crate equipped with a model 3988 crate controller from KineticSystems [26] . The CAMAC crate contains cards for controlling our experiment.

Timing signals for the experiment are provided using the model 221 timing simulator card from Jorway [27]. This card is capable of providing 12 channels of TTL output with microsecond resolution. Three channels of this card are dedicated to sending control pulses to our YAG laser and sending the trigger pulse to the tran-

sient recorder. The remaining channels are designated as flexible timing channels that can be used for meeting any additional timing needs.

The transient recorder is a six channel, twelve bit analog to digital converter. It is model TR612 manufactured by Joerger [28]. On receiving a trigger pulse, the transient recorder fills each channel with up to 128K samples taken at rates ranging from $20\ Hz$ to $1\ MHz$. We use the transient recorder to monitor voltages coming from the signal PMT, the reference PMT, the cryogenic cell thermometer, the control voltage for the probe laser, and the current flowing through the trapping magnet.

A 16 channel, 12-bit digital to analog converter (model DAC-16 from Joerger [28]) provides the capability of sending specific analog voltages to various pieces of equipment. We use these analog outputs to control the frequency of our probe laser (when not in "sweeping" mode) and to provide low resolution timing signals for other equipment such as our shutters.

Switching is provided by an electronically controlled mechanical relay card (model 3075 from KineticSystems [26]). This card provides 16 independently controllable switches. We use these switches to control the currents used to heat our cryogenic cell in preparation for buffer gas cooling.

2.5 Experimental Procedure

Figure 2.3 nicely illustrates the timing sequence used in a typical run of the experiment for measuring the inelastic scattering rate at a trap depth of $0.9\ K$ (5 amp

magnet current). In order to clearly show the timing of the experiment, the duration of the data run shown in Figure 2.3 is deliberately shorter than what we would typically use for an actual inelastic rate measurement. This figure will be used in providing a detailed description of a typical run of the experiment.

Figure 2.3.a shows the voltage pulses sent to the cell top heater. The resultant heating (Figure 2.3.b) boils off the liquid ^4He film that covers the inner surface of the cell. This fills the cell volume with ^4He buffer gas.

At the end of the first heating pulse, two things happen. The ablation laser is fired (denoted by the cross in Figure 2.3.b) to introduce hot chromium atoms into the buffer gas. Simultaneously, the current through the trapping magnet is ramped down (Figure 2.3.c).

The ensuing 10 to 15 seconds see some very complicated dynamics. The atoms are thermalizing with the buffer gas as it is cryopumped to the walls by the falling temperature of the cell. At the same time, the trap depth is steadily decreasing. As the buffer gas atoms are cryopumped to the walls, they are able to knock some of the chromium atoms out of the steadily weakening trap. After the magnet is ramped down and the buffer gas removed, the remaining number of chromium atoms depends on the dynamics of the cell temperature and trap depth. The cell heater pulse and magnet ramping speed are varied to empirically maximize the remaining number of atoms.

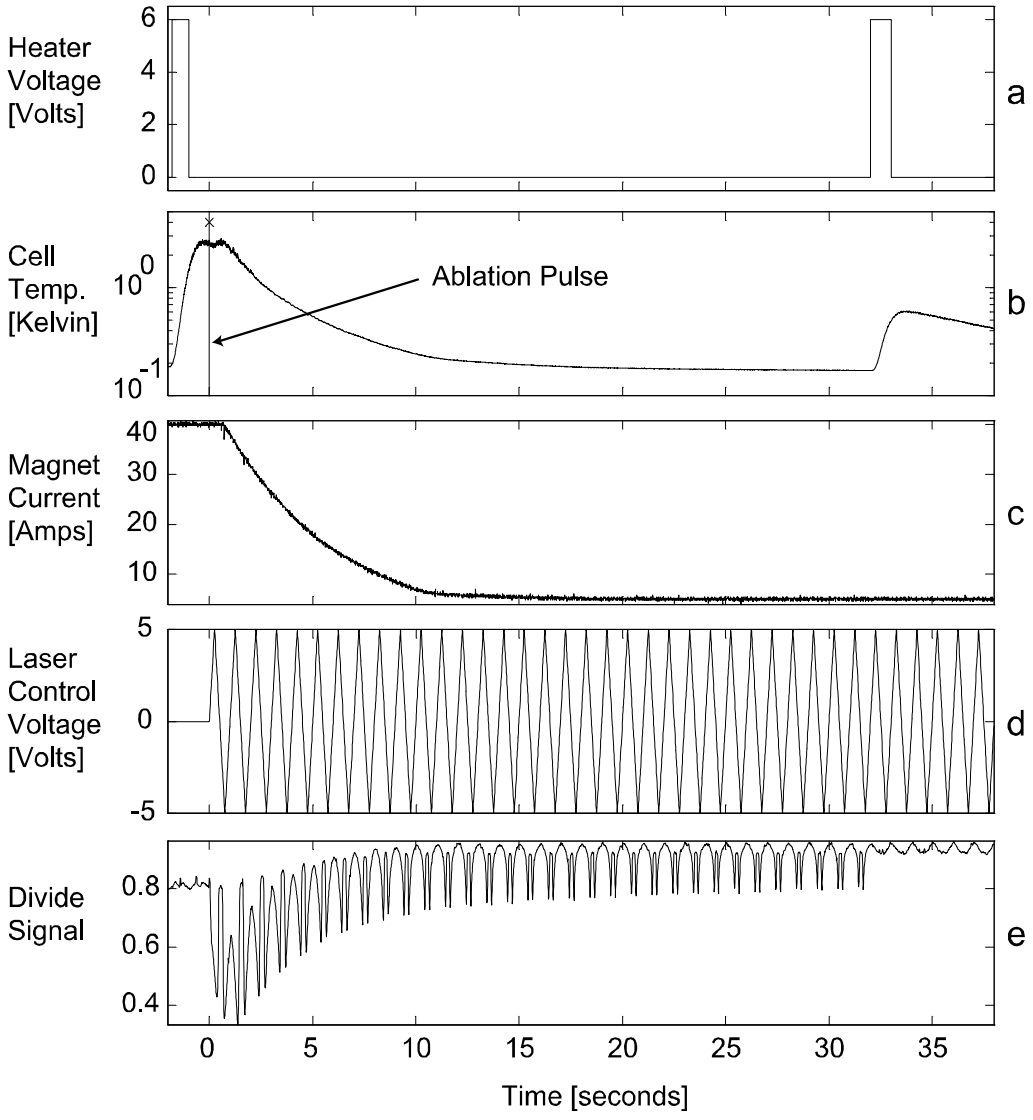

Figure 2.3: Timing for a single run of the experiment. **a)** Voltage pulses sent to cell-heater. **b)** Temperature dynamics of cryogenic cell caused by the heater and energy deposited by ablation pulse. **c)** Current flowing through trapping magnet. Ramping down the current results in adiabatic and evaporative cooling of trapped atoms. **d)** Control voltage used to scan the laser. The laser frequency is linearly proportional to this control voltage. **e)** Absorption peaks caused by scanning the laser through an optical transition of the trapped atoms. The atoms are deliberately removed near the end of the run to provide a baseline.

Throughout each run of the experiment, we monitor the intensity of the probe laser as it passes through the cell. The frequency of this laser is continuously swept over a preset scanwidth. This is accomplished by sending a $\pm 5\ V$ signal to the frequency control input of our Ti:Saph. laser. This control voltage, which is triggered to start scanning at the firing of the ablation pulse, is shown in Figure 2.3.d.

The intensity of the probe laser after passing through the trapped atom cloud is shown in Figure 2.3.e. The observed intensity dips are caused by the probe laser passing through an optical resonance of the trapped atoms.

After a sufficient time of monitoring the absorption peaks, the cell heater is pulsed once again to fill the cell with buffer gas. At the time of this second heating pulse, the trap depth has been reduced. This allows the buffer gas to remove the trapped atoms thereby providing a nice baseline to use in extracting the absorption of the trapped atoms.

2.6 Data Processing

2.6.1 Calculating the Measured Absorption

The voltages coming from the "signal" and "reference" PMT's are processed to reduce the effects of several different sources of noise. There are three sources of noise that dominate our detection. These are due to laser intensity fluctuations, mechan-

ical vibration of the cryogenic cell, and shot noise. Intensity fluctuations and cell vibrations introduce multiplicative noise whereas shot noise is additive.

To measure the absorption of the atoms we perform the following operations on the voltages acquired from the PMTs. After low pass filtering, we divide the signal PMT voltage by the reference PMT voltage to obtain a quantity we call the divide signal. We then subtract the divide signal during the time the atoms are present from the divide signal taken during the baseline and divide the result by the baseline signal. This quotient is exactly the absorption presented by the atoms plus some noise terms which will now be quantified.

We begin with the following definitions.

$$
\begin{aligned}
S &\equiv \text{Signal PMT voltage (atoms present)} \\
B &\equiv \text{Signal PMT voltage (during baseline)} \\
R_S &\equiv \text{Reference PMT voltage (atoms present)} \\
R_B &\equiv \text{Reference PMT voltage (during baseline).}
\end{aligned}
$$

The intensity of the laser at the face of the signal PMT when atoms are present is $I_{atoms} \propto (1 + L_s)(1 + V_s) T I_0$ where L_s is the fractional intensity fluctuations of the laser, V_s is the fractional intensity fluctuation caused by cell vibrations and T is the transmission through the atom cloud. During the baseline, the signal PMT will see $I_{baseline} \propto (1 + L_B)(1 + V_B) I_0$. The expressions for the intensity at the face of the reference PMT will be the same except that, since the reference beam does

not pass through the cryostat, the cell vibration term will be absent. Let the ratio of output voltage to optical intensity be denoted by q_1 for the signal PMT and q_2 for the reference PMT. Shot noise is denoted by H_1 for the signal PMT and H_2 for the reference PMT. This allows us to write

$$\begin{aligned} S &= q_1 (1 + L_s)(1 + V_s) T I_0 + H_{s1} \\ B &= q_1 (1 + L_B)(1 + V_B) I_0 + H_{B1} \\ R_S &= q_2 (1 + L_s) I_s + H_{s2} \\ R_B &= q_2 (1 + L_B) I_B + H_{B2} \end{aligned}$$

Dividing the signal PMT voltages by the reference PMT voltages results in two divide signals, one from when atoms are present and the other during the baseline. They are

$$\begin{aligned} D_s &= \frac{q_1 (1 + L_s)(1 + V_s) T I_0 + H_{s1}}{q_2 (1 + L_s) I_s + H_{s2}} \\ D_B &= \frac{q_1 (1 + L_B)(1 + V_B) I_0 + H_{B1}}{q_2 (1 + L_B) I_B + H_{B2}} \end{aligned}$$

We now consider the case where all fractional noises as well as the absorption are much less than one. We also assume that the shot noise on each of the two PMTs is of the form $H = const\sqrt{I}$. Taking the difference, $D_B - D_s$, we expand to first order in the noise sources and the atom absorption. Being a bit cavalier about the addition of the various noise terms we obtain

$$\frac{D_B - D_s}{D_B} \simeq A + 2V + \frac{const}{\sqrt{I_0}} \tag{2.1}$$

where A is the absorption presented by the atoms, D_B is the divide signal during the baseline, D_s is the divide signal when atoms are present, V is the typical size of the fractional noise due to cell vibrations, and I_0 is the typical full scale intensity when the PMTs are fully illuminated by the probe laser.

The dominant noise on the measured absorption signal depends on the intensity of the laser. For low laser intensities the $const/\sqrt{I_0}$ contribution from the shot noise dominates. Increasing the laser intensity sufficiently reduces the shot noise until the noise from cell vibration dominates.

The low pass filtering of our amplifiers combined with the technique of subtracting two divide signals results in our being sensitive to typically $\sim 1\%$ absorption per run of the experiment. We believe vibrations in our cryogenic cell are responsible for this lower limit. Of course, greater sensitivity can be obtained by averaging together several runs of the experiment.

It should be noted that for most of the analysis we do, the optical density is of greater interest than the absorption. For a uniform density of atoms, n, having a homogeneous optical scattering cross section, σ, the optical density presented by the atoms to a beam passing through a length l of the cloud is defined by the equation $I = I_0 e^{-n\sigma l} = I_0 e^{-OD}$. This means that the atom density is proportional to the optical density. The relationship between optical density and absorption is $OD = -\ln(1-A)$. Using $1 - A = \frac{D_s}{D_B}$ from Eq. 2.1, we obtain

$$OD = -\ln\left(\frac{D_s}{D_B}\right).$$

It is easy to show that for small absorption, the optical density and the absorption converge to the same value. Since this is the same limit in which the noise calculation was performed, Eq. 2.1 remains true when A is replaced by OD.

2.6.2 Measuring the Absorption Spectra

Figure 2.4 illustrates how we extract, not only the absorption spectrum of our trapped atoms, but also how we track atom loss. Figures 2.4.a and 2.4.b are simply the result of zooming in on 5 seconds of the same data set depicted in Figure 2.3. The intensity dips occurring as the laser passes through the atomic resonance are clearly resolved in Figure 2.4.b. A much more useful way of viewing this data is to plot these intensity dips as a function of laser frequency instead of as a function of time.

Figure 2.4.c shows 5 seconds of probe intensity data plotted against the laser control voltage. In an ideal world, the laser control voltage would be strictly proportional to the laser frequency. In the real world, however, there is a lag between the control voltage sent to our Ti:Saph. and the frequency it produces. This leads to a hysteretic type effect that finds its way into our data. The two intensity dips visible in Figure 2.4.c are an artifact of this hysteresis. One of the dips corresponds to the laser passing through the resonance on the way up in frequency and the other dip corresponds to the laser passing through resonance on its way down.

We deal with this problem using one of two techniques. One technique is to simply discard all data corresponding to the laser scanning towards higher (or,

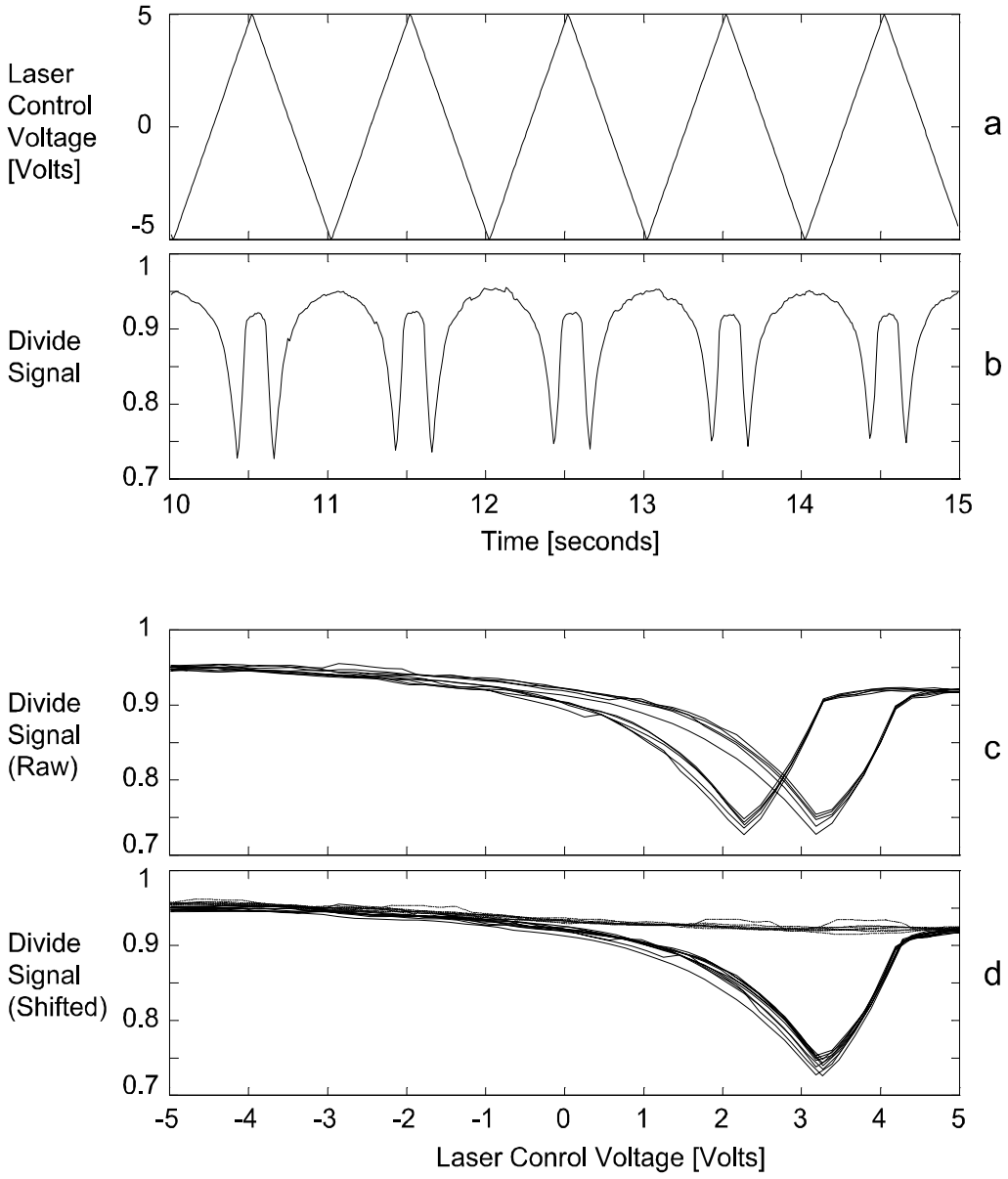

Figure 2.4: Raw data for obtaining the spectrum and temporal behavior of trapped atoms. **a)** Control voltage used to scan the laser **b)** Temporal behavior of absorption peaks caused by scanning the laser across atomic resonance. **c)** Raw spectrum obtained by plotting the divide signal against laser control voltage. Notice the disparity between scanning the laser up and down in frequency. **d)** The same spectrum with one of the absorption peaks shifted in frequency. A good overlap of upward and downward going spectra is observed. The straighter lines show a baseline spectrum obtained after the atoms have been removed.

equivalently, towards lower) frequencies. Whenever possible, however, we employ a different technique that allows us to use all the collected data. This technique involves separating the data into positive and negative going spectra. Simply shifting one of the these spectra by a fixed amount results in excellent overlap, as shown in Figure 2.4.d. This allows us to make full use of our data and eliminates (to first order) the hysteretic effects of our laser.

We did not fully investigate the character of this hysteresis. A possible concern is that, in addition to the observed offset of positive and negative going sweeps, there could be a nonlinearity between the control voltage and the laser frequency. We do not believe that such a nonlinearity, if it exists, seriously impacts our measurements. Measuring the absorption of Fermionic ^{53}Cr, we find the hyperfine splitting to be in good agreement with previously measured values [29] when a linear relationship between laser control voltage and frequency is assumed. This provides assurance that our laser scans are behaving as we expect, at least at the larger scanwidths used for observing the hyperfine structure.

The virtually flat traces in Figure 2.4.d show the spectrum of the probe laser taken during the baseline ($t > 32s$ in Figure 2.3.e). The difference between the two sets of traces in this figure is due to the absorption of the atoms. Eq. 2.1 can be used to extract the average absorption spectrum from 20 to 25 s. This spectrum can then be fit using a model of the probe beam passing through a Boltzmann distribution of

trapped atoms. From this fit, and independent knowledge of the oscillator strength of the transition, the peak density and temperature of the atoms can be extracted.

2.6.3 Measuring the Time Dependence

In the data sets taken to measure the inelastic scattering rates, we find that the shape of our measured spectra remains relatively unchanged as a function of time, indicating the atoms reach a steady state temperature. We use this fact to greatly simplify the process of measuring the time dependant density in our trap.

For distributions at constant η, (where η is the ratio of trap depth to atom temperature) the peak density in the trap will be proportional to the area under the optical density spectrum. For small absorptions, the optical density and absorption are essentially equal to each other, and the peak density in the trap is proportional to the area enclosed by the traces in Figure 2.4.d.

The time dependence of the density can be calculated as follows. We first define the scan range that contains the signal of interest. For the spectrum in Figure 2.4.d, this scan range might be set to be from 0 to 5 volts. Then, for each sweep the laser makes across the resonance, we calculate the mean of the divide signal across the scan range and call it $\langle D_s \rangle$. We then calculate the mean baseline over this same scan range and call it $\langle D_B \rangle$. In the limit of a spectrally flat baseline, the mean optical density over the scan range can be approximated by

$$\langle OD \rangle \simeq -\ln\left[\frac{\langle D_s \rangle}{\langle D_B \rangle}\right].$$

Since the optical density is proportional to the atom density in the trap, we can write an expression for the atom density at the time of the k'th sweep as

$$n_k \propto -\ln\left[\frac{\langle D_s\rangle_k}{\langle D_B\rangle_k}\right]$$

This equation is useful because if we know the density for one of the sweeps (call it k_0), the density for all other sweeps can be obtained,

$$n_k = n_{k_0}\frac{\ln\left[\frac{\langle D_s\rangle_k}{\langle D_B\rangle_k}\right]}{\ln\left[\frac{\langle D_s\rangle_{k0}}{\langle D_B\rangle_{k_0}}\right]} \tag{2.2}$$

Figure 2.5 shows a plot of Eq. 2.2 for the sample data set of this section. In this plot k_0 is defined by the first sweep that occurs after 10 seconds, and n_{k_0} has been arbitrarily set to unity.

2.6.4 Extracting Density Time Dependence

All the tools are now in place for extracting the time dependant density from a given data set. The first step in this process is to select a time window over which to measure a spectrum of the atoms. In our example data set, this time window is from 10 to 15 seconds. (See Fig. 2.4.d) After fitting this spectrum to obtain the density and temperature of the trapped spectrum, we can track the density time dependence by applying Eq. 2.2 to the data set. The extracted temperature and density time dependance are then ready to be analyzed to obtain a value for the two body loss rate coefficient. This is discussed in Chapter 3.

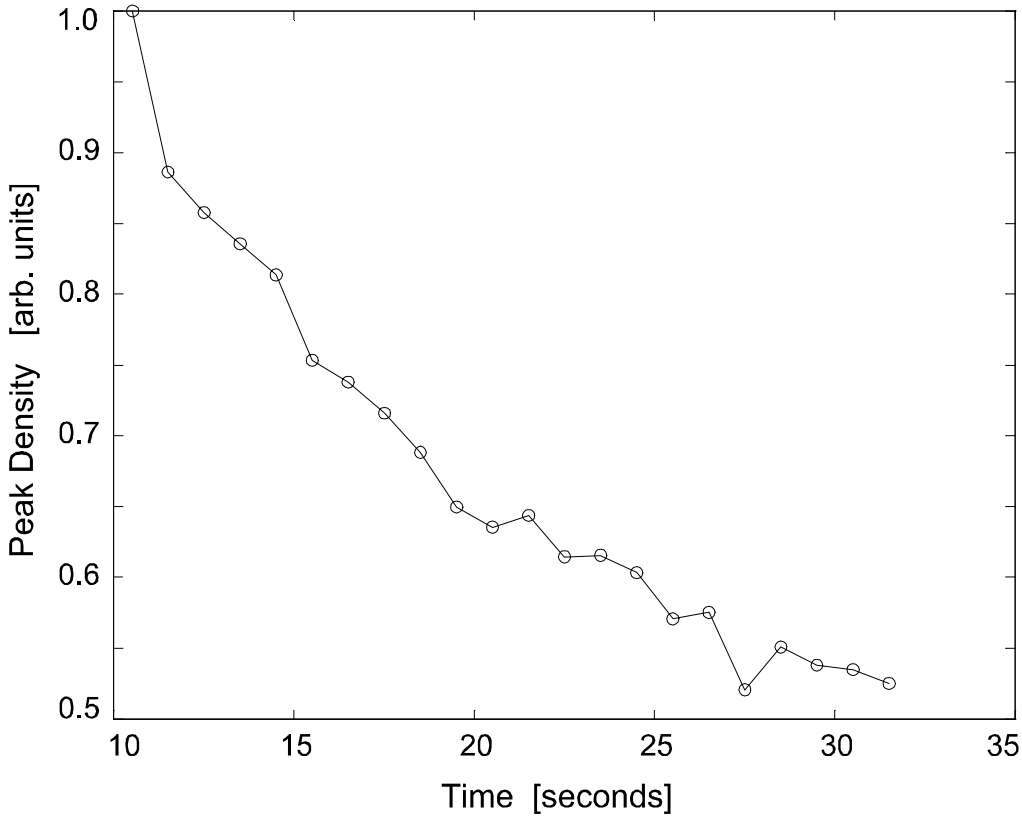

Figure 2.5: Each point in this time profile represents the average value of the optical density over a frequency window containing the absorption peak. The average optical density is proportional to the peak density in the trap.

2.6.5 Averaging over Data Sets

In order to improve the signal to noise ratio, data from several identical runs of an experiment can be averaged together. We use the following procedure to average our data sets.

Spectrum Averaging

We first extract an absorption spectrum for each data set as described above. During the time required for multiple runs of the experiment, the center frequency of the laser scan will often drift. This requires that we compensate for the drift by artificially introducing a frequency offset to each of the spectra we wish to average together. These offsets are manually selected by visually overlapping the spectra from each of the individual data sets. The spectra from each of the data sets are combined into one big data set and then binned in frequency. The mean and standard deviation is then calculated for each frequency bin. Figure 2.6 shows the result of this binning for the actual data used in determining the inelastic scattering rate at a trap depth of $18\ mK$. This spectrum is the average of thirteen data sets.

Time Profile Averaging

For each data set, we create a time profile plot like that of Figure 2.5. At the lower trap depths, the signal to noise ratio is too small for obtaining useful data. We circumvent this problem by averaging together the results obtained from several different runs of the experiment. To do this, we bin the optical density in time. The

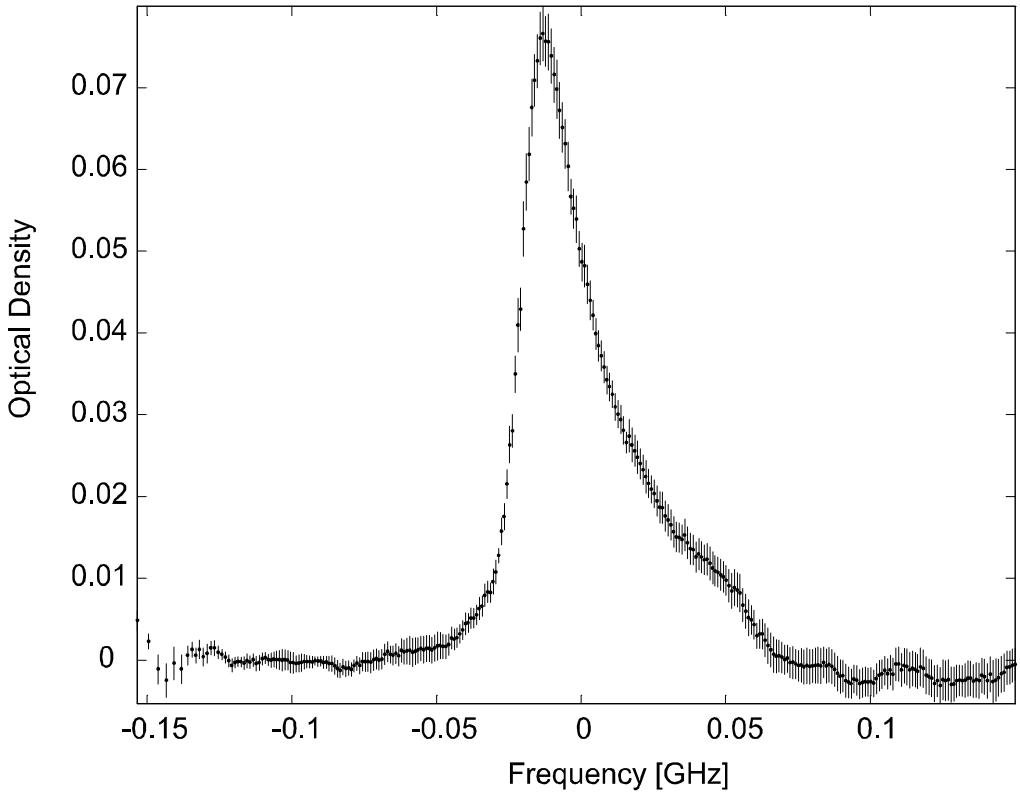

Figure 2.6: The spectrum obtained by averaging together 13 runs of the experiment. Averaging is performed by frequency binning the points of the combined spectra. The points represent the mean in each frequency bin and the vertical hash marks represent the standard deviations.

mean and standard deviation is calculated for each time bin. Examples of these average time profiles are shown in Chapter 3.

Chapter 3
Data Analysis Techniques

Once the data has been processed to obtain the spectrum and time dependant optical density, it can be analyzed to obtain a value for the two body loss rate coefficient. From this information, we can extract a value for the inelastic scattering rate coefficient.

3.1 Analysis Foundation

There are several assumptions and approximations that we make about our system when performing measurements of the inelastic scattering rates. The justification for each of these will now be discussed.

3.1.1 Assumptions

We assume that the only significant trap loss mechanisms are due to collisions between two chromium atoms. Other possible loss mechanisms that we neglect are collisions with background gas, three body recombination, and Majorana losses.

During the time our measurements are being taken, the cell wall temperature is $\lesssim 200\ mK$. If the extrapolated vapor pressure curve for the ^{4}He buffer gas in our cell is to be believed (see Appendix C), the background gas density is $\lesssim 1cm^{-3}$

in this temperature range. This background density is so small that any interaction between it and the trapped atoms can be safely neglected.

Majorana losses in our magnetic trap depend only on the size of the trapped cloud. The decay time of the resulting exponential loss would scale like

$$\tau \propto m\frac{\Delta\mu}{\mu}R^2$$

where m is the mass of the atom, μ is its magnetic moment, $\Delta\mu$ is the change in magnetic moment caused by the spin flip and R is the radius of the trapped cloud. Running the numbers for the smallest clouds we observe, the Majorana loss should be well below our ability to observe it [13].

Furthermore, the loss we observe from our trap fits quite well to the two-body loss equation. This provides experimental justification not only for eliminating the one-body loss processes due to background gas collisions and Majorana losses, but also three-body collisional processes.

3.1.2 Approximations

Density Distribution Approximation

As will be shown in Chapter 5, there are two approximations that can be used to model our trapped gas. The "large η approximation" is valid for large ratios of trap depth to temperature (this ratio is called η). In the low η regime, where this approximation fails, one can model the trapped gas as if it were confined in a spheri-

cally symmetric trapping potential. This model is, at best, a crude approximation to the ellipsoidal-looking equipotential surfaces in our actual magnetic trap. However, the spherical trap model produces analytic expressions for important parameters of the gas. Since these expressions remain valid at low η, we will use the spherical trap model, detailed in Chapter 5, to calculate the average energies, collision rates, etc. These parameters are needed to extract the scattering rate coefficients from any given data set.

Spectral Fit Approximations

In the spectral fits described below, we assume that the atom density takes the form of a Boltzmann distribution in potential energy. As will be discussed at length in Chapter 5, phase space consideration can significantly alter the the atom distribution from its ideal Boltzmann shape. This is particularly as the ratio between trap depth and atom temperature becomes small. In the terminology developed in Chapter 5, we find that using the "large η approximation" for the density distribution produces better fits to the observed spectra than using the results of the linear spherical trap model. A possible explanation for this, is that the simulations used to create the spectral fits to our data incorporate the actual magnetic fields present in our spherical quadrupole trap. The selection rules for scattering polarized light combine with the effects of non-uniform field gradients to make the simulated spectrum quite sensitive to the actual geometry of the magnetic field. It is possible that this fact causes the magnetic field geometry to play a more prominant role in determin-

ing the character of the observed spectrum than it does in determining the dynamics of the trapped gas.

Homogeneous Scattering Cross Sections

We assume throughout our analysis that the elastic and inelastic scattering cross sections are homogeneous throughout the trap. However, in reality, it is quite possible that the magnitude of the scattering cross sections depends on magnetic field. Given the steep magnetic field gradients in our trap, the existence of field dependant cross sections could seriously impact not only the calculation of average scattering rates, but also the average energies of atoms being lost due to both evaporation and spin-changing collisions. This would modify the numbers we obtain for the scattering rate coefficients.

Ongoing theoretical investigation seems to suggest that the inelastic scattering rate does indeed depend on magnetic field. However, at the writing of this thesis, we have no information, either theoretical, or experimental, that would allow us to characterize the field dependence of the elastic and inelastic scattering cross sections. Because of this, we approximate the scattering cross sections as homogeneous and await theoretical results to refine this approximation.

3.2 Fitting Techniques

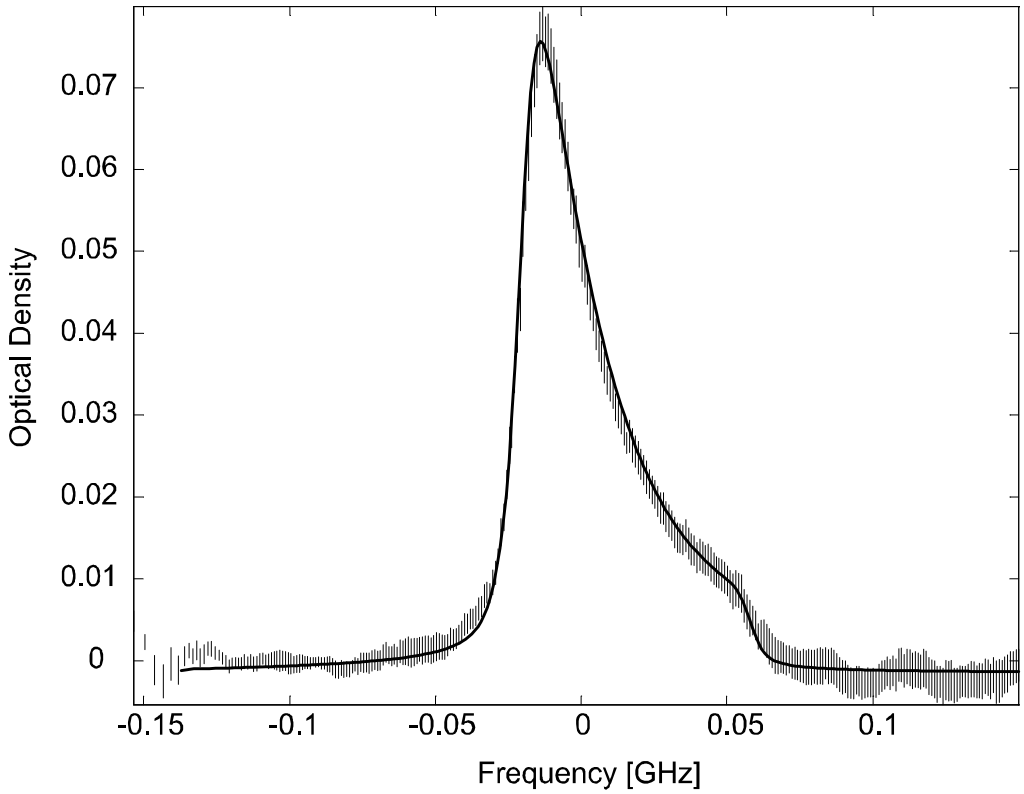

Figure 3.1: The solid strace is the result of fitting a model of a Boltzmann distribution to the spectrum measured in our trap. The data is the same as that shown in Figure 2.6. The density and temperature values resulting in the best fit are $n_0 = 7.5 \times 10^8$ cm^{-3} and $T = 6.4\ mK$ respectively.

3.2.1 Spectral Fits

Figure 3.1 shows a sample fit to the same spectrum shown in Figure 2.6. The solid line is a simulated spectrum generated by assuming the atoms maintain a Boltzmann distribution in potential energy. The method used in constructing the simulated spectra is discussed at length in the thesis of Jonathan Weinstein [13]. We adopt this method, with a few modifications, to simulate our spectra. These modifications will now be discussed.

Low Trap Depth Modifications to Spectral Fit

There are three physical phenomena which become important to our spectrum simulations at low trap depths. These are, Doppler broadening, natural linewidth broadening, and the effects of gravity.

At large trap depths, the Zeeman broadening in the magnetic field of the trap dominates our spectral features. The spectrum is calculated as if atoms at any given magnetic field produced a delta function spectrum at their resonant frequency. Scaling the strength of this delta function by the atom density at that particular field and properly taking into account the field gradient, and polarization effects, the contribution these atoms make to the total absorption spectrum can be calculated. This is the method described in the thesis of Jonathan Weinstein.

As the trap depth is lowered, however, approximating the atomic absorption spectrum at a given field by a frequency delta function becomes less valid. The correct line shape must account not only for the natural linewidth, but for Doppler broadening as well. If we define a unit-normalized Lorentzian, $G(\nu, \nu')$ to represent the natural linewidth of the detection transition and define a unit-normalized Gaussian $D(\nu', \nu'')$ to represent the Doppler broadening, the real spectrum in the trap, $A(\nu)$, is obtained by convolving these profiles with the results of the delta function approximation, $A_\delta(\nu'')$, to obtain

$$A(\nu) = \iint G(\nu, \nu')\, D(\nu', \nu'')\, A_\delta(\nu'') d\nu'' d\nu'.$$

This convolution is added to the simulation code used to model our data.

An additional complication presents itself for very low trap depths. For ^{52}Cr, the gravitational potential gradient is $0.6\frac{mK}{cm}$. At the lowest trap depths in our experiment, $\sim 4.5\ mK$, the difference in gravitational potential between the top and bottom of our trap becomes comparable to the magnetic potential. We modify the spectrum simulation code to account for the distortion this presents to the trapping potential.

Implementing the Spectral Fit

The input parameters for the simulation include trap depth, peak density, temperature, beam trajectory through the trap, and beam parameters such as polarization, and beam diameter. For each set of data we take, the beam parameters are measured. The precision to which we control our magnet current sets our trap depth to a known value. We take great pains when setting up the experiment to ensure that the beam is passing through the center of the trap cloud. This leaves only the temperature and peak density as free floating parameters in the fit to our spectra. (Note that at our lowest trap depths, trapped fluxes in our superconducting magnet reduce the precision to which we know our trap depths. This has implications on the number of free floating parameters. See discussion on error analysis.)

We use a non-linear least squares routine to determine the best fit between the simulation and the data. From this, we extract the peak density and temperature of the trapped atoms. This, combined with a knowledge of the trap depth and physical volume of the trap, allows us to determine η and number of confined atoms.

3.2.2 Time Decay Fits

Based on our assumptions that the loss from our trap is due strictly to chromium-chromium collisions, and that the atom density is proportional to the optical density, we obtain a two-body loss equation for the optical density,

$$\frac{d\left(OD\right)}{dt} = -g_{od}\left(OD\right)^2. \tag{3.1}$$

The solution to this equation can be written as

$$OD\left(t\right) = \frac{1}{1 + g_{od}\left(t - t_0\right)}. \tag{3.2}$$

Writing the proportionality between peak atom density and optical density as $OD = \beta n_0$, we can substitute into Eq. 3.1 to arrive at

$$\frac{dn_0}{dt} = -\beta g_{od} n_0^2.$$

If the peak density and optical density are measured over some time interval, resulting in values of $\overline{OD}$ and $\bar{n}_0$, the proportionally constant, β, can be measured, and we can write

$$\frac{dn_0}{dt} = -g_{2b} n_0^2$$

where the two body loss rate coefficient is given by

$$g_{2b} = \frac{\overline{OD}}{\bar{n}_0} g_{od}. \tag{3.3}$$

The heavy line in figure 3.2 shows a fit of Eq. 3.2 to the data obtained by averaging together the optical density time profiles from several data sets. Fits such as this one provide values for g_{od}. The two lighter traces show best fits for 1-body, $n =$

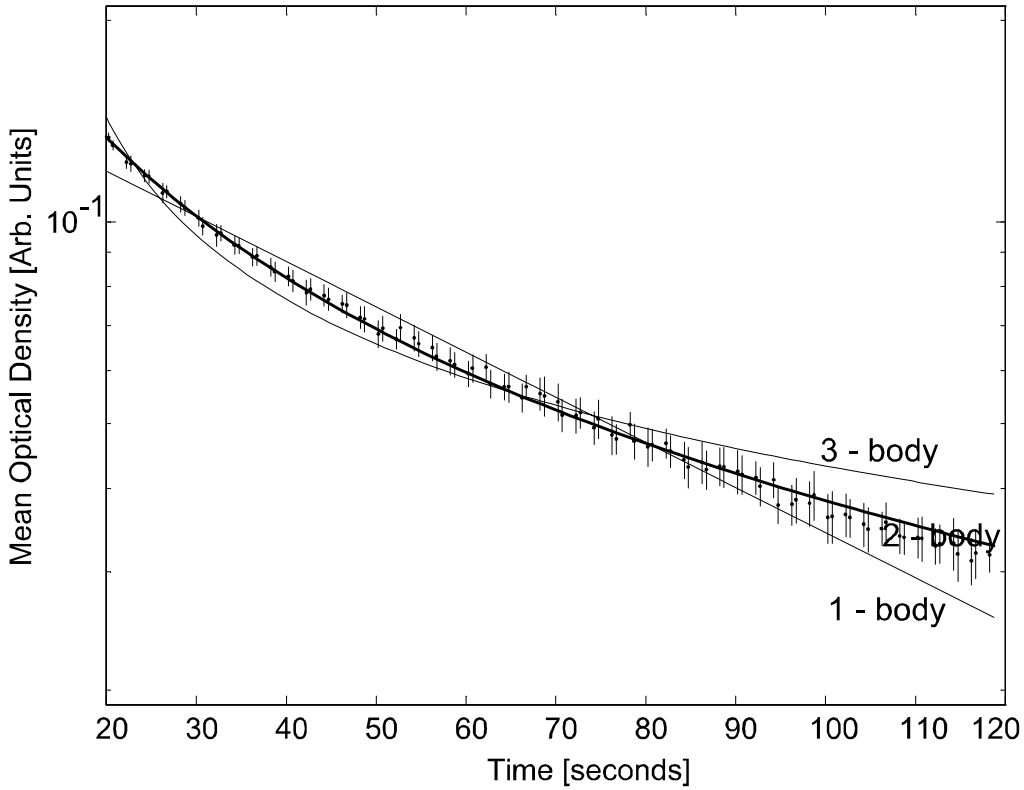

Figure 3.2: The solid lines are one, two and three body fits to the average measured time profile for 21 data sets at a trap depth of $54\ mK$. The averaging is performed by binning the combined data points in time. The points and vertical hash marks represent the mean and standard deviation for each time bin. Our data is best fit to a two-body loss.

$\exp\left[\left(t-t_0\right)/\tau\right]$, and 3-body, $n=\left[2K_3\left(t+t_0\right)\right]^{-1/2}$ decay respectively. The two-body equation clearly provides the best fit to the data. (note 3 body equation is $\dot{n}=-K_3n^3$ which has solution $n=\left[2K_3\left(t+t_0\right)\right]^{-1/2}$.

3.3 Error Analysis

3.3.1 Least Squares Fitting

Performing a least squares fit to an arbitrary function is a non trivial process. An excellent treatment of this procedure can be found in chapter 8 of the book on error analysis and fitting procedures written by P.R. Bevington and D. K. Robinson [30]. The least squares fitting procedure described in Bevington calls for the minimization of a quantity called χ^2, which we will now define.

Suppose there exists a model that gives a functional relationship between two variables. Take, for example, the two-body loss equation that gives the optical density in our trap as a function of time, Eq. 3.2. Given quantities we can measure (e.g. time and optical density) we seek the "best" values for the non-measured quantities in the functional relation (e.g. g_{od} and t_0).

Lets say a typical measurement can be described by two variables. One of these we'll call the independent variable (in our case, time). The i'th measurement of this variable is denoted by x_i. The other variable is called the dependant variable (in our case, optical density), and the results of the i'th measurement will be written as y_i. Let the the expected functional relationship between these variables be given by $y\left(a_1, a_2, ..., x\right)$, where the a_i are parameters that enter into the fitting equation. (In our case, these would be g_{od} and t_0). In general, the dependant variable should be the variable with the greatest uncertainty. For each value of the dependant variable,

y_i, let there be an associated uncertainty σ_i. We can then make the definition

$$\chi^2 (a_1, a_2, ...) \equiv \sum_i \left\{ \frac{1}{\sigma_i^2} [y_i - y (a_1, a_2, ..., x_i)]^2 \right\}. \tag{3.4}$$

Stated in words, χ^2 is the sum of the squares of the ratio between the deviation of the measurement from its predicted value and the uncertainty of the measurement. A least squares "best fit" is obtained by finding the values of $a_1, a_2, ...$ that result in a minimum value of χ^2.

In our analysis, a least squares fit is obtained by using the canned routine "fminsearch" provided by the MATLAB software we use to manipulate our data sets. This routine, however, does not calculate the uncertainties in the parameters $a_1, a_2, ...$ We must calculate these ourselves. On page 145 of the book by Bevington, [30] we find a clear statement that varying the parameter a_i by one standard deviation from it's best value (i.e. minimum χ^2), results in increasing χ^2 by one. That is, $\chi^2 \rightarrow \chi^2_{\min} + 1$ for $a_i = (a_{\min})_i \pm (\sigma_a)_i$.

Bevington refines this argument in Chapter 11 of his book for the case of a multi-parameter fit. His explanation can be summarized as follows. Imagine a least squares fit has been performed and the best values for the parameters $a_1, a_2, ...$ have been found. Consider what happens by varying the parameter a_1 away from its optimum value. This results in an increase in χ^2. But now imagine keeping a_1 fixed at its new deviated value and readjusting the other parameters $a_2, a_3, ...$ to compensate for this increased χ^2. This readjustment of the other parameters will allow a_1 to be dragged further away from its optimum value while maintaining χ^2

below some threshold value. The 1 σ uncertainty of the parameter a_1 is given by the maximum distance it can be dragged from its optimum value while adjusting the other parameters to maintain χ^2 below the "1 σ threshold" of $\chi^2 \leq \chi^2_{\min} + 1$.

3.3.2 Least Squares Fitting Applied

Calculating χ^2

In our experiment, each measurement of the inelastic cross section involves averaging the results from several runs of the experiment. This averaging procedure not only improves our signal to noise, but also provides an estimate of our statistical uncertainties. The mean and standard deviations obtain from these averages and demonstrated in Figures 3.1 and 3.2 are used in calculating the χ^2 of Eq. 3.4.

Floating Parameters in Spectral Fits

At all but the lowest trap depths, the floating parameters in our spectral least squares fit are the temperature and peak density. At lower trap depths, however, we allow the trap depth itself to become a floating parameter. This is part of our method of accounting for the uncertainties in our trap depth due to trapped magnetic fluxes in our superconducting magnet.

As the current through our magnet is reduced to obtain ever decreasing trap depths, a point is reached where the magnetic field due to the current becomes equal to the magnetic field arising from trapped fluxes. The magnetic fields produced by

the trapped fluxes are measured to be on the order of $10\ gauss$ [13]. In the absence of trapped fluxes, a $10\ gauss$ ($4\ mK$) trap depth corresponds to a magnet current of 22 mA. The lowest current we use in taking our measurements is 25 mA. At this current, we expect the trapped fluxes to alter our trapping potential in a way that is not completely understood. As a first order approximation backed by earlier measurements of trapped fluxes in very similar magnets, we assume that the trapped fluxes produce a magnetic field that has roughly the same geometry as the trapping field. In this approximation, the net effect of the trap fluxes is to produce magnetic fields consistent with an altered, or "effective" current flowing through the coils. We use our χ^2 fitting routine to determine the size of this effective current. As will be shown in chapter 4, our three lowest magnet currents, 25, 50 and $70\ mA$, produce better fits to the data if we introduce a $+25\ mA$ offset to the magnet current. This is roughly consistent with our expectation for the size of the trapped fluxes.

The utility of allowing the trap depth to float in our least squares fit goes beyond characterizing the size of our trapped fluxes. By adding an additional floating parameter in the fits, the calculated uncertainties in temperature and density are increased. This is because the additional floating variable allows dragging any given fit parameter, say, the temperature, further away from its optimum value while maintaining $\chi^2 \leq \chi^2_{\min} + 1$. This allows us to estimate the uncertainty in our measurements due to the effects of trapped fluxes in our superconducting magnet.

Floating Parameters in Time Profile Fits

Fitting our time decay data is considerably more simple than fitting our spectra. We fit our decay curve to the equation

$$OD\,(t) = \frac{1}{1 + g_{od}\,(t - t_0)}$$

and use g_{od} and t_0 as the free floating parameters. The uncertainties are calculated as detailed in the discussion on least squares fitting above.

3.3.3 Error Propagation

We now trace the calculational steps required in obtaining the inelastic rate coefficient from our measurements. This is done to explicitly demonstrate the associated error propagation.

From the spectral fits, we obtain values for the peak density and temperature of the trapped atoms. We denote these, along with their uncertainties as $n_0 \pm \sigma_{n_0}$ and $T \pm \sigma_T$. The mean optical density during the time required to take the spectral measurement is given by $\overline{OD} \pm \sigma_{OD}$.

From the two-body fits of the optical density time profiles, we obtain a value for the optical two-body loss rate coefficient and its uncertainty, $g_{od} \pm \sigma_{g_{od}}$.

From the expression for the two body loss rate coefficient,

$$g_{2b} = \frac{\overline{OD}}{\bar{n}_0} g_{od},$$

the uncertainties are correctly propagated according to

$$\begin{aligned}\sigma_{g_{2b}} &= \sqrt{\left(\frac{\partial g_{2b}}{\partial \overline{OD}}\right)^2 \sigma_{OD}^2 + \left(\frac{\partial g_{2b}}{\partial g_{od}}\right)^2 \sigma_{g_{od}}^2 + \left(\frac{\partial g_{2b}}{\partial \bar{n}_0}\right)^2 \sigma_{n_0}^2} \\ &= \sqrt{\left(\frac{g_{od}}{\bar{n}_0}\right)^2 \sigma_{OD}^2 + \left(\frac{\overline{OD}}{\bar{n}_0}\right)^2 \sigma_{g_{od}}^2 + \left(\frac{g_{od}\overline{OD}}{\bar{n}_0^2}\right)^2 \sigma_{n_0}^2}.\end{aligned}$$

These equations are used to produce the error bars for our measurements of the inelastic scattering rate coefficients.

Chapter 4
Experimental Results

4.1 Scattering Rate Measurements

Figure 4.1 shows a summary of our chromium scattering rate measurements. The points marked with open circles are measurements of the elastic scattering rate coefficient. Previous measurements of the inelastic scattering rate coefficients are designated by the filled circles. The points enclosed by the large triangles are the results of our most recent measurements of the inelastic scattering rate coefficient.

Our measurements of the elastic scattering rate coefficients are described in the thesis of Jonathan Weinstein [13]. Briefly, we use a resonant laser to selectively remove atoms via optical pumping from a given region of our trap. This distorts the atom distribution from its "equilibrium" Boltzmann distribution. The elastic scattering rate is obtained from the timescale over which the distorted distribution relaxes back to its thermal Boltzmann configuration.

Our previous measurements of the inelastic rate coefficient (solid circles) were obtained by analyzing single runs of the experiment. The analysis is virtually the same as that described in this thesis. There are subtle differences in the analysis due to the fact that the measurements were obtained from single runs of the experiment. These measurements are detailed in the thesis of Jonathan Weinstein.

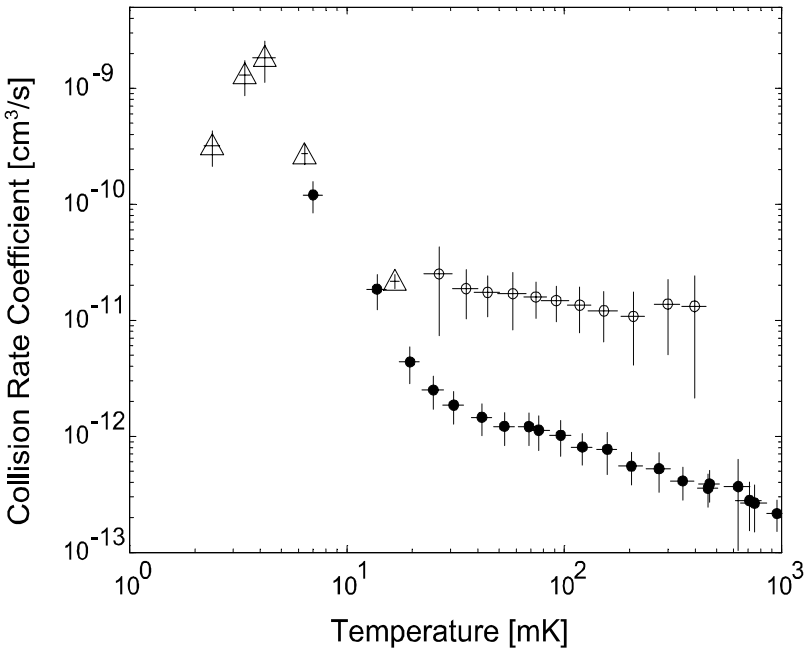

Figure 4.1: Summary plot of measured ^{52}Cr-^{52}Cr collision rates. The points enclosed by triangles show the most recent measurements of the inelastic scattering rate coefficient described in this thesis. The circles indicate previously reported values of the elastic (open circles) and inelastic (filled circles) collision rate coefficients measured at higher temperatures. [13]

Our latest experiments extend our measurements to lower temperatures. The low densities obtained at these lower temperatures require averaging together the results of several runs of the experiment to obtain sufficient signal-to-noise ratios for making the measurements.

4.2 Supporting Data

4.2.1 300 mA Data

Figure 4.2 shows the measured spectrum of our trapped atoms at a magnet current of $300\ mA$. At this current, the trap depth is about $50\ mK$. The data is portrayed by vertical hash marks representing the statistical uncertainty of the optical density. The solid line is the result of a least squares fit from the spectrum simulation.

On either side of the large absorption peak from the trapped ^{52}Cr isotope, the smaller absorption peaks due to other isotopes can be seen. We have previously observed these isotopes in our trap [13]. Our simulation only takes into account the absorption due to the ^{52}Cr in our trap. This is responsible for the disparity between the measured and simulated spectral shapes.

Figure 4.3 shows the time profile of the ^{52}Cr absorption peak. The data is again shown with the statistical error bars. The two-body decay fit is shown by a solid line. At this trap depth, the data fits quite well to the two-body loss equation.

The ability to resolve the different chromium isotopes allows us to compare their loss rates at this trap depth. Figure 4.4 shows the measured time profile for trapped ^{53}Cr atoms that has been scaled to overlap the time profile for the ^{52}Cr atoms. As can be seen, the signals from the two isotopes exhibit similar decay in the trap.

We don't believe the presence of ^{53}Cr in the trap contributes significantly to the observed loss dynamics of ^{52}Cr. The high quality of the two-body fit for the ^{52}Cr isotope, Figure 4.3, indicates that the dominant loss process is consistent with two-body ^{52}Cr-^{52}Cr interactions. Additionally, in our previous experiments, we observed

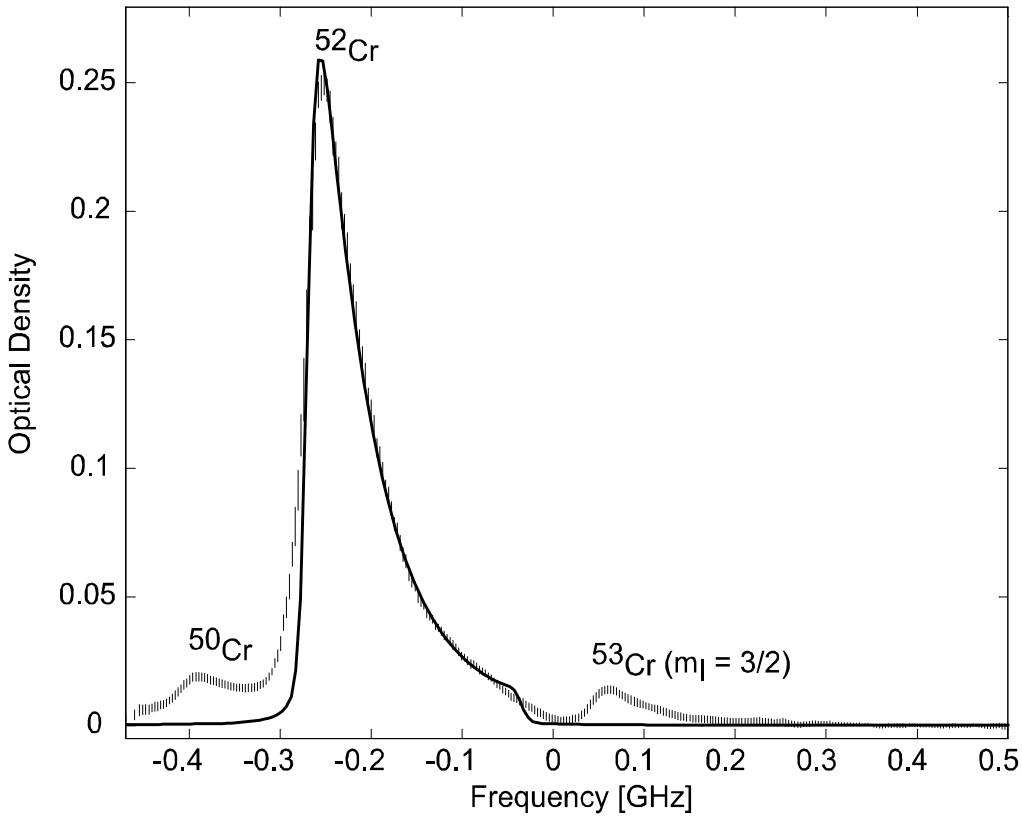

Figure 4.2: The vertical hash marks represent the result of averaging together 21 experimental runs at a trap depth of $300\ mA$, or $54\ mK$. The spectrum is taken from 20 to $25\ s$ after the ablation pulse. The main spectral feature is caused by ^{52}Cr absorption. The smaller features on either side are due to absorption from the ^{50}Cr and ^{53}Cr isotopes. The solid line is the spectral fit to the ^{52}Cr spectrum which gives temperature and density values of $T = 16\ mK$ and $n_0 = 6.9 \times 10^9$ respectively.

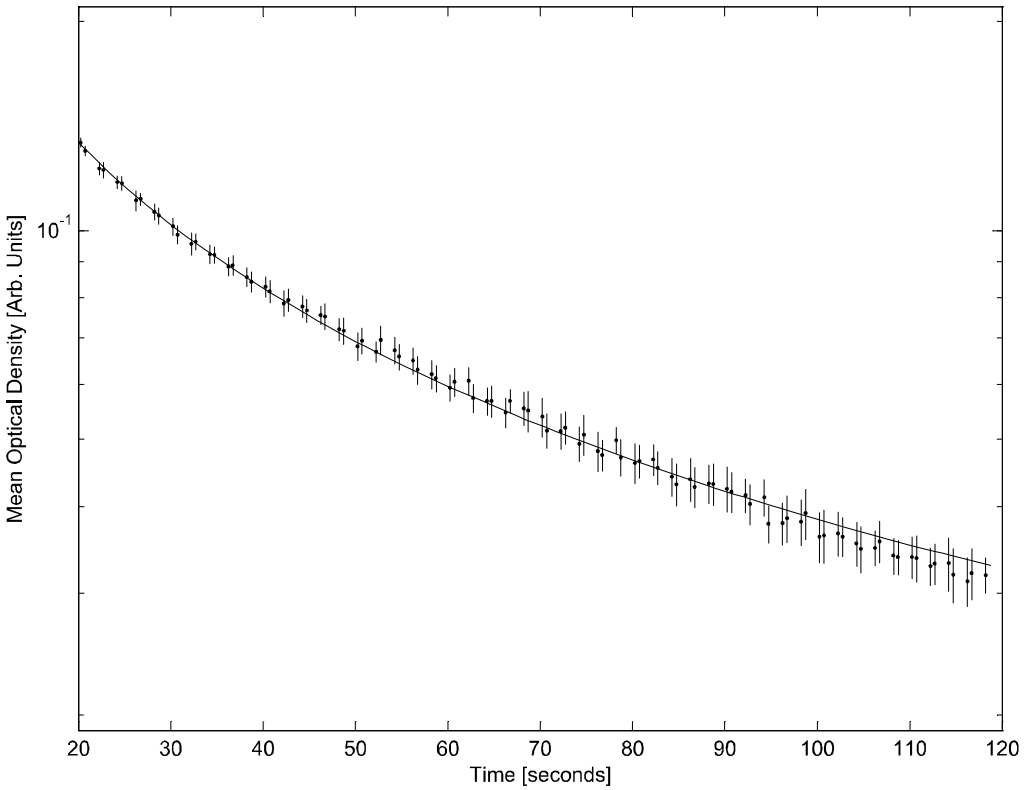

Figure 4.3: The hash marks and points are the mean and standard deviation obtained by time binning the combined data from 21 runs of the experiment at a trap depth of $300\ mA$ or $54\ mK$. The $300\ mA$ spectrum shown in Figure 4.2 shows the average spectrum of this data taken from 20 to 25 seconds. The solid line is a fit to a two body decay resulting in best values of $g_{od} = 0.2325\ s^{-1}$ and $t_0 = -7.842\ s$.

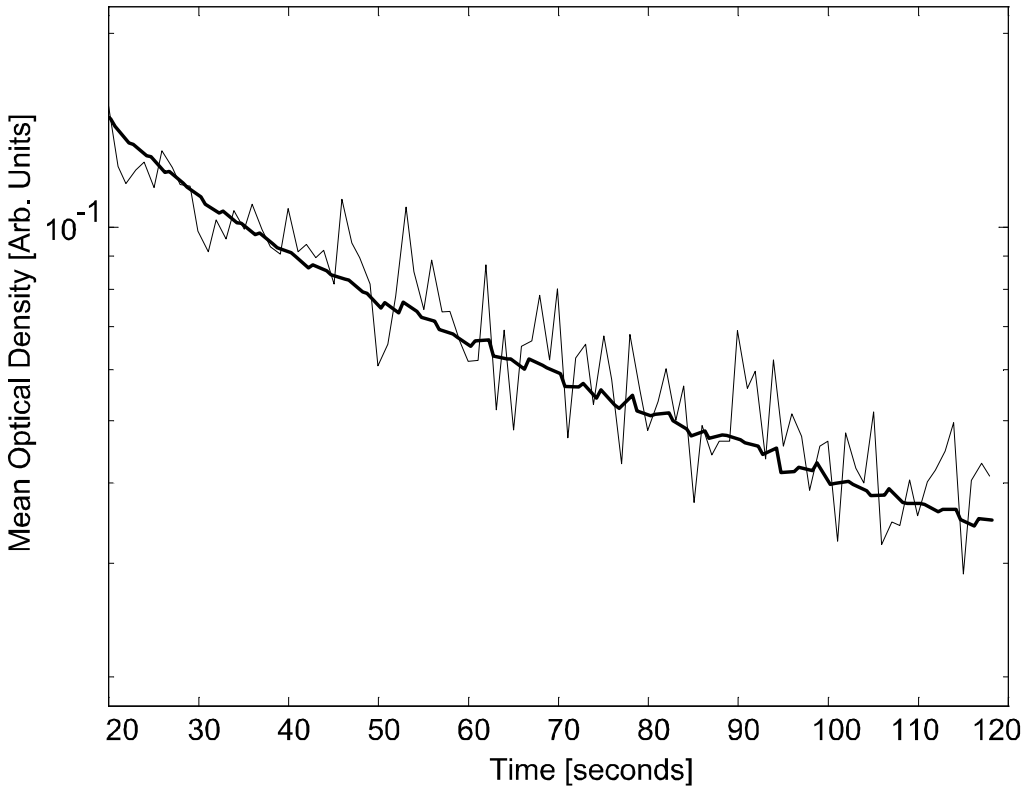

Figure 4.4: The heavy line is the optical density time profile of trapped Bosonic ^{52}Cr. The lighter trace is the result of scaling the time profile of Ferminic ^{53}Cr by a constant to obtain the best overlap. Given the signal to noise, we find the temporal behavior of the Fermion to be indistinguishable from that of the Boson.

the ^{52}Cr loss rate to remain unchanged by removal of ^{53}Cr from the trap. These checks, of course, leave the possibility that the ^{52}Cr-^{53}Cr collision rate is very close, or equal, to the ^{52}Cr-^{52}Cr collision rate, but this would not change our results.

4.2.2 100 mA Data

Figure 4.5 shows the measured spectrum of atoms confined in the $18\ mK$ deep trap provided by a magnet current of $100\ mA$. The ability of our spectrum simulation to accurately represent the physics occurring in our trap is demonstrated by the excellent agreement between the two curves in this figure. The reduced Zeeman broadening at this trap depth allows us to zoom in on the spectrum of the ^{52}Cr isotope, thereby eliminating any distortion arising from ^{53}Cr. Furthermore, at this trap depth, the magnetic fields due to trapped fluxes are not strong enough to significantly distort the the shape of the trap.

The $100\ mA$ time profile is shown in Figure 4.6. Notice that the relative size of our error bars is increasing as we reduce our trap depth. This lack of signal to noise doesn't allow us to measure our optical density over multiple orders of magnitude. This makes it difficult to distinguish between exponential and two-body loss. Although the shown two-body curve fits our data quite well, a straight line due to exponential one-body loss could easily be drawn through our error bars. Since we have no physical reason to introduce a one-body loss mechanism, we assume that our observed atom loss is due to two-body processes.

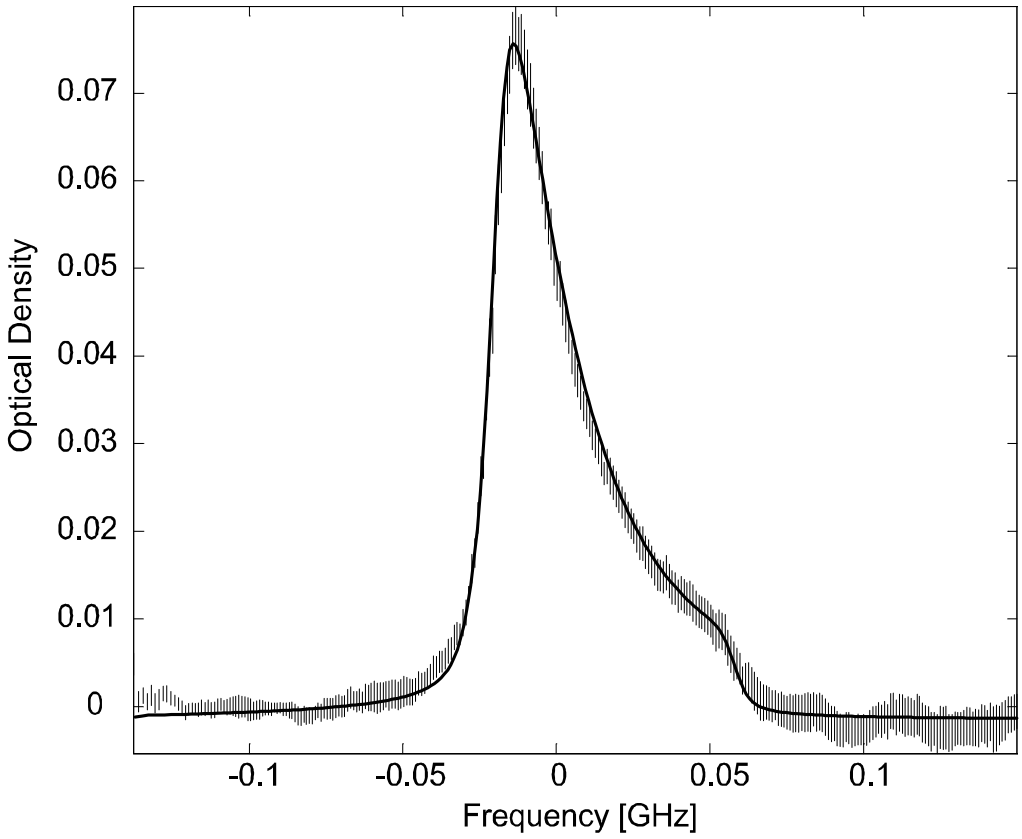

Figure 4.5: The vertical hash marks represent the result of averaging together 13 experimental runs at a trap depth of $100\ mA$, or $18\ mK$. The spectrum is taken from 20 to 25 s after the ablation pulse. The solid line is a fit to the ^{52}Cr spectrum which gives temperature and density values of $T = 6.4\ mK$ and $n_0 = 7.5 \times 10^8\ cm^{-3}$ respectively.

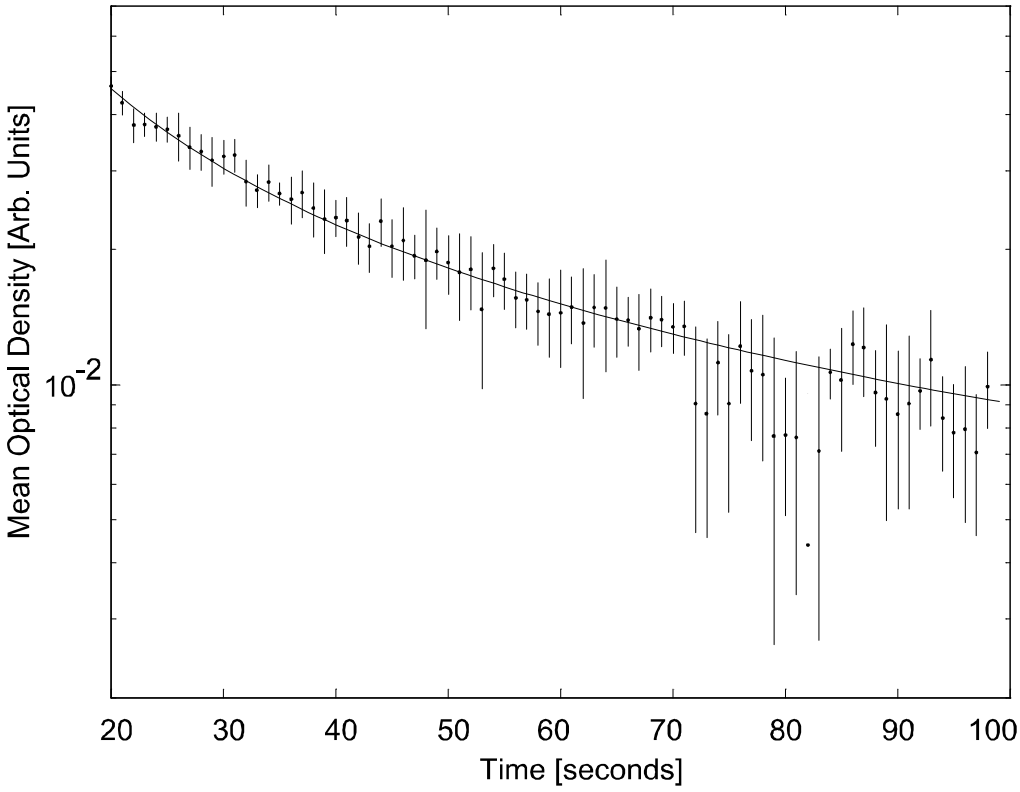

Figure 4.6: The hash marks and points are the mean and standard deviation obtained by time binning the combined data from 13 runs of the experiment at a trap depth of $100\ mA$ or $18\ mK$. The $100\ mA$ spectrum shown in Figure 4.5 is the average spectrum of this data taken from 20 to 25 seconds. The solid line is a fit to a two body decay resulting in best values of $g_{od} = 1.106\ s^{-1}$ and $t_0 = 1.17\ s$.

4.2.3 70 mA Data

Reducing our magnet current to $70\ mA$ ($13\ mK$ trap depth for $70\ mA$) results in a further decrease of the signal to noise. Additionally, fields arising from trapped fluxes in our superconducting magnet begin to effect our measurement. Figure 4.7 show the result of two separate simulations superimposed on our measured spectrum. The heavy line assumes that our trapped fluxes act to add a $25\ mA$ effective current to the $70\ mA$ provided by our power supply. The lighter line is the result of running the simulation assuming the trapping fields come only from the $70\ mA$ of supplied current. As can be seen, the addition of the effective current coming from trapped fluxes results in only a slight improvement in the quality of the fit.

The 70 mA time profile shown in Figure 4.8 now spans only about a factor of five in optical density. The ability to convincingly distinguish between one-body and two-body behavior is essentially gone. However, we still have no physical reason to abandon our two-body loss assumption and fit the decay accordingly.

4.2.4 50 mA Data

At a magnet current $50\ mA$ ($9\ mK$ trap depth) the trapped fluxes are able to appreciably modify the trapping potential. Running our spectrum simulations with an additional $25\ mA$ effective current (to account for trapped fluxes) produces a noticeably better fit than running the simulation using only the $50\ mA$ applied current.

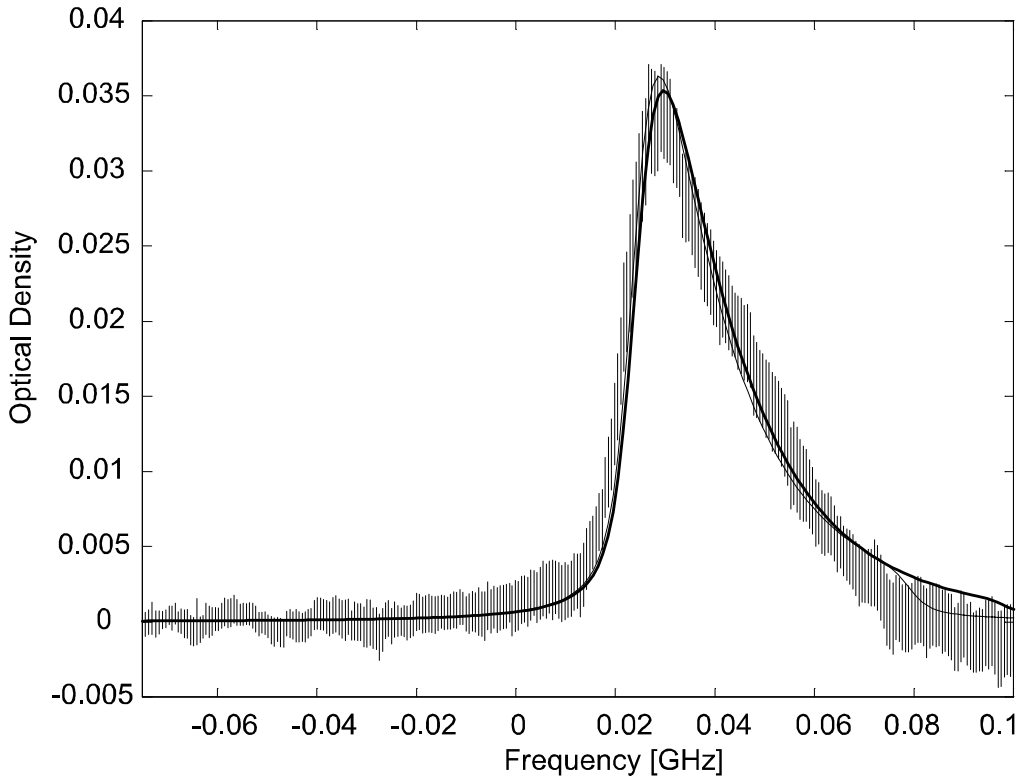

Figure 4.7: The vertical hash marks represent the result of averaging together 20 experimental runs at a trap depth of $70\ mA$, or $13\ mK$. The spectrum is taken from 20 to $25\ s$ after the ablation pulse. The heavy solid line is a fit to the ^{52}Cr spectrum assuming the trapped fluxes add an effective current of $25\ mA$ to the current supplied to the magnet. This fit gives temperature and density values of $T = 6.4$ mK and $n_0 = 7.5 \times 10^8\ cm^{-3}$ respectively. The ligher solid line is the fit obtained without accounting for trapped fluxes in any way. It gives values of $T = 4.4\ mK$ and $n_0 = 3.8 \times 10^8\ cm^{-3}$.

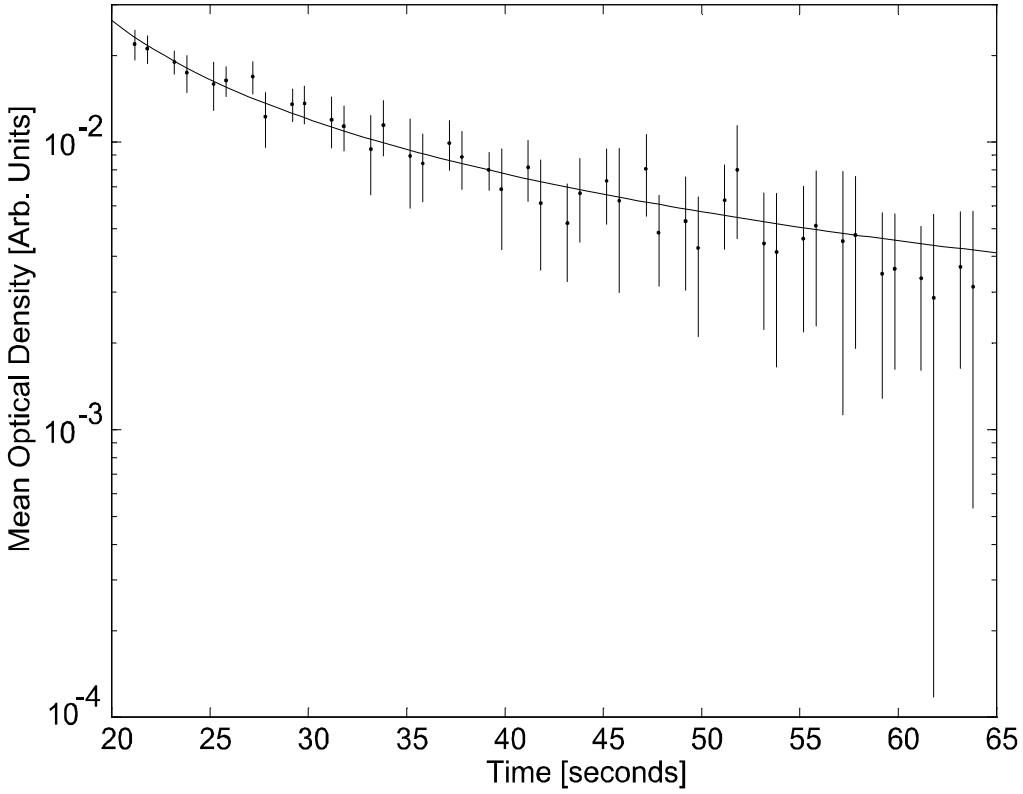

Figure 4.8: The hash marks and points are the mean and standard deviation obtained by time binning the combined data from 13 runs of the experiment at a trap depth of $70\ mA$ or $13\ mK$. The $70\ mA$ spectrum shown in Figure 4.7 is the average spectrum of this data taken from 20 to 25 seconds. The solid line is a fit to a two body decay resulting in best values of $g_{od} = 4.557\ s^{-1}$ and $t_0 = 11.93\ s$.

Figure 4.9 shows a plot of these two fits. Note that while the peak densities obtained from the two fits are different, the temperature remains relatively unchanged.

The $50\ mA$ time profile is shown in Figure 4.10. Although the two-body fit passes through the points quite well, the optical density only varies by a factor of four. By itself, this data does not support the use of a specific functional form for the loss. We must again rely on our assumption that the loss is two-body in nature.

4.2.5 25 mA Data

Although we do observe signal at lower trap depths, the lowest magnet current at which we conduct our measurements is $25\ mA$ ($5\ mK$ trap depth). At this low current, we believe the trapped fluxes in our magnet are significantly modifying the trapping potential. Shown in Figure 4.11 is our data superimposed on the results of two spectral simulations. As can be seen, introducing the $25\ mA$ effective current to mimic our trapped fluxes results in a much better fit to the measured spectrum.

The only information we have about the trapped fluxes is that their magnitude is roughly $10\ gauss$ [13]. This is consistent with the $25\ mA$ effective current added to our simulations. We do not know exactly how these trapped fluxes influence the shape of our trap. Because of this, it would be pointless to take measurements in a regime where the trapping potential would be dominated by fields caused by the unpredictable trapped fluxes. This sets the limit on how low we can ramp our trap depth.

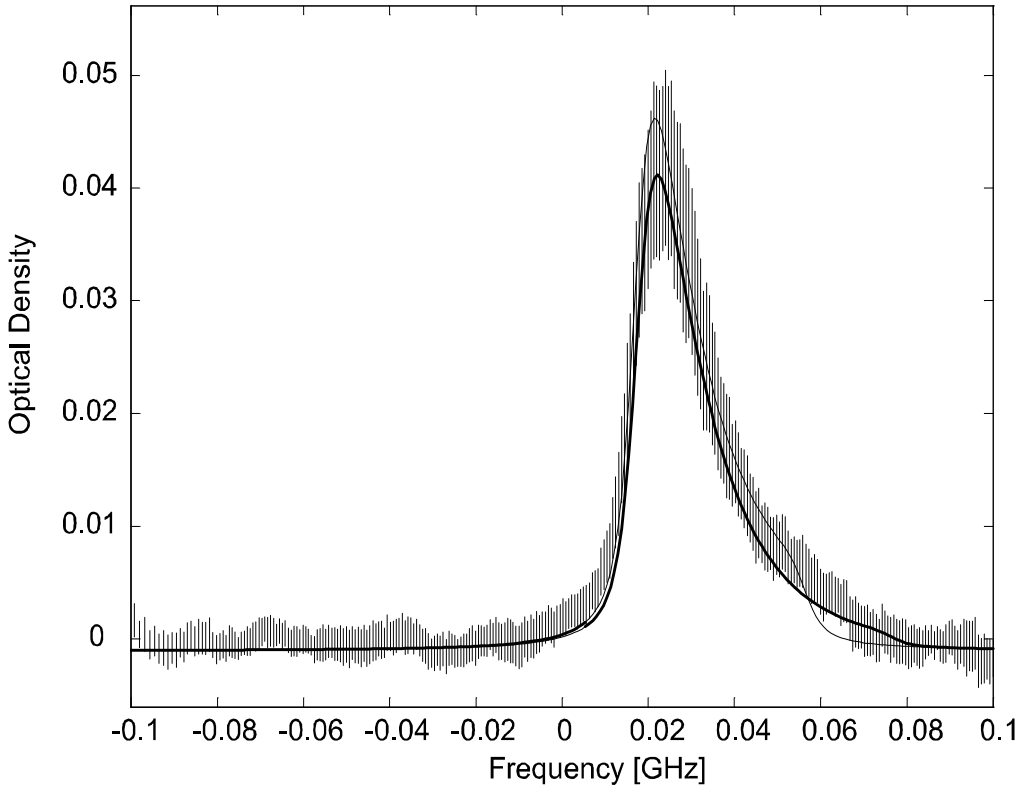

Figure 4.9: The vertical hash marks represent the result of averaging together 28 experimental runs at a trap depth of $50\ mA$, or $9\ mK$. The spectrum is taken from 20 to $25\ s$ after the ablation pulse. The heavy solid line is a fit to the ^{52}Cr spectrum assuming the trapped fluxes add an effective current of $25\ mA$ to the current supplied to the magnet. This fit gives temperature and density values of $T = 3.3$ mK and $n_0 = 3.9 \times 10^8\ cm^{-3}$ respectively. The ligher solid line is the fit obtained without accounting for trapped fluxes in any way. It gives values of $T = 3.3\ mK$ and $n_0 = 2.7 \times 10^8\ cm^{-3}$.

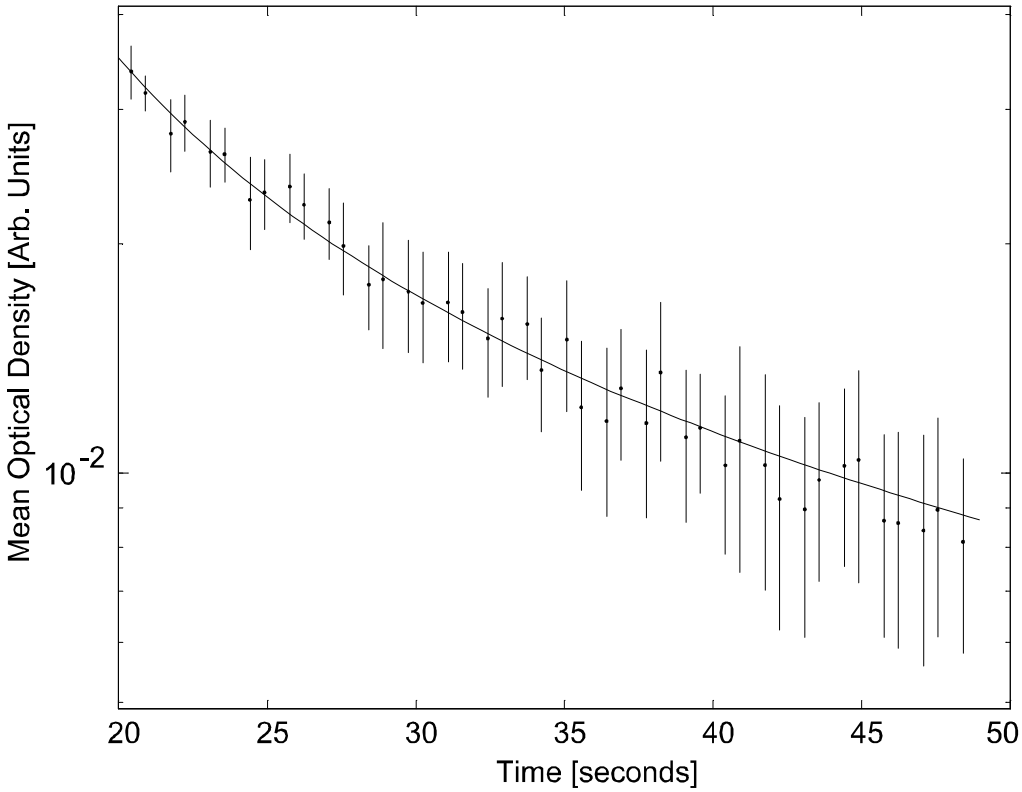

Figure 4.10: The hash marks and points are the mean and standard deviation obtained by time binning the combined data from 13 runs of the experiment at a trap depth of $50\ mA$ or $9\ mK$. The $50\ mA$ spectrum shown in Figure 4.9 is the average spectrum of this data taken from 20 to 25 seconds. The solid line is a fit to a two body decay resulting in best values of $g_{od} = 2.99\ s^{-1}$ and $t_0 = 10.81\ s$.

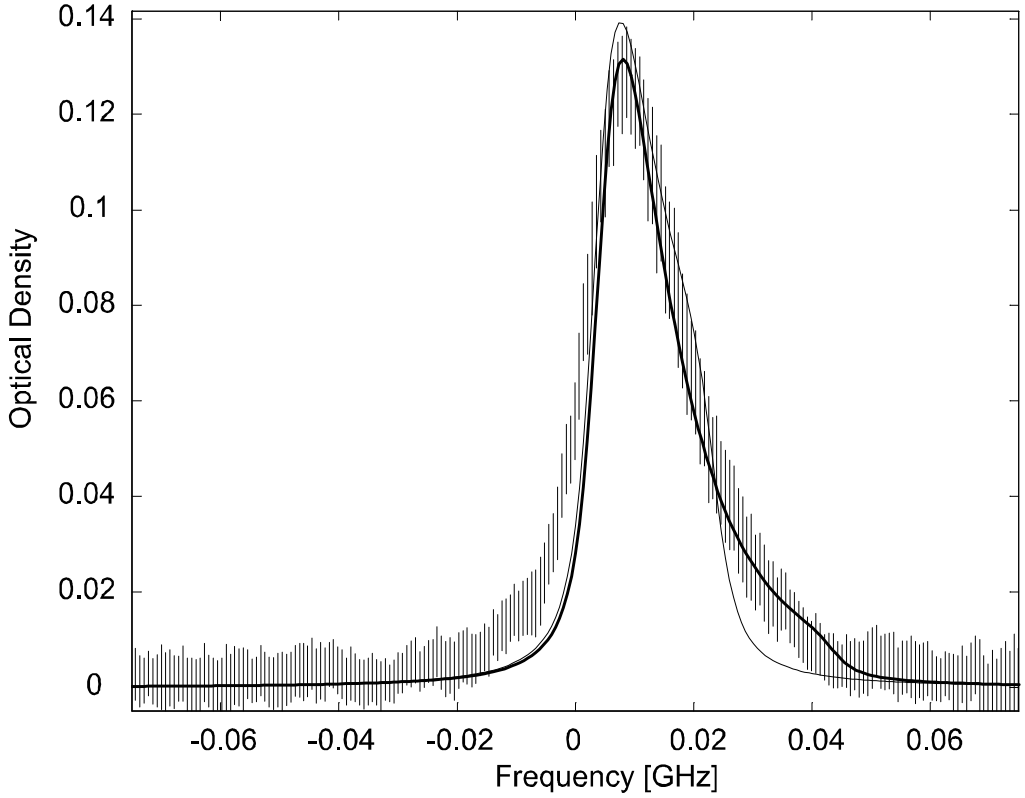

Figure 4.11: The vertical hash marks represent the result of averaging together 30 experimental runs at a trap depth of $25\ mA$, or $4.5\ mK$. The spectrum is taken from 20 to $25\ s$ after the ablation pulse. The heavy solid line is a fit to the ^{52}Cr spectrum assuming the trapped fluxes add an effective current of $25\ mA$ to the current supplied to the magnet. This fit gives temperature and density values of $T = 2.5\ mK$ and $n_0 = 8.8 \times 10^8\ cm^{-3}$ respectively. The ligher solid line is the fit obtained without accounting for trapped fluxes in any way. It gives values of $T = 2.5\ mK$ and $n_0 = 4.1 \times 10^8\ cm^{-3}$.

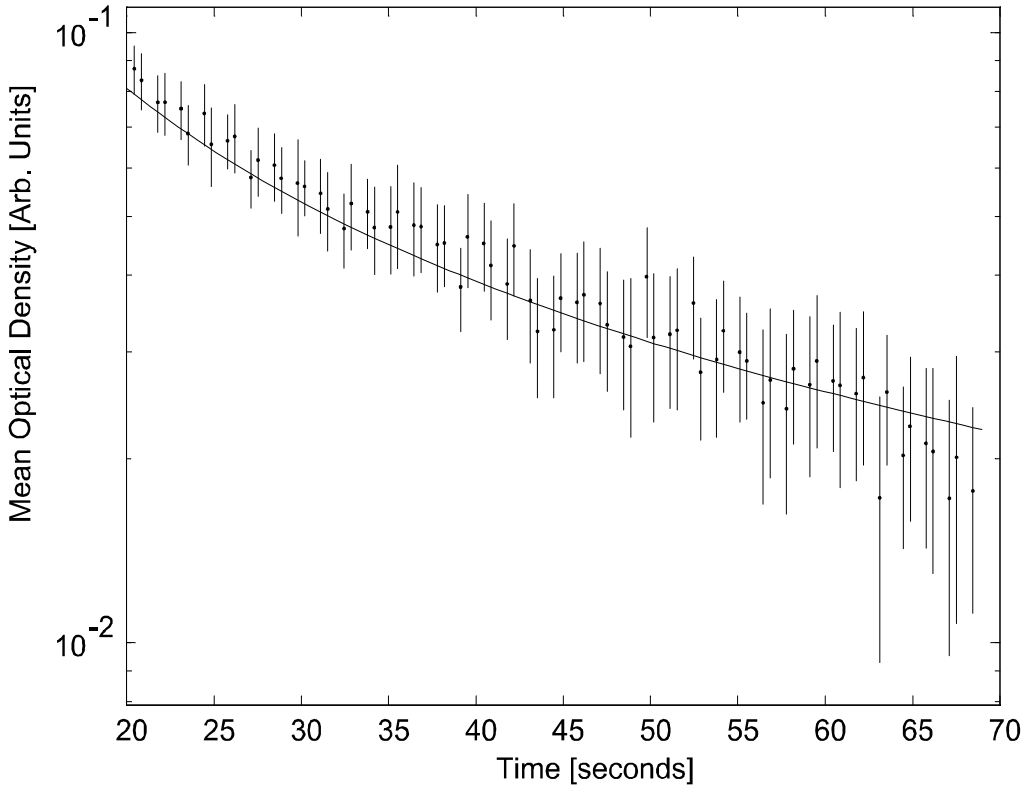

Figure 4.12: The hash marks and points are the mean and standard deviation obtained by time binning the combined data from 13 runs of the experiment at a trap depth of $25\ mA$ or $4.5\ mK$. The $25\ mA$ spectrum shown in Figure 4.11 is the average spectrum of this data taken from 20 to 25 seconds. The solid line is a fit to a two body decay resulting in best values of $g_{od} = 0.6618\ s^{-1}$ and $t_0 = 4.32\ s$.

Figure 4.12 shows a two-body fit to our $25\ mA$ time profile. With the large error bars and the small range of optical densities, the functional form of the loss rate is completely undetermined. We again rely on our two-body assumption to model the trap loss.

4.3 Summery of Observations

It is useful to summarize the results of our chromium measurements. The figures in this section contain plots showing the dependence of our measurements on trap depth, temperature and η.

The ensemble averaged collision rates fit quite well to the functional forms.

$$\left(\frac{g_{elastic}}{cm^3 s^{-1}}\right) = 8.17\times10^{-12}\left(\frac{T}{Kelvin}\right)^{-0.268} + 4.11\times10^{-20}\left(\frac{T}{Kelvin}\right)^{-4.48} \quad (4.1)$$

$$\left(\frac{g_{inelastic}}{cm^3 s^{-1}}\right) = 2.34\times10^{-13}\left(\frac{T}{Kelvin}\right)^{-0.566} + 4.11\times10^{-20}\left(\frac{T}{Kelvin}\right)^{-4.48}. \quad (4.2)$$

The range of validity for these fits is given by their overlap with the measured values as shown in Figure 4.13. The low ratio of trap depth to temperature we observe as we cool indicates that the ratio between elastic and inelastic scattering is of order unity. The last term in Eq. 4.1 for the elastic scattering rate is included to drive the elastic and inelastic rates towards the same value at lower temperatures. The addition of this term represents our guess at the unmeasured behavior of the elastic scattering rate at low temperatures.

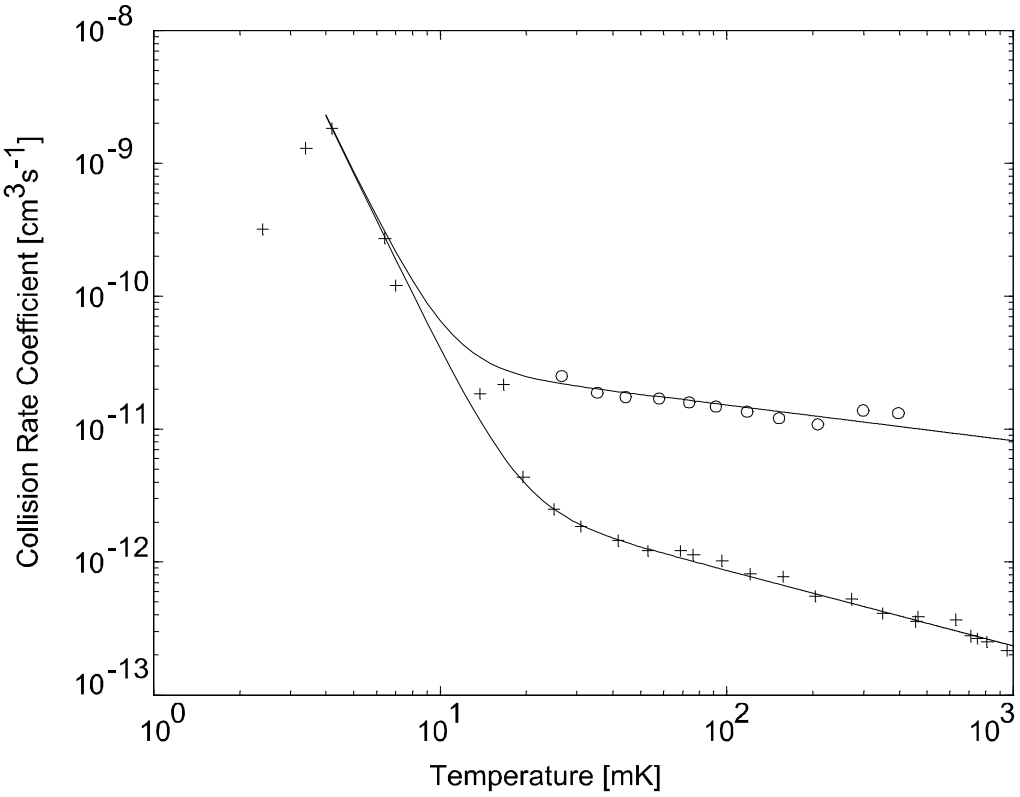

Figure 4.13: The circles are the measured elastic scattering rate coefficients. The crosses are the measured inelastic scattering rate coefficients. The solid lines are ad-hoc functional fits to the elastic and inelastic rates. The elastic functional fit is only valid for temperatures between 20 and $400\ mK$. The inelastic functional fit is only valid for temperatures between 4 and $1000\ mK$. The units in the fitting equations are $[g] = cm^3 s^{-1}$ and $[T] = Kelvin$.

For the specific cryogenic cell and magnet used in these measurements the measured peak density and peak temperature scale with the magnet current according to

$$\left(\frac{T}{Kelvin}\right) = 0.03 \left(\frac{I}{Amps}\right)^{0.75} \tag{4.3}$$

$$\left(\frac{n_o}{cm^{-3}}\right) = 2.4 \times 10^{10} \left(\frac{I}{Amps}\right)^{0.77}. \tag{4.4}$$

$I_{mag}\ [mA]$	$n_0\ \left[\frac{cm^3}{s}\right]$	$\sigma_{total}\ \left[\frac{cm^3}{s}\right]$	$\sigma_{stat}\ \left[\frac{cm^3}{s}\right]$	$\sigma_{beam}\ \left[\frac{cm^3}{s}\right]$	$\sigma_{field}\ \left[\frac{cm^3}{s}\right]$
300	6.9×10^9	0.6×10^9	0.1×10^9	0.3×10^9	0.5×10^9
100	7.5×10^8	2×10^8	0.2×10^8	0.3×10^8	2×10^8
70	3.8×10^8	1×10^8	negligible	negligible	1×10^8
50	3.9×10^8	1×10^8	negligible	negligible	1×10^8
25	8.8×10^8	5×10^8	negligible	negligible	5×10^8

Table 4.1: This table shows measured peak density in the trap as a function of the current running through the trapping magnet. The uncertainties are broken down into the components arising from statistical fluxuations, error due to probe beam uncertainties, and uncertainties of the magnetic field due to trapped fluxes.

$I_{mag}\ [mA]$	$T\ [mK]$	$\sigma_{total}\ [mK]$	$\sigma_{stat}\ [mK]$	$\sigma_{beam}\ [mK]$	$\sigma_{field}\ [mK]$
300	16.1	0.7	0.1	negligible	0.7
100	6.4	0.4	0.3	0.1	0.3
70	4.4	0.6	0.4	negligible	0.4
50	3.3	0.4	0.2	negligible	0.4
25	2.5	0.6	0.4	negligible	0.4

Table 4.2: This table shows measured temperatures in the trap as a function of the current running through the trapping magnet. The uncertainties are broken down into the components arising from statistical fluxuations, error due to probe beam uncertainties, and uncertainties of the magnetic field due to trapped fluxes.

Tables 4.1 and 4.2 show a summary of the error analysis for our density and temperature measurements. As can be seen, trapped fluxes in our superconducting magnet cause the uncertainty in our trapping field to be the dominant source of error at the lower trap depths.

4.4 Discussion of Results

For chromium, the ultra-cold regime (s-wave scattering) occurs at temperatures just below $1\ mK$. Our data clearly shows a dramatic variation in the ^{52}Cr–^{52}Cr inelas-

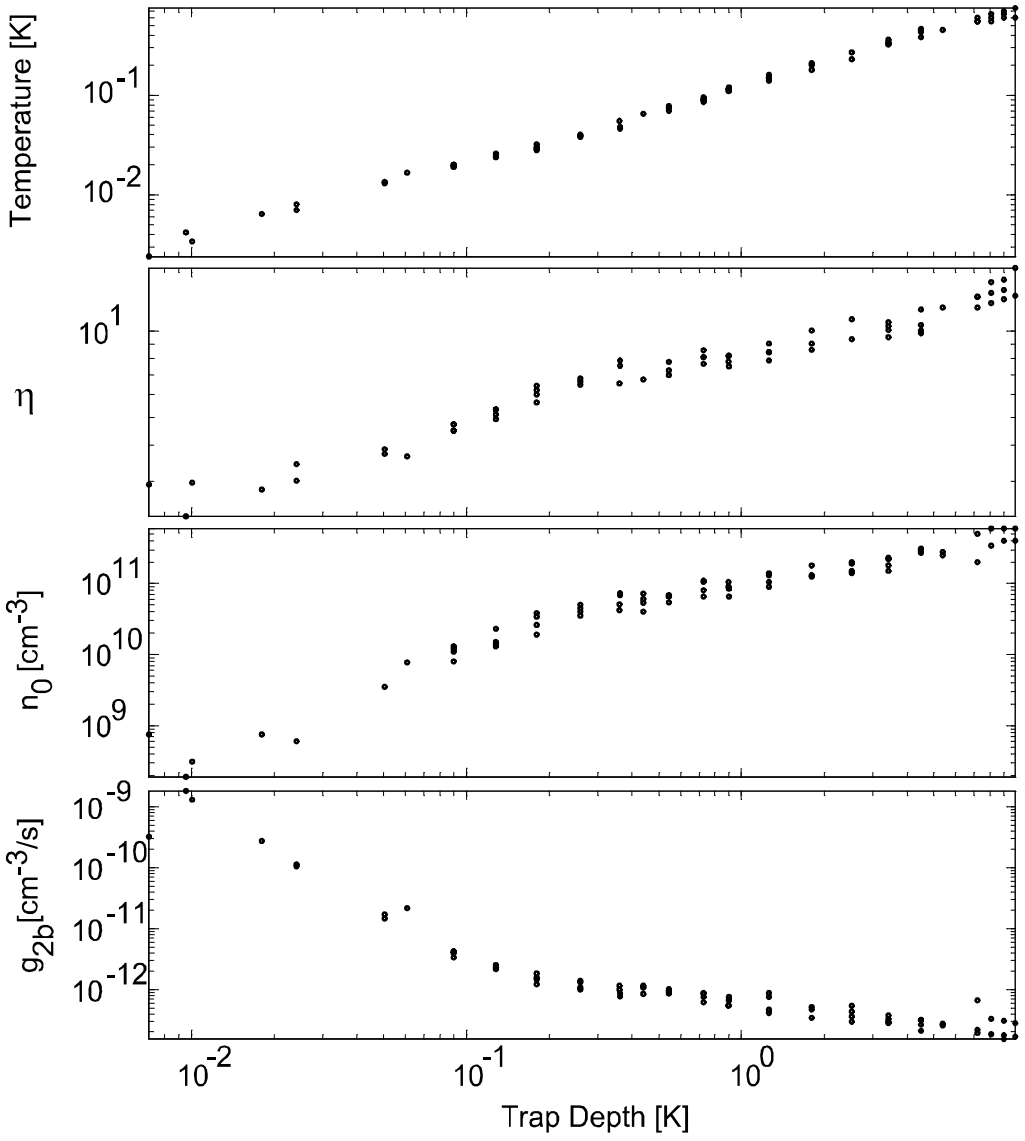

Figure 4.14: Summary of measurements as a function of trap depth.

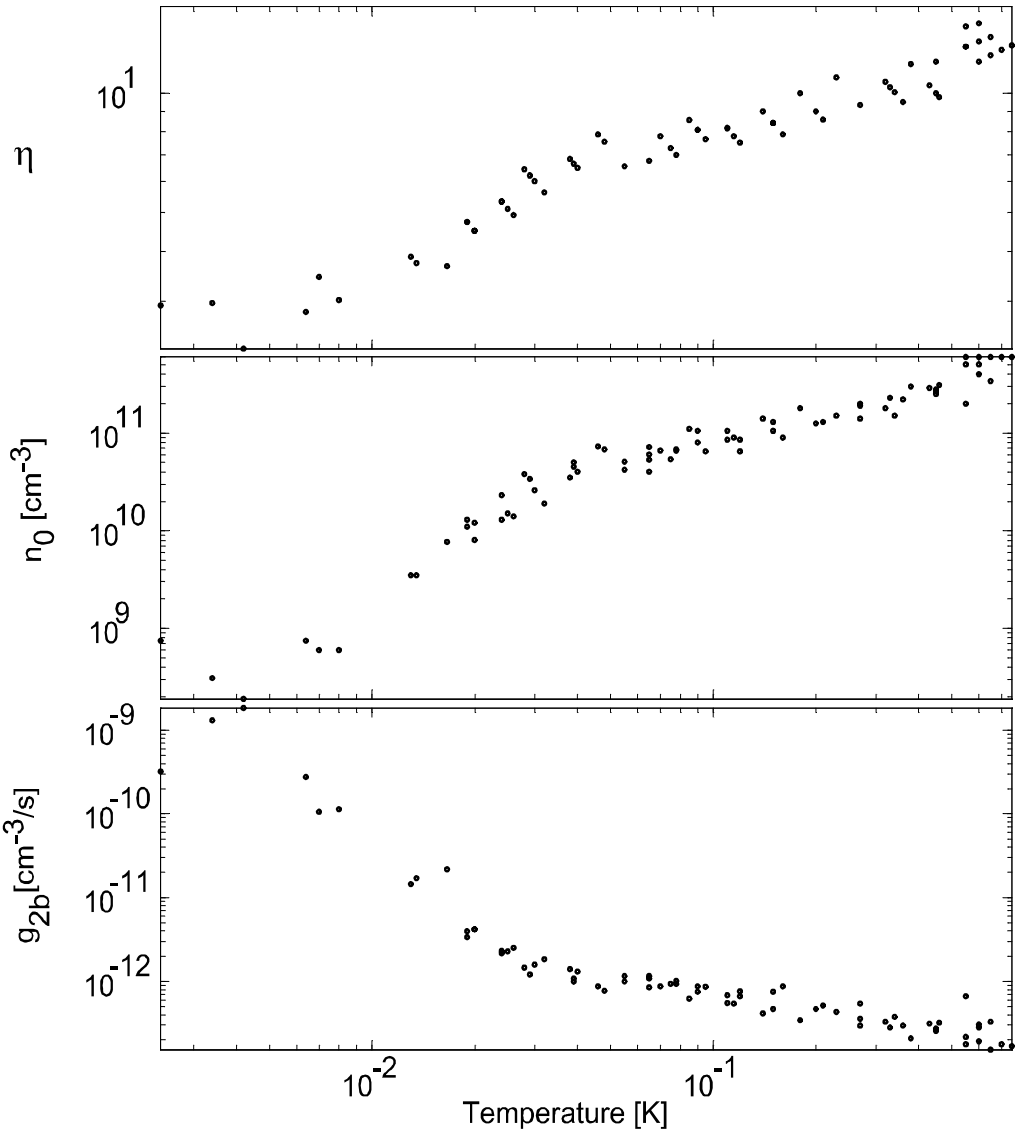

Figure 4.15: Summary of measurements as a function of temperature.

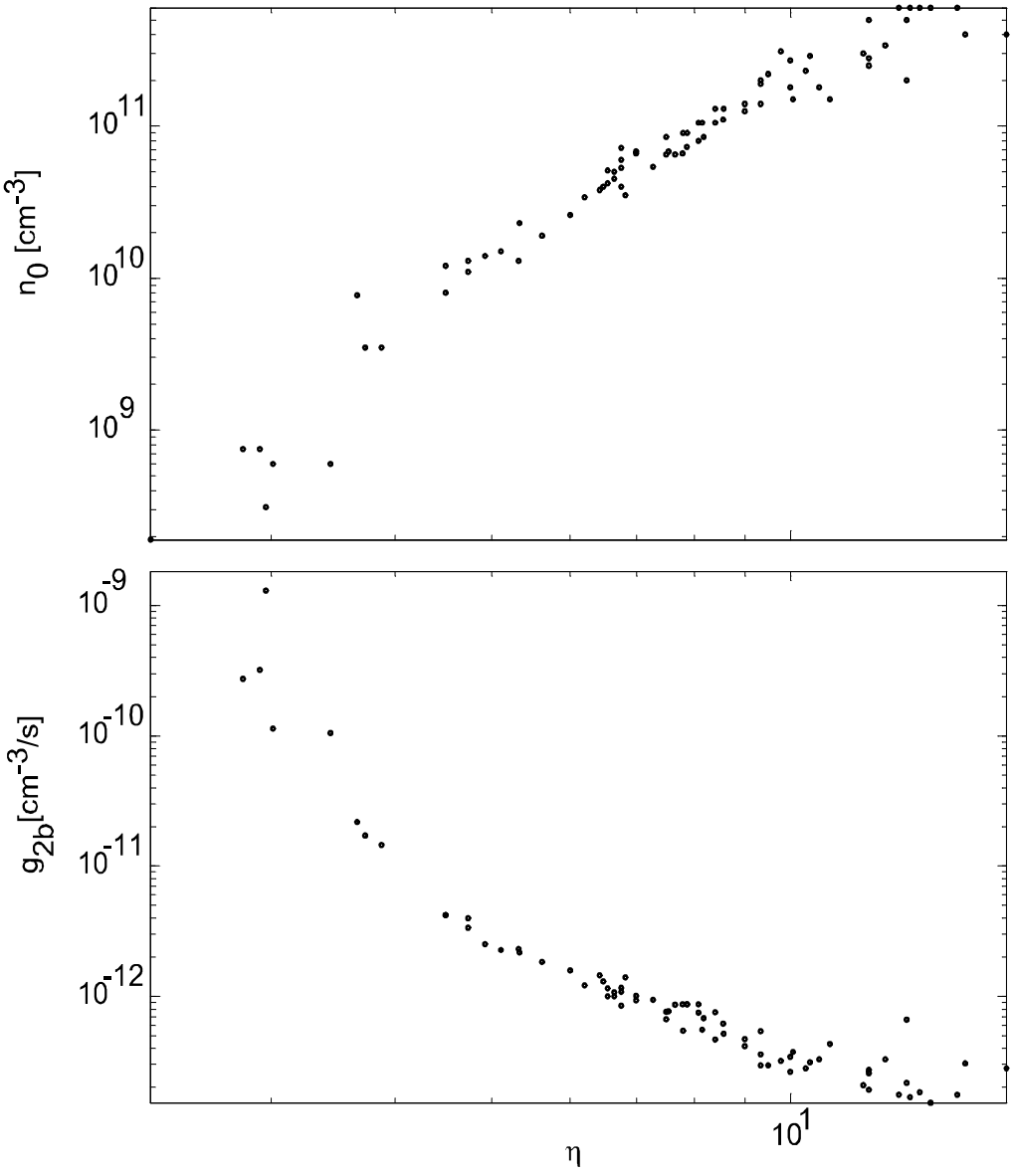

Figure 4.16: Summary of measurements as function of η.

tic collision rate coefficient just warmer than the ultra-cold regime. This may be indicative of either a shape resonance (See Chapter 6), a magnetic field effect, a general feature of dipolar relaxation in this cross-over region, or perhaps something else unique to either chromium or large-dipole atoms in general.

The enormity of the inelastic scattering rate in chromium causes large inefficiencies in our evaporative cooling. We do see an indication, however, that the inelastic rate is decreasing at temperatures below $4\ mK$. Thus, it is possible that as one continues to cool, the efficiency of evaporative cooling will become good enough to make continued attempts worthwhile. The large numbers of atoms we have at $2\ mK$ makes this possibility attractive. However, the limitations due to trapped fluxes in our superconducting magnet prevent us from making progress in the immediate future. These trapped fluxes could be removed in the future by heating the magnet after the initial evaporative cooling cycle. Chapter 7 describes our attempt to circumvent the problem of trapped fluxes by laser cooling our atoms in the hopes of reaching temperatures resulting in a more favorable ratio of elastic to inelastic collisions.

A consistency check can be performed on the data taken in this experiment. There is a one-to-one correspondence between the steady state η of a trapped gas and the ratio of elastic to inelastic scattering rates. The next chapter is devoted to developing the theory required to ensure that the steady state η observed in our experiment is consistent with the scattering rates we measure.

Chapter 5
Properties of Trapped Gases

The literature contains several different treatments on understanding the non-equilibrium thermodynamics of magnetically trapped gases [31, 32, 14]. However, none of these seems to contain an appropriate treatment for the case in which the trap depth is only slightly larger than the temperature of the atoms (the low η limit). Since much of the new data discussed in this thesis was taken for trap depth to temperature ratios (referred to as η) as low as 3, understanding this low η regime is important for grasping the full meaning of our data. As will be shown, there is a one-to-one correspondence between the observed η in a magnetic trap and the ratio of elastic to inelastic scattering cross sections. This relation can be used to provide a consistency check on our measurements.

5.1 Overview of the Analysis

The dynamics of magnetic gases confined in experimentally realizable magnetic traps is too complex to be perfectly treated analytically. A full description of such a system can only be obtained by employing numerical techniques. Fortunately, analytic descriptions can be formulated by making suitable approximations.

The most common, and perhaps most useful, of these is the "large η approximation." This approximation results in very simple, yet useful, expressions for various

quantities describing trapped gases. Since the analysis in this chapter will focus on the special case of spherically symmetric traps, the reader is referred to the excellent treatments by Ketterle and Doyle [14, 32] for discussions of other trap geometries.

In the regime where the large η approximation breaks down, progress can be made by introducing other approximations. The simplest of these is perhaps the "spherical trap approximation." In this model, the actual geometry of experimentally realizable traps is approximated as if it had spherical symmetry. The anti-Helmholtz trap used in our experiment has cylindrical, not spherical symmetry. However, constructing a spherically symmetric toy model of this trap can provide a great deal of insight into the dynamics of trapped gases.

This chapter is devoted to modeling our trapped gases as if they were confined by a spherically symmetric trap in which the potential energy of the atoms varies linearly with its radial coordinate. We make the additional assumptions that the only important processes are those arising from the interactions between trapped particles. We will neglect any effects due to collisions with non-trapped atoms. We also neglect any optical effects that could be introduced by a laser passing through the gas.

5.2 The large η Approximation

The large η approximation is discussed at length in the treatments by Doyle [32] and Ketterle [14]. A general overview of the results for the special case of a spherical, linear trap is included here for comparison with the exact results developed in the next

section. The heart of the large η approximation is that the density of atoms at any point in the trap is given by a Boltzmann distribution in the potential energy. This distribution is assumed to be abruptly truncated at the trap wall without taking into consideration the distortion to the distribution which occurs near the trap edge. At large values of η, the density of atoms in the region of this distortion is exponentially suppressed and its effects can be safely neglected.

5.2.1 Distribution Functions

The energy and density distribution functions are easily obtained as functions of radius (r) and momentum (p) by considering the case of an infinitely deep trap containing atoms at a temperature T. The partition function will be

$$Z = \int_0^\infty \exp\left[\frac{-U(r)}{kT}\right] d^3r \int_0^\infty \exp\left[\frac{-\frac{p^2}{2m}}{kT}\right] d^3p, \tag{5.1}$$

where $U(r)$ is the potential energy, m is the mass of a trapped atom and k is the Boltzmann constant. The separability of position and momentum coordinates in Eq. 5.1 leads to a counter-intuitive result. In an infinitely deep trap, the kinetic energy distribution of atoms is independent of position (i.e. potential energy) in the trap. In a trap of finite depth, the kinetic energy distribution will be distorted as potential energies approach the trap edge. However, in the large η approximation, atoms are almost never found near the trap edge, and the infinite trap partition function, Eq. 5.1, is a good approximation of the actual partition function.

From Eq. 5.1, it is straightforward to calculate the density and momentum distributions in the trap. They are

$$n\left(r\right)=n_{0}\exp\left[\frac{-U\left(r\right)}{kT}\right] \tag{5.2}$$

and

$$P\left(p\right)dp=\sqrt{\frac{2}{\pi\left(mkT\right)^{3}}}\exp\left[\frac{-\frac{p^{2}}{2m}}{kT}\right]p^{2}dp, \tag{5.3}$$

where n_0 is the peak density in the trap and $P\left(p\right)dp$ is the probability of having momentum between p and $p+dp$.

The energy density of states, $g\left(E\right)$, can be calculated using two methods. The first method counts the total number of states, N, having energy **less** than some value E. For the special case of a linear spherical potential with $U\left(r\right)=Gr$, this number is

$$N\left(E\right)=\frac{\left(4\pi\right)^{2}}{h^{3}}\int_{0}^{E/G}r^{2}dr\int_{0}^{\sqrt{2m(E-Gr)}}p^{2}dp=\frac{512\pi^{2}\sqrt{2m^{3}}}{945\left(hG\right)^{3}}E^{9/2}. \tag{5.4}$$

Taking the derivative with respect to E results in the expression for the density of states

$$g\left(E\right)=\frac{256\pi^{2}\sqrt{2m^{3}}}{105\left(hG\right)^{3}}E^{7/2}. \tag{5.5}$$

The second method [31] involves integrating the momentum and position coordinates over all values that result in energies **equal** to some value E,

$$g\left(E\right)=\frac{1}{h^{3}}\int_{0}^{E/G}d^{3}r\int_{0}^{\sqrt{2m(E-Gr)}}\delta\left(E-Gr-\frac{p^{2}}{2m}\right)d^{3}p. \tag{5.6}$$

Using the property of delta functions [33], $\delta\left[f\left(x\right)\right]=\left|\frac{df(x)}{dx}\right|^{-1}\delta\left(x-x_{0}\right)$, Eq. 5.6 can be evaluated to confirm the result of Eq. 5.5. This delta-function technique for

finding the density of states will prove quite useful later when we calculate the exact expression for the density of states.

Once the density of states has been found, an expression for the energy distribution in the trap can be written down. The probability of finding an atom with energy between E and $E + dE$ is simply

$$P(E)\,dE = \frac{g(E)\exp\left(-\frac{E}{kT}\right)}{\int_0^\infty g(E)\exp\left(-\frac{E}{kT}\right)dE} = \frac{16}{105\sqrt{\pi}}\frac{E^{7/2}}{(kT)^{9/2}}\exp\left(-\frac{E}{kT}\right). \quad (5.7)$$

5.2.2 Average Energies

Using the energy distribution function, Eq. 5.7, the mean energy of trapped atoms is calculated to be

$$\bar{E} = \frac{9}{2}kT. \quad (5.8)$$

The average potential energy of the atoms lost due to inelastic collisions in a spherical-linear trap is calculated by noting that collisions are two body processes that scale with the square of the density. The average potential energy of collisionally lost atoms is

$$\overline{U}_d = \frac{\int_0^\infty U(r)\,n^2(r)\,r^2dr}{\int_0^\infty n^2(r)\,r^2dr} = \frac{G\int_0^\infty \exp\left[\frac{-2Gr}{kT}\right]r^3dr}{\int_0^\infty \exp\left[\frac{-2Gr}{kT}\right]r^2dr} = \frac{3}{2}kT.$$

Adding to this the average kinetic energy of an ideal gas, $KE = \frac{3}{2}kT$, the average energy of atoms lost due to inelastic collisions is

$$\bar{E}_d = 3kT. \quad (5.9)$$

It should be noted that the average kinetic in the trap is not quite the same as the average kinetic energy of atoms lost due to inelastic collisions. The collision rate depends on the relative velocity between atoms. This causes high energy atoms to collide at a higher rate than there lower energy counterparts. We neglect this effect for now, but will take it into consideration in the exact calculation developed in the next section.

The average energy of an evaporating atom can be approximated by calculating the average kinetic energy of atoms evaporating over the edge of a box potential of depth $\eta k_B T$. This is found to be

$$\begin{aligned} \bar{E}_v &= \frac{\int_{\eta kT}^{\infty} E_K^{3/2} \exp\left(-\frac{E_K}{kT}\right) dE_K}{\int_0^{\infty} E_K^{1/2} \exp\left(-\frac{E_K}{kT}\right) dE_K} \\ &= \frac{kT}{2} \frac{3\sqrt{\pi} e^{\eta} \left[1 - \operatorname{erf}\left(\sqrt{\eta}\right)\right] + 2\sqrt{\eta}\,(2\eta + 3)}{\sqrt{\pi} e^{\eta} \left[1 - \operatorname{erf}\left(\sqrt{\eta}\right)\right] + 2\sqrt{\eta}} \\ &\simeq (\eta + 1)\, kT \quad \text{(for large } \eta\text{)} \end{aligned} \tag{5.10}$$

5.2.3 Evaporation Fraction

The fraction of elastic collisions that result in an atom with enough energy to leave the trap is called the evaporation fraction. In the large η approximation, it can be calculated using the detailed balance model described by Ketterle [14]. This model starts off considering a thermal ideal gas confined in a finite box potential of depth ηkT.

For a Boltzmann distribution, the fraction of atoms with kinetic energy, E_K, greater than some arbitrary threshold value, say ηkT, is simply

$$F = \frac{\int_{\eta kT}^{\infty} \sqrt{E_K} \exp\left(-\frac{E_K}{kT}\right) dE_K}{\int_{0}^{\infty} \sqrt{E_K} \exp\left(-\frac{E_K}{kT}\right) dE_K} \underset{\eta \gtrsim 4}{\rightarrow} 2\sqrt{\frac{\eta}{\pi}} e^{-\eta}.$$

If the box potential were infinitely deep, an atom with energy greater than the arbitrary threshold, ηkT, would remain confined. However, for large η, ($\gtrsim 4$) there is a high probability that even a single collision will knock this atom to an energy lower than ηkT. If this is true, then, in order for the energy distribution to remain constant in time, a different atom somewhere in the trap must be promoted to an energy greater than ηkT. This means that the rate at which atoms are promoted to energies greater than some threshold, ηkT, is the same as the collision rate rate experience by the energetic ($E_K \geq \eta kT$) atoms. This rate is just $\Gamma_{thresh} = n\sigma_{el} v_\eta$, where n is the atom density in the infinite box potential, σ_{el} is the elastic scattering cross section, $v_\eta = \frac{1}{2}\bar{v}\sqrt{\pi\eta}$ is the velocity of atoms with energy ηkT, and $\bar{v} = \sqrt{\frac{8kT}{\pi m}}$ is the mean thermal velocity.

The equality between the rates of upscattering in energy and downscattering in energy is called detailed balance. It is important to note that the phenomenon of detailed balance remains unchanged when considering a trap of finite depth, ηkT. However, in the finite trap case, the upscattered atoms will be ejected from the trap. This allows us to immediately write down an expression for the evaporation rate from

a box potential of depth ηkT.

$$\Gamma_{box} = n\sigma_{el}v_{\eta}FN = n\sigma_{el}\bar{v}\eta e^{-\eta}N, \tag{5.11}$$

where N is the number of trapped atoms.

We can now adapt this box potential argument to create an evaporation model for the linear spherical trap. In such a trap, the kinetic energy required to evaporate an atom from some radius r is equal to the difference in potential energy experienced by the atom in going from the radius r to the maximum radius in the trap, r_{wall}. Stated mathematically, $E_{K\,thresh} = U(r_{wall}) - U(r)$. This kinetic energy threshold for ejecting an atom from the trap can be used to define an effective η for evaporation from within a differential volume at a given radius r in the trap, $\eta_{eff}(r) = [U(r_{wall}) - U(r)] / (k_B T)$. Defining $\rho \equiv \frac{r}{r_{wall}}$, using the linearity of the potential to show $\frac{U(r)}{k_B T} = \eta\rho$, and letting

$$dN = n(r)\, d^3r = 3V_0 n_0 e^{-\eta\rho}\rho^2 d\rho,$$

(V_0 is the physical volume of the trap), Eq. 5.11 can be used to write the radially dependant differential evaporation rate as

$$\begin{aligned} d\Gamma_v(\rho) &= n(\rho)\,\sigma_{el}\bar{v}\eta_{eff}\exp\left(-\eta_{eff}\right)dN \\ &= 3V_0 n_0^2\sigma_{el}\bar{v}\eta e^{-\eta}(1-\rho)\,e^{-\eta\rho}\rho^2 d\rho. \end{aligned} \tag{5.12}$$

The evaporation fraction is simply the ratio of the evaporation rate to the elastic collision rate. Eq. 5.12 gives us an evaporation rate. We must now calculate the corresponding elastic collision rate.

The rate at which one atom undergoes collisions in the trap is given by $n\sigma_{el}\bar{v}\sqrt{2}$ (the mean relative velocity between atoms is $\bar{v}\sqrt{2}$). The total collision rate for dN atoms found at a radius r in the trap is then just

$$\begin{aligned} d\Gamma_{el}(\rho) &= n(\rho)\,\sigma_{el}\bar{v}\sqrt{2}dN \\ &= 3V_0 n_0^2 \sigma_{el}\bar{v}\sqrt{2}e^{-2\eta\rho}\rho^2 d\rho. \end{aligned} \tag{5.13}$$

As a function of radius, the fraction of elastic collisions resulting in evaporation is then given by

$$\tilde{f}(\rho) \equiv \frac{d\Gamma_v(\rho)}{d\Gamma_{el}(\rho)} = \frac{1}{\sqrt{2}}\eta(1-\rho)\exp\left[-\eta(1-\rho)\right].$$

To calculate the mean evaporation fraction for the trapped ensemble, we must average this collision rate over the entire volume of the trap. To do this, we first write the normalized radial probability distribution for collisions in the trap,

$$P_c(\rho)\,d\rho = \frac{n^2(\rho)\,\rho^2 d\rho}{\int_0^1 n^2(\rho)\,\rho^2 d\rho} = \frac{4\eta^3\rho^2 e^{-2\eta\rho}}{1-(2\eta^2+2\eta+1)\,e^{-2\eta}}.$$

The average evaporation fraction for the trapped ensemble is then calculated to be

$$\begin{aligned} f &= \int_0^1 P_c(\rho)\,\tilde{f}(\rho)\,d\rho \\ &= \frac{2\sqrt{2}\left[e^{-\eta}(2\eta-6)+e^{-2\eta}(\eta^2+4\eta+6)\right]}{1-(2\eta^2+2\eta+1)\,e^{-2\eta}}. \end{aligned} \tag{5.14}$$

5.2.4 Effective Volumes

In many calculations involving trapped ensembles of atoms, the size of the atom cloud is an important parameter. A useful definition for the size of the cloud is the

effective volume. The effective volume is defined such that the total number of atoms is given by the peak density in the trap multiplied by the effective volume, or $N = n_0 V_{eff}$. From this, it is straightforward to show that, in the large η approximation of the linear spherical trap,

$$V_{eff} = 3V_0 \int_0^1 e^{-\eta\rho}\rho^2 d\rho \simeq \frac{6V_0}{\eta^3}. \tag{5.15}$$

It is also useful to introduce a collisional effective volume. The collisional effective volume is defined such that the total scattering rate for a trapped ensemble is given by $\Gamma = n_0^2 \sigma \left(\bar{v}\sqrt{2}\right) \Lambda_{eff}$, where Λ_{eff} is the collisional effective volume, and $n_0\sigma\left(\bar{v}\sqrt{2}\right)$ is the single atom collision rate at the center of the trap.

As mentioned in the discussion of the evaporation fraction, the scattering rate for dN atoms interacting with a cloud of density n is given by $d\Gamma = n\sigma\left(\bar{v}\sqrt{2}\right) dN$. Letting $dN = n\left(r\right) d^3r$, the total scattering rate is

$$\Gamma = \sigma\left(\bar{v}\sqrt{2}\right) \int_0^1 n^2\left(r\right) d^3r = 3V_0 n_0^2 \sigma\left(\bar{v}\sqrt{2}\right) \int_0^1 \left[\frac{n\left(\rho\right)}{n_o}\right]^2 \rho^2 d\rho.$$

It follows that the collisional effective volume for a linear spherical potential is

$$\Lambda_{eff} = 3V_0 \int_0^1 \left[\frac{n\left(\rho\right)}{n_o}\right]^2 \rho^2 d\rho \simeq \frac{3V_0}{4\eta^3}. \tag{5.16}$$

These effective volumes can then be used to calculate the average scattering rate for a trapped ensemble. The mean scattering rate is just the total scattering rate divided by the number of atoms, or

$$\bar{\Gamma} = \frac{\Gamma}{N} = \frac{\Lambda_{eff}}{V_{eff}} n_0 \sigma\left(\bar{v}\sqrt{2}\right) = \frac{1}{8} n_0 \sigma\left(\bar{v}\sqrt{2}\right). \tag{5.17}$$

This says that the mean scattering rate of a cloud of atoms confined at large η in a linear spherical trap is eight times smaller than the scattering rate at the center of the trap.

5.3 Exact Solution for the Spherical Trap

As η is reduced, the primary mechanism responsible for the failure of the large η approximation is the distortion of the atom density from the ideal Boltzmann distribution. This distortion effects all integrals involving the density distribution in the trap. The average energies, evaporation fraction, effective volumes, etc. all contain such integrals in their derivation. Therefore, an accurate expression for the density distribution function is absolutely crucial for describing trapped gases in the small η regime. This section is devoted to developing an expression for the trap density that will be valid for all η in a linear spherical trap. The generalized expressions for the average energies, evaporation fraction, effective volumes, etc. can then be obtained.

5.3.1 Good Coordinates for Spherical Trap

The distribution functions for a trapped ensemble can all be calculated from the partition function. Since the partition function is derived from integrating over all available phase space,

$$Z = \int\int \exp\left[\frac{-E\left(r,p\right)}{kt}\right] d^3r d^3p,$$

it is useful to transform the phase space volume element, d^3rd^3p, into coordinates appropriate for describing the spherically symmetric system, $d^3rd^3p \rightarrow drd\theta d\phi dp_r dLdL_z$, where r, θ, and ϕ are the spherical position coordinates, p_r is the radial momentum, L is the total angular momentum, and L_z is its projection along the z axis ($\theta = 0$) of the coordinate system.

This transformation involves the use of Jacobians. A Jacobian transformation is simply a procedure for expressing differentials of one coordinate system in terms of differentials of another coordinate system [34]. Applied to the phase space volume element, this transformation looks like

$$\begin{aligned} dp_x dp_y dp_z dx dy dz &= \frac{\partial\left(p_x, p_y, p_z\right)}{\partial\left(\dot{r}, \dot{\theta}, \dot{\phi}\right)} \frac{\partial\left(\dot{r}, \dot{\theta}, \dot{\phi}\right)}{\partial\left(p_r, p_\theta, p_\phi\right)} dp_r \times \\ & \frac{\partial\left(p_\theta, p_\phi\right)}{\partial\left(L, L_z\right)} dL dL_z \frac{\partial\left(x, y, z\right)}{\partial\left(r, \theta, \phi\right)} dr d\theta d\phi. \end{aligned} \tag{5.18}$$

Each of the Jacobian transformations in Eq. 5.18 can be written as a determinant of derivatives. For example, the first Jacobian is

$$\frac{\partial\left(p_x, p_y, p_z\right)}{\partial\left(\dot{r}, \dot{\theta}, \dot{\phi}\right)} = \begin{vmatrix} \frac{\partial p_x}{\partial \dot{r}} & \frac{\partial p_x}{\partial \dot{\theta}} & \frac{\partial p_x}{\partial \dot{\phi}} \\ \frac{\partial p_y}{\partial \dot{r}} & \frac{\partial p_y}{\partial \dot{\theta}} & \frac{\partial p_y}{\partial \dot{\phi}} \\ \frac{\partial p_z}{\partial \dot{r}} & \frac{\partial p_z}{\partial \dot{\theta}} & \frac{\partial p_z}{\partial \dot{\phi}} \end{vmatrix}. \tag{5.19}$$

Using $p^2 = p_r^2 + p_\theta^2 + p_\phi^2$, $L^2 = p_\theta^2 + p_\phi^2$, $L_z = p_\phi$, and applying Lagrangian formalism to calculate the generalized momenta,

$$\begin{aligned} p_r &= m\dot{r} \\ p_\theta &= mr^2\dot{\theta} = \sqrt{L^2 - L_z^2} \\ p_\phi &= m\left(r\sin\theta\right)^2 \dot{\phi} = L_z, \end{aligned}$$

the derivatives of the transformation equations

$$\begin{aligned} p_x &= m\left[(\dot{r})\sin\theta\cos\phi + \left(\dot{\theta}\right) r\cos\theta\cos\phi - \left(\dot{\phi}\right) r\sin\theta\sin\phi\right] \\ p_y &= m\left[(\dot{r})\sin\theta\sin\phi + \left(\dot{\theta}\right) r\cos\theta\sin\phi + \left(\dot{\phi}\right) r\sin\theta\cos\phi\right] \\ p_z &= m\left[\dot{r}\cos\theta - \left(\dot{\theta}\right) r\sin\theta\right] \end{aligned}$$

can be substituted into the Jacobian determinant of Eq. 5.19 to get

$$\begin{aligned} \frac{\partial\left(p_x, p_y, p_z\right)}{\partial\left(\dot{r}, \dot{\theta}, \dot{\phi}\right)} &= \begin{vmatrix} m\sin\theta\cos\phi & mr\cos\theta\cos\phi & -mr\sin\theta\sin\phi \\ m\sin\theta\sin\phi & mr\cos\theta\sin\phi & mr\sin\theta\cos\phi \\ m\cos\theta & -mr\sin\theta & 0 \end{vmatrix} \\ &= r^2 m^3 \sin\theta. \end{aligned}$$

Calculation of the complete Jacobian of transformation of Eq. 5.18 is too lengthy to be traced out in detail, but gives the following result for the phase space volume element in spherically symmetric coordinates,

$$d^3r d^3p = \frac{L}{\sqrt{L^2 - L_z^2}} dr d\theta d\phi dP_r dL dL_z. \tag{5.20}$$

5.3.2 Dimensionless Units

The conserved angular momentum imposed by the spherical symmetry of the trapping potential allows the energy of a trapped atom to be written as

$$E = p_r^2/(2m) + L^2/(2mr^2) + Gr \tag{5.21}$$

The motion of the radial coordinate can be described as if the atom were confined in an effective radial potential

$$V_L(r) = L^2/\left(2mr^2\right) + Gr. \tag{5.22}$$

In order to simplify the equations which follow, it will be convenient to define dimensionless units. This will not only minimize the number of constants to keep track of, but will also generalize the results to ensembles with arbitrary trap depths, temperatures, etc.

If an atom is to be confined to a volume of radius less than some value r_E, the maximum energy it can have, will be realized by placing it in a circular orbit of radius r_E. This corresponds to the radial coordinate being nestled in the minimum of the effective radial potential corresponding to the maximum allowed angular momentum L_E. This angular momentum can be found by setting the radial derivative of Eq. 5.22 equal to zero giving

$$\frac{L_E^2}{mr_E^2} = Gr_E. \tag{5.23}$$

The relationship between the maximum angular momentum, and maximum energy for orbits enclosed by the $r = r_E$ sphere is found by substituting Eq. 5.23 into Eq. 5.21,

$$\frac{L_E^2}{2mr_E^2} = \frac{1}{3}E. \tag{5.24}$$

Finally, the expression relating maximum allowed energy for an atom confined to $r \leq r_E$ can be found by substituting Eq. 5.23 and Eq. 5.24 into Eq. 5.22,

$$Gr_E = \frac{2}{3}E. \tag{5.25}$$

Defining the potential at the wall of the trap to be $Gr_w \equiv U_w$, and setting $r_E = r_w$ in Eqs. 5.24 and 5.25, we can express the maximum energy and the maximum

angular momentum in the trap as

$$\begin{aligned} E_m &= \frac{3}{2}U_w \\ L_m^2 &= mr_w^2 U_w. \end{aligned}$$

We can now scale any angular momentum, radius, or potential energy by the corresponding maximum allowed value to get the following definitions for dimensionless variables.

$$\begin{aligned} \rho &\equiv \frac{r}{r_w} \\ \pounds &\equiv \frac{L}{L_m} \\ Q &\equiv \frac{E}{U_w} \end{aligned} \tag{5.26}$$

The dimensionless variables of Eq. 5.26 will be used through the remainder of this discussion. A firm grasp on their definitions will greatly facilitate the understanding of the following discussion.

5.3.3 Allowed Orbits

For a given angular momentum, the effective potential, Eq. 5.22, can be recast in dimensionless units as

$$V_{\pounds}(\rho) = \frac{\pounds^2}{2\rho^2} + \rho. \tag{5.27}$$

A plot of this effective potential for several different values of $\pounds$ is shown in Fig. 5.1. The lowermost curve (i.e. the straight line) is the effective potential for zero angular momentum. The uppermost curve is the effective potential for the highest

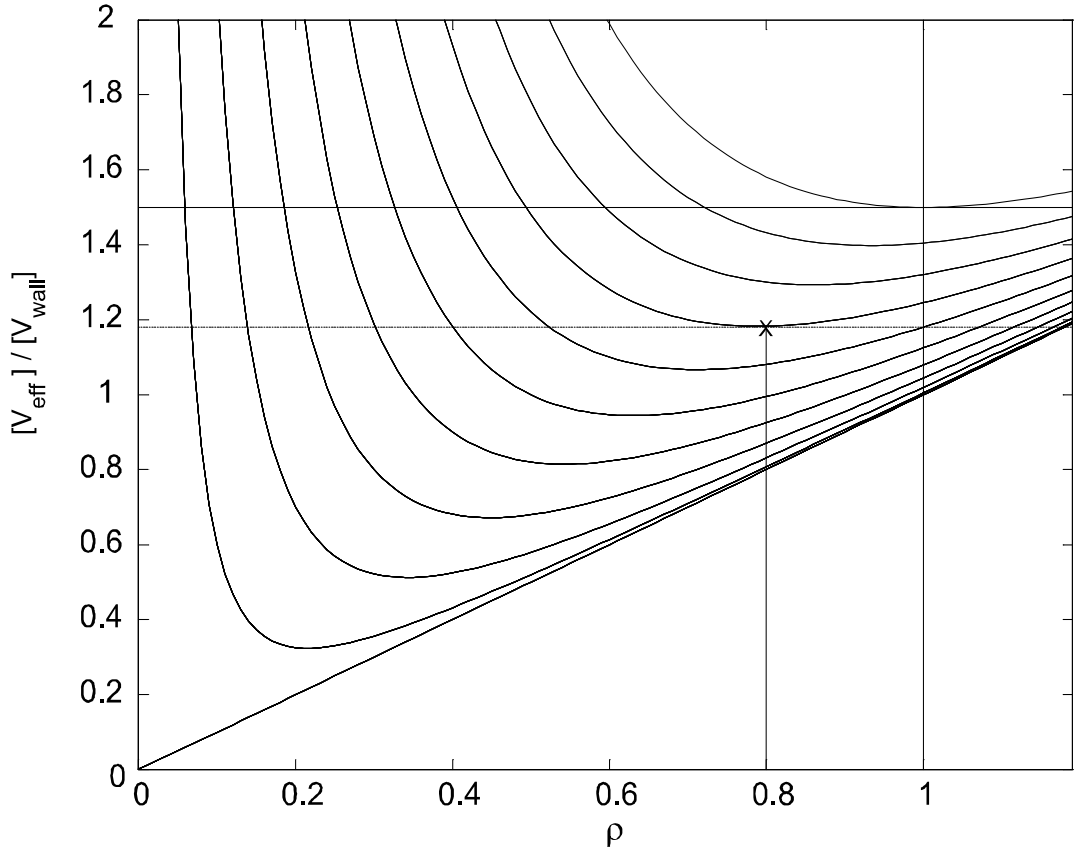

Figure 5.1: Effective trapping potentials for atoms with angular momentum taking on values of $\pounds = 0, 0.1, ..., 1$. The x axis of this plot is the radial coordinate of the trap in units of the maximum trap radius. The y axis is the effective potential (including angular momentum barrier) in units of the potential energy at the trap wall.

angular momentum allowed in the trap, (i.e. $\pounds^2 = 1$). A great deal of insight can be gained from this graph.

Angular Momentum Constraints

Consider all atoms with some energy, Q, that pass through a given radius ρ. If they are to occupy orbits that remain confined in the trap, their angular momenta must be constrained in some way. Let the energy of one of these atoms correspond

to the dotted line in Fig. 5.1. The classical turning points for this atom are given by the intersection of the dotted line with the effective potential curve corresponding to whatever angular momentum it can take. As this angular momentum is increased, the distance between the two turning points is decreased until they meet to define a circular orbit (at the cross in figure 5.1). It is impossible to have angular momentum greater than this value while maintaining the atom at the fixed energy of the dashed line. This condition is stated mathematically as

$$\pounds^2_{\max}(Q,\rho) = 2\rho^2(Q-\rho). \tag{5.28}$$

Now consider the possible outer turning points for atoms of energy Q. As the angular momentum is decreased from its maximum value ($\pounds = 1$), the outer turning point occurs at ever increasing radii. At some point, the angular momentum will reach a value that causes the outer turning point to intersect with the radius of the trap wall which would result in atom loss. This condition defines the minimum angular momentum for trapped atoms having energy Q and passing through radius ρ,

$$\pounds^2_{\min}(Q,\rho) = 2(Q-1). \tag{5.29}$$

(Subject to the constraint that $\pounds^2_{\min} \geq 0$).

Energy Constraints

A similar argument can be used to calculate the allowed energy values for atoms passing through a given radius ρ. The minimum energy an atom at radius

ρ can have is found by setting its kinetic energy to zero. Its total energy will then be equal to its potential energy,

$$Q_{\min}(\rho) = \rho. \tag{5.30}$$

The maximum energy for an atom passing through some radius ρ can be found by first identifying the effective potential curve with an inner turning point at ρ and the outer turning point at the trap wall. The value of the effective potential at the turning points is then equal to the maximum allowed energy for an atom passing through radius ρ,

$$Q_{\max}(\rho) = 1 + \frac{\rho^2}{1+\rho}. \tag{5.31}$$

Radial Constraints

The effective radial potential will confine atoms with a given energy Q to certain radii in the trap. The largest possible radius these atoms can reach is achieved by riding out on the $\pounds = 0$ effective potential curve to the outer turning point, see Fig. 5.1. At this point the atom will have no kinetic energy and

$$\rho_{\max}(Q) = Q. \tag{5.32}$$

(Subject to the constraint that $\rho_{\max} \leq 1$).

As mentioned earlier, the effective potential is the sum of the actual potential and the "angular momentum barrier." As long as the energy of an atom is less than the actual potential energy at the trap wall (neglecting the angular momentum barrier) it is possible to place the atom in an $\pounds = 0$ orbit which samples the center of the trap.

This means $\rho_{\min}(Q \leq 1) = 0$. However, the only way to trap an atom with total energy greater than the trap depth ($Q > 1$) is to place it in an orbit with $\pounds > 0$. Due to the angular momentum barrier, no orbits with $\pounds > 0$ are allowed to sample the center of the trap. Therefore, atoms with energy greater than the trap depth will be confined to radii larger than some minimum value. This minimum value can be calculated by first identifying the effective potential curve that gives an orbit with an outer turning point at the trap edge. The inner turning point on this curve will then be the minimum allowed radius. Solving the cubic equation for this inner turning point and selecting the appropriate root gives a result for the minimum radius that can be sampled by an atom of energy Q,

$$\begin{aligned} \rho_{\min}(Q &\leq 1) = 0 \\ \rho_{\min}(Q &> 1) = \frac{1}{2}(Q-1) + \frac{1}{2}\sqrt{Q^2 + 2Q - 3} \end{aligned} \tag{5.33}$$

Summary of Allowed Orbits

The grey area in Figure 5.2 represents the region of allowed radii and energy for orbits that can be confined in a spherical linear trap. The allowed radii for a given energy can be found by drawing a horizontal line along the energy of interest and observing the intersection of this line with the allowed region. Similarly the allowed energies at any radius can be found by drawing a vertical line along the allowed radius and observing the intersection of this line with the allowed region to get the allowed energies.

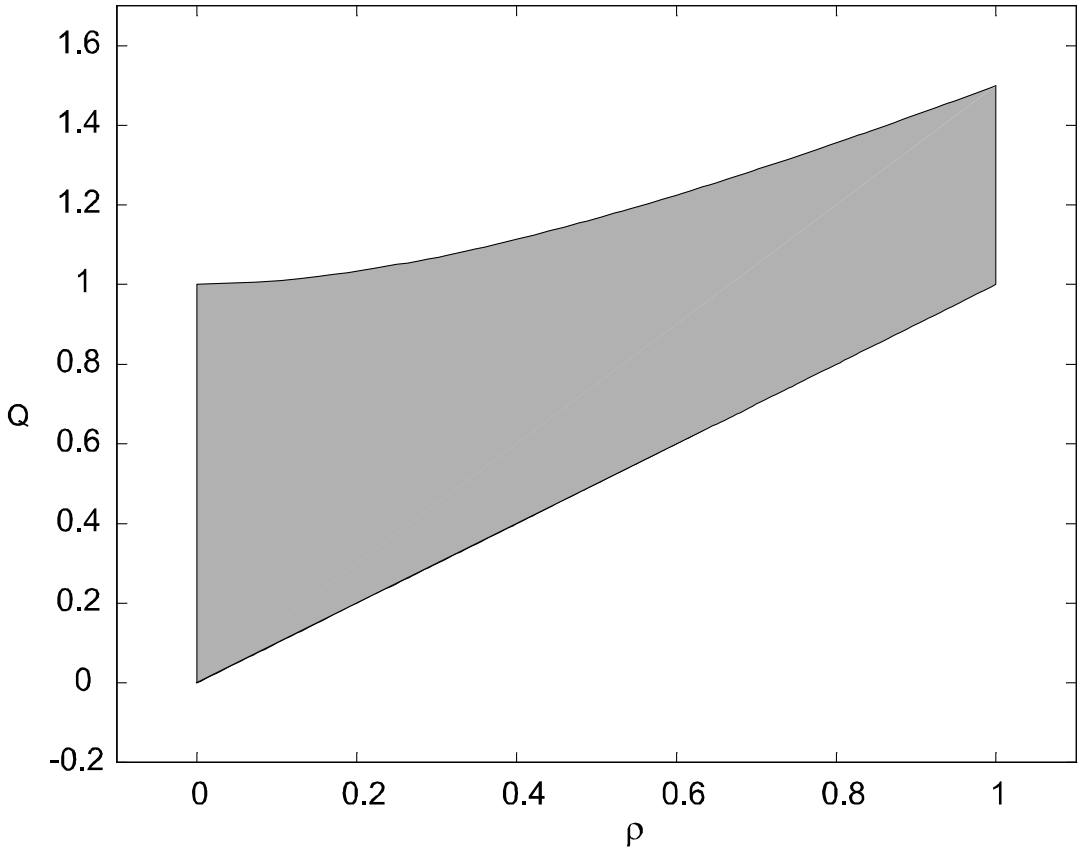

Figure 5.2: The shaded area represents the region in radius/energy space that supports confined orbits in the trap. Any combination of radius and energy not falling within the shaded region must follow a trajectory that removes it from the trap.

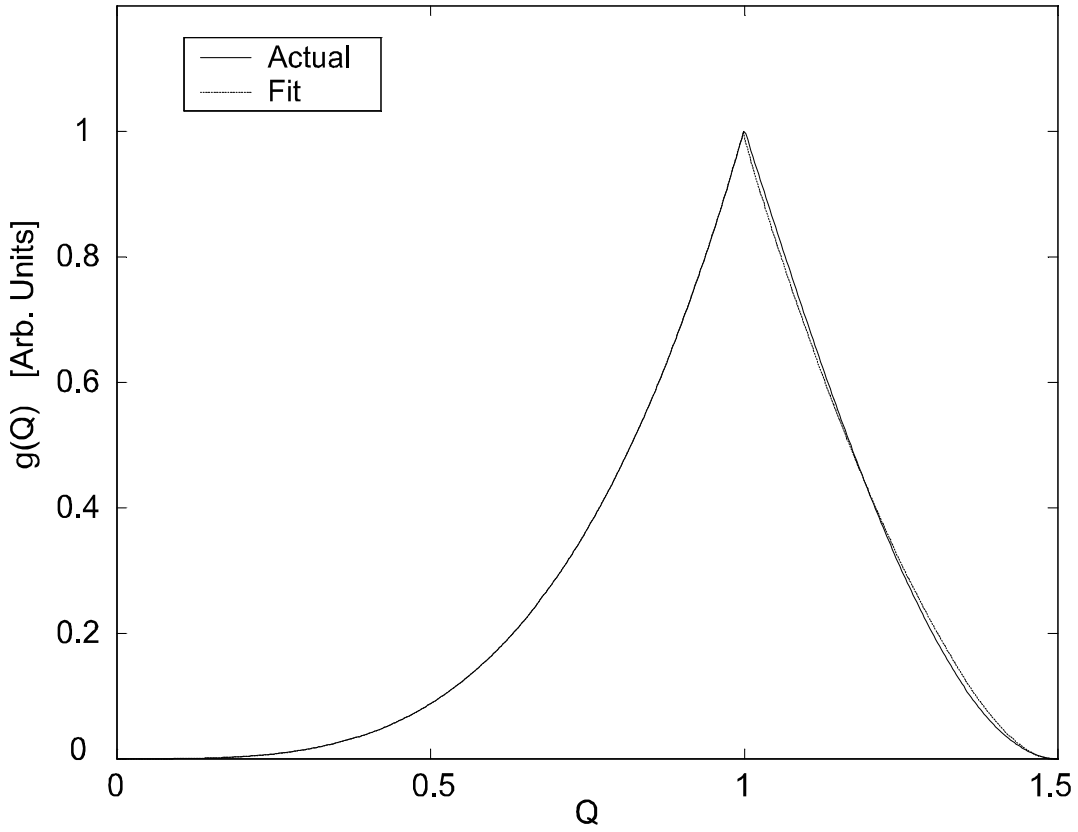

Figure 5.3: The solid line is the density of states in a linear, spherical trap obtained by evaluating the integral of Eq. 5.34. The dotted line shows the ad-hoc fit of Eq. 5.35.

5.3.4 Density of States

Using the delta function technique for calculating the density of states, (see Eq. 5.6), we can write

$$g\left(E\right)dE = dE\frac{1}{h^3}\iint \delta\left(E - Gr - \frac{p^2}{2m}\right) d^3r d^3p.$$

The formalism need to transform this equation into spherically symmetric coordinates has already been discussed. The result is

$$
\begin{aligned}
g(E)\,dE &= dE\frac{1}{h^3}\int dr\int LdL\int_{-L}^{L}\frac{dL_z}{\sqrt{L^2-L_z^2}}\delta\left[E-\frac{p_r^2}{2m}-\frac{L^2}{2mr^2}-Gr\right]\times \\
&\quad \int_0^{\pi} d\theta\int_0^{2\pi} d\phi \\
&= dE\left(\frac{\pi}{h}\right)^3\iiint\delta\left[E-p_r^2/(2m)-L^2/(2mr^2)-Gr\right]d\left(L^2\right)dP_r dr.
\end{aligned}
$$

Integrating over p_r and using $\delta\left[f\left(x\right)\right]=\left|\frac{df(x)}{dx}\right|^{-1}\delta\left(x-x_0\right)$, this simplifies to

$$
g(E)\,dE = dE\left(\frac{\pi}{h}\right)^3\sqrt{2m}\iint\frac{d\left(L^2\right)dr}{\sqrt{E-L^2/\left(2mr^2\right)-Gr}}.
$$

Finally, transforming to dimensionless variables and integrating over all allowed orbits, the number of trapped states with energies between Q and $Q+dQ$ (i.e. the density of trapped states) can be written as

$$
\begin{aligned}
g(Q) &= A\int_{\rho_{\min(Q)}}^{\rho_{\max(Q)}}d\rho\int_{\pounds^2_{\min}(Q,\rho)}^{\pounds^2_{\max}(Q,\rho)}\frac{d\left(\pounds^2\right)}{\sqrt{Q-\frac{\pounds^2}{2\rho}-\rho}} \\
&= \left\{\begin{array}{cc} \frac{64}{105}AQ^{7/2}, & Q\in[0,1] \\ 4A\int_{\rho_{\min(Q)}}^{\rho_{\max(Q)}}\sqrt{Q\left(\rho^2-1\right)-\left(\rho^3-1\right)}d\rho & Q\in(1,\frac{3}{2}] \\ 0 & Q\in(\frac{3}{2},\infty]\end{array}\right\} \qquad (5.34)
\end{aligned}
$$

where $A\equiv\left(\frac{\pi}{h}\right)^3\sqrt{2\left(m\eta kT\right)^3}$, and the limits of integration are defined in the previous discussion on allowed orbits. Since the integral in Eq. 5.34 doesn't have a simple solution, one can construct an analytic expression in an ad-hoc fashion and adjust its parameters to approximate the density of states. This approximation is

$$
g(Q)\simeq\left\{\begin{array}{cc} \frac{64}{105}AQ^{7/2}, & Q\in[0,1] \\ 70A\exp\left[-4\left(\frac{3}{2}-Q\right)^{-1/4}-(Q-1)\right] & Q\in(1,\frac{3}{2}) \\ 0 & Q\in(\frac{3}{2},\infty]\end{array}\right\} \qquad (5.35)
$$

Figure 5.3 shows a comparison of this ad-hoc fit to the density of states with the exact result obtained by numerically integrating Eq. 5.34. This ad-hoc fit will prove quite useful in calculating the fraction of elastic collisions that result in an atom being evaporated.

5.3.5 Energy Dependant Density Distribution

From the expression for the density states, Eq. 5.34, the probability that a particle with energy between Q and $Q + dQ$, and angular momentum between $\pounds^2$ and $\pounds^2 + d\left(\pounds^2\right)$ can be found between radii ρ and $\rho + d\rho$, is given by (in a Boltzmann distribution)

$$P\left(\rho, Q, \pounds^2\right) d\rho dQ d\left(\pounds^2\right) \propto \frac{d\rho dQ d\left(\pounds^2\right)}{\sqrt{Q - \frac{\pounds^2}{2\rho} - \rho}} \exp\left(-\eta Q\right).$$

The dependence on $\pounds^2$ and be removed with the integral

$$\begin{aligned} P\left(\rho, Q\right) d\rho dQ &\propto d\rho dQ \exp\left(-\eta Q\right) \int_{\pounds^2_{\min}(Q,\rho)}^{\pounds^2_{\max}(Q,\rho)} \frac{d\left(\pounds^2\right)}{\sqrt{Q - \frac{\pounds^2}{2\rho} - \rho}} \\ &\propto \left\{ \begin{array}{cc} \rho\sqrt{Q\left(\rho^2 - 1\right) + \left(1 - \rho^3\right)} \exp(-\eta Q) dQ, & Q > 1 \\ \rho^2\sqrt{Q - \rho} \exp(-\eta Q) dQ, & Q \leq 1 \end{array} \right\}. \end{aligned} \tag{5.36}$$

Using the fact that the density goes like probability divided by the differential volume, we arrive at

$$n\left(\rho, Q\right) dQ \propto \left\{ \begin{array}{cc} \frac{1}{\rho}\sqrt{Q\left(\rho^2 - 1\right) + \left(1 - \rho^3\right)} \exp(-\eta Q) dQ, & Q > 1 \\ \sqrt{Q - \rho} \exp(-\eta Q) dQ, & Q \leq 1 \end{array} \right\}. \tag{5.37}$$

Eq. 5.36 is the probability of finding an atom with energy between Q and $Q + dQ$, at a radius between ρ and $\rho + d\rho$. Similarly, Eq. 5.37 can be thought of as the density distribution for atoms whose energy lies between Q and $Q + dQ$.

Intuition for the allowed orbits in the trap can be built by examining the graphical representations of the probability function, Eq. 5.36 as shown in Figure 5.4. These distributions have been rescaled to have peak values of unity. Figure 5.4.a shows the shows the spatial distribution for atoms at a few representative energy values. As can be seen, for energies $Q < 1$, the radial distribution vanishes for $\rho > Q$. For $Q > 1$, on the other hand, the distribution starts to "peel away" from the center of the trap.

Figure 5.4.b shows the energy distribution of atoms passing through a few representative radii. It is interesting to note that the energy distribution for atoms near the center of the trap is closely approximated by a Boltzmann distribution truncated at $Q = 1$. This is interesting because most of the atoms in ensembles confined at large η, will be near the center of the trap. Therefore, approximating the energy distribution as a truncated Boltzmann distribution introduces only small errors when η is large. As η is decreased, however, the size of the trapped cloud grows, causing the distorted energy distributions at larger radii to play a more prominent role. This leads to a breakdown in the large η approximation.

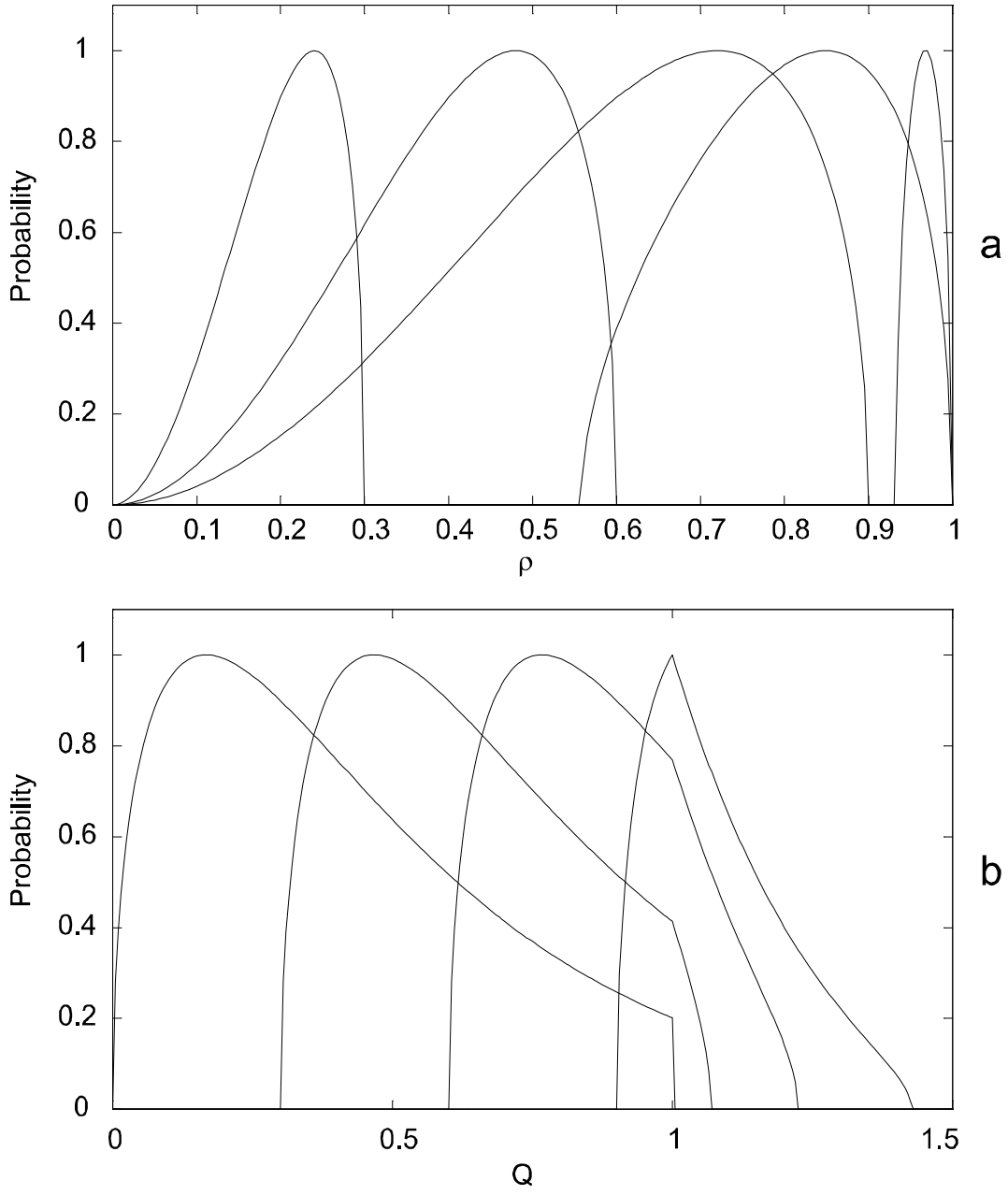

Figure 5.4: **a)** These five traces are the radial probability distributions for energies of $Q = 0.3, 0.6, 0.9, 1.2, 1.45$. The distributions have been scaled to have a peak value of unity. **b)** These four traces are the energy probability distributions for atoms found at radii $\rho = 0, 0.3, 0.6, 0.9$. They have also been scaled to have peak values of unity.

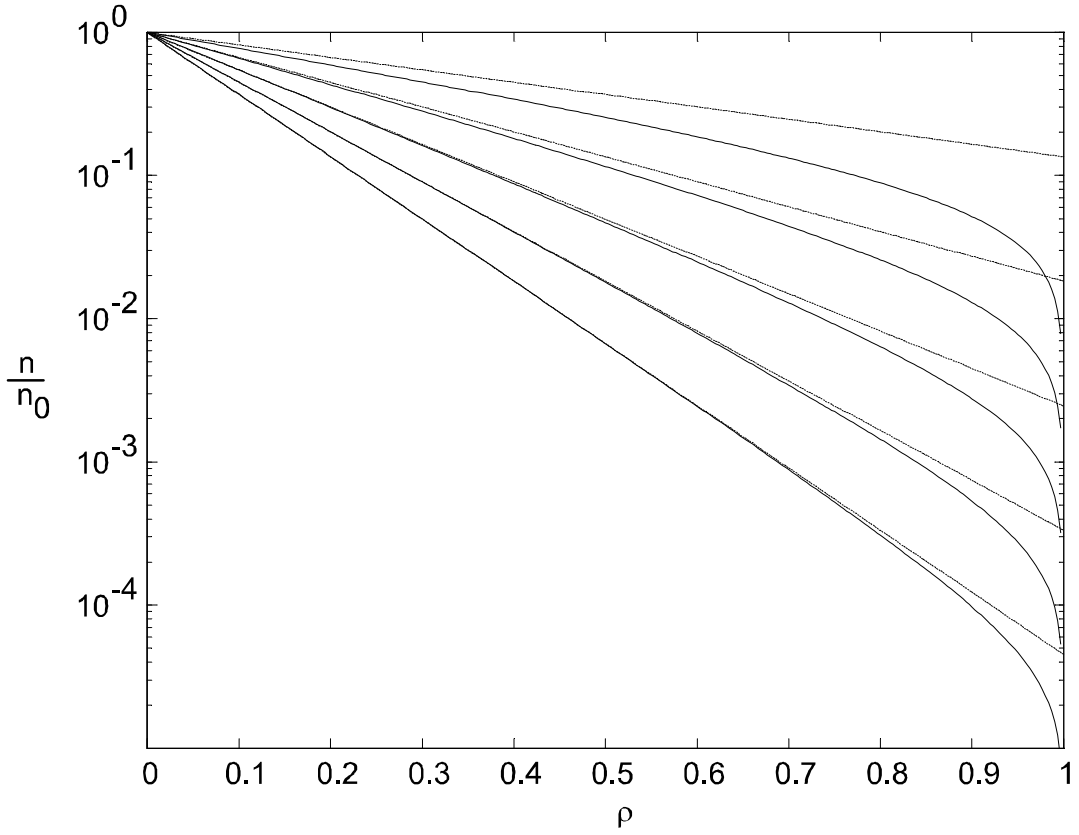

Figure 5.5: The solid lines show the trapped density distributions obtained by numerically integrating Eq. 5.38 for $\eta = 2, 4, 6, 8, 10$. The high η approximation for the density, $n = n_0 e^{-\eta\rho}$, is shown by the dotted traces for the same values of η.

5.3.6 Density Distribution

The density at any point in the trap can then be found by integrating Eq. 5.37 over the allowed energy values to get

$$n(\rho) = n_0 \frac{\left[\int_{Q_{\min}(\rho)}^{Q_{\max}(\rho)} n(\rho, Q)\, dQ\right]}{\left[\int_0^1 n(0, Q)\, dQ\right]}, \tag{5.38}$$

where n_0 is the density at the center of the trap. Evaluating this integral for the density is a bit tricky. The numerator of Eq. 5.38 can be written as

$$\begin{aligned} & \int_{\rho}^{1} \sqrt{Q-\rho}\exp\left(-\eta Q\right) dQ \\ & + \int_{1}^{1+\frac{\rho^2}{1+\rho}} \sqrt{Q\left(\rho^2-1\right)+\left(1-\rho^3\right)}\exp\left(-\eta Q\right) dQ \\ = \; & I_1 + I_2 \end{aligned} \tag{5.39}$$

The integral I_1 is straightforward to evaluate. The difficulty lies in evaluating I_2. Performing two changes of variables on I_2 by letting $y = \sqrt{Q\left(\rho^2-1\right)+\left(1-\rho^3\right)}$, and then letting $u = \sqrt{\eta/\left(1-\rho^2\right)}y$, we arrive at

$$I_2 = \frac{2}{\eta}\sqrt{\frac{1-\rho^2}{\eta\rho^2}}\exp\left[-\eta\left(\frac{1-\rho^3}{1-\rho^2}\right)\right]\int_0^{\sqrt{\eta(\rho^2-\rho^3)/(1-\rho^2)}} u^2\exp\left(u^2\right) du.$$

This is a considerable simplification allowing us to evaluate

$$n\left(\rho\right) = n_0\frac{\left(I_1+I_2\right)}{\lim\limits_{\rho\to 0}\left(I_1+I_2\right)}$$

to get

$$n\left(\rho\right) = n_o\frac{\exp\left(x^2\right)\operatorname{erf}\left(x\right) - \frac{x}{y}\frac{1}{i}\operatorname{erf}\left(iy\right)\exp\left(-y^2\right)}{\exp\left(\eta\right)\operatorname{erf}\left(\sqrt{\eta}\right) - 2\sqrt{\eta/\pi}},$$

where $x \equiv \sqrt{\eta\left(1-\rho\right)}$ and $y \equiv \sqrt{\eta\frac{\rho^2}{1+\rho}}$.

The complex error function can be expanded in the infinite series [35]

$$\operatorname{erf}\left(x+iy\right) = \left[\begin{array}{c} \operatorname{erf} x + \frac{e^{-x^2}}{2\pi x}\left[\left(1-\cos 2xy\right)+i\sin 2xy\right] \\ +\frac{2}{\pi}e^{-x^2}\sum\limits_{n=1}^{\infty}\frac{e^{-\frac{1}{4}n^2}}{n^2+4x^2}\left[f_n\left(x,y\right)+ig_n\left(x,y\right)\right] \end{array}\right]$$

where

$$\begin{aligned} f_n(x,y) &= 2x - 2x\cosh ny\cos 2xy + n\sinh ny\sin 2xy \\ g_n(x,y) &= 2x\cosh ny\sin 2xy + n\sinh ny\cos 2xy. \end{aligned}$$

Taking $x = 0$ as is the case for a purely imaginary argument, the error function becomes

$$\frac{1}{i}\operatorname{erf}(iy) = \frac{y}{\pi} + \frac{2}{\pi}\sum_{n=1}^{\infty}\frac{e^{-\frac{1}{4}n^2}}{n}\sinh(ny).$$

So, defining

$$S_N(y) \equiv \frac{y}{\pi} + \frac{2}{\pi}\sum_{n=1}^{N}\frac{e^{-\frac{1}{4}n^2}}{n}\sinh(ny), \tag{5.40}$$

we arrive at the following analytic expression for the density in the trap:

$$n(\rho) = n_o\frac{\exp(x^2)\operatorname{erf}(x) - \frac{x}{y}S_N(y)\exp(-y^2)}{\exp(\eta)\operatorname{erf}\left(\sqrt{\eta}\right) - 2\sqrt{\eta/\pi}}, \tag{5.41}$$

where $x \equiv \sqrt{\eta(1-\rho)}$ and $y \equiv \sqrt{\eta\frac{\rho^2}{1+\rho}}$. Numerically integrating the exact expression for the density, Eq. 5.38, and comparing with the analytic expansion of Eq. 5.41, we obtain an agreement of around 2% when only five terms $(N = 5)$ are included in the sum for S_N.

Shown in Figure 5.5 is a comparison between the result of the large η approximation and the exact solution for the density distribution in the trap. As can be seen, at large η's, the two distributions are quite similar. The distortion leading to the breakdown of the large η approximation is clearly visible. As a rule of thumb, the large-η approximation can be used $\eta \gtrsim 4$.

5.3.7 Collisional Energy Transfer

In preparation for the discussion on calculating the evaporation rate from a spherical trap, we must develop an understanding of how energy is transferred during an elastic collision between two atoms of equal mass. Specifically, we seek an answer to the following question. Given two atoms of kinetic energy E_1 and E_2, what is the probability that one of the atoms comes away with kinetic energy U_1?

Consider two atoms that collide in free space (i.e. no external forces). Call them atom 1 and atom 2. Before they collide, they have momenta $\mathbf{P}_1$ and $\mathbf{P}_2$, and kinetic energies E_1 and E_2. After they collide, they have momenta $\mathbf{Q}_1$ and $\mathbf{Q}_2$ and kinetic energies U_1 and U_2. Let's make the following definitions:

$$\begin{array}{cc} \mathbf{P} \equiv \frac{1}{2}(\mathbf{P}_1 + \mathbf{P}_2) & \mathbf{Q} \equiv \frac{1}{2}(\mathbf{Q}_1 + \mathbf{Q}_2) \\ \mathbf{p} \equiv \frac{1}{2}(\mathbf{P}_1 - \mathbf{P}_2) & \mathbf{q} \equiv \frac{1}{2}(\mathbf{Q}_1 - \mathbf{Q}_2) \\ E \equiv E_1 + E_2 & U \equiv U_1 + U_2 \\ G^2 \equiv E_1 E_2 & \end{array}$$

From these definitions we can immediately write that

$$\mathbf{P}^2 + \mathbf{p}^2 = \mathbf{Q}^2 + \mathbf{q}^2 = mE = mU,$$

where m is the mass of one atom. Furthermore, conservation of energy and momentum give

$$\mathbf{Q} = \mathbf{P}$$

$$q = p. \tag{5.42}$$

We will solve for the energy of atom 1 after the collision has occurred. Expressing this energy in terms of $\mathbf{Q}$ and $\mathbf{q}$, we write

$$U_1 = \frac{\mathbf{Q}_1^2}{2m} = \frac{1}{2m}\left(\mathbf{Q}+\mathbf{q}\right)^2.$$

But, from conservation of energy and momentum, Eq. 5.42, this can be written as

$$U_1 = \frac{1}{2}E + \frac{Pp}{m}\cos\theta$$

where θ is the angle between $\mathbf{q}$ and $\mathbf{Q}$. Substituting for Pp results in

$$\begin{aligned} U_1 &= \frac{1}{2}E + \frac{1}{2}\left[\sqrt{E^2 - 4G^2\cos^2\alpha}\right]\cos\theta \\ U_2 &= \frac{1}{2}E - \frac{1}{2}\left[\sqrt{E^2 - 4G^2\cos^2\alpha}\right]\cos\theta \end{aligned} \tag{5.43}$$

where α is the angle between $\mathbf{P}_1$ and $\mathbf{P}_2$.

A few words about the angles θ and α are in order. θ is the angle that the relative momentum of the scattered particles, $\mathbf{q}$, makes with the center of mass momentum, $\mathbf{Q}$. We will assume that after the two particles collide, their direction, in the center of mass frame, is randomized in solid angle. We also assume that the initial momenta $\mathbf{P}_1$ and $\mathbf{P}_2$ are uniformly distributed over solid angle. Stated mathematically, this says the probability that $\mathbf{P}_1$ and $\mathbf{P}_2$ are oriented at angles α and ϕ with respect to one another (arbitrary axis defining ϕ) is just

$$P\left(\alpha,\phi\right)d\Omega = \frac{1}{4\pi}d\Omega = -\frac{1}{2}d\left(\cos\alpha\right).$$

Similarly, the distribution of the angles between $\mathbf{q}$ and $\mathbf{Q}$ is

$$P(\theta, \phi')\, d\Omega' = \frac{1}{4\pi} d\Omega' = -\frac{1}{2} d(\cos\theta).$$

The distribution over both sets of angles is then given by

$$P(\alpha, \phi, \theta, \phi')\, d\Omega d\Omega' = \frac{1}{4} d(\cos\alpha)\, d(\cos\theta) \tag{5.44}$$

If we define

$$\begin{aligned} x &\equiv \cos\alpha \\ y &\equiv \cos\theta, \end{aligned}$$

we can then rewrite Eq. 5.43 for the outgoing kinetic energy of atom 1 as

$$U_1 = \frac{1}{2}E + \frac{1}{2}\left[\sqrt{E^2 - 4G^2x^2}\right] y, \tag{5.45}$$

and the probability distribution over the angles, Eq. 5.44, simplifies to

$$P(y, x)\, dydx = \frac{1}{4} dydx. \tag{5.46}$$

It should be noted that $y \in [-1, 1]$, $x \in [-1, 1]$. Furthermore, $x^2 \leq \frac{U_1(E-U_1)}{G^2}$, to ensure the kinetic energy of Eq. 5.45 remains real.

Differentiating Eq. 5.45 with respect to y, and substituting for dy in Eq. 5.46, the distribution in scattered energy becomes

$$P(x, U_1)\, dU_1 dx \propto \frac{dU_1 dx}{\sqrt{E^2 - 4G^2x^2}}. \tag{5.47}$$

To find the probability of scattering into U_1, we must integrate over all allowed values of x,

$$P_s\left(U_1\right) dU_1 \propto dU_1 \int_{-x_{\max}}^{x_{\max}} \frac{dx}{\sqrt{E^2 - 4G^2x^2}}$$

where $x_{\max} = \frac{1}{G}\sqrt{U_1\left(E - U_1\right)}$. Properly normalizing, we obtain the probability distribution

$$P_s\left(E, U_1\right) dU_1 = \frac{2}{E} \sin^{-1}\left(\frac{2\sqrt{U_1\left(E - U_1\right)}}{E}\right) dU_1. \tag{5.48}$$

When two atoms with kinetic energies summing to E collide, Eq. 5.48 is the probability that one atom exits the collision with kinetic energy between U_1 and $U_1 + dU_1$. (Note that this result is easily transformed to the dimensionless units used in the rest of this chapter by simply dividing all energies by ηkT.)

5.3.8 Evaporation Probability

In order to calculate the evaporation rate from the trap, the following question must be answered. What is the probability that an atom of energy Q evaporates from the trap? Or equivalently, what is the probability that an atom of energy Q remains in the trap?

Imagine that a trapped atom comes away from an elastic collision with an energy Q. The collision will place it into one of many possible trajectories in the trapping potential. If the trap were infinitely deep, each of these trajectories would remain confined in the trap. In a finite trap, however, it is possible that only a frac-

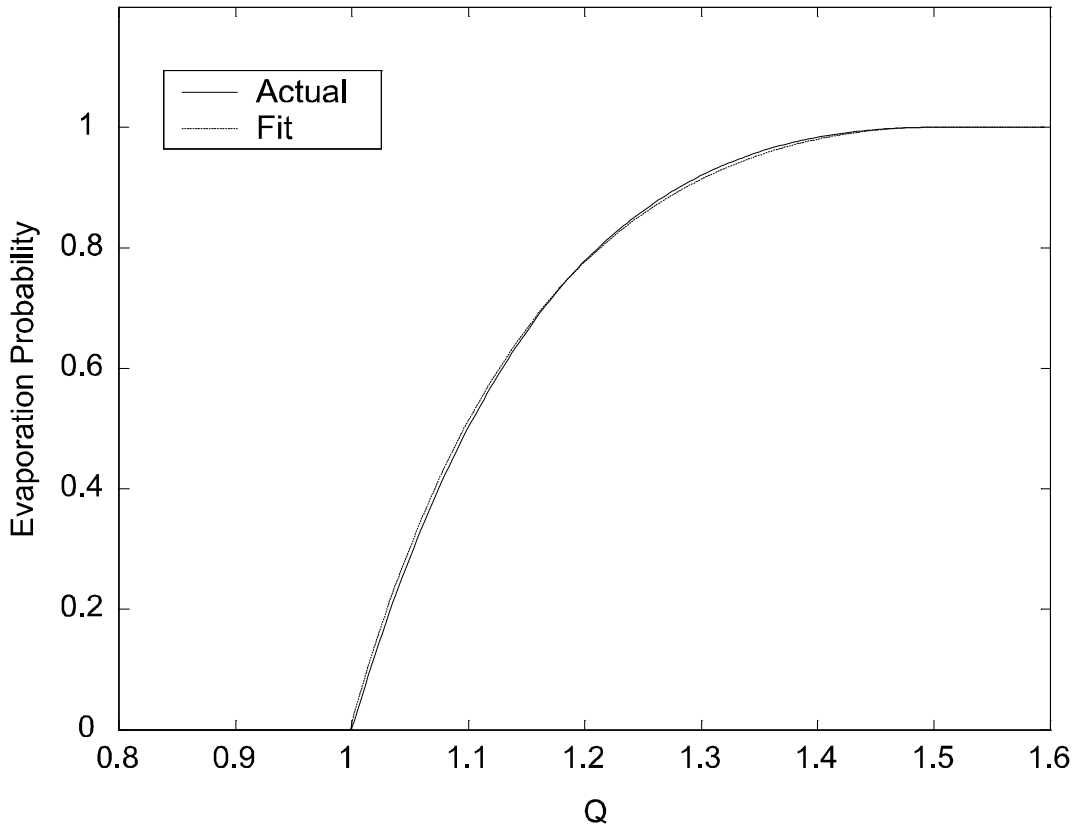

Figure 5.6: The solid line shows the probability that an atom of energy Q will evaporate from the trap. The dashed line is a plot of the analytic result for the evaporation probability obtained by using the ad-hoc fit for the density of trapped states, Eq. 5.35

tion of these trajectories will result in confined orbits. This suggests a method of calculating the probability that an atom remains trapped.

The probability that an atom of energy Q is found in a confined orbit of the trap is given by the ratio of the number of trapped orbits of energy Q in a finite trap to the number of these orbits in an infinite trap. This is identically the ratio between the density of states of a finite trap to that of an infinite trap. Thus the probability of evaporation is

$$P_v(Q) = 1 - \frac{g(Q)}{g_\infty(Q)} \tag{5.49}$$

Using the fit to the density of states derived in Eq. 5.35,

$$g(Q) \simeq \left\{ \begin{array}{cc} \frac{64}{105} A Q^{7/2}, & Q \in [0,1] \\ 70A \exp\left[-4\left(\frac{3}{2} - Q\right)^{-1/4} - (Q-1)\right] & Q \in (1, \frac{3}{2}) \\ 0 & Q \in (\frac{3}{2}, \infty] \end{array} \right\},$$

and

$$g_\infty(Q) = \frac{64}{105} A Q^{7/2},$$

we arrive at the following expression for the probability that an atom of energy Q occupies an orbit leading to evaporation.

$$P_v(Q) \simeq \left\{ \begin{array}{cc} 0 & Q \in [0,1] \\ 1 - \frac{3675}{32Q^{7/2}} \exp\left[-4\left(\frac{3}{2} - Q\right)^{-1/4} - (Q-1)\right] & Q \in (1, \frac{3}{2}) \\ 1 & Q \in (\frac{3}{2}, \infty] \end{array} \right\}. \tag{5.50}$$

Figure 5.6 shows the evaporation probability as a function of energy, Q. Notice that an atom must have energy at least that of the trap depth in order to evaporate. Furthermore, any atom with energy greater than 1.5 times the trap depth is guaranteed to evaporate.

5.3.9 Evaporation Fraction

The groundwork has now been laid to calculate the evaporation fraction for atoms confined in a spherical linear trap. Eq. 5.13 for the differential elastic scattering rate occurring at some radius ρ in reproduced here

$$d\Gamma_{el}(r) = n_0^2(r)\,\sigma_{el}\bar{v}\sqrt{2}d^3r.$$

This expression can be specialized to account for the energies involved in the collision by using by Eq. 5.37 for $n(\rho, Q)$, the density distribution of atoms with a particular energy. The collision rate between atoms of energy Q_1 and atoms of energy Q_2 in the differential volume about some radius, ρ, is given by

$$d\Gamma_{el}(\rho, Q_1, Q_2) \propto \sigma_{el} v_{rel}(Q_1, Q_2, \rho)\, n(\rho, Q_1)\, n(\rho, Q_2)\, dQ_1 dQ_2 \rho^2 d\rho,$$

where $v_{rel}(Q_1, Q_2, \rho) \propto \sqrt{Q_1 + Q_2 - 2\rho}$ is the average relative velocity between atoms. Integrating over all possible energies Q_1 and Q_2, the total collision rate for atoms in the differential volume about ρ is

$$d\Gamma_{el}(\rho) \propto \sigma_{el}\rho^2 d\rho \int_{Q_{\min(\rho)}}^{Q_{\max}(\rho)} \int_{Q_{\min(\rho)}}^{Q_{\max}(\rho)} n(\rho, Q_1)\,\overline{v}(Q_1, Q_2, \rho)\, n(\rho, Q_2)\, dQ_2 dQ_1 \tag{5.51}$$

where, as before, $Q_{\min}(\rho) = \rho$ and $Q_{\max}(\rho) = 1 + \frac{\rho^2}{1+\rho}$.

The dimensionless kinetic energy of atoms with Q_1 and Q_2 is given by $\tau_1 = Q_1 - \rho$ and $\tau_2 = Q_2 - \rho$ respectively. The sum of these kinetic energies is simply $\tau = Q_1 + Q_2 - 2\rho$. We can now use Eq. 5.48 to write the probability, $P_s(\tau, H_1)$, that a collision between two atoms whose kinetic energies sum to τ, results in one of the

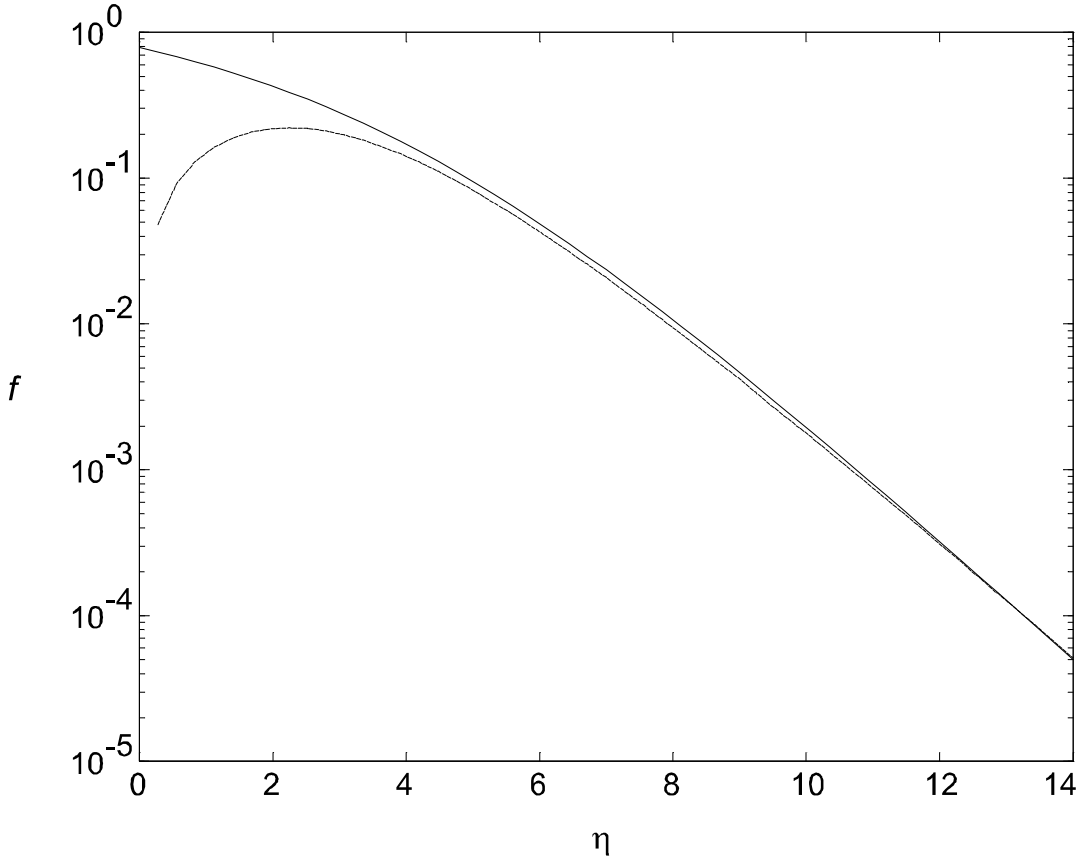

Figure 5.7: The solid line is the result of numerically integrating Eq. 5.52 to obtain the fraction of elastic collisions that result in an evaporating atom. The dashed line is a plot of the large η approximation for the evaporation fraction given in Eq. 5.14.

atoms exiting the collision with kinetic energy H_1. The total energy of this scattered atom is the sum of its kinetic and potential energies, $\rho + H_1$. The probability that this atom evaporates is then given by $P_v(\rho + H_1)$ which was derived in Eq. 5.50. The evaporation rate of the atoms found in the differential volume about ρ can then be written as

$$d\Gamma_{evap}(\rho) = \left[\begin{array}{c} \sigma_{el}\rho^2 d\rho \int_{Q_{\min(\rho)}}^{Q_{\max}(\rho)} \int_{Q_{\min(\rho)}}^{Q_{\max}(\rho)} n(\rho, Q_1)\, \overline{v}(Q_1, Q_2, \rho)\, n(\rho, Q_2) \times \\ \int_0^{\tau} P_s(\tau, H_1)\, P_v(\rho + H_1)\, dH_1 dQ_2 dQ_1 \end{array} \right].$$

The fraction of elastic collisions that result in an evaporating atom is then given by the mean of the ratio between the evaporation rate and the collision rate, or

$$f = \frac{\langle d\Gamma_{evap} \rangle}{\langle d\Gamma_{el} \rangle}.$$

The expression for this average can be explicitly written out as

$$f = \frac{\int_0^1 \rho^2 d\rho \left[\begin{array}{c} \int_{Q_{\min}}^{Q_{\max}} n(\rho, Q_1)\, dQ_1 \int_{Q_{\min}}^{Q_{\max}} \overline{v}(Q_1, Q_2, \rho)\, n(\rho, Q_2)\, dQ_2 \times \\ 2 \int_{\frac{\tau}{2}}^{\tau} P_s(\tau, H_1)\, P_v(\rho + H_1)\, dH_1 \end{array} \right]}{\int_0^1 \rho^2 d\rho \left[\int_{Q_{\min}}^{Q_{\max}} n(\rho, Q_1)\, dQ_1 \int_{Q_{\min}}^{Q_{\max}} \overline{v}(Q_1, Q_2, \rho)\, n(\rho, Q_2)\, dQ_2 \right]} \tag{5.52}$$

The integrals in Eq. 5.52 do not have simple analytic solutions, and we resort to numerical integration. The solid line of Figure 5.7 shows the result of numerically integrating Eq. 5.52 to get the evaporation fraction. The dotted line is a plot of the evaporation fraction in the large η approximation given by Eq. 5.14. As expected, the large η approximation gives good agreement for $\eta \gtrsim 4$.

5.3.10 Average Energies

The average energies in the trap can be expressed in terms of integrals. These integrals do not lend themselves to simple analytic solutions. For each of the energies discussed below, the integral expression is written out explicitly along with a plot for comparison with the large η approximation.

Average Energy in the Trap

The average energy in the trap is straightforward to calculate. We know $n(\rho, Q)$ from Eq. 5.37. The mean energy is then

$$\bar{Q} = \frac{\int_0^1 \rho^2 d\rho \int_{Q_{\min}}^{Q_{\max}} Q n(\rho, Q)\, dQ}{\int_0^1 \rho^2 d\rho \int_{Q_{\min}}^{Q_{\max}} n(\rho, Q)\, dQ} \tag{5.53}$$

where $Q_{\min} = \rho$ and $Q_{\max} = 1 + \frac{\rho^2}{1+\rho}$. Figure 5.8 shows a comparison of the average energy in the trap compared with the results of the large η approximation.

Average Energy of Inelastic Loss

Although Eq. 5.51 was derived to describe elastic collisions, it can also be used to describe inelastic collisions as well. The only requirement is that the elastic cross section, σ_{el}, be replaced with the inelastic cross section σ_{in}. Assuming that each inelastic collision ejects one atom from the trap, the atom loss rate will be the same as the collision rate. The expression for the average energy of the atoms lost due to

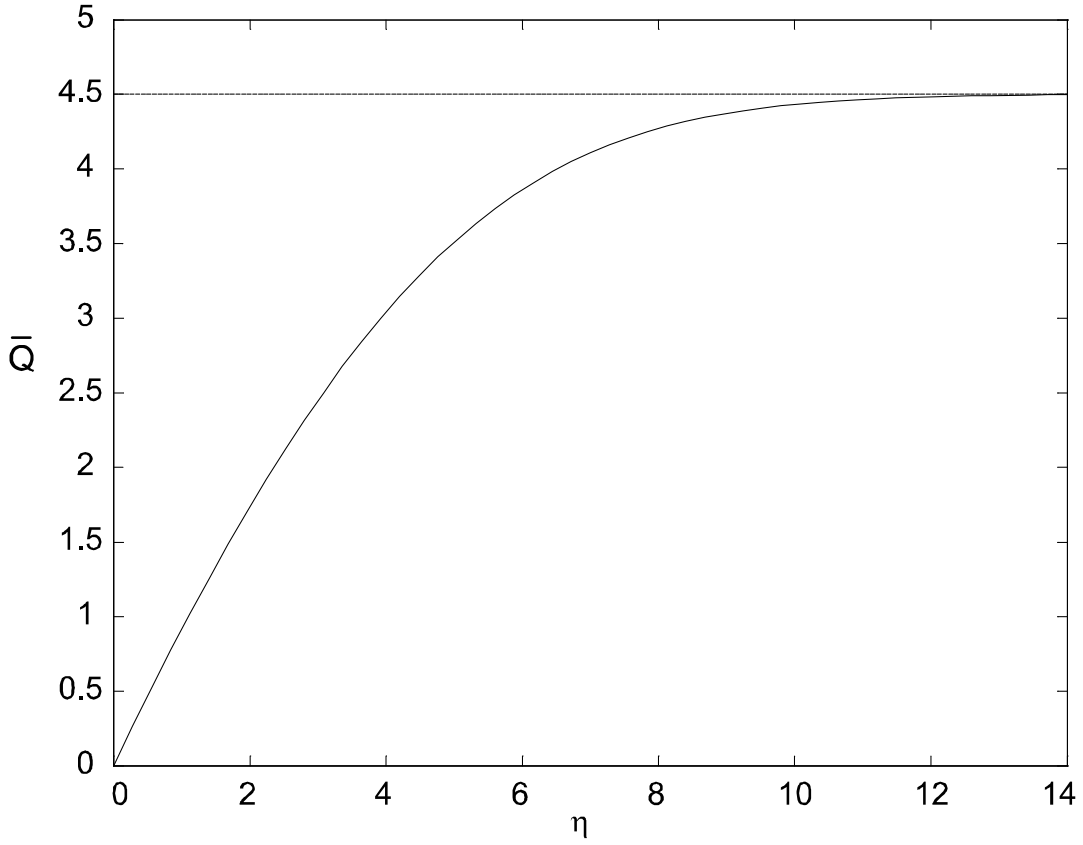

Figure 5.8: The solid line shows the η dependance of the average energy of a trapped atom, $\bar{Q}$, as given by numerically integrating Eq. 5.53. The dashed line is a plot of the large η approximation for $\bar{Q}$.

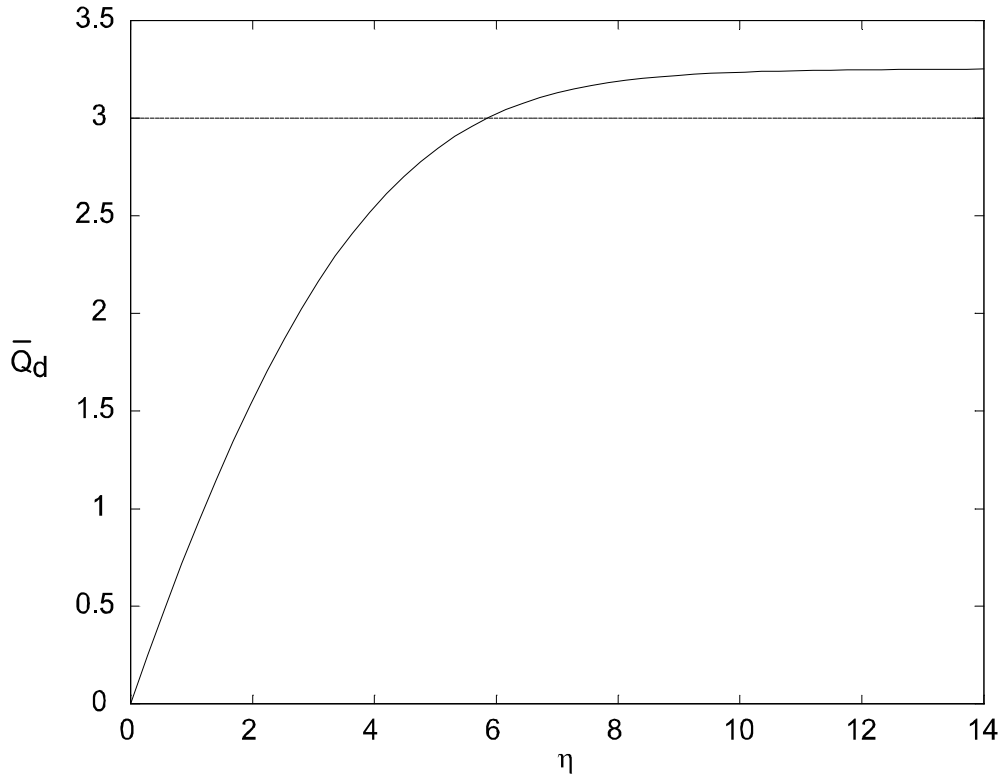

Figure 5.9: The solid line shows the η dependance of the average energy of atoms lost due to inelastic collisions, $\bar{Q}_d$, as given by numerically integrating Eq. 5.54. The dashed line is a plot of the large η approximation for $\bar{Q}_d$.

inelastic scattering is then

$$\bar{Q}_d = \frac{\int_0^1 \rho^2 d\rho \int_{Q_{\min}}^{Q_{\max}} Q_1 n(\rho, Q_1)\, dQ_1 \int_{Q_{\min}}^{Q_{\max}} \overline{v}(Q_1, Q_2, \rho)\, n(\rho, Q_2)\, dQ_2}{\int_0^1 \rho^2 d\rho \int_{Q_{\min}}^{Q_{\max}} n(\rho, Q_1)\, dQ_1 \int_{Q_{\min}}^{Q_{\max}} \overline{v}(Q_1, Q_2, \rho)\, n(\rho, Q_2)\, dQ_2} \tag{5.54}$$

Figure 5.9 shows a comparison of the average energy removed by inelastic collisions compared with the results of the large η approximation. The discrepancy at large η is caused by a failure to properly account for the relative velocities between atoms in the large η approximation.

Average Energy of Evaporative Loss

The average energy of an evaporating atom is calculated by multiplying the differential evaporation rate by the energy removed by an evaporating atom, $(\rho + H_1)$. Integrating and normalizing by the evaporation rate gives

$$\bar{Q}_v = \frac{\int_0^1 \rho^2 d\rho \left[\int_{Q_{\min}}^{Q_{\max}} n(\rho, Q_1)\, dQ_1 \int_{Q_{\min}}^{Q_{\max}} \overline{v}(Q_1, Q_2, \rho)\, n(\rho, Q_2)\, dQ_2 \times \int_{\frac{\tau}{2}}^{\tau} (\rho + H_1) P_s(\tau, H_1) P_v(\rho + H_1)\, dH_1 \right]}{\int_0^1 \rho^2 d\rho \left[\int_{Q_{\min}}^{Q_{\max}} n(\rho, Q_1)\, dQ_1 \int_{Q_{\min}}^{Q_{\max}} \overline{v}(Q_1, Q_2, \rho)\, n(\rho, Q_2)\, dQ_2 \times \int_{\frac{\tau}{2}}^{\tau} P_s(\tau, H_1) P_v(\rho + H_1)\, dH_1 \right]} \tag{5.55}$$

The solid line in Figure 5.10 shows the average energy removed by evaporating atom. The dashed line is the trap depth. As can be seen, the average evaporated energy is $E_v = (\eta + \kappa)\, kT$, where κ, is the given by the difference between the two lines in Figure 5.10.

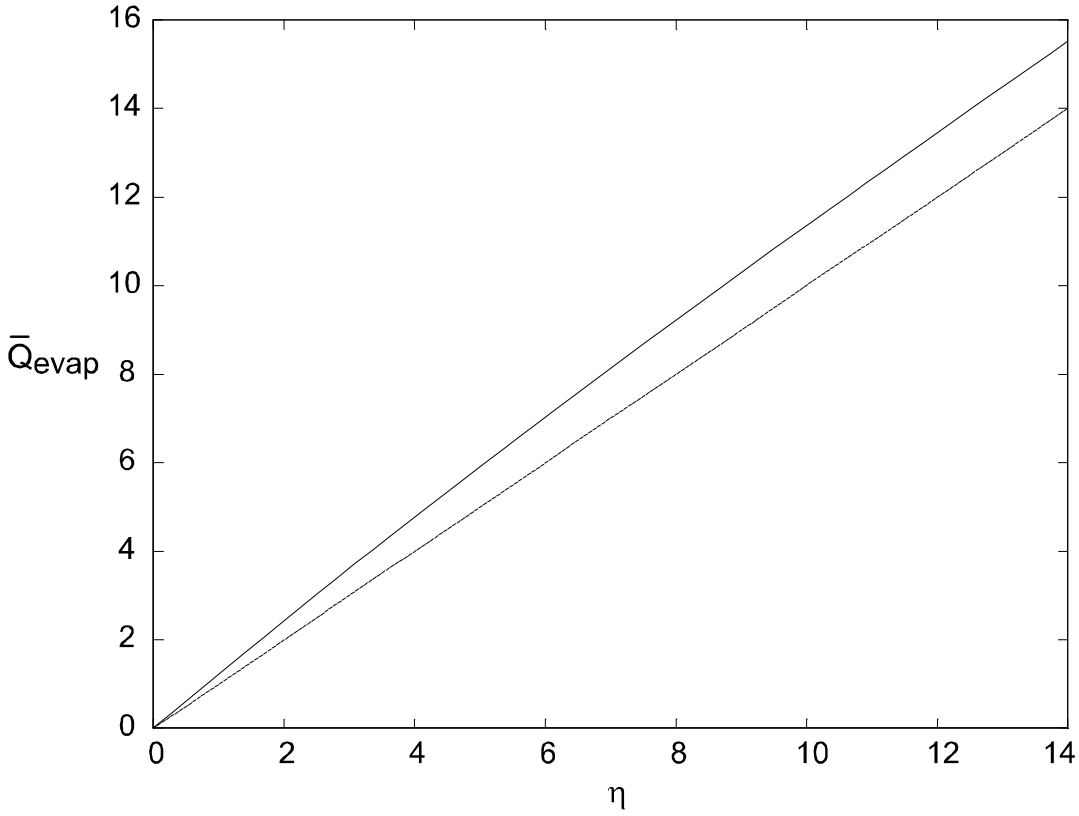

Figure 5.10: The solid line shows the η dependance of the average energy of an evaporated atom, $\bar{Q}_v$, as given by numerically integrating Eq. 5.55. The dashed line is simply a plot of η. The difference between the solid line $\left(\bar{Q}_v\right)$ and the dotted line (η) is given by κ in Eq. 5.10 for the average evaporation energy in the large η approximation.

5.3.11 Effective Volumes

The effective volumes can be calculated using the same procedure as was taken in the large η approximation. However, the resulting integrals are not easy to evaluate analytically. Recalling the defining equations, $N = n_0 V_{eff}$, and $\Gamma = n_0^2 \sigma \left(\bar{v}\sqrt{2}\right) \Lambda_{eff}$. The effective volume becomes

$$\begin{aligned} V_{eff}(\eta) &= 3V_0 \int_0^1 \frac{n(\rho)}{n_0} \rho^2 d\rho \\ &= 3V_0 \int_0^1 \tilde{n}(\rho) \rho^2 d\rho \end{aligned}$$

where

$$\begin{aligned} \tilde{n}(\rho) &\equiv \frac{n(\rho)}{n_0} = \frac{\exp(x^2)\operatorname{erf}(x) - \frac{x}{y} S_N(y) \exp(-y^2)}{\exp(\eta)\operatorname{erf}\left(\sqrt{\eta}\right) - 2\sqrt{\eta/\pi}}, \\ S_N(y) &\equiv \frac{y}{\pi} + \frac{2}{\pi} \sum_{n=1}^{N} \frac{e^{-\frac{1}{4}n^2}}{n} \sinh(ny), \end{aligned}$$

N is an integer, $x \equiv \sqrt{\eta(1-\rho)}$ and $y \equiv \sqrt{\eta \frac{\rho^2}{1+\rho}}$.

Similarly,

$$\Lambda_{eff}(\eta) = 3V_0 \int_0^1 \tilde{n}^2(\rho) \rho^2 d\rho.$$

Recall from Eq. 5.17 that the average collision rate is given by

$$\bar{\Gamma} = \frac{\Gamma}{N} = \frac{\Lambda_{eff}(\eta)}{V_{eff}(\eta)} \left[n_0 \sigma \left(\bar{v}\sqrt{2}\right) \right]. \tag{5.56}$$

The quantity in brackets is the scattering rate experienced by a single atom at the center of the trap. For large η, we previously found that the ratio, $\Lambda_{eff}(\eta)/V_{eff}(\eta)$ evaluates to $1/8$. Figure 5.11, shows the reciprocal of this ratio compared to its value in the large η limit.

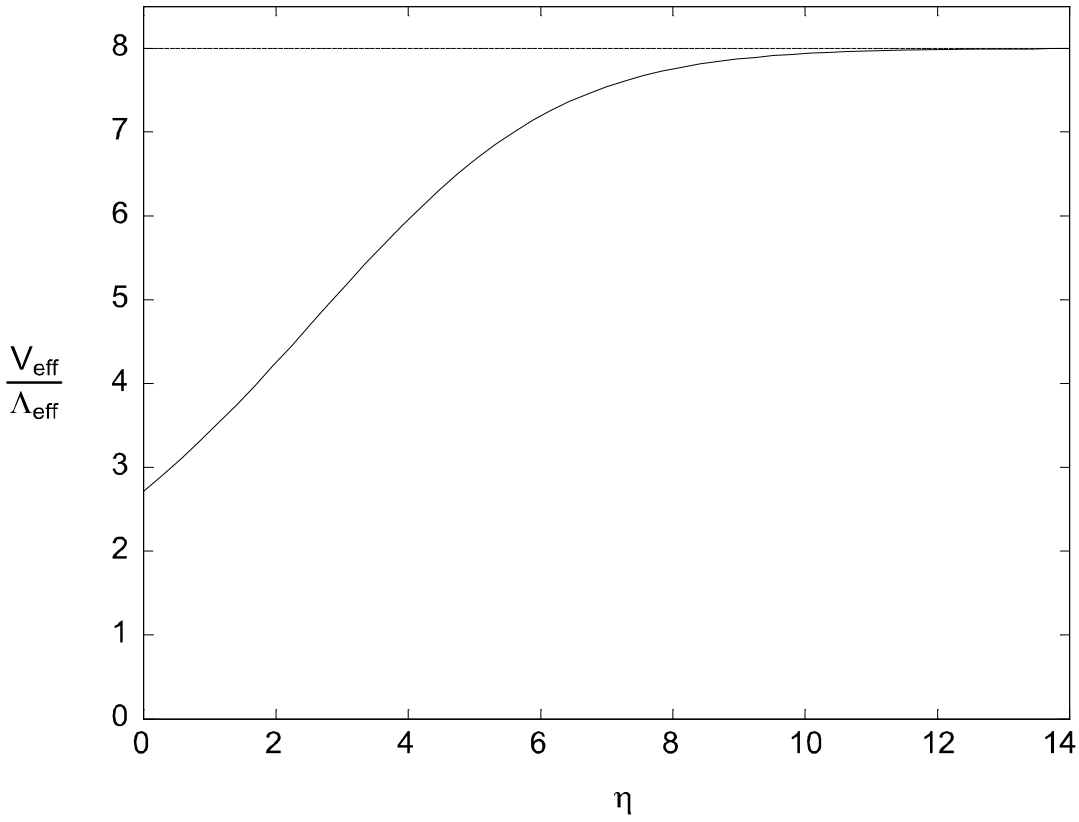

Figure 5.11: The solid line shows the η dependance of the reciprocal to the average density correction factor, $\frac{\Lambda_{eff}(\eta)}{V_{eff}(\eta)}$. In the large η approximation, this correction factor approches $1/8$ as shown by the dotted line.

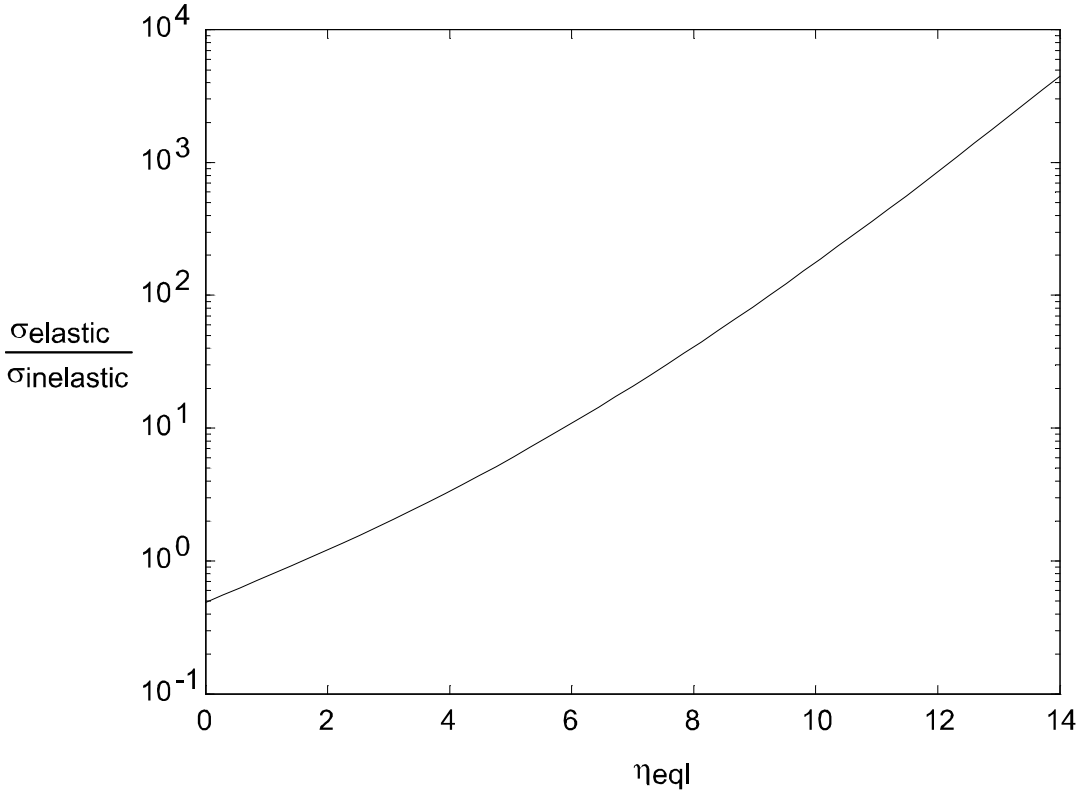

Figure 5.12: A given ratio between the elastic and inelastic scattering rates causes the temperature of the trapped atoms to approach a fixed fraction of the trap depth. This figure shows the cross section ratio that must exist to produce a given "equilibrium η."

5.3.12 Equilibrium η and Cross Section Ratio

Atoms confined in a trap and undergoing only collisional loss processes, will be driven to a thermal distribution with a steady state temperature. This can be understood by noting that evaporative loss produces cooling whereas inelastic loss produces heating. These two processes compete against each other to drive the system to a steady state temperature. The ratio of the trap depth to this steady state temperature is defined to be the equilibrium η.

We now show that the equilibrium η will depend only on the ratio of elastic to inelastic cross sections, $\gamma \equiv \sigma_{el}/\sigma_{in}$. To prove this, we differentiate the total energy in the trap $E = N\bar{E}$ to get

$$\frac{dE}{dt} = \bar{E}\frac{dN}{dt} + N\frac{d\bar{E}}{dt}.$$

But for steady state temperature, $\frac{d\bar{E}}{dt} = 0$, so

$$\bar{E} = \frac{\dot{E}}{\dot{N}} = \frac{\dot{N}_v\bar{E}_v + \dot{N}_d\bar{E}_d}{\dot{N}_v + \dot{N}_d},$$

where $\dot{N}_v$ is the evaporative loss rate and $\dot{N}_d$ is the inelastic loss rate. If the total elastic and inelastic scattering rates are Γ_{el} and Γ_{in} and their ratio is $\gamma = \Gamma_{el}/\Gamma_{in} = g_{el}/g_{in} = \sigma_{el}/\sigma_{in}$, the steady state value for the average energy is

$$\bar{E} = \frac{f\gamma\bar{E}_v + \bar{E}_d}{f\gamma + 1}.$$

Dividing through by ηkT, the dimensionless steady state value for the mean energy is

$$\bar{Q} = \frac{f\gamma\bar{Q}_v + \bar{Q}_d}{f\gamma + 1}.$$

Solving for γ, the following expression for the ratio of cross sections is obtained

$$\gamma \equiv \frac{\sigma_{el}}{\sigma_{in}} = \frac{\bar{Q} - \bar{Q}_d}{f\left(\bar{Q}_v - \bar{Q}\right)}. \tag{5.57}$$

Since each variable on the right hand side of Eq. 5.57 depends only on η, the correspondence between cross section ratio and equilibrium η is demonstrated. Figure 5.12 shows the relation between the equilibrium η and the cross section ratio.

5.3.13 Collision Rate Coefficients

Recall our assumption that the only trap loss mechanisms stem from Cr-Cr interactions. These interactions allow only two avenues for atom loss: inelastic collisions, and evaporation over the edge. The quantity we experimentally measure is the sum of these two loss processes, or equivalently, the two-body loss rate. At very large η, the loss is dominated by inelastic collisions, but as η is decreased one could imagine the evaporation loss making a significant contribution. It is important to understand the size of the evaporative contribution to the trap loss.

We assume each inelastic collision results in one atom being evaporated from the trap. From the defining equation for the collisional effective volume, $\Gamma = n_0^2 \sigma \left(\bar{v}\sqrt{2}\right) \Lambda_{eff}$, we can write

$$\begin{aligned} \dot{N}_{in} &= \Gamma = \Lambda_{eff} \sigma \left(\bar{v}\sqrt{2}\right) n_0^2 \\ &= \Lambda_{eff}(\eta)\, g_{in} n_0^2. \end{aligned}$$

where $g_{in} \equiv \sigma_{in}\left(\bar{v}\sqrt{2}\right)$. For a trapped ensemble at constant temperature, $\dot{N} = V_{eff}(\eta)\, \dot{n}_0$. Substituting for $\dot{N}$, we obtain a differential equation for the peak density in the trap when only inelastic losses are considered

$$\left[\dot{n}_0\right]_{in} = -g_{in} \frac{\Lambda_{eff}}{V_{eff}} n_0^2.$$

Using a similar analysis for the evaporation process, the differential equation for the peak density in the trap due to both inelastic collisions and evaporation becomes

$$\dot{n}_0 = -\left(g_{in} + f g_{el}\right) \frac{\Lambda_{eff}}{V_{eff}} n_0^2 = -g_{2b} n_0^2, \tag{5.58}$$

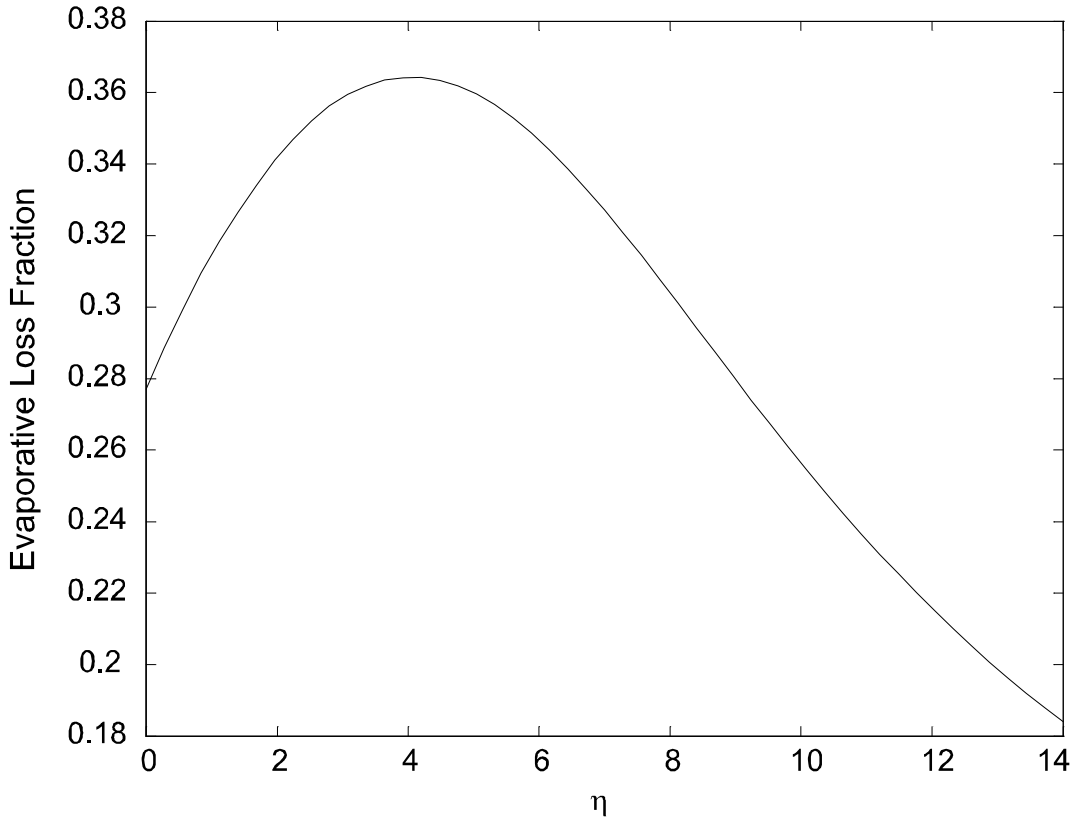

Figure 5.13: There are two avenues whereby atoms can leave the trap. They can either be driven out by inelastic collions, or they can be evaporated over the edge of the trap. For atoms confined at a steady state temperature, this plot shows the fraction of the total atom loss attributable to evaporation.

where g_{el} and g_{in} are the elastic and inelastic scattering rate coefficients, f is the evaporation fraction, and $g_{2b} \equiv \frac{\Lambda_{eff}}{V_{eff}}(g_{in} + f g_{el})$ is the two-body loss rate that we measure in our experiments. Defining the ratio of elastic to inelastic collisions as $\gamma \equiv g_{el}/g_{in}$, the elastic and inelastic rate coefficients are

$$g_{in} = \frac{V_{eff}}{\Lambda_{eff}} \frac{1}{f\gamma + 1} g_{2b} \tag{5.59}$$

and

$$g_{el} = \frac{V_{eff}}{\Lambda_{eff}} \frac{\gamma}{f\gamma + 1} g_{2b}. \tag{5.60}$$

The fraction of the two-body loss due to evaporation over the edge of the trap is

$$F_{evap} = \frac{f\gamma}{1 + f\gamma} = \frac{\bar{Q} - \bar{Q}_d}{\bar{Q}_v - \bar{Q}_d}. \tag{5.61}$$

The last step in Eq. 5.61 uses the relationship between the cross section ratio and the equilibrium η obtained earlier, $\gamma = \frac{\bar{Q} - \bar{Q}_d}{f(\bar{Q}_v - \bar{Q})}$, where $\bar{Q}$, $\bar{Q}_v$, and $\bar{Q}_d$ are the average energies of trapped, evaporated and inelastically lost atoms respectively. A plot of this fraction is shown in Figure 5.13. As can be seen, the evaporative contribution to the atom loss rate peaks at around 20% of the total two-body loss rate.

5.3.14 Comparison with Data

We are now prepared to use this model to provide a consistency check on our data. Shown in Figure 5.14 is a summary of the scattering rate measurements taken in our experiment. The points and error bars in the upper trace come from our direct measurements of the elastic scattering rate. The points and error bars in the lower plot

are our measurements of the two body loss rate from our trap. These measurements were taken some time ago and are fully described in the thesis of Jonathan Weinstein [13].

The new information on this graph is contained in the solid lines. Given the measured two-body decay rate, and the measured equilibrium η of the trapped atoms, we can use Eq. 5.59 and Eq. 5.60 to calculate the elastic and inelastic scattering rates. These inferred rates are shown by the solid traces.

It should first be noticed that the inelastic scattering rate is slightly smaller than the measured two-body loss rate. This is because some of the atoms are being lost due to evaporation. Secondly, it can be seen that the values inferred for the elastic rate fall to within a factor of 3 of our independently measured values. There is, however, a disturbing systematic trend. While the measured elastic rate appears to be either flat or slightly increasing at lower temperatures, the elastic rate predicted by the equilibrium η calculation is decreasing at smaller temperatures.

One possible reason for this systematic discrepancy is the inadequacy of the spherical approximation in describing our actual trap geometry. Another possibility is that the collisional cross sections are not uniform throughout the volume of the trap. One could imagine a situation where the inelastic scattering rate at low magnetic fields is much larger than at higher fields. Our model of trapped gases implicitly assumes uniform scattering cross sections throughout the trap volume. A violation

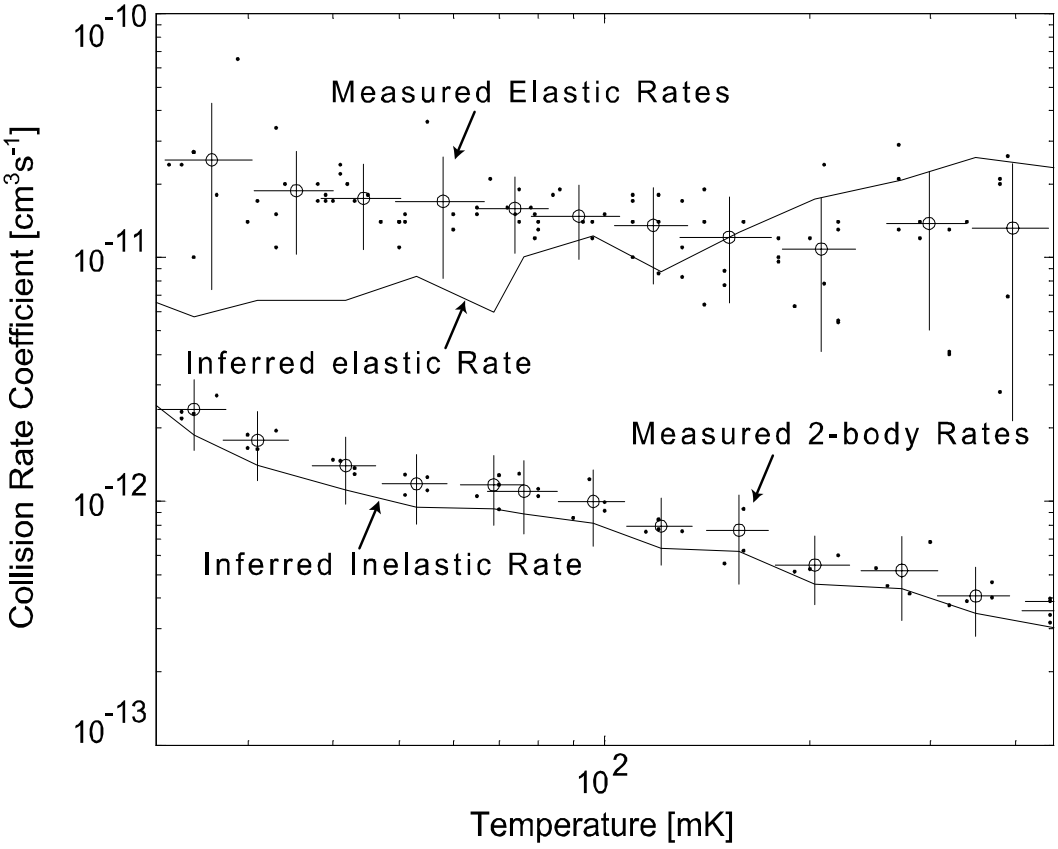

Figure 5.14: The points and accomanying error bars show our measured values for the elastic (upper) and two-body (lower) loss rate coefficients for temperatures between 20 and 400 mK. Measurements of the "equilibrium η" (not shown) can be combined with the measured two-body loss rate to infer values for the elastic and inelastic scattering rate coefficients. These are plotted with solid lines. The inferred elastic rate coefficient falls within the error bars of the values we obtain from independant measurements. This provides a self-consistency check on our data.

of this assumption would lead to different predictions for the equilibrium η. This would impact the inferred scattering rates in Figure 5.14.

Chapter 6
Scattering Theory

At the writing of this thesis, there is no theoretical explanation for the enormous inelastic scattering rates observed in our experiment. The energy scales for the collisions in our experiment are in the fuzzy region between classical and quantum physics. It is somewhat surprising that the theory of quantum scattering in the few-partial-wave regime is understood so poorly. This chapter represents the efforts of a poor experimentalist in desperately trying to wrap his brain around the surprisingly complicated analyses needed to theoretically describe collisional processes in this energy regime. Although a rigorous treatment of the scattering theory involved in this problem will not even be attempted, this chapter will hopefully provide an intuitive grasp of the problem at hand. The arguments will be qualitative and hand-wavy in nature. Vigorous theoretical work is currently being undertaken to provide a thorough and rigorous treatment of the scattering processes we observe in our experiment.

6.1 Experimental Energy Regime

The standard approach to collisional physics is to consider the problem in the center of mass frame of the colliding atoms. If the interaction potential between the two atoms depends only on their separation, the center-of-mass angular momentum will

be preserved in the collision. Considering the problem from the framework of quantum mechanics, the center-of-mass angular momentum will be quantized in units of $\hbar$. This introduces the so called "angular momentum barrier" term to the interaction potential. The effective radial potential for the collision is then given by

$$\begin{aligned} U_l(r) &= \frac{L^2}{2\mu r^2} + V(r) \\ &\underset{r\to\infty}{\simeq} \frac{\hbar^2 l(l+1)}{2\mu r^2} - \frac{C_6}{r^6}, \end{aligned}$$

where l is the angular momentum quantum number and C_6/r^6 is the long-range interatomic interaction potential. Figure 6.1.a shows a plot of this effective potential for various values of l. As can be seen, the effect of the angular momentum barrier is to create a maximum for each $l \neq 0$ effective potential curve. Crudely speaking, a collision will not occur unless the initial kinetic energy of the system is larger than the effective potential imposed by the angular momentum barrier. The height of this barrier, for the various values of l is shown in Figure 6.1.b. This height can be thought of as a threshold below which scattering in the l'th partial wave cannot occur.

Assuming a C_6/r^6 long range interaction, the threshold radius and energy [36] corresponding to the peak in the effective potential are

$$\begin{aligned} b^2 &= \sqrt{\frac{6C_6\mu}{\hbar^2 l(l+1)}} \\ E_{thresh} &= \frac{\hbar^2 l(l+1)}{2\mu b^2} - \frac{C_6}{b^6}, \end{aligned}$$

where μ is the reduced mass of the colliding atoms, b is the radius of the peak in the effective potential and E_{thresh} is the corresponding theshold energy.

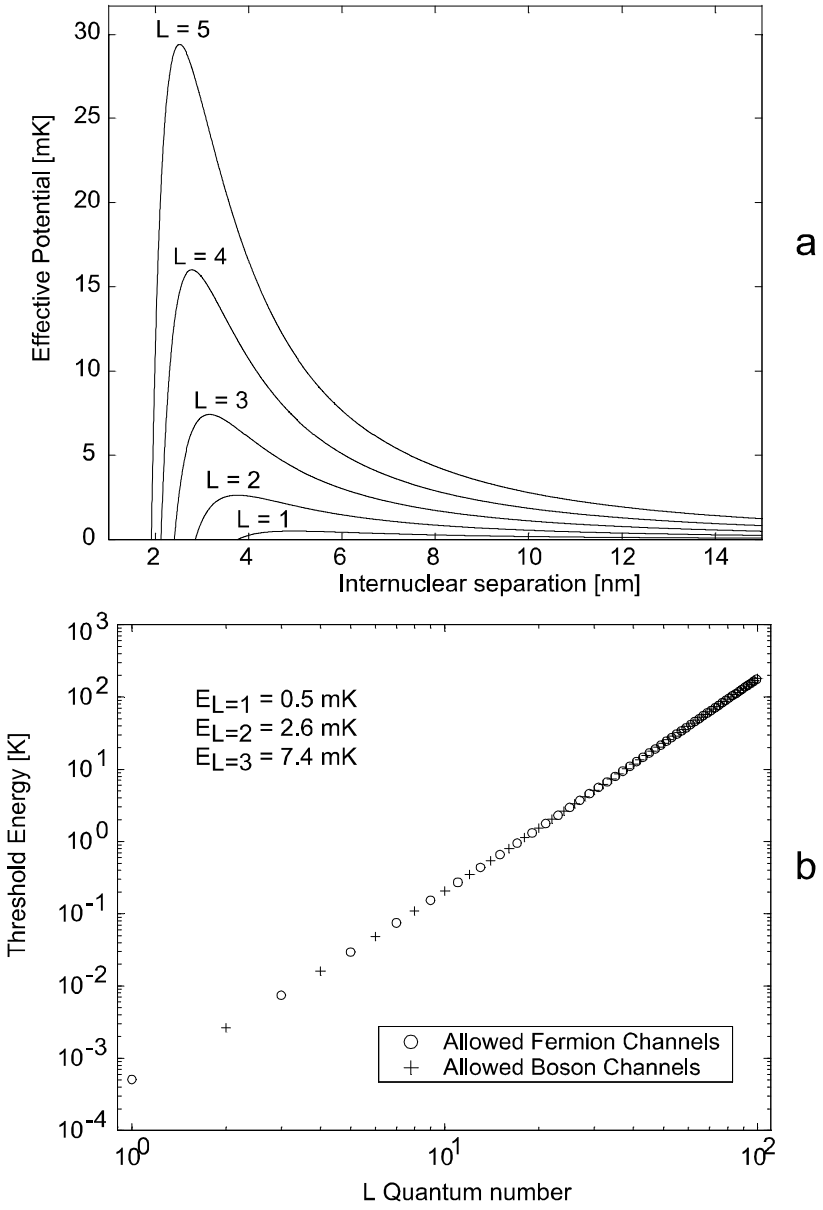

Figure 6.1: **a)** The effective potential between two chromium atoms are plotted for five different values of the angular momentum quantum number. The peak of these effective potential curves corresponds to the threshold energy below which scattering in l'th partial is frozen out. **b)** These threshold energies are plotted as a function of the angular momentum quantum number.

In calculating the values for Figure 6.1, the chromium C_6 coefficient is estimated by using the relationship between atom polarizability and the C_6 coefficient. Assuming the dominant contribution to the polarizability comes from the $a^7S_3 \rightarrow z^7P_{2,3,4}$ transitions in chromium, this relationship is given by

$$C_6 \simeq \frac{3}{4}\alpha^2 h\nu,$$

where $\alpha = 11.6\mathring{A}^3$ is the chromium polarizability [37] h is Plank's constant and ν is the $a^7S_3 \rightarrow z^7P_{2,3,4}$ transition frequency. This gives the estimate,

$$\begin{aligned} C_6 &\simeq 3.8 \times 10^{-77} Joule \cdot meter^6 \\ &= 390\ Hartree \cdot bohr^6. \end{aligned}$$

In the usual partial wave expansion for elastic scattering [38], the total collision cross section is given by

$$\sigma = \frac{4\pi}{k^2} \sum_l (2l+1) \sin^2 \delta_l.$$

Due to the symmetrization requirements for interactions between two-identical bosons (e.g. two ^{52}Cr atoms), only even angular momenta contribute and the cross section is enhanced by a factor of two. In the ultra-cold limit, scattering between identical Bosons is entirely due to the s-wave ($l = 0$) contribution. Since p-wave ($l = 1$) scattering is forbidden by symmetrization, the ultra-cold limit is achieved when the collision energy is less than the d-wave ($l = 2$) energy threshold, which for chromium, is estimated to be $\sim 2.6\ mK$.

6.2 Possible Observation of Shape Resonances

The inelastic scattering rates measured in our experiments show a sharp increase at temperatures just above the ultra-cold regime. Although the mechanism behind this enormous increase is not completely understood, we have a working hypothesis that seems to form a consistent picture of our results.

We think the behavior of the measured inelastic rates could be caused by the presence of a shape resonance. Shape resonances can be understood by examining the two plots in Figure 6.2. In each of these plots, the x-axes represent the interatomic separation. The thicker curve represents an interatomic effective potential with non-zero angular momentum. The peak in this effective potential is due to the interplay between the angular momentum barrier and the long-range interaction potential. Bound states have been sketched in the inner region of this potential. One of these "bound states" has energy greater than zero. This state is called a quasi-bound state.

Resonant scattering can be understood as follows. Imagine two particles colliding with a kinetic energy shown by the thin straight line in Figure 6.2.a. The wave function can tunnel through the angular momentum barrier to create a non-vanishing probability of finding the atoms at small separation. However, due to tunneling, the wavefunction amplitude is exponentially suppressed in the inner region of the potential.

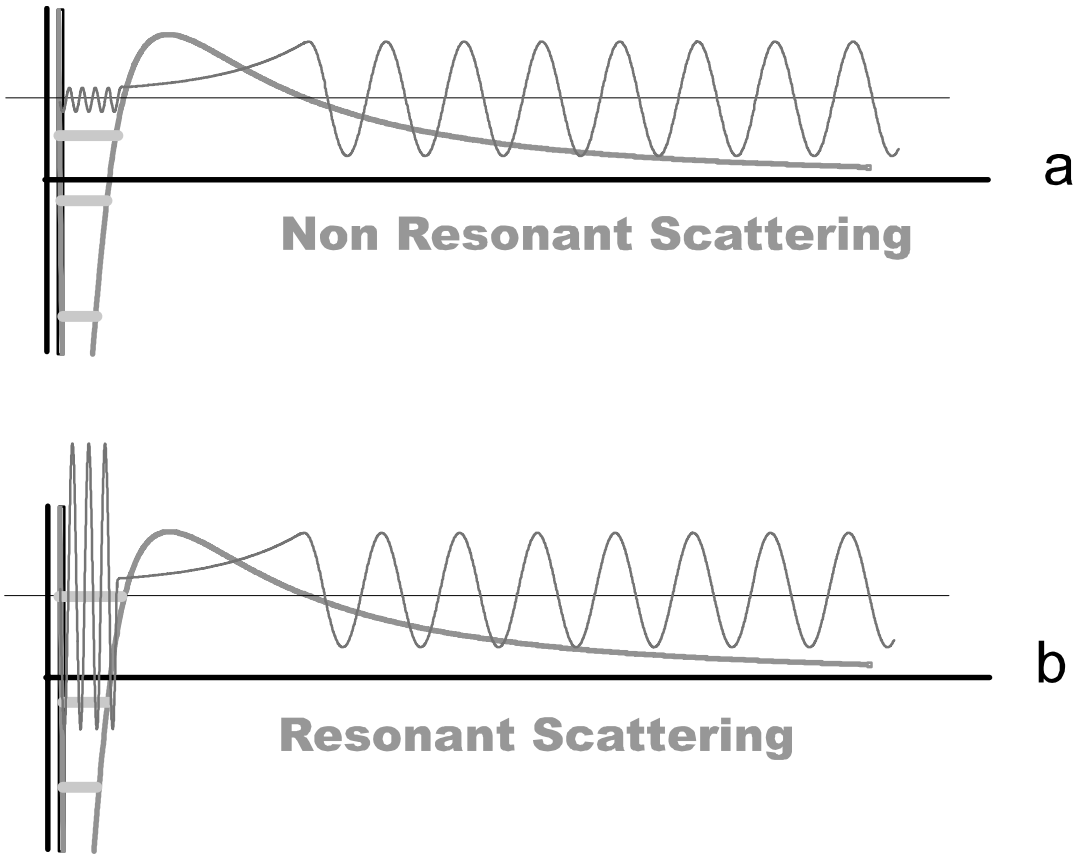

Figure 6.2: **a)** The effective interaction potential (including the "angular momentum barrier") is sketched as a function of the distance between atoms. Bound states are drawn in the resulting energy well. A sketch of a radial wave function for scattering at an arbitary (non-resonant) energy is supperimposed on the potential. **b)** The picture is slightly different when the scattering energy coincides with one of the quasi-bound states in the potential well. The wave function is resonantly enhanced in the region of the energy well. This mechanism for enhancing the wavefunction at small distances is called a shape resonance.

When the kinetic energy of the system coincides with the energy one of the quasi-bound states in the effective potential as shown in Figure 6.2.b, the wavefunction at small separations is resonantly enhanced. This enhancement is analogous to the electric field enhancement inside a resonant optical cavity. In this analogy, the inner region of the potential takes on the role of the cavity, and the wave function corresponds to the electric field.

The enhanced probability of finding the two atoms at small separations may have a significant impact on the inelastic scattering rates. Both of the mechanisms discussed below for inelastic scattering involve interactions whose strength depends on the inter-atomic separation. The dipole-dipole interaction varies as $\sim 1/r^3$, and second order spin-orbit coupling requires an overlap of the atoms' electron clouds. Since the strength of these interactions would be dominated by the portion of the wavefunction found at short range, one can imagine that a resonant enhancement of the short-range wavefunction amplitude would also cause a resonant enhancement of the inelastic scattering processes.

Understanding our observed inelastic rates beyond this hand-waving, qualitative picture requires a full quantum calculation. Although such a calculation is beyond the scope of this thesis, a few words about the possible mechanisms for inelastic scattering are in order.

6.3 Mechanisms of Inelastic Scattering

Throughout this thesis, the term "inelastic scattering" has been continually used. This section defines what we mean when we say "inelastic collision" and discusses the various underlying mechanisms.

Chromium has a $^7S_3$ configuration in its ground state. It has total angular momentum $J = 3$ which is due entirely to the spin of its electrons. There is no orbital angular momentum in the ground state, $l = 0$. The Bosonic isotope of chromium, ^{52}Cr, has no nuclear spin. The resulting absence of nuclear-spin hyperfine interactions greatly simplifies the understanding of its internal structure.

When trapped in a magnetic field, the angular momentum (i.e. the spin) of a chromium atom will be aligned with the magnetic field. In this orientation, the atom-field interaction energy, $U_B = -\boldsymbol{\mu} \cdot \mathbf{B}$, is maximized. Collisions between two chromium atoms can result in one or both of them changing its spin projection to reduce the interaction energy with the field. Any interaction between two chromium atoms that drives a spin flip to a lower energy state in one or both atoms is defined to be an inelastic collision.

The interactions involved in the collision between two chromium atoms are due to the following Hamiltonian

$$V = -\frac{\hbar^2}{2\mu}\frac{\partial^2}{\partial R^2} + V_{es}(R) + 2J(R)\,\mathbf{S}_1 \cdot \mathbf{S}_2 + V_{dip}(R) + V_{so}(R).$$

The first term in this interaction is just the kinetic energy of the colliding atoms in the center of mass frame. The spin-independent part of the electrostatic interaction is represented by the $V_{es}(R)$ term. At large inter-atomic separation this term becomes the Van-der-Waals interaction. The term involving the dot product of the two atom spins is due to the exchange interaction. It is used to model Pauli exclusion effects when the wavefunctions of the atoms begin to overlap [39, 40]. The dipole-dipole magnetic interaction between the two atoms is represented by $V_{dip}(R)$. The $V_{so}(R)$ term represents interactions stemming from the second-order spin-orbit coupling in the diatomic molecule temporarily formed by the colliding atoms

6.3.1 Exchange Interaction

The exchange interaction gives rise to spin exchange collisions. These are collisions in which the orbital angular momentum of the collision trajectory remains constant while the spin projections of the two atoms along the quantization axis is interchanged. This spin exchange property is easily seen by noting that the spherically symmetric $J(R)$ cannot change angular momentum. The dot product $\mathbf{S}_1 \cdot \mathbf{S}_2 = S_{1x}S_{2x} + S_{1y}S_{2y} + S_{1z}S_{2z}$, however, can be expressed in terms of the projection operator, S_z, and the ladder operators $S_+ = S_x + iS_y$ and $S_- = S_x - iS_y$. This gives

$$2J(R)\,\mathbf{S}_1 \cdot \mathbf{S}_2 = J(R)\left[S_{1+}S_{2-} + S_{1-}S_{2+} + 4S_{1z}S_{2z}\right].$$

From this expression it is clear that, for inelastic collisions, the only role played by the exchange interaction is that of exchanging spin projections between atoms. The total angular momentum, and its projection along a quantization axis remain unchanged.

6.3.2 Dipolar Interaction

The magnetic dipole-dipole interaction between two magnetic moments, $\mathbf{s_1}$ and $\mathbf{s_2}$, can be written as

$$H_D = \frac{\mu_0}{4\pi}\frac{\gamma^2}{r^3}\left[\mathbf{S_1}\cdot\mathbf{S_2} - 3\left(\mathbf{S_1}\cdot\mathbf{n}\right)\left(\mathbf{S_2}\cdot\mathbf{n}\right)\right],$$

where γ is the gyromagnetic ratio for each of the spins, r is the separation distance between them, and $\mathbf{n}$ is the unit vector pointing from one spin to the other. As two atoms collide with one another, this interaction will present a time varying Hamiltonian in the quantum mechanical description of the two atoms. The inelastic collisions caused by this time varying Hamiltonian can be broken down into a spin exchange compenent and a "dipolar relaxation" component.

Spin Exchange Term

To understand the spin exchange interaction, imagine a collision between two atoms with spins denoted by $|s_1, m_1\rangle$ and $|s_2, m_2\rangle$ respectively. The atomic spins before the collision are described by the product state $|\alpha\rangle = |s_1, m_1\rangle\,|s_2, m_2\rangle$, and after the collision by $|\alpha'\rangle = |s_1', m_1'\rangle\,|s_2', m_2'\rangle$.

A spin exchange collision is a process that doesn't change the overall combined spin of the two atoms. It simply swaps angular momentum between them. This can be symbolically stated as

$$|s_1, m_1\rangle |s_2, m_2\rangle \rightarrow |s_1, (m_1 + 1)\rangle |s_2, (m_2 - 1)\rangle$$

As in the case of the exchange interaction, the $\mathbf{S_1} \cdot \mathbf{S_2}$ term in the dipole interaction is responsible for the spin-swapping between atoms. Notice that this process cannot occur if both colliding atoms are in thea state with $|m| = s$. This means that spin exchange processes do not occur between atoms that are completely aligned with the magnetic field.

Dipolar Relaxation

The other process caused by the dipole interaction is often called dipolar relaxation. Dipolar relaxation can be understood by expanding on the notation of the previous section to include the projection, , m_l, of the orbital angular momentum of the colliding atoms along the quantization axis. The state of the two atom system before and after the collision can then be written as $|\alpha\rangle = |m_1\rangle |m_2\rangle |m_l\rangle$, and $|\alpha'\rangle = |m_1'\rangle |m_2'\rangle |m_l'\rangle$ respectively. Dipolar relaxation is a collisional process that exchanges angular momentum between the individual atom spins and the orbital angular momentum the atoms have in their center of mass frame. There are three possibilities for this, which are schematically described by

$$|m_1\rangle |m_2\rangle |m_l\rangle \rightarrow \left\{ \begin{array}{c} |m_1 \pm 1\rangle |m_2 \pm 1\rangle |m_l \mp 2\rangle \\ |m_1\rangle |m_2 \pm 1\rangle |m_l \mp 1\rangle \\ |m_1 \pm 1\rangle |m_2\rangle |m_l \mp 1\rangle \end{array} \right\}.$$

Notice that in dipolar relaxation, each atom has its spin projection changed by one. Conservation of angular momentum is maintained by putting the extra angular momentum into the relative motion of the atoms.

Dipole-Dipole Selection Rules

The dipole-dipole interaction is explained quite nicely on page 1120 of Cohen Tanoudi's book on quantum mechanics [41]. This treatment is reproduced here to demonstrate how the various inelastic loss processes can be derived from the dipole-dipole interaction Hamiltonian, and to determine the so-called selection rules for spin changing collisions mediated by this interaction.

Consider the interaction of two spins denoted by $\mathbf{s_1}$ and $\mathbf{s_2}$. Let the gyromagnetic ratio for either spin be denoted by γ. If the two spins are separated by a distance r, and the unit vector pointing from one spin to the other is $\mathbf{n}$, the magnetic dipole-dipole interaction between the two spins can be written as

$$H_D = \frac{\mu_0}{4\pi}\frac{\gamma^2}{r^3}\left[\mathbf{s_1}\cdot\mathbf{s_2} - 3\left(\mathbf{s_1}\cdot\mathbf{n}\right)\left(\mathbf{s_2}\cdot\mathbf{n}\right)\right].$$

This Hamiltonian can be expressed in terms of quantum mechanical operators by making the definitions

$$\begin{aligned}
T_0 &= A_0 Y_2^0 S_{1z} S_{2z} \\
T_0' &= A_0' Y_2^0 \left(S_{1+}S_{2-} + S_{1-}S_{2+}\right) \\
T_{\pm 1} &= \mp A_1 Y_2^{\mp 1}\left(S_{1z}S_{2\pm} + S_{1\pm}S_{2z}\right) \\
T_{\pm 2} &= A_2 Y_2^{\mp 2} S_{1\pm} S_{2\pm},
\end{aligned}$$

where $A_0 = 4\sqrt{\frac{\pi}{5}}$, $A_0' = \sqrt{\frac{\pi}{5}}$, and $A_1 = A_2 = 3\sqrt{\frac{2\pi}{15}}$, are normalization constants , Y_l^m are the spherical harmonic functions, S_{1z}, $S_{1\pm}$ are the projection and ladder operators for the spin of atom 1 and S_{2z}, $S_{2\pm}$ are the projection and ladder operators for the spin of atom 2. In terms of these operators, the Hamiltonian can be written as

$$H_D = U(r)\left[(T_0)_{non-spin-flipping} + (T_0')_{spin\,exchange} + (T_1 + T_{-1} + T_2 + T_{-2})_{dipolar\,relaxation}\right],$$

where the different terms have been labeled to indicate the physical process they are responsible for. The T_0 term does not flip any spins. The T_0' term is responsible for spin exchange processes. The $T_{\pm 1}$ and the $T_{\pm 2}$ terms are responsible dipolar relaxation.

Before scattering, let the two atom wavefunction be represented by

$$|\alpha\rangle = |n, l, m_l\rangle\,|m_1, m_2\rangle$$

where m_1 and m_2 are the spin projections of the individual atoms and $|n, l, m_l\rangle = R(n, l, r)Y_l^m(\theta, \phi)$ is the orbital wave function of the two atom system. If the scattered wavefunction is denoted by $|\alpha'\rangle$, the scattering calculation will require solutions with the matrix elements

$$\begin{aligned} S_{\alpha',\alpha} &= \langle\alpha'|\,T_0\,|\alpha\rangle + \langle\alpha'|\,T_0'\,|\alpha\rangle \\ &\quad + \langle\alpha'|\,T_{+1}\,|\alpha\rangle + \langle\alpha'|\,T_{-1}\,|\alpha\rangle \\ &\quad + \langle\alpha'|\,T_{+2}\,|\alpha\rangle + \langle\alpha'|\,T_{-2}\,|\alpha\rangle\,. \end{aligned}$$

Each term in this matrix element will involve the integral of a triple product of spherical harmonics

$$\int Y_{l'}^{m'*} Y_2^q Y_l^m d\Omega.$$

This triple product integral is exactly what we would obtain if we were adding an angular momentum of $l = 2$, $m_l = q$ to the initial orbital angular momentum of the two-particle system. As a matter of fact, the so called "triangle rule" of angular momentum addition is derived from precisely such an integral. This "triangle rule" constrains the post-scattering angular momentum to $l' = |l-2|, |l-1|, ... |l+2|$.

A further constraint is imposed by the fact that the integrand must possess even parity if the integral is not to vanish. Since spherical harmonics have even parity for $l = even$, and odd parity for $l = odd$, the integrand will be even if $l - l' = even$. This additional constraint leaves us with the orbital angular momentum selection rule for spin changing collision mediated by the dipole-dipole interaction,

$$\begin{array}{cc} \Delta l = 0, \pm 2 & \text{for } l \text{ and } l' > 0 \\ \Delta l = +2 & \text{for } l \text{ or } l' = 0 \end{array}$$

The integral of triple spherical harmonics also imposes conservation of the z component of the total system angular momentum. In any collision, it must be true that

$$m_1' + m_2' + m_l' = m_1 + m_2 + m_l.$$

6.3.3 Second-Order Spin-Orbit Coupling

Second order spin-orbit coupling is properly understood in terms of molecular theory. It is called second order because in the molecular theory, it makes its appearance

only in second order perturbation theory. Although it is expected to be a small effect for chromium, current theoretical work is being carried out to confirm this. A description of second-order spin-orbit coupling is beyond the scope of this discussion. As such, we will not discuss it further, but merely mention its existence for completeness.

6.4 Current State of Theory

The theoretical description of chromium scattering is an area of active research. Although steady progress is being made, a full theoretical description does not yet exist. Preliminary calculations produce a seeming disparity with our measured results for both the elastic and inelastic scattering rates. The source of this disagreement is being vigorously investigated. The sensitivity of the calculated scattering rates on the scattering potentials, combined with uncertainty of the ab-initio methods used to generate them, makes the scattering potentials a likely suspect for causing the discrepancy between calculated and measured values of the inelastic scattering rates.

6.5 Unanswered Questions

The behavior of our measured inelastic scattering rates is poorly understood. The unexpected results of our measurements give rise to several unanswered questions worthy of consideration.

The broadest question is, what causes the sharp increase in the inelastic scattering rate as the temperature approaches the ultracold limit? What are the physical mechanisms behind this increase?

Are the inelastic rates caused by dipolar interactions, second-order spin-orbit coupling, or some other process we don't fully understand? Is it possible we are observing a scattering resonance? In the present incarnation of our experiment we are unable to distinguish between temperature effects and magnetic field effects. If we are seeing a resonance, is it more sensitive to the temperature of the atoms, or to the average magnetic field they sample?

The peak in the measured scattering rate occurs at energies not far from the estimated threshold for d-wave scattering which marks the onset of the ultra-cold limit. What is the possible significance of this?

How general are these observations? Is this sharp increase in the inelastic rate a general phenomenon of scattering in this energy regime? Or is it an effect likely to be observed only for atoms with large magnetic moments like chromium? Or could it be due to some effect that is unique to the chromium system?

It will be up to further experiment and theory to sort out the full features of this system.

Chapter 7
Laser Cooling

Our measurements on magnetically trapped chromium show a dramatic increase in the inelastic collision rate as the temperature is reduced. There is reason to believe that this inelastic rate could decrease with a further reduction in temperature. At the end of our initial experiments on creating cold chromium, evaporation did not look promising as a tool for cooling chromium through this regime of unusually large inelastic scattering rates. The enormity of the inelastic rate causes very poor efficiency in the evaporative cooling process. In hopes of pushing through this region of "bad" inelastic scattering rates, we embarked on a program to implement laser cooling in our spherical quadrupole magnetic trap.

7.1 Overview of the Model

Lasers are rarely used to provide cooling for magnetically trapped atoms. The large Zeeman broadening produced by the trapping fields makes it difficult to address a significant fraction of the atoms. Additionally, at temperatures typically found in magnetic traps, the Doppler broadening is small compared to the natural line width of the cooling transition. The combination of these two factors limit the cooling power attainable with a laser of a given intensity.

There is a strong, non-trivial interdependence between the various parameters that are relevant for laser cooling. These include laser beam parameters (diameter, intensity, spacial offset), magnetic trap depth, atom density, initial atom temperature and density (before laser cooling), final atom temperature and density (after laser cooling), the optical transition strength, and Zeeman broadening. In our chromium experiment, this parameter space is constrained by the conditions that are experimentally realizable in our trap. The transition strength and Zeeman broadening are set by the properties of chromium. For a given trap depth, the atom density and initial atom temperature are uniquely determined by the "equilibrium η" imposed by the ratio of elastic to inelastic scattering rates. The relationship between the other parameters (trap depth, beam parameters, and final temperature and density) is non-trivial to model and numerical methods must be employed.

To do this, a simulation can be performed that accounts for all the possible heating and cooling and atom loss mechanisms in the trap. By adding the thermal effects, and additional losses caused by the laser, to the collisional heating/cooling processes, the number of atoms and their temperature can be traced out as a function of time.

7.2 Laser Induced Heating and Cooling

7.2.1 Zero-field Doppler Heating/Cooling

In order to understand Doppler cooling in our trap, it is instructive to first consider the case of Doppler cooling in the absence of a trapping field. In this case, the transition used for Doppler cooling will not be subjected to the spatially dependant Zeeman shifts associated with the trapping fields. The thermal effects of the laser are then more easily understood.

The atom's kinetic energy before absorbing a photon can be written as $E = \frac{p^2}{2m}$. For a small change in momentum, the change in kinetic energy is simply $dE = \frac{\mathbf{p}}{m} \cdot d\mathbf{p}$. If the change in momentum is due to the absorption of a photon, one can replace $d\mathbf{p}$ with the momentum of the photon, $\hbar\mathbf{k}$, to get

$$dE = \hbar\mathbf{k} \cdot \frac{\mathbf{p}}{m} = \hbar\mathbf{k} \cdot \mathbf{v} \tag{7.1}$$

The validity of assuming the photon kick is small compared to the momentum of the atom can be confirmed as follows. For temperatures as low as 70 μK, the momentum of the average Cr atom is still ten times larger than that of a photon resonant with the $a^7S_3 \rightarrow z^7P_4$ transition of ^{52}Cr at $427\ nm$. The average momentum does not become equal to that of a resonant photon until a temperature of $670\ nK$.

Due to the Doppler shift, the red detuned photons of the cooling laser are preferentially absorbed by atoms counterpropagating to the laser beam. The photons reemitted by these atoms will be randomly directed. The probability a photon is emitted in an arbitrary direction is identical to the probability that it is emitted in the opposite direction. This causes the expectation value for the emitted photon fre-

quency in the lab frame to be that of the Doppler free transition regardless of atom velocity (neglecting relativistic effects).

Since the cooling laser photons are red detuned from the Doppler-free transition frequency, each of their energies will be less than that of the average photon reemitted by an atom. This detuning presents a discrepancy between the energy of an absorbed photon and the average energy of an emitted photon. This discrepancy is accounted for by a change in the atom's kinetic energy. It follows that the average photon-atom energy transfer is simply Plank's constant multiplied by the detuning from resonance. This argument can be formalized by substituting the expression for the Doppler shift, $\Delta\omega = -\mathbf{k} \cdot \mathbf{v}$, into Eq. 7.1 which leads directly to

$$dE = h\Delta\nu,$$

where dE is the change in kinetic energy for the atom, and $\Delta\nu$ is the detuning of the laser from resonance.

It is useful to compare this change in energy to the energy carried by a photon, $E_{photon} = h\nu$. The ratio $\frac{dE}{E_{photon}} = \frac{\Delta\nu}{\nu}$ can be thought of as the fraction of the photon's energy that goes into heating/cooling the the atom. This can be generalized to the case of a laser passing through a cloud of atoms by taking the fraction of photons that get scattered by the laser (a.k.a. the optical absorption of the atoms) and multiplying that by the fractional change in energy between scattered and incident photons. This gives

$$\frac{P_{therm}}{P_{laser}} = A(\nu) \cdot \frac{\Delta\nu}{\nu} \tag{7.2}$$

where P_{laser} is the power in the laser beam, P_{therm} is the heating/cooling power it provides, and $A(\nu)$ is the absorption experienced as the beam passes through a thermal cloud of atoms having a Doppler broadened transition.

7.2.1 Doppler Heating/Cooling in Trapping Fields

Zeeman Broadening

In a magnetic trap, the Zeeman shift imposed by the trapping fields complicates the Doppler cooling process. The effect of this field can be readily understood by first considering the case in which Doppler effects are neglected. Imagine being able to take a snapshot of the magnetically trapped ensemble. Each atom is natural-linewidth broadened and sitting in a slightly different magnetic field from virtually all other atoms. The Zeeman shift causes the resonant frequency of a single atom's optical transition to be slightly different from that its neighbors. This one-to-one correspondence between an atom's resonant frequency and the strength of the magnetic field engulfing it, can be used to determine its location in the trap. A laser beam of a given frequency passing through an ensemble of magnetically trapped atoms will be resonant only with those atoms residing at a particular magnetic field. The optical density that these atoms present to the laser beam is directly proportional to their number density. By sweeping the laser frequency and monitoring the resulting absorption, the optical density can be measured as a function of magnetic field, thereby providing a determination of the atom density distribution in the trap.

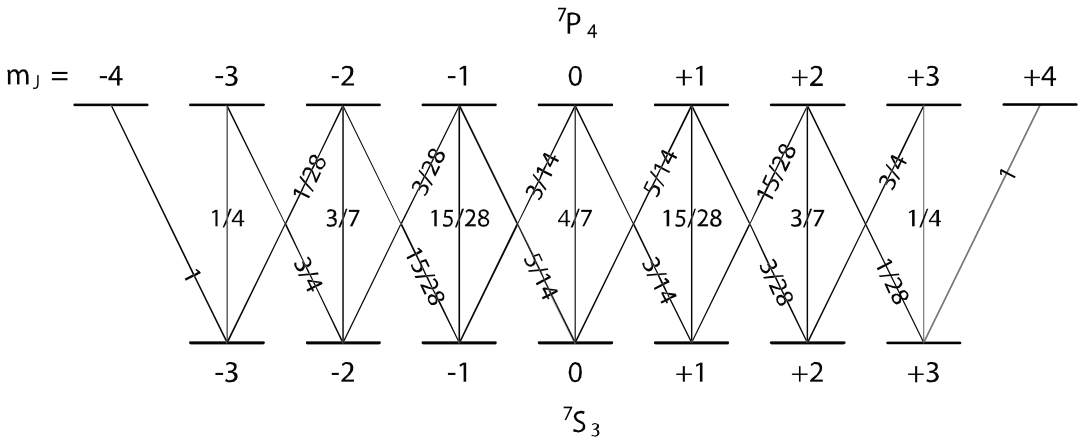

Figure 7.1: Clebsch Gordon coefficients for the $^7S_3 \rightarrow ^7 P_4$ transition of chromium.

Doppler Cooling Spectrum for Chromium

Laser cooling of chromium is most efficiently performed by cycling on the virtually closed $|a^7S_3, m_j = 3\rangle \rightarrow |z^7P_4, m_j = 4\rangle$ transition. Figure 7.1 shows the three allowed dipole transitions for atoms excited from the $|a^7S_3, m_j = 3\rangle$ ground state of chromium. They are the $\Delta m = +1$ transition for $|a^7S_3, m_j = 3\rangle \rightarrow |z^7P_4, m_j = 4\rangle$, the $\Delta m = 0$ transition for $|a^7S_3, m_j = 3\rangle \rightarrow |z^7P_4, m_j = 3\rangle$ and the $\Delta m = -1$ transition for $|a^7S_3, m_j = 3\rangle \rightarrow |z^7P_4, m_j = 2\rangle$. Each of the excited m_j states has a different magnetic moment causing each of the associated transitions to experience differing shifts in the presence of a magnetic field. These differing Zeeman shifts allow frequency discrimination between the possible transitions from the $|a^7S_3, m_j = 3\rangle$ ground state. Figure 7.2.a shows a calculated spectrum for a thermal distribution of atoms confined in a magnetic trap. The large, broad peak on the right is due to absorption on the $\Delta m = +1$ transition. The smaller, more narrow peak on the

left is due to $\Delta m = 0$ transitions. Not visible on this spectrum, but also present is the absorption from the $\Delta m = -1$ transition. The shown calculation is for a peak ^{52}Cr number density of $2 \times 10^{10}\ cm^{-3}$ in thermal equilibrium at a temperature of $30\ mK$ while confined in $180\ mK$ deep trap. The solid trace is calculated neglecting Doppler broadening. The details of this calculation have been expounded elsewhere [13] and are beyond the scope of this discussion. The dashed trace, however, shows the changes introduced to the spectrum by taking Doppler broadening into account. The Doppler broadening can be calculated by a simple convolution of the Doppler-free spectrum with the unit-normalized Doppler profile [42],

$$D\left(\nu, \nu'\right) = \frac{1}{\sqrt{2\pi v^2}} \sqrt{\frac{mc^2}{k_B T}} \exp\left[-\frac{mc^2}{2k_B T}\left(\frac{\nu' - \nu}{\nu}\right)^2\right],$$

where ν is the Doppler-free resonant frequency, m is the mass of the atom, k_B is Boltzmann's constant, T is the temperature, and ν' is the probe frequency. The full-width-half-max of this Doppler profile is

$$\Delta\nu = \frac{2\nu_0}{c}\sqrt{\frac{2k_B T \ln\left(2\right)}{m}}.$$

A rough estimate of the cooling power obtainable from a laser passing through a trapped atom ensemble can be obtained from graphs such as Figure 7.2.a by using the difference in absorption between the Doppler-free and Doppler-broadened spectra as the relevant absorption factor in Eq. 7.2. A more rigorous approach, however is to determine the thermal to optical power ratio by convolving the field-free power ratio

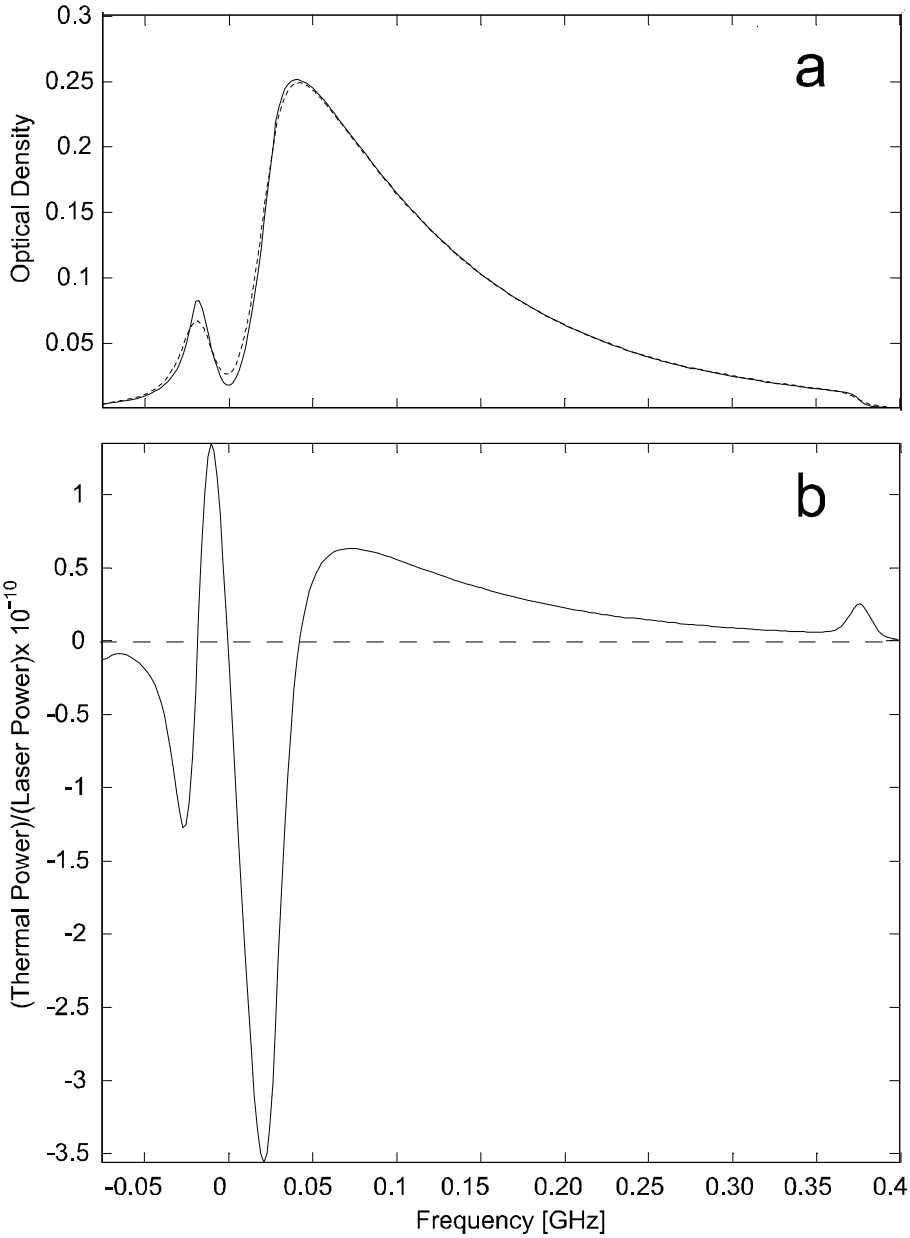

Figure 7.2: **a)** Simulation results for spectrum of trapped atoms. The solid line neglects Doppler broadening. The dotted line is Doppler broadend. The larger feature on the right is due to $\Delta m = +1$ transitions. The smaller feature on the left is due to $\Delta m = 0$ transitions. **b)** The fraction of laser power that gets converted to thermal power is plotted as a function of frequency.

with the effects of Doppler broadening,

$$\frac{P_{therm}(v)}{P_{laser}} = \int \left[A_{doppler\_free}(\nu) \cdot D(v, v') \cdot \frac{(v - v')}{\nu} \right] dv', \tag{7.3}$$

where $D(v, v')$ is the Doppler profile, and $A_{doppler\_free}(\nu)$ is the Doppler free absorption spectrum of the atoms. This convolution can be understood by considering the Doppler free absorption at a given laser frequency which is given by $A_{doppler\_free}(\nu)$. This absorption is caused by atoms passing through a small equal-field volume in the trap at which the Zeeman shift brings the atoms into resonance at the frequency ν. Doppler broadening, however, will cause the absorption of some of the atoms at neighboring field strengths resonant at a frequency ν' to spill-over into the absorption measured in the ν-resonant region. The amount of spill-over that occurs from ν' into ν is given by the Doppler profile $D(v, v')$. Since this spill-over is due to the Doppler shift, Eq. 7.2 states that the resulting thermal power is given by the detuning/frequency ratio, $\frac{(v-v')}{\nu}$. Summing these thermal power contributions over all possible frequencies ν' leads to the convolution of Eq. 7.3.

Figure 7.2.b shows the fraction of the laser power that gets converted to useful thermal power acting on a trapped ensemble having the same parameters as the spectra of Figure 7.2.a. The shape of this curve in relation to the spectrum can be understood by noting that red detuning leads to Doppler cooling whereas blue detuning leads to Doppler heating. Tuning to frequencies where the spectrum exhibits a positive slope results in the laser being red detuned from most of the atoms it interacts with, thereby providing a net cooling effect. Conversely, frequencies where the

spectrum has a negative slope result in net heating. For the chromium parameters used in the simulation of Figure 7.2, the maximum cooling power obtainable is on the order of 10^{10} times smaller than the optical power of the laser. For laser powers well below the saturation intensity, this fraction scales linearly with both the power of the laser and the absorption of the atoms.

7.2.2 Maximum Cooling Power Fraction for Chromium

This method for calculating laser cooling power will now be used to model laser cooling for experimentally realizable conditions in our magnetic trap. For the remainder of this discussion, consider the conditions obtained by ramping the magnetic trap depth down to $180\ mK$. The density, number, and temperature we observe in ramping to this trap depth are $n_0 = 3 \times 10^{10} cm^3/s$, $N = 8.8 \times 10^{10}$, and $T = 28\ mK$ respectively. A $1.5\ mm$ diameter laser beam centered $2.5\ mm$ away from the center of the trap and having power ranging from 4 to $250\ \mu W$ is selected for laser cooling. For these beam parameters the power corresponding to the resonant saturation intensity is $600\ \mu W$.

The maximum fraction of the laser power that can get converted to cooling power will be a function of both the temperature and the peak density in the trap as calculated from Eq. 7.3. The points in Figure 7.3 show this maximum power fraction as a function of density and temperature. These points can be fit to the

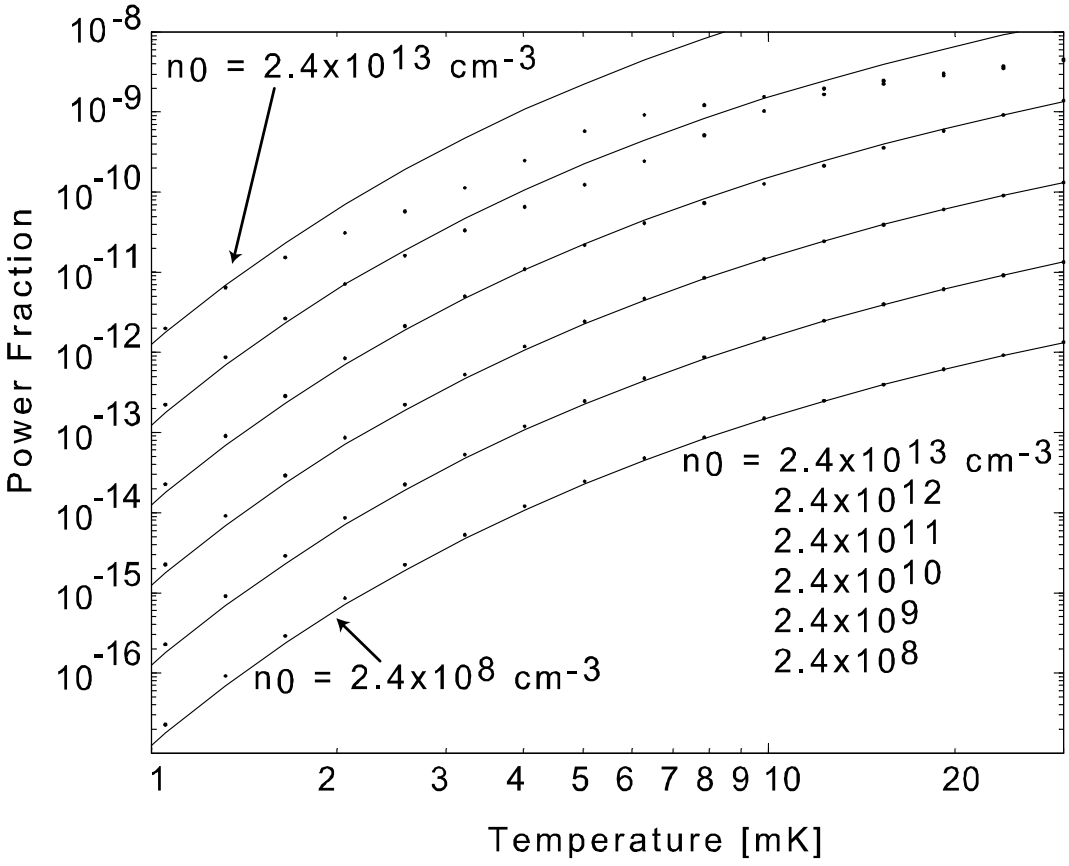

Figure 7.3: For the **particular parameters** selected in this simulation, the points show the maximum fraction of the laser power that can be converted to cooling power as a function of atom density and temperature. An ad-hoc approximation to the functional form of this dependance, Eq. 7.4, is plotted with solid lines.

functional form

$$P_{frac} = 9.1 \times 10^{-21} \left(\frac{n_0}{cm^{-3}}\right) \left(\frac{T}{mK}\right)^{1/2} \exp\left[\frac{-12.1}{\left(\frac{T}{mK}\right)^{1/2}}\right] \tag{7.4}$$

as shown by the solid traces. Eq. 7.4 can be used to calculate the maximum cooling power obtainable for the selected beam parameters ONLY.

7.3 Loss Mechanisms

Trap loss mechanisms fall into two broad categories: optical loss processes, and collisional loss processes. Each of these will now be discussed.

7.3.1 Optical Pumping to Other Zeeman Sublevels

During laser cooling, the laser is tuned to the frequency that provides the maximum conversion of laser power to cooling power. (See Fig. 7.2.) At this frequency, the optical density is dominated by $\Delta m = +1$ transitions. However, the $\Delta m = 0$, and $\Delta m = -1$ also make small contributions. These contributions are suppressed by a factor of roughly $\left(\frac{\Delta\nu}{\Gamma}\right)^2$ ($\sim 10^{-2}$ for this simulation), where $\Delta\nu$ is the detuning of the maximum cooling frequency from the maximum of the $\Delta m = 0$ peak, and Γ is the natural linewidth of the transition.

As shown earlier in Figure 7.1, $\Delta m = 0$ and $\Delta m = -1$ optical transitions from the $|a^7S_3, m_j = 3\rangle$ ground state of chromium have significant probability of transferring atoms to the $|a^7S_3, m_j = 2\rangle$ and $|a^7S_3, m_j = 1\rangle$ states. Not only are these states less tightly confined, resulting in higher evaporation rates, but they are

also more susceptible to the large inelastic scattering rates caused by spin-exchange collisions.

It is possible that the increased trap loss due to $\Delta m \neq +1$ transitions can be reduced if the atoms undergoing these transitions scatter more than one photon before leaving the trap. The $\left(\frac{\Delta\nu}{\Gamma}\right)^2$ suppression of the $\Delta m \neq +1$ transitions could result in optically pumping any $|a^7S_3, m_j \neq 3\rangle$ atoms back to the fully polarized $|a^7S_3, m_j = 3\rangle$ state thereby reducing the loss. However, in the remainder of the analysis, we will consider the worst case scenario in which all atoms experiencing a $\Delta m \neq +1$ transition are ejected from the trap.

The points in Figure 7.4 show the calculated optical density of $\Delta m \neq +1$ transitions as a function of density and temperature for the specific experimental beam parameters used for this analysis. The solid lines show a fit of these points to the functional form

$$OD_{pump} = 2.951 \times 10^{-14} \left(\frac{n_0}{cm^{-3}}\right) \exp\left[\frac{-11.43}{\left(\frac{T}{mK}\right)^{0.7861}}\right]. \tag{7.5}$$

Eq. 7.5 can be used to calculate the optical density of $\Delta m \neq +1$ transitions for the selected beam parameters ONLY. By turning on and off the loss due to optical pumping to $|a^7S_3, m_j \neq 3\rangle$ states in the simulation described below, it is determined that this process plays only a small role in changing the overall efficiency of the laser cooling process.

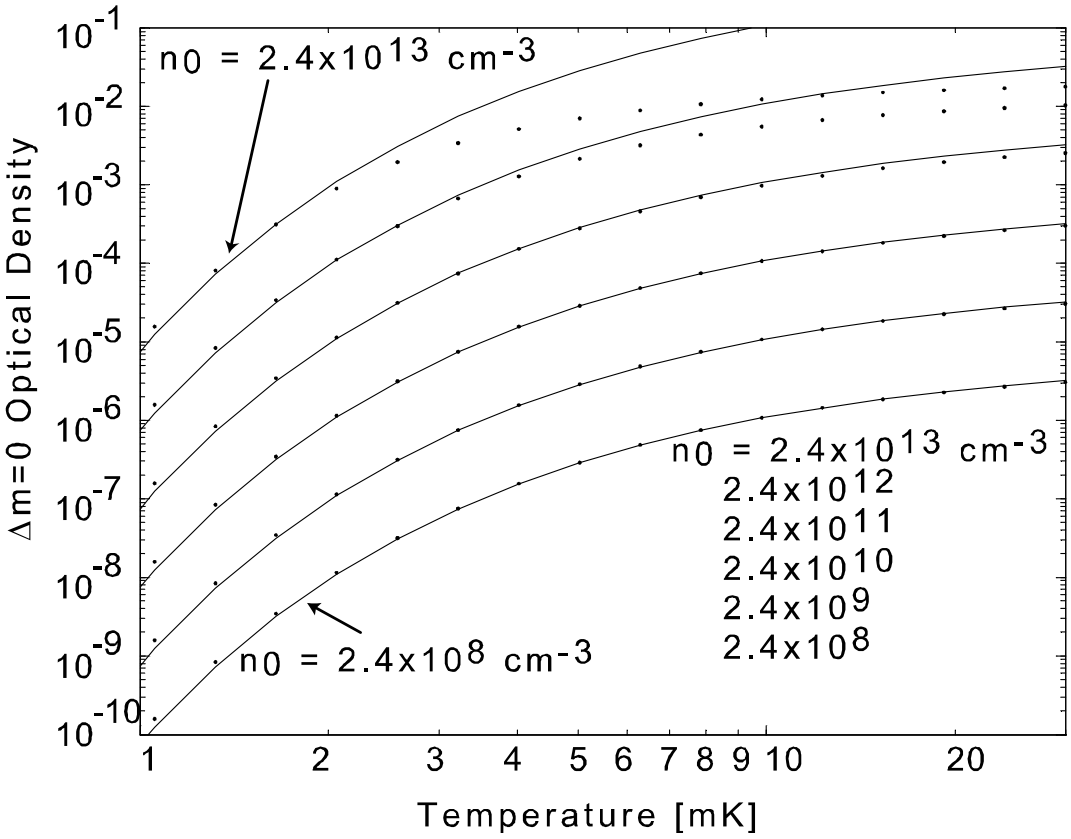

Figure 7.4: For the **particular parameters** selected in this simulation, the points show the optical density contribution from the $\Delta m = 0$ transition. An ad-hoc approximation to the functional form of this dependance, Eq. 7.5, is plotted with solid lines.

7.3.2 Optical Pumping to Metastable States

Photon scattering can also cause atoms loss when atoms in the z^7P_4 excited state decay to one of two metastable states, either the $^5D_3$, or the $^5D_4$ state. For a laser that fully saturates the $|a^7S_3, m_j = 3\rangle \rightarrow |z^7P_4, m_j = 4\rangle$ transition, the decay rate to these metastable states [43] is measured to be $\sim 10^3\ s^{-1}$. This corresponds to roughly one out of every 10^4 transitions decaying to a metastable state. We again take the worst case scenario and assume that atoms in either of these metastable states undergo processes that eject them from the trap (e.g. increased inelastic scattering stemming from the non-zero orbital angular momentum of these states). Comparing this to the fraction of transitions that drive an atom to a $|a^7S_3, m_j \neq 3\rangle$ Zeeman sub-level in the ground state, (roughly one out of every 10^2), we conclude that the loss rate stemming from decay to metastable states can safely be neglected.

7.3.3 Excited State Collisions

Yet another mechanism whereby photon scattering can increase the atom loss rate from the trap is a collision event between an atom in the optically excited state and a ground state atom. In a magneto-optic trap with laser intensity causing an excited state population fraction of 0.1, this rate is measured [43] to be around 3×10^{-9} cm^3s^{-1}. In the low intensity limit, this rate scales linearly with laser intensity to give

$$g_{optical} \simeq \left(3 \times 10^{-8} cm^3 s^{-1}\right) \left(\frac{I}{I_{sat}}\right). \tag{7.6}$$

Even for very low laser intensities, this is a very large scattering rate. Fortunately, the impact it has on atom loss rate is suppressed by the ratio of the "on resonance volume" to the volume of the trapped cloud of atoms. An estimate of the "on resonance volume" can be obtained by multiplying the cross sectional area of the laser beam by the length over which the magnetic field gradient causes a Zeeman shift of approximately one natural linewidth. For our trap this corresponds to

$$V_{resonant} = A_{laser} \frac{4.9\ cm}{\left(\frac{Trap\ Depth}{mK}\right)}. \tag{7.7}$$

For the trap depth and beam diameter used in this analyses this gives a trap volume of $4 \times 10^{-3} cm^3$. Even at the lowest temperatures considered in this simulation, this volume is substantially smaller then the trapped cloud volume. By turning on and off the role of excited state collisions in the simulation described below, it is determined that they play only a small role in changing the overall efficiency of the laser cooling process.

7.3.4 Ground State Collisions

The role of elastic and inelastic collisions between ground state atoms in setting a steady state temperature for a trapped ensemble confined at constant trap depths is discussed at length in Chapter 5. Those considerations can be extended to include the role of a cooling laser. Qualitatively, the effect of laser cooling is to drive the temperature of the atoms lower than the steady state value obtained in its absence. This causes two things to happen. First, as the temperature of the atoms is lowered,

evaporative loss is exponentially suppressed. Secondly, the lower temperatures result in higher number densities leading to a sharp increase in the losses due to inelastic collisions. A quantitative understanding of the resulting interplay between temperature and peak density is non trivial to model analytically. However, a numerical simulation is quite straightforward.

7.4 Time Evolution

A numerical simulation of the temperature, and number of atoms remaining in a magnetic trap as a function of time can be performed by making a key assumption about the behavior of the scattering rates. As seen in Figure 4.1, we have no measurements of Cr-Cr elastic scattering rate at temperatures lower than $\sim 20\ mK$. However, the measurement of the inelastic rate combined with the steady state ratio of trap depth to temperature can be used to estimate the elastic scattering rate. For temperatures below $20\ mK$, this measured "equilibrium η" gives elastic to inelastic scattering ratios of order unity. This fact motivates an approximation of the elastic scattering rate constructed by smoothly joining its measured values at high temperatures with the values of the inelastic rate as the temperature is decreased.

7.4.1 Equations of motion

The number and temperature dynamics for atoms confined in a spherical quadrupole trap with $\eta \equiv E_{trap\,depth}/k_B T \gtrsim 4$ are described by a coupled set of differential

equations. [32, 14]. Let there be N atoms confined in a spherical quadrupole magnetic trap with the trapped cloud having an effective volume of $V_{eff} = 6V_0/\eta^3$ (V_0 is the volume of the trap itself). Elastic collisions occur with a rate coefficient of g_{el} to create a thermal distribution with average energy of $\bar{E} = (9/2)\, k_B T$. Inelastic collisions, occurring with a rate coefficient of g_{in}, combine with evaporation over the edge of the trap and the losses caused by the laser itself (denoted by $\dot{N}_{opt}$) and cause the total atom loss rate to be $\dot{N} = \dot{N}_v + \dot{N}_d + \dot{N}_{opt}$, where $\dot{N}_v = -\frac{1}{8} g_{el} f \frac{N^2}{V_{eff}}$ is the evaporative loss rate, $\dot{N}_d = -\frac{1}{8} g_{in} \frac{N^2}{V_{eff}}$ is the inelastic loss rate, and f is the fraction of elastic collisions that result in an atom evaporating out of the trap. The average energies of atoms lost due to evaporation and inelastic collisions are $\bar{E}_v = (\eta + \kappa)\, k_B T$ and $\bar{E}_d = 3 k_B T$ respectively (κ is an η-dependant constant with a value around one). Let the heating/cooling power provided by the laser be denoted by P_{opt}. Assuming that $\dot{N}_{opt}$ is small enough to have negligible impact on the energy loss rate, the energy loss rate from the trap is given by

$$\dot{E} = \dot{N}_v \bar{E}_v + \dot{N}_d \bar{E}_d + P_{opt}. \tag{7.8}$$

This energy loss rate must equal the time derivative of the total energy in the trap, $E = N\bar{E}$, which can be written as $\dot{E} = \dot{\overline{E}} N + \dot{N}\bar{E}$. Explicitly noting the temperature dependence of the average energy, this can be rewritten as

$$\dot{E} = \frac{\partial \bar{E}}{\partial T} \dot{T} N + \dot{N} \bar{E} + P_{opt}. \tag{7.9}$$

Equating Eq. 7.8 and Eq. 7.9 yields a coupled set of differential equations governing the number/temperature dynamics of trapped atoms:

$$\dot{T} = \frac{1}{N\frac{\partial \bar{E}}{\partial T}}\left[\left(\bar{E}_v - \bar{E}\right)\dot{N}_v + \left(\bar{E}_d - \bar{E}\right)\dot{N}_d + P_{opt}\right] \tag{7.10}$$

$$\dot{N} = \dot{N}_v + \dot{N}_d + \dot{N}_{opt}. \tag{7.11}$$

Using the expressions derived above for the cooling power of the laser, P_{opt}, as well as the additional losses it imposes, $\dot{N}_{opt}$, this system of differential equations can be integrated to track the behavior of the trapped atom cloud as a function of time.

7.4.2 Time profiles of cooling

Figure 7.5 summarizes the temporal behavior of a trapped atom cloud exposed to a cooling beam for several different laser powers. An intuitive understanding of these results is as follows. The cooling laser is turned on at 0 seconds. As time progresses, the temperature of the atoms decreases. This causes a reduction in the effective volume of the trapped cloud thereby increasing the number density which is reflected by an increase in the phase space density. Since the loss rate due to collisional processes increases as the square of the number density, the increase in number density results in the sharp increase in the inelastic loss rate. The time scale for this behavior depends on the optical power of the cooling laser.

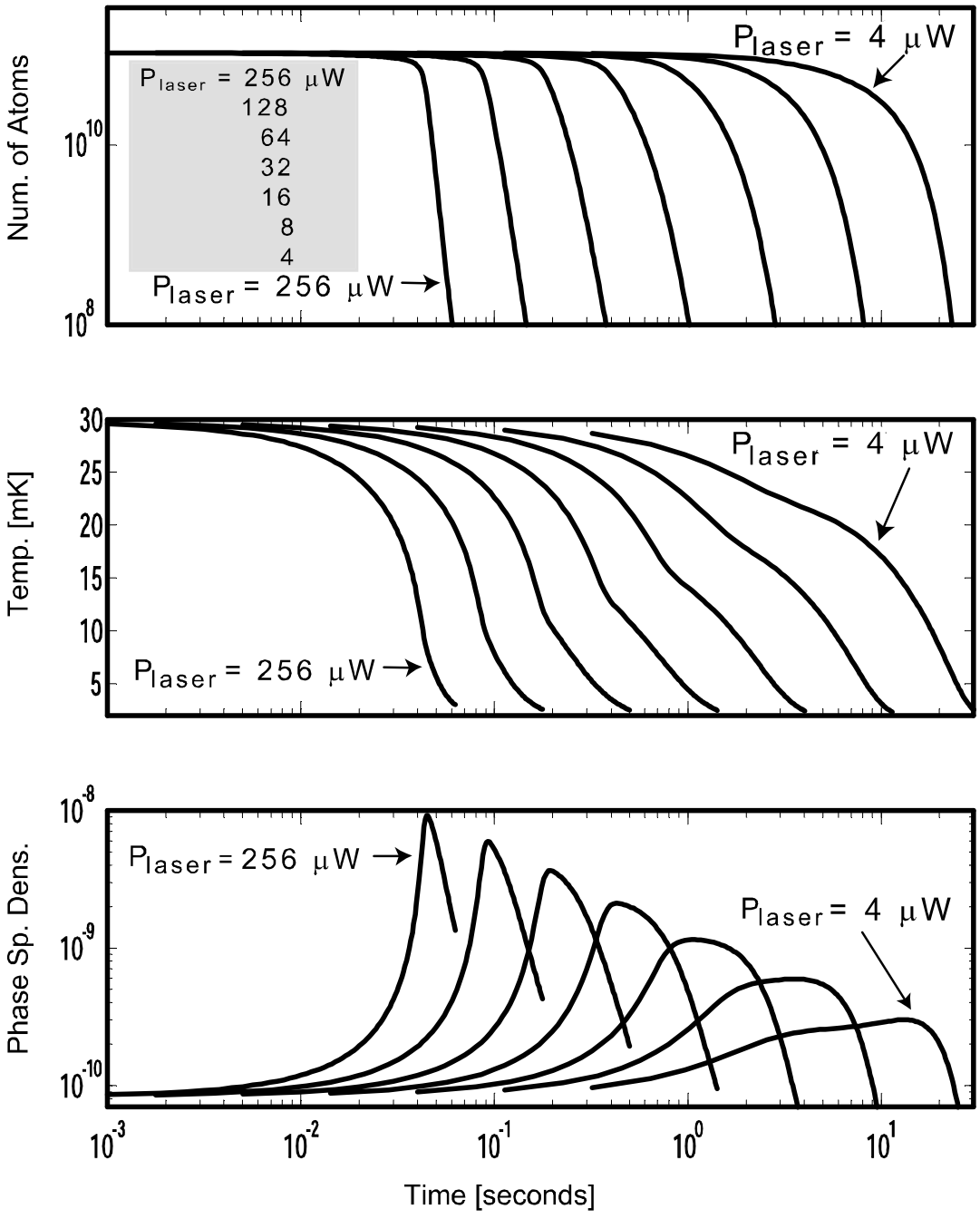

Figure 7.5: For different powers of the cooling laser, the time dependances of the temperature, number of atoms and phase space density are plotted. As the temperature falls, the density goes up. This causes a steep increase in the two-body loss which leads to a rapid loss of atoms.

7.4.3 Efficiency of cooling

Figure 7.6 shows another way of looking at the simulation results. It shows the number of remaining atoms as a function of either temperature of phase space density. Increasing the power of the cooling laser results in a larger number of atoms remaining after cooling to some target temperature. However, the time these atoms remain trapped decreases dramatically with increasing laser power.

The peak phase space density obtainable also increases with the laser power as shown in Figure 7.6.b. There is, however, a trade-off between phase space density and the number of atoms remaining.

7.5 Experimental Implementation

Experimental attempts to observe laser cooling in our trap were met with disappointment. We find that laser powers of a fraction of a microwatt or greater effect both the temperature and density of the atoms in our trap. We conducted tests to understand the cause of this optically generated loss mechanism

The tests are performed by loading our magnetic trap at an initial trap depth of $7.2\ K$ then ramping to a final depth of $0.18\ K$ in about $12\ s$. Roughly $30\ s$ after ramping down the trap depth, we introduce a $1\ cm$ diameter, off resonant pump beam into the cell for $20\ s$. We then measure the spectrum of the remaining atoms with a $0.2\ \mu W$ probe beam to determine the effect of the off resonant pump on the atoms. Figure 7.7 shows the observed spectrum in our trap after the trapped cloud has been

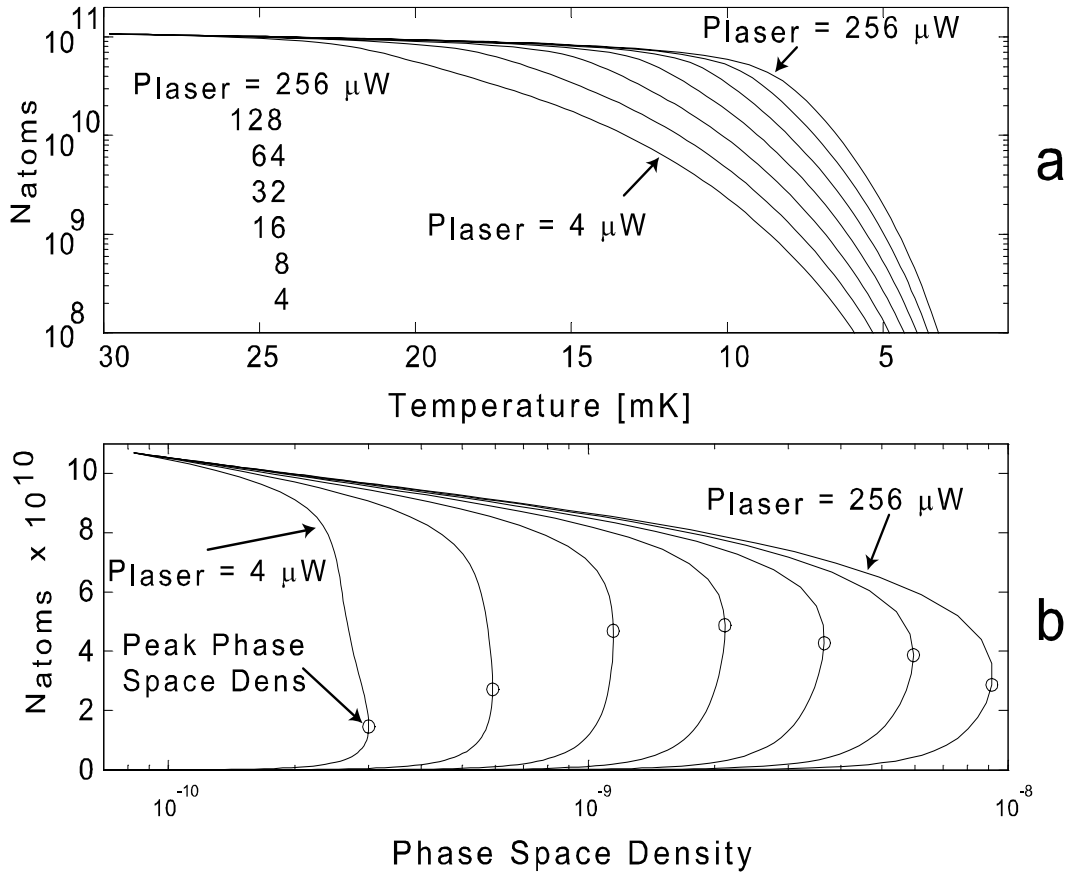

Figure 7.6: **a)** The number atoms remaining after laser cooling is plotted as a function of final temperature for several different powers of the cooling laser. Lowering the temperature of the atoms comes at a cost of atom loss. **b)** The number of remaining atoms as a function of phase space density is plotted for various powers of the cooling laser. The maximum attainable phase space densities are denoted by the circles.

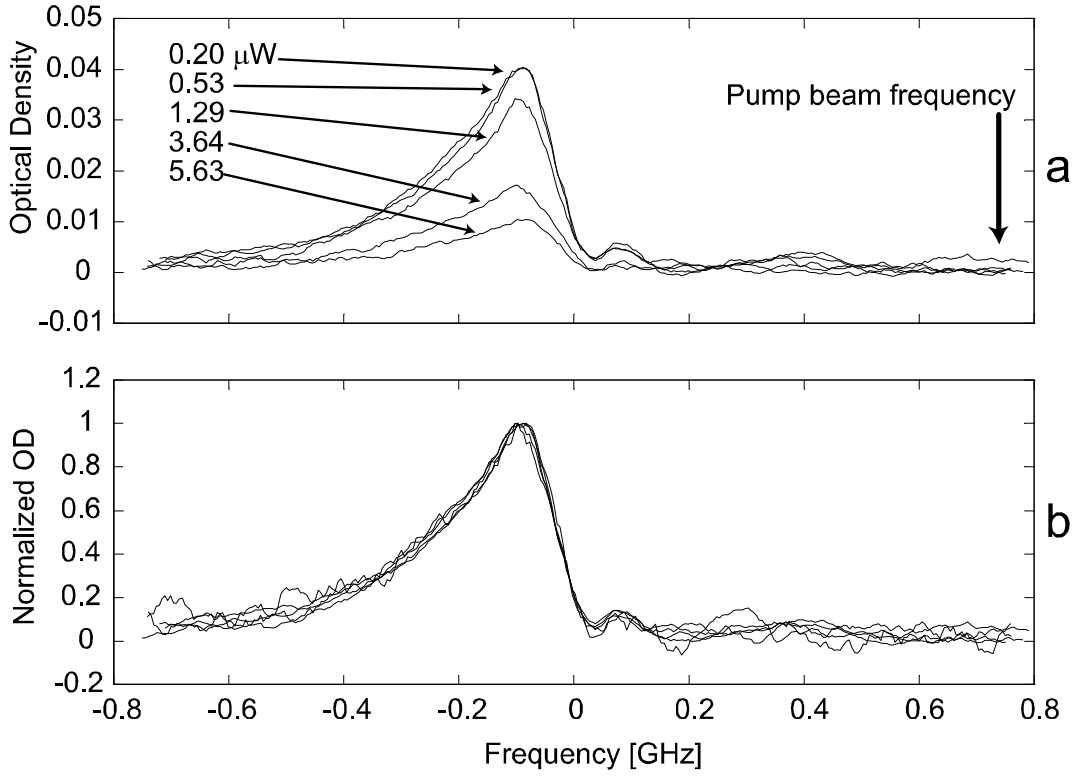

Figure 7.7: Under identical conditions at a trap depth of $180\ mk$ $(1\ Amp)$, the cell is exposed to $20\ s$ bursts of light from a non-resonant laser beam of $1\ cm$ diameter. The power in the beam is then varied. **a)** Measuring the post-burst optical density spectrum shows a devastating atom loss occuring around laser powers of a few hundred nW. **b)** Scaling the individual spectra to have the same magnitude, we observe no change in their shape. This indicates the atom loss is occuring at constant temperature.

subjected to off resonant pump beams of various powers. Since the pump beam is far off resonance, direct atom-photon interactions can be ruled out as the cause of the observed atom loss at pump powers greater than about half a microwatt. The likely culprit for this loss is the evaporation of superfluid ^{4}He film that coats the optical surfaces within the cell.

Figure 7.7.b shows that the width of the observed spectrum, and hence the temperature of the trapped ensemble, remains relatively constant as the pump power is varied. Also observed, but not shown in Figure 7.7 is the fact that even at the higher pump powers, we observe the post-pump and pre-pump temperatures of the trapped atoms to be the same. The pump laser causes atom loss without changing the temperature of the trapped cloud. If one assumes that the helium atoms liberated by the pump laser have at least $0.17\ K$ of energy (the bulk temperature of the cell at this time), then, the impact of a helium atom is likely to eject a chromium atom out of the $0.18\ K$ deep trap before it has a chance to collide with another chromium atom. This would explain the increase in loss rate without a simultaneous increase in temperature.

7.6 Laser Cooling Summary

We had hoped that laser cooling would provide a method for cooling trapped chromium to temperatures below those obtainable by our implementation of evaporative cooling. There was some hope that the inelastic scattering rate would decrease from its enormous values at lower temperatures.

The cooling power of a laser can be calculated by convolving the Doppler-free spectrum of the trapped ensemble with a "Doppler cooling kernel." Adding the effects of this cooling power as well as the laser-induced loss rates into the model for calculating the number and temperature dynamics of trapped atoms is a straightfor-

ward process. The results of this calculation show that as the temperature is reduced, the large inelastic scattering rates lead to extremely rapid decay from the trap. For the inelastic scattering rates measured in our experiment, laser cooling offers little or no advantage over evaporative cooling in reaching lower temperatures.

Attempts at implementing laser cooling in our trap were stymied by cryogenic technical difficulties. We are unable to pass more than a fraction of a microwatt of laser power through our experimental cell without observing significant trap loss. We believe this loss stems from the laser evaporating the superfluid ^4He film which covers the entire inner surface of our cell. In the future, higher laser power could be introduced to the cell by using ^3He as a buffer gas and implementing an alternative to cryopumping for buffer gas removal.

Chapter 8
Conclusions and Future Work

8.1 Summary of Experimental Results

Using the techniques of buffer gas loading and magnetic trapping, we have successfully confined chromium in a magnetic trap. For any given trap depth, the temperature of our trapped ensemble approaches a steady state value given by the ratio of elastic to inelastic collision rates. This ratio is important not only in determining the temperature of the trapped ensemble, but also the efficiency with which the atoms can be evaporatively cooled.

We embarked on a program of measuring the elastic and inelastic collision rates for magnetically trapped atomic chromium. For ^{52}Cr, the ultra-cold regime (where only a single partial wave dominates the scattering properties) occurs at a temperature of $\sim 3\ mK$. Our data clearly shows a dramatic variation in the ^{52}Cr–^{52}Cr inelastic collision rate just above the ultra-cold regime. This may be indicative of either a shape resonance, a magnetic field effect, a general feature of dipolar relaxation in the classical to quantum cross-over region, or perhaps something else unique to either chromium or to large-dipole atoms in general.

The enormity of the inelastic scattering rate in chromium causes large inefficiencies in evaporative cooling. However, our measurements indicate the inelastic

rate is decreasing below $4\,mK$. This provides hope that, as one continues to cool, the decreasing inelastic rate will lead to more efficient evaporative cooling, thus validating continued attempts at obtaining quantum degeneracy in atomic chromium. The large number of atoms we have at $2\ mK$ makes this possibility attractive. However, the limitations imposed by trapped fluxes in our superconducting magnet prevent us from making progress in the immediate future.

We attempted laser cooling in our magnetic trap in the hopes reducing the temperature of our atoms to a region with cross sections more favorable for evaporative cooling. These attempts were frustrated by our inability to maintain the vacuum in our cryogenic experimental cell while introducing the required laser cooling beam.

8.2 Possible Future Work

Further progress can be made in measuring the scattering properties of chromium to lower temperatures. Doing so, however, would require significant modifications to our experimental apparatus which we have not yet implemented.

Trapped fluxes in our superconducting magnet set a lower limit on the trap depths we can obtain reliably. In the future, this problem could be circumvented by heating the magnet to drive it normal, thereby illuminating the trapped fluxes.

Laser cooling could be more thoroughly explored by developing an alternative method for removing buffer gas from the cell. For example, a valve could be used in conjunction with a charcoal cryopump to remove ^{3}He buffer gas from the cell. This

would eliminate the superfluid film-flow that we believe is responsible for limiting the laser power we are able to use.

Perhaps the most interesting modification to our experiment would be the introduction of an Ioffe-Pritchard trapping magnet in place of the anti-Helmoltz magnet we currently use. Since we implement evaporative cooling by ramping down the trap depth, there is a one-to-one correspondence between the temperature of the atoms and the average magnetic field they experience. Because of this, we are unable to distinguish between magnetic and temperature effects in our scattering rate measurements. By varying the bias field of an Ioffe-Pritchard trap, magnetic field effects could be isolated from temperature effects. This could shed valuable insight into the scattering processes we observe.

8.3 Ramifications of our Work

Our work clearly demonstrates unexpected scattering behavior in the transition between the quantum and classical regime. If the surprisingly large values of the inelastic scattering rate we observe turn out to be a general phenomena for magnetically trapped atoms in this temperature regime, it could have serious ramifications to the efficacy of buffer-gas loading techniques in the creation of quantum degenerate gases. If, on the other hand, our observations are unique to a small subset of the atoms in the periodic table (perhaps only those with large magnetic moments), our results preclude a simple path to degeneracy for merely a handful of atoms. A firm

understanding of the mechanisms behind these enormous scattering rates is essential in determining the general utility of buffer gas loading techniques in the production of ultra-cold atoms.

Atomic scattering theory in this energy regime is itself quite interesting. The relatively poor understanding of the physics involved in these collisions is quite surprising. It is very difficult to model the problem intuitively. The quantum to classical cross-over regime precludes the use of many of the approximations usually made in scattering theory, and large scale numerical calculations are required to accurately describe the physics. It is hoped that the experimental results described in this thesis will provide the experimental input needed to further the understanding of scattering in this energy regime.

Bibliography

[1] A. Migdall, J. Prodan, and W. Phillips, "First obvservation of magnetically trapped neutral atoms," *Physical Review Letters* **54**, pp. 2596–99, 1985.

[2] H. F. Hess, "Evaporative cooling of magnetically trapped and compressed spin-polarized hydrogen," *Physical Review B* **34**, pp. 3476–79, 1986.

[3] M. H. Anderson, J. R. Ensher, M. R. Matthews, C. E. Wieman, and E. A. Cornell, "Observation of bose-einstein condensation in a dilute atomic vapor," *Science* **269**, pp. 198–201, 1995.

[4] K. B. Davis, M. O. Mewes, M. R. Andrews, N. J. van Druten, D. S. Durfee, and D. M. Kurn., "Bose-einstein condensation in a gas of sodium atoms," *Physical Review Letters* **75**, pp. 3969–73, 1995.

[5] C. C. Bradley, C. A. Sackett, and R. G. Hulet, "Bose-einstein condensation of lithium," *Physical Review Letters* **78**, pp. 985–89, 1997.

[6] K. S. Johnson, J. H. Thywissen, N. H. Dekker, K. K. Berggren, A. P. Chu, R. Younkin, and M. Prentiss, "Localization of metastable atom beams with optical standing waves: nanolithography at the Heisenberg limit," *Science* **280**, pp. 1583–1586, 1998.

[7] M. Kasevich and S. Chu, "Atomic interferometry using stimulated raman transitions," *Physical Review Letters* **67**, pp. 181–184, 1991.

[8] K. Goral, K. Rzazewski, and T. Pfau, "Bose-einstein condensation with magnetic dipole-dipole forces," *Physical Review A* **61**, p. 051601, 2000.

[9] D. DeMille, "Quantum computation with trapped polar molecules," *Physical Review Letters* **88**, p. 067901, 2002.

[10] M. A. Baranov, M. S. Mar'enko, V. S. Rychkov, and G. V. Shlyapnikov, "Superfluid pairing in a polarized dipolar fermi gas," *Physical Review A* **66**, p. 013606, 2002.

[11] K. Goral, L. Santos, and M. Lewenstein, "Quantum phases of dipolar bosons in optical lattices," *Physical Review Letters* **88**, p. 170406, 2002.

[12] J. M. Doyle, B. Friedrich, J. Kim, and D. Patterson, "Buffer-gas loading of atoms and molecules into a magnetic trap," *Physical Review A* **52**, pp. R2515–R2518, 1995.

[13] J. D. Weinstein, *Magnetic Trapping of Atomic Chromium and Molecular Calcium Monohydride*. PhD thesis, Harvard University, 2001.

[14] W. Ketterle and N. V. Druten, "Evaporative cooling of trapped atoms," *Advances in Atomic, Molecular, and Optical Physics* **37**, pp. 181–236, 1996.

[15] P. J. Leo, E. Tiesinga, and P. S. Julienne, "Elastic and inelastic collisions of cold spin-polarized 133cs atoms," *Physical Review Letters* **81**, p. 1389, 1998.

[16] S. P. Walch, C. W. Bauschlicher, B. O. Roos, and C. J. Nelin, "Theoretical evidence for multiple 3d bonding in the v2 and cr2 molecules," *Chemical Physics Letters* **103**, pp. 175–9, 1983.

[17] K. A. Anderson, B. O. Roos, P. A. Malmqvist, and P. O. Widmark, "The cr2 potential energy curve studied with multiconfigurational second-order perturbation theory," *Chemical Physics Letters* **230**, pp. 391–7, 1994.

[18] C. W. Bauschlicher and H. Partridge, "Cr2 revisited," *Chemical Physics Letters* **231**, pp. 277–82, 1994.

[19] K. Anderson, "The electronic spectrum of cr2," *Chemical Physics Letters* **237**, pp. 212–21, 1995.

[20] K. E. Edgecombe and A. D. Becke, "Cr2 in density-functional theory: approximate spin projection," *Chemical Physics Letters* **244**, pp. 427–32, 1995.

[21] H. Stoll and H. Werner, "The cr2 potential curve: a mulireference pair functional treatment," *Molecular Physics* **88**, pp. 793–802, 1996.

[22] H. Dachsel, R. J. Harrison, and D. A. Dixon, "Multireference configuration interaction calculations on cr2: Passing the one billion limit in mrci/mracpf calculations," *J. Phys. Chem. A* **103**, pp. 152–5, 1999.

[23] N. Desmarais and F. A. Reuse, "Magnetic coupling in neutral and charged cr2,mn2, and crnm dimers," *Journal of Chemical Physics* **112**, pp. 5576–84, 2000.

[24] C. J. Barden, J. C. Rienstra-Kiracofe, and H. F. Schaefer, "Homonuclear 3d transition-metal diatomics: A systematic density functional theory study," *ournal of Chemical Physics* **113**, pp. 690–700, 2000.

[25] F. Pobell, *Matter and Methods at Low Temperatures*, Springer-Verlag, 1992.

[26] KineticSystems Corporation, 900 N. State St. Lockport, Ill 60441, (815) 838-0005.

[27] Jorway Corporation, 27 Bond St., Westbury, NY 11590, (516) 997-8120.

[28] Joerger Enterprizes Inc., 166 Laurel Rd., East Northport, NY 11731, (516) 757-6200.

[29] T. Reinhardt, J. Maichel, M. Baumann, and J. Kruger, "Hyperfine structure of the resonance lines of ^{53}Cr and lifetimes of some excited states of the Cr I spectrum," *Zeitschrift Fur Physik D* **34**, pp. 1093–1097, 1995.

[30] P. R. Bevington and D. D. Robinson, *Data Reduction and Error Analysis for the Physical Sciences*, McGraw-Hill Inc., second ed., 1992.

[31] O. J. Luiten, M. W. Reynolds, and J. T. M. Walraven, "Kinetic theory of the evaporative cooling of a trapped gas," *Physical Review A* **53**, pp. 381–389, 1996.

[32] J. M. Doyle, *Energy Distribution Measurement of Magnetically Trapped Spin Polarized Atomic Hydrogen: Evaporative Cooling and Surface Sticking*. PhD thesis, MIT, 1991.

[33] G. Arfken, *Mathematical Methods for Physicists*, Academic Press, Inc., third ed., 1985.

[34] C. H. Penny and D. E. Penny, *Calculus and Analytic Geometry*, Prentice-Hall, 1982.

[35] M. Abramowitz and I. A. Stegun, eds., *Handbook of Mathemetical Functions With Formulas, Graphs, and Mathematical Tables*, 55, U.S. Department of Commerce, National Bureau of Standards and Applied Mathematics, 1965.

[36] B. DeMarco and D. S. Jin, "Exploring a quantum degenerate gas of fermionic atoms," *Physical Review A* **58**, pp. 4267–70, 1996.

[37] www.chemicool.com.

[38] R. Liboff, *Introductory Quantum Mechanics*, Addison-Wesley Publishing Company, second ed., 1993.

[39] P. Wormer and A. van-der Avoird, "Heisenberg exchange and electrostatic interactions between o2 molecules: An ab initio study," *Journal of Chemical Physics* **81**, pp. 1929–39, 1984.

[40] F. Reif, *Fundamentals of Statistical and Thermal Physics*. McGraw-Hill Inc., 1965.

[41] C. Cohen-Tannoudji and B. D. Laloe, *Quantum Mechanics*, vol. 2, John Wiley and Sons, first ed., 1977.

[42] B. H. Bransden and C. J. Joachain, *Physics of Atoms and Molecules*, Longman, first ed., 1983.

[43] J. Stuhler, P. O. Schmidt, S. Hensler, J. Werner, J. Mlynek, and T. Pfau, "Continuous loading of a magnetic trap," *Physical Review A* **64**, p. 031405(R), 2001.

[44] B. G. Lindsay, K. A. Smith, and F. B. Dunning, "Control of long-term output frequency drift in commercial dye lasers," *Review of Scientific Instruments* **62**, pp. 1656–7, 1991.

[45] W. Z. Zhao, J. E. Simsarian, L. A. Orozco, and G. D. Sprouse, "A computer-based digital feedback control of frequency drift of multiple lasers," *Review of Scientific Instruments* **69**, pp. 3737–40, 1998.

[46] E. Riedle, S. H. Ashworth, J. T. Farrell Jr., and D. J. Nesbitt, "Stabilization and precise calibration of a continuous-wave difference frequency spectrometer by use of a simple transfer cavity," *Review of Scientific Instruments* **65**, pp. 42–48, 1994.

[47] Coherent, Inc., Santa Clara, CA., http://www.coherentinc.com.

[48] Melles Griot 05 STP 901 www.mellesgriot.com.

[49] E. Hecht, *Optics*, Addison Wesley Publishing Company, second ed., 1987.

[50] P. W. Milonni and J. H. Eberly, *Lasers*, John Wiley and Sons, first ed., 1988.

[51] A. E. Siegman, *Lasers*, University Science Books, first ed., 1986.

[52] W. Demtroder, *Laser Spectroscopy*, Springer, second ed., 1996.

[53] Lamda Research Optics Inc, Cerritos, CA. http://www.lambda.cc.

[54] M. Steffes, "Control frequency response and noise in broadband, photodetector, transimpedance amplifiers," *EDNmag, www.ednmag.com, July 4, 1996* , pp. 113–125.

[55] "Speedplus wideband low noise voltage feedback operational amplifier," *Texas Instruments technical document for OPA2686 OP AMP, www.ti.com* , 1997.

Appendix A
General Technique for Laser Locking

In all the work presented in this thesis, detection is achieved by means of laser absorption. The optical setup used has been briefly described in Chapter 2. The factory-supplied stabilization circuitry in our *Coherent 899* ring laser determines the frequency stability of our detection light. Over very short time scales ($\sim 1\ ms$) the laser is stable to within roughly $2\ MHz$. Over timescales of $\sim$ 1s, the variation in the laser frequency is measured to be between 5 and $10\ MHz$. On the tens of minutes timescale, we observed the laser frequency to drift as much as a few hundred MHz. For laser cooling applications, it is important to work with a stabile laser capable of accurately producing the frequency needed to achieve optimal cooling efficiency.

Examining the Doppler cooling spectrum shown in Figure 7.2, shows that the laser must be stable to $\lesssim 10\ MHz$. In many laser cooling experiments, this level of stabilization is achieved by locking to the saturated absorption peak obtained from a vapor cell containing the species to be laser cooled. For chromium, however, vapor cell construction is complicated by the very high temperatures needed to develop a useful vapor density.

Although the *Coherent 899* ring laser has good short term stability, the large long-term drifts would be detrimental to successfully implementing laser cooling. To achieve the required stability, an external stabilization system is required to eliminate the long timescale drifts. We chose to adapt a known [44, 45, 46] frequency stabiliza-

tion scheme involving the combined use of a scanning confocal cavity and a stabilized He-Ne laser. This scheme has the advantage of being general. With a simple change of optics, it can be used to control any laser operating at any reasonable wavelength.

A.1 Overview of Technique

The system is designed to use an ultra-stable master laser for measuring and controlling the average length of a scanning confocal cavity. This, in turn provides a very stable reference to which a slave laser can be locked. A diagram of the system is shown in Figure 8.1.

The master and slave beam are orthogonally polarized. This allows them to be combined, passed through the scanning confocal cavity, and guided into separate detectors. A triangle voltage wave, Figure 8.2.a is applied to the scanning piezo of the cavity, causing it sweep through resonances for each of the beams. The respective resonances can be recorded separately by monitoring the signals coming from each of the detectors, Figure 8.2.b. Since the master and slave lasers have different wavelengths, the peaks arriving at each detector will not occur at the same scanning voltage. The relative position of the two peaks will depend on their frequency difference. Their absolute position will depend on the average length of the cavity, which, if left unstabilized, will drift over time.

As the cavity is scanned, its average length is stabilized by adding a controlled offset to the piezo scanning voltage. This voltage is generated as follows. The piezo

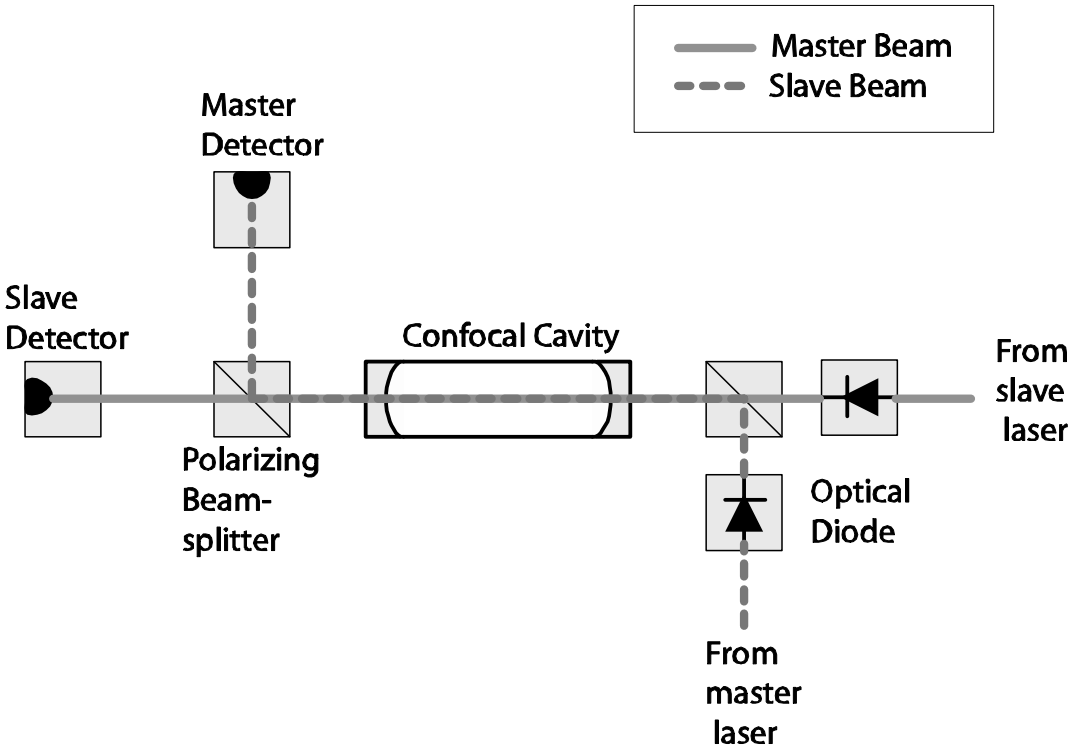

Figure 8.1: Optical layout of frequency stabilization system. The master and slave beams are orthogonally polarized. The polarizing beam splitters serve to combine the beams before entering the scanning confocal cavity and then separate them into different detectors. The optical diodes are important to prevent cavity reflections from feeding back into the lasers.

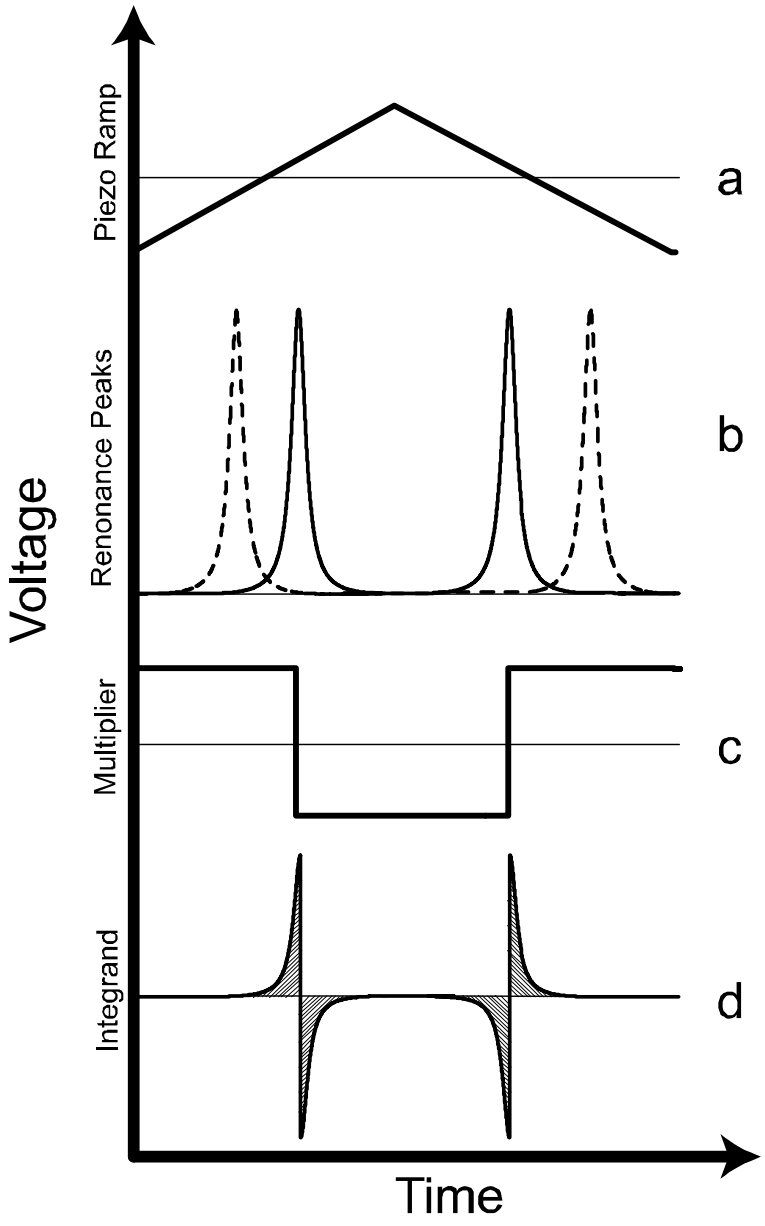

Figure 8.2: Time dependance of various system voltages. **a)** A triangle ramp is applied to the cavity scanning piezo. **b)** The cavity scans through resonances of the master (solid) and slave (dashed) laser beams causing the detectors to record peaks. **c)** A square wave is derived by setting a comparator threshold on the piezo scanning voltage. **d)** The master laser peak is multiplied by the square wave to produce the error signal which is integrated to provide feedback to correct for cavity drifts.

scanning voltage is put into a voltage comparator along with a controllable, stable DC voltage. The output of the comparator, shown in Figure 8.2.c, is then multiplied by the signal coming from the resonance peaks of the master laser detector. When a resonance peak coincides with the comparator changing state, their product will be as shown in Figure 8.2.d. This product signal is then sent to an integrator which produces an output proportional to the shaded area in Figure 8.2.d. An amplified version of this integrated signal is then used as the cavity offset voltage.

Under the conditions shown in Figure 8.2.d, there is equal positive and negative area resulting in a zero voltage coming from the integrator and zero offset applied to the cavity. If the cavity length drifts slightly, perhaps due to thermal expansion, the position of the peaks in Figure 8.2.c will shift. This will introduce asymmetry into the product signal of Figure 8.2.d, which in turn, causes the integrator to send an offset voltage to the cavity. This offset voltage will correct for the cavity drift, bringing the position of the resonance peak back to the conditions shown in Figure 8.2.d.

An identical locking scheme can be used to lock the slave laser to the cavity. In that case, however, the offset voltage, instead of controlling the average cavity length, controls the frequency of the slave laser.

A.2 System Design

The design considerations for building this stabilization system fall into two categories, optical and electronic. A description of both the optical and electronic setup used is described below.

A.2.1 The Lasers

The slave laser, in our system, is a *Coherent 899* Ti:Saph. ring laser [47] with a linewidth of approximately 1 MHz. We measured the short term ($\sim$ 1 second) drift of the Ti:Saph to be between 5 and 10 MHz. Over much longer timescales ($\sim$ 20 minutes) the drift can be as much as a few hundred MHz. For optimum Doppler cooling performance, the Ti:Saph. requires stabilization to about a natural linewidth, which, for chromium, is $\sim$ 5 MHz.

The master laser is a Melles Grio stabilized Helium-Neon laser [48] with a specified drift of less than $\pm$2 MHz/Hour. The excellent stability of this laser makes it particularly well suited for frequency standard applications. The stabilization circuitry within this laser makes it very sensitive to feedback arising from retroreflections. To prevent damage to the He-Ne circuitry, it is very important that an optical diode be placed between the laser and the confocal cavity.

Property	**Exact Expression**	**Approximate** Expression ($\mathbf{R \approx 1}$)	**Description**
Free Spectral Range (FSR)	$\frac{c}{\text{(round trip length)}}$	-	Frequency separation of resonance peaks. Also reciprocal of round trip time.
Finesse	$\frac{\pi}{2\sin^{-1}\left(\frac{1-R}{2\sqrt{R}}\right)}$	$\frac{\pi\sqrt{R}}{1-R} \simeq \frac{\pi}{1-R}$	Ratio of FSR to resonance peak width.
Q	$\frac{\omega}{FSR\ln(1/R^2)}$	$\frac{\nu}{FWHM}$	Ratio of optical frequency to resonance peak width.
Ring-down time	$\tau = \frac{\text{(round-trip time)}}{\ln(1/R^2)}$	$\tau =$ round-trip time$\times$ finesse / 2π	Round-trip time multiplied by finesse (to within 2π).
Resonant circulating intensity	$I_{circ} = \frac{I_{input}}{(1-R)}$	$I_{circ} = \frac{I_{input}}{\pi} \times finesse$	Circulating to incident power ratio is transmissivity

Table 8.1: Parameters used to characterize optical cavities. R is the intensity reflectivity of the optics. FWHM is the full-width-half-max of the resonance peaks, and c is the speed of light.A Fabry-Perot cavity of length d has a round trip length of 2d and a round trip time of c/2d. A confocal cavity of length d has a round trip length of 4d and a round trip time of c/4d.

A.2.2 The Cavity

The scanning confocal cavity is central to the implementation of this stabilization scheme. There are several important parameters that are useful when discussing the behavior of resonant optical cavities. The most important of these are summarized in Table 8.1. The exact expressions [49, 50, 51, 52] in the second column of Table 8.1 are a bit cumbersome. Since most optical cavities are constructed with high reflectivity optics, the approximation $R \approx 1$ usually applies, leading to the simplified expressions of the third column.

As the heart of this system, we chose the scanning confocal cavity provided with the *Coherent* Model 240 spectrum analyzer. When equipped with standard optical coatings, this cavity is specified to have a free spectral range of $1.5\ GHz$ and a finesse

> 200. This results in a resonance peak of FWHM less than $7.5\ MHz$. This is sufficiently narrow to allow stabilizing the slave laser to about $5\ MHz$ with respect to the master laser.

To meet the specifications needed to Doppler cool chromium, the cavity reflectors require a custom coating to provide the requisite reflectivity for both the He-Ne master laser ($633\ nm$) and the Ti:Saph. slave laser ($850\ nm$). We purchased the uncoated fused silica substrates directly from Coherent. The substrates were then sent to Lamda Research Optics [53] for coating at the required wavelengths. Each cavity optic must be coated on both surfaces. The specifications provided by Coherent for achieving a finesse > 200 are that the high reflector surface have $99.75 \pm 0.15\ \%$ reflectivity. The opposite surface should be anti-reflection coated for a reflectivity of less than $0.25\ \%$. These reflectivities result in theoretical finesse of 1255. However, practical considerations such as cleanliness, alignment, etc., result in the actual finesse falling short of this predicted value.

A.2.3 The Electronics

A block diagram of the stabilization electronics is shown in Figure 8.3. The system consists of two essentially identical subsystems which we will call the master and slave subsystem. The master subsystem locks the cavity to the master laser. The slave subsystem locks the slave laser to the cavity. Each subsystem consists of three modules. The detector module serves as a variable gain transimpedance amplifier for the photodiode detectors. The discriminator module eliminates unwanted peaks from

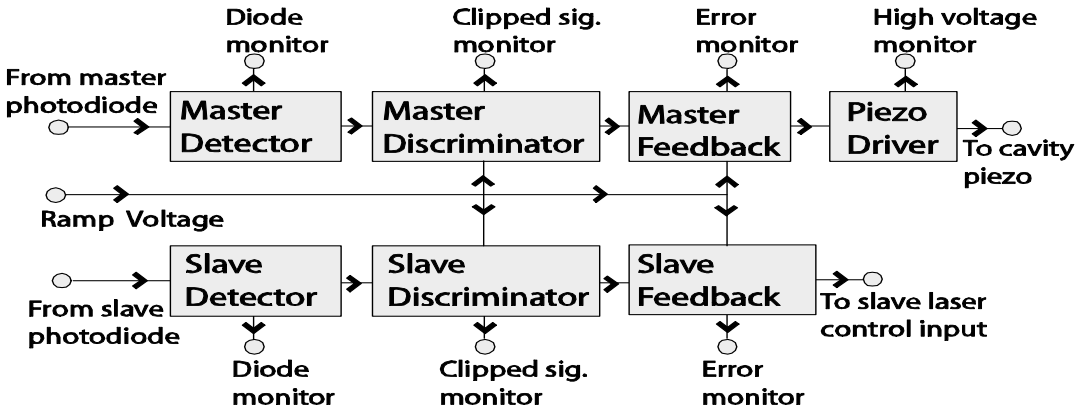

Figure 8.3: Block Diagram of Laser Locking System

the raw detector signal. The feedback module creates the control voltages which are used to control the offset of the cavity and the frequency of the slave laser. The design of these modules will now be discussed.

Detector Module

The detector module is a two stage variable gain amplifier that takes the current from the photodiodes and produces a voltage to be sent to the discriminator module. A schematic diagram of the detector module is shown in Figure 8.4. It has two parts, a transimpedance amplifier and a variable gain voltage amplifier.

The gain and frequency characteristics of a transimpedance amplifier depend on the value of the feedback impedance. This impedance is set by the values of the feedback resistor and capacitor. The appropriate resistor and capacitor values depend onthe gain bandwidth product of the OP AMP and the desired frequency response.

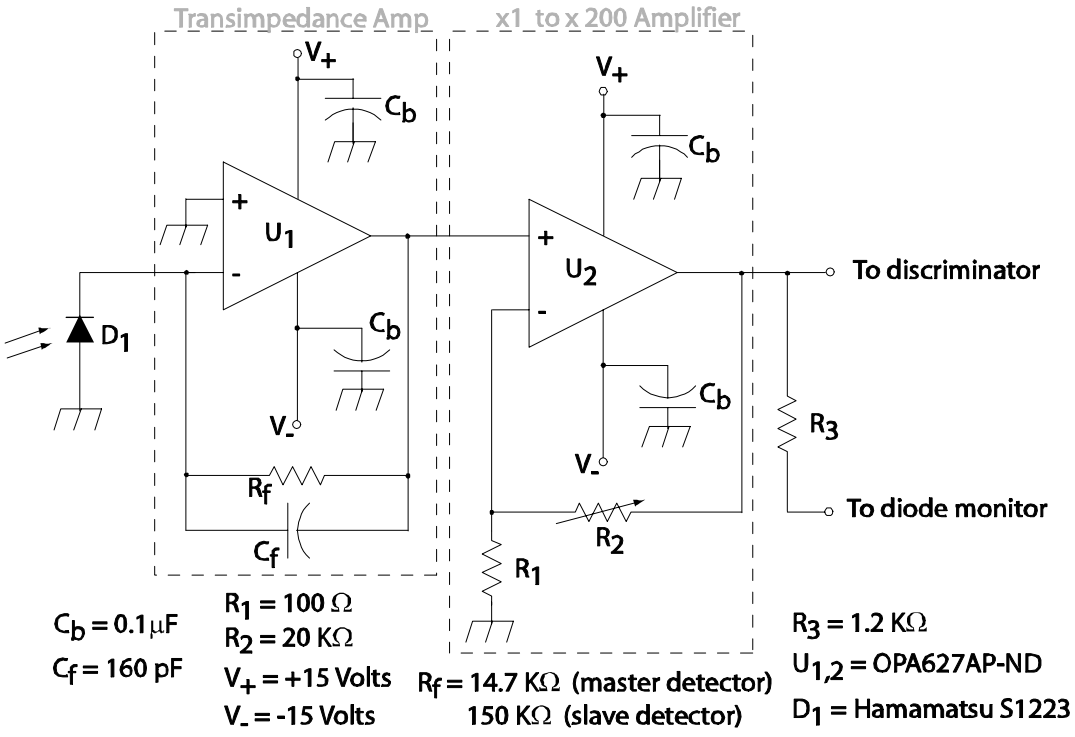

Figure 8.4: Laser Locking Detector Module

The important design equations are [54, 55]

$$\frac{1}{2\pi R_f C_f} = \sqrt{\frac{(GBP)}{4\pi R_f C_d}} \tag{A.1}$$

and

$$f_{-3db} = \sqrt{\frac{(GBP)}{2\pi R_f C_d}} \tag{A.2}$$

where C_d is the photodiode capacitance (plus other input capacitance), R_f is the feedback resistance, C_f is the feedback capacitance, GBP is the gain bandwidth product of the op amp, and f_{-3db} is the frequency at which the amplifier gain will be suppressed by 3db.

The component selection process starts with selecting a photodiode. In addition to spectral response, sensitivity, and the size of the detector area, the capacitance of the photodiode must be considered. Next comes the selection of the OP AMP. It must have a gain-bandwidth product large enough to handle the frequencies of the expected signals. Once the photodiode and OP AMP have been selected, Eqs. A.1 and A.2 are used in selecting the feedback resistance and capacitance for the desired frequency response. The output voltage, of course, will be simply the product of the photodiode current and the feedback resistance.

The first stage transimpedance amplifier is followed by a standard non-inverting variable-gain voltage amplifier. This second stage of amplification provides a means for varying the gain of the amplifier without significantly effecting its frequency response. For a given light level incident on the photodetector, the gain can be manually adjusted to send an appropriate signal level to the discriminator module.

Discriminator Module

The confocal cavity, unless precisely aligned and mode matched, produces multiple voltage peaks on the detector when scanned over a single laser line. Operation of the locking scheme requires the presence of one and only one resonance peak per scan for each laser. The role of the discriminator module is to suppress any superfluous resonance peaks. This is accomplished by adjusting the laser alignment into the cavity such that one of the peaks becomes larger than the others. The discriminator then passes only voltages greater than some threshold, and suppresses all others to ground. In this way, only the single large- amplitude peak remains unsuppressed.

In addition to eliminating redundant peaks, the discriminator module is designed to eliminate a hysteresis-related problem generated by scanning the confocal cavity. Ideally, there would be a one-to-one correspondence between the voltage applied to the cavity scanning piezo and the optical length of the cavity. In practice, however, the cavity length at a given piezo voltage will depend on whether the voltage is increasing or decreasing. This hysteresis would introduce unacceptable variation in the position of the resonance peaks. The discriminator is used to suppress the voltage coming from the detector module to ground when the piezo is ramping up. This passing of only negatively sloped scans eliminates one of the hysteresis paths from consideration thereby ensuring a one to one correspondence between the scanning voltage and the optical length of the cavity.

Figure 8.5 shows a schematic diagram of the discriminator module. It has three subcomponents: the threshold clamp, the slope clamp and a differentiator. The threshold clamp consists of a comparator whose output drives the gate of an analog switch. If the input signal from the detector module is less than the threshold voltage set by adjusting R_1, the output of the threshold clamp will be driven to ground. Above threshold, the input signal is passed on to the output.

The slope clamp is a comparator that gets its input from a differentiator acting on the piezo ramp signal and sends its output to an analog switch. For rising ramp signals, the comparator goes high, closing switch S_2. This sends the output of the slope to ground. When the ramp signal falls, the switch will be open causing the input signal to pass through the slope clamp. The threshold and slope clamps work together to only pass peaks above an adjustable threshold when the piezo ramp voltage is falling.

Feedback Module

The feedback module is responsible for generating the output signals that control the cavity offset voltage (average cavity length) and the frequency of the slave laser. To accomplish this, it takes the resonance peaks that are detected and passed through the discriminator and processes them together with the piezo ramp voltage to produce an error signal similar to that of Figure 8.2.d. This error signal is then passed through an analog integrator whose output can be used to send the required control voltages to the cavity offset and slave laser frequency controls.

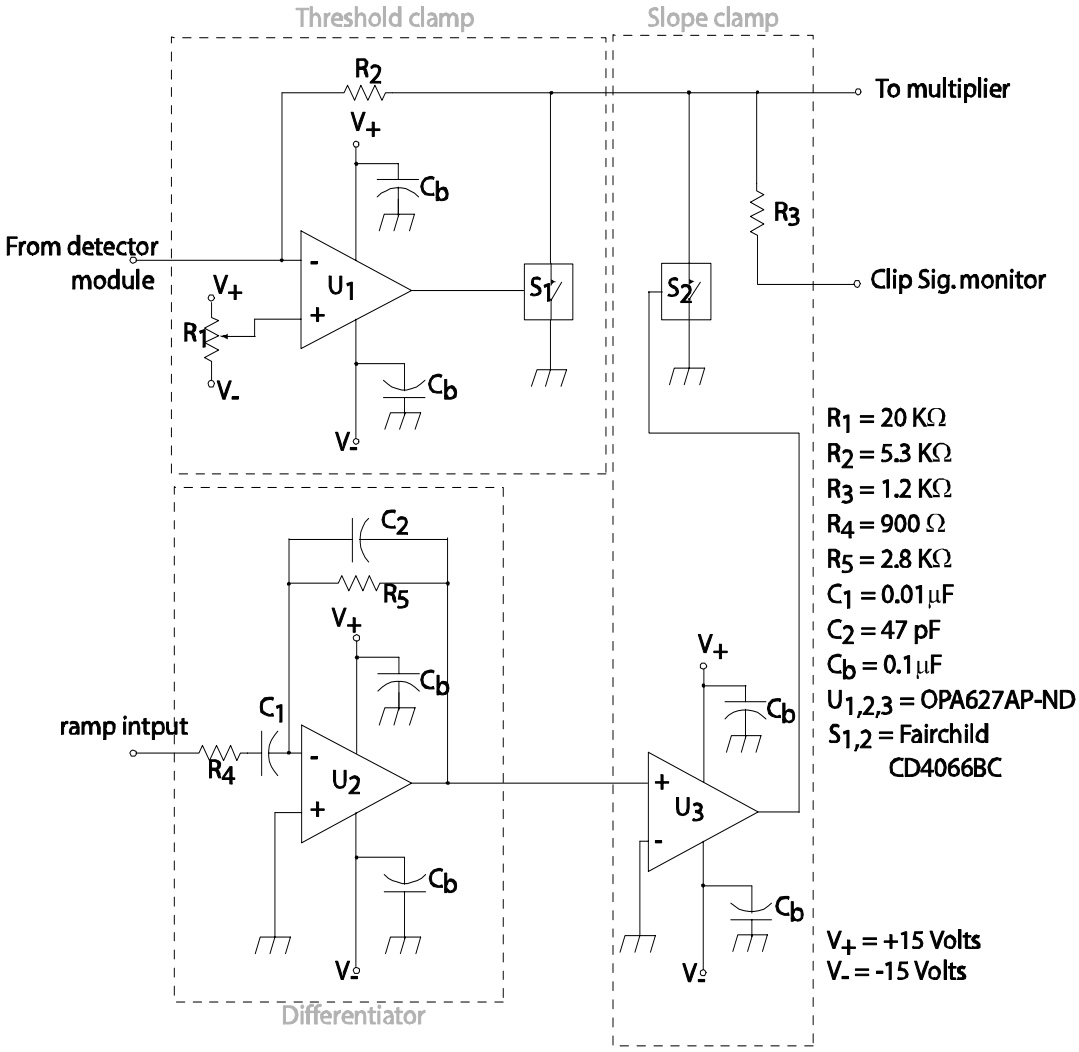

Figure 8.5: Laser Locking Discriminator Module

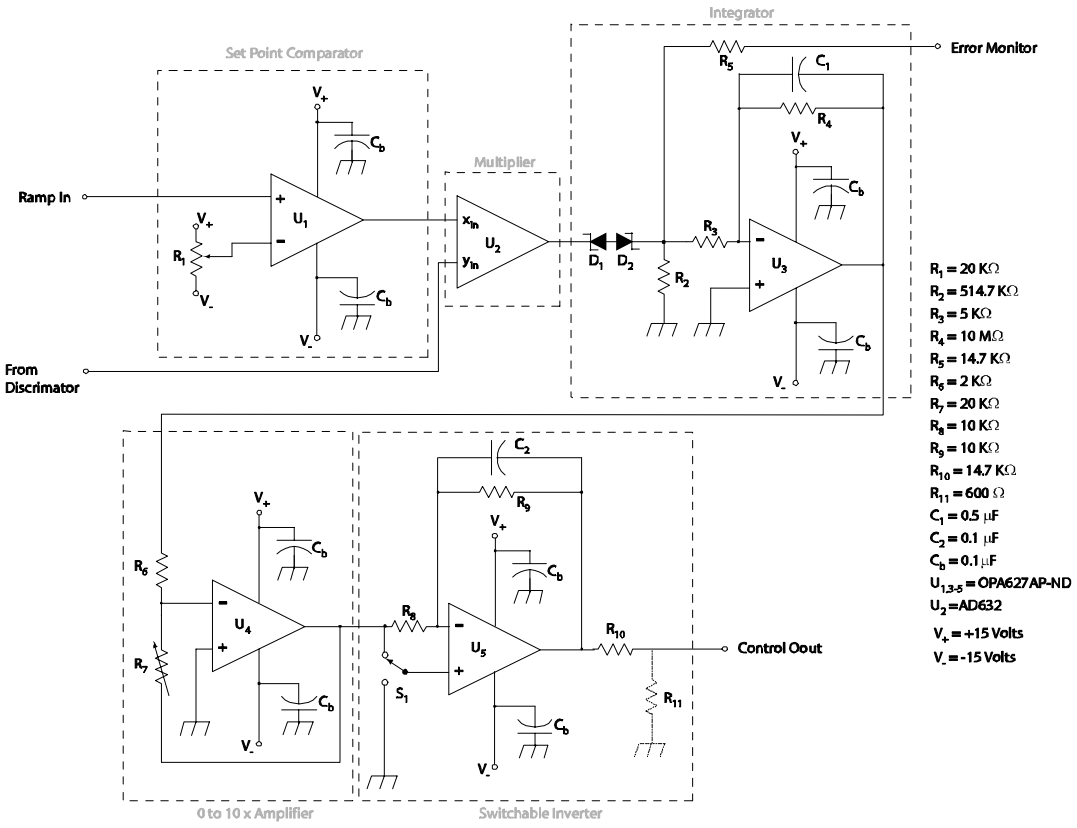

Figure 8.6: Laser Locking Feedback Module

A schematic diagram of the feedback module is shown in Figure 8.6. It consists of five subcomponents: the setpoint comparator, the multiplier, the integrator, the amplifier, and the inverter.

As can be seen by referring back to Figure 8.2.d, the resonance peaks passing through the cavity are detected and multiplied together with the output of a comparator acting as a threshold detector on the piezo ramp voltage. This is accomplished by the set point comparator and multiplier shown in Figure 8.6. The setpoint at which the comparator changes state is determined by the potentiometer R_1. The comparator

output is fed directly into an analog multiplication chip which also receives the resonance peaks signals and produces the error signal output. The stability of the set point will be directly dependant not only on the stability of the voltage sources V_+ and V_-, but also on the stability of R_1. Because of this, high quality power supplies and potentiometers must be used for these components.

An analog multiplication chip is used to produce the error signal. The output of this chip can have small offsets. Since the output of the chip is sent to an integrator, these offsets can significantly impact the performance of the feedback circuit. The long-lived, small-amplitude offsets coming from the multiplier chip integrate to values large enough to interfere with the desired integration of the short-lived, large-amplitude signals coming from the resonance peaks. To solve this problem, the back-to-back zener diodes, D_1 and D_2, were introduced. These diodes suppress the offset voltage coming from the multiplier to values low enough to have little impact on the performance of the circuit. Once the offset of the multiplier chip has been suppressed with the zener diodes, the remaining signal is passed to the integrator.

The integrator is the key component for providing the feedback signal. It can be easily understood by ignoring the existence of the bypass resistor, R_4, which simply sets the timescale over which the integration takes place. The voltage pulses coming from the multiplier will drive current through R_3. This current will pile charge onto C_1. The voltage created by the charge across C_1 is the desired output of the integrator and will be sent to control the offset of the cavity or the frequency of the slave laser.

Consider what happens when the signal coming from the multiplier is like that of Figure 8.2.d. In this specific case, the setpoint comparator and the resonance peak are phased such that their product is symmetric about zero. This will cause the current through R_3 to contribute no net charge across C_1. Each scan across the resonance peak will reproduce the shape of this product signal, causing the charge on C_1 to remain fixed thereby maintaining the voltage across it constant. Now consider what happens when the phase of the resonance peak drifts slightly from that of the setpoint comparator. In this case, there will more area under, say, the positive peak. Now each cycle will contribute some net charge across C_1 resulting in a changing voltage. Since this voltage is used to control the cavity length offset (or the slave laser frequency), when it varies, it will produce a change in the cavity length (slave laser frequency). This will, in turn, shift the phase of the resonance peak with respect to the setpoint comparator and alter the positive/negative area ratio of the error signal sketched in Figure 8.2.d. The resulting change in cavity length (slave frequency) will continue until each cycle of the error signal contributes no net charge across C_1. This stabilization of the cavity (slave laser) to the set point comparator provides the desired locking.

The two remaining components of the feedback module are quite straightforward. The output of the integrator is passed through a variable gain voltage amplifier which allows for adjusting the feedback level of the system. The output of this am-

plifier is sent through a switchable inverter which sets the sign of the feedback control voltage.

Piezo Driver Module

The length of the confocal cavity is controlled by sending a relatively high voltage signal to a piezoelectric transducer that supports one of the cavity reflectors. The piezo driver module is designed to amplify the low voltage cavity control signals into the higher voltage signals required to drive the piezo. A schematic diagram of the piezo drive module is shown in Figure 8.7. It consists of two components, a summing circuit and an amplifier. It takes two inputs, a ramp signal and an offset signal. The voltages of these two signals are added together with a summing circuit. The resulting sum is then passed through an amplifier capable of producing the $\pm 40V$ signals which are then sent to the piezo of the scanning confocal cavity.

A.3 Results/Improvements

Due to the constraints on laser power forced on us by cryogenic concerns, the laser locking system was not needed in our experiment. Although it was never used in its designed capacity, the system was tested. These tests indicated several shortcomings which would need to be addressed in a next-generation implementation of this laser-locking scheme.

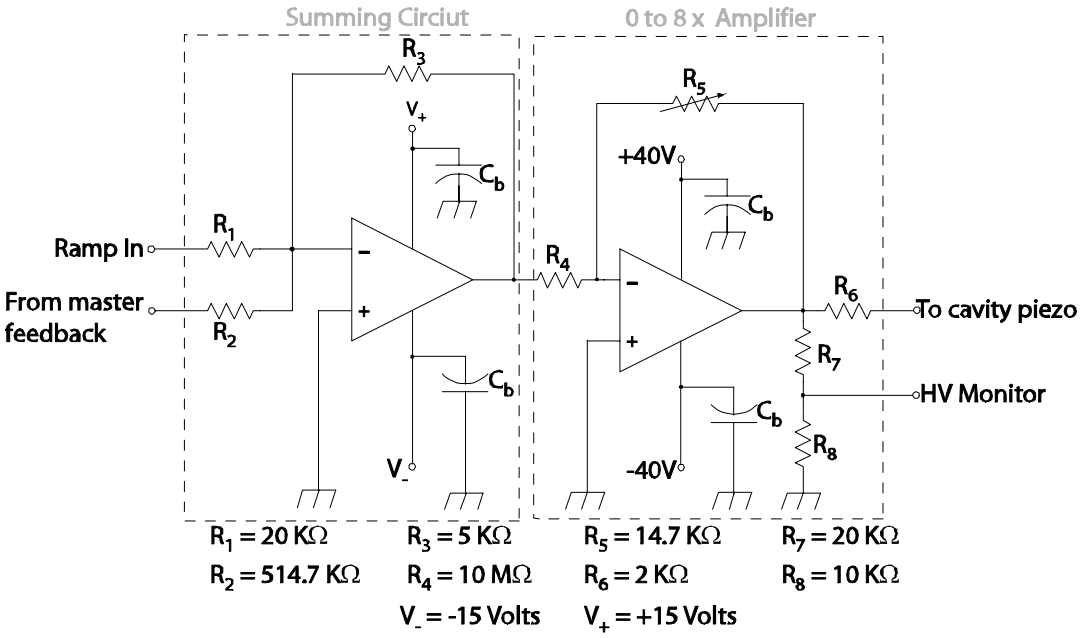

Figure 8.7: Laser Locking Piezo Driver

These tests of the system are performed by using an oscilloscope to monitor the transmission peaks passing through our scanning cavity. We determine that the laser locking system is able to maintain a stable frequency separation between the titanium-sapphire laser and the helium-neon master laser. This frequency separation is stable to within approximately the width of the cavity transmission peak. Assuming the width of the transmission peak corresponds to a finesse ≥ 200, we are able to stabilize our titanium sapphire laser to a constant frequency with a jitter of between 5 and $10\ MHz$. The uncertainty in this number is dominated by the uncertainty in the finesse of the cavity. The response time of the electronics also becomes important in determining this uncertainty when the cavity is scanned at frequencies greater than about $100\ Hz$.

When in locked mode, this system imposes a jitter on the slave laser. Although this jitter is not large enough to significantly impact the expected performance of the slave laser for Doppler cooling purposes, it adds unacceptable interference if used to control a probe laser for absorption detection of trapped atoms. The cause of this jitter stems from an unforeseen problem related to the way the discriminator and feedback modules create and process the error signal.

As the cavity is continuously scanned, there is some variation in the height of the resonance peaks measured by the detector module. The discriminator passes resonance peaks having a magnitude greater than some threshold, but does nothing to change the magnitude of the unsuppressed peaks. Furthermore, the time for which a given peak remains unsuppressed by the discriminator depends on its magnitude. This causes the amplitude variation in peak height to be mapped onto a position/width variation in the discriminator output leading to the observed frequency jitter of the locked slave laser. A solution to this problem would be to add the functionality of a discriminator module to the published method of using a peak detector to stabilize one laser with respect to another [44].

Another shortcoming of this system is its inability to accommodate scanning the slave laser. This system was designed to lock the laser to a specific frequency with the idea of laser cooling in mind. However, after it was built, we recognized the need for a method of measuring the frequency of a tunable detection laser relative to that of a fixed frequency master laser. Combining the idea of a discriminator with the idea

of using a peak detector to measure the position of the resonance peaks[44], a cavity could readily be used to measure the frequency difference between two lasers. More to the point, the drift of one laser with respect to the other could be monitored as a function of time and used to calibrate measured spectra of trapped atoms.

Appendix B
Machine Drawings

This appendix contains many of the machine drawings used in designing our experiment. These drawings are intended to be used as a reference to those who are familiar with the apparatus. As such, each of the drawings is presented as an AutoCAD printout with minimal explanation. It is hoped that these drawing will prove useful in designing the changes required for future generations of the experiment.

The designs presented are the work of the various students who worked on this experiment. Special acknowledgement should be given to Dima Egorov for doing most of the design work on our superconducting magnet.

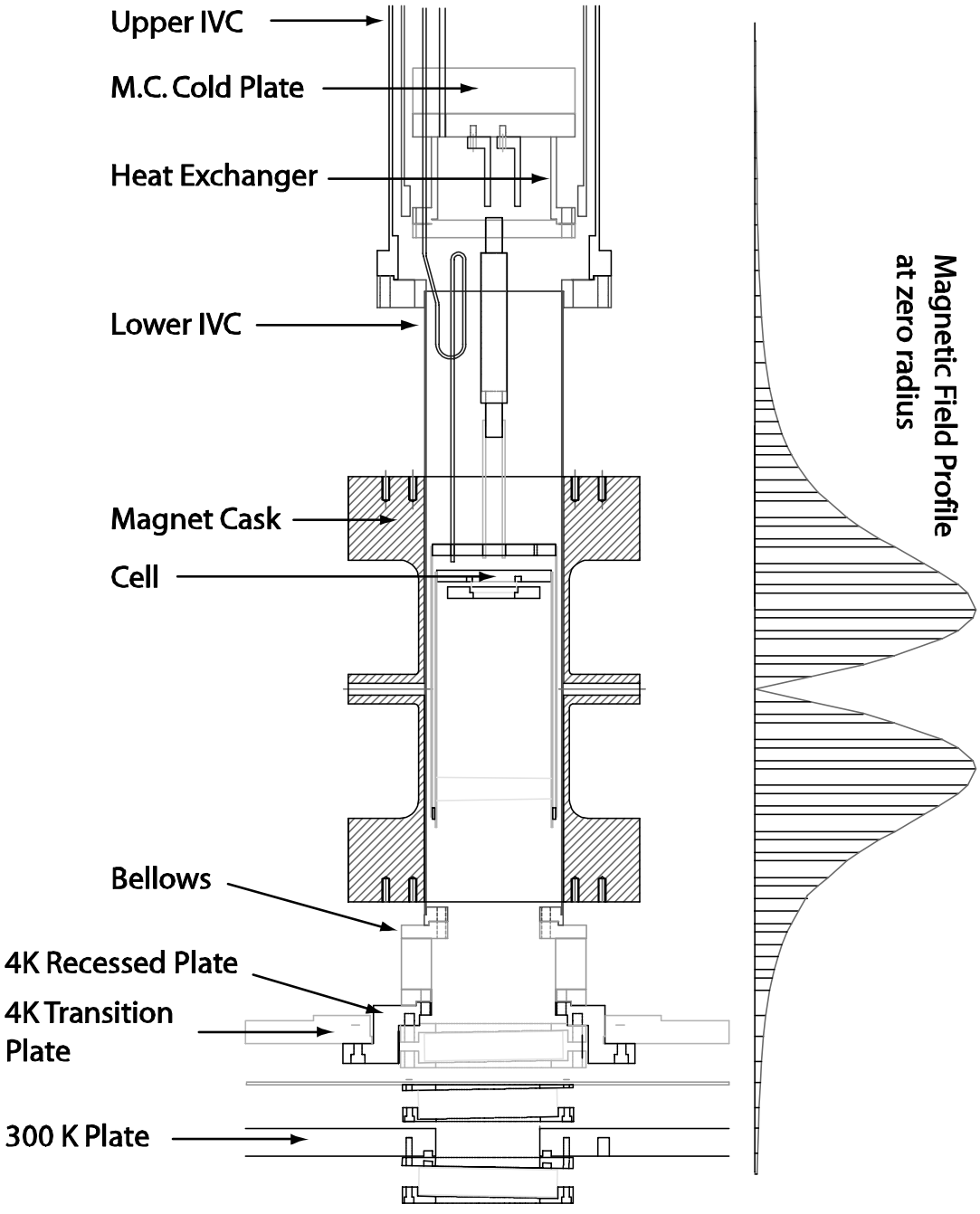

Figure 8.8: Full Assembly

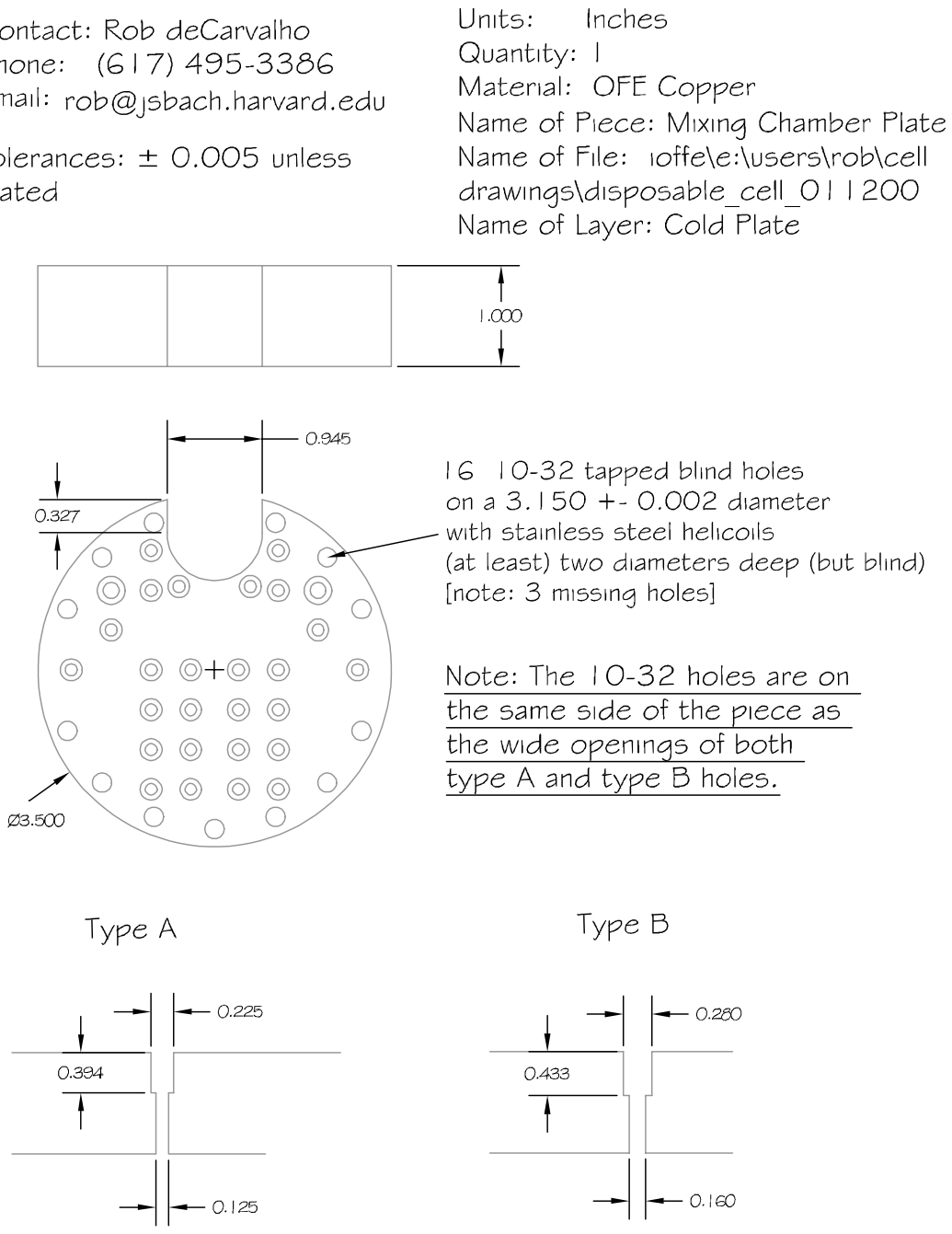

Figure 8.9: Mixing Chamber Cold Plate

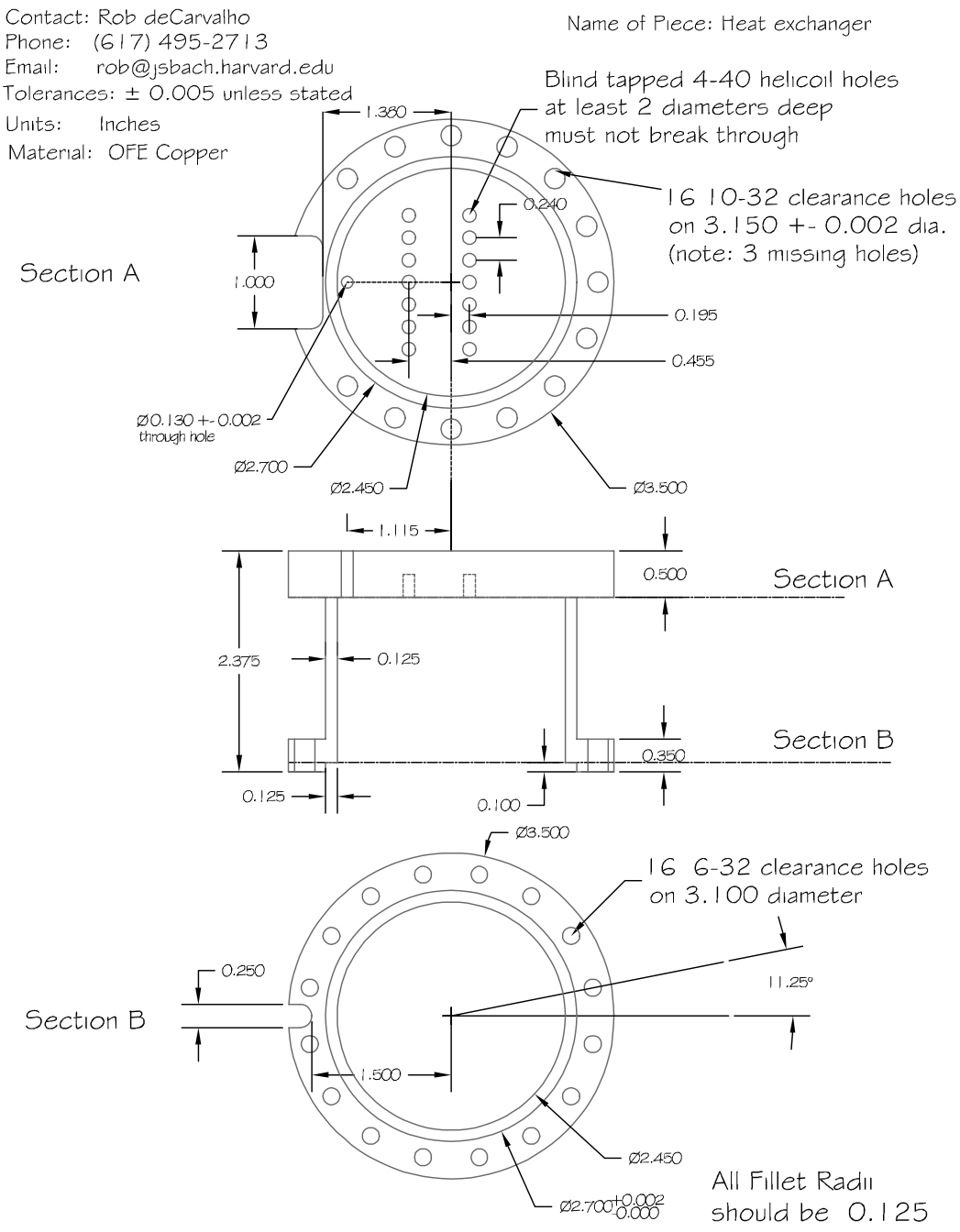

Figure 8.10: Heat Exchanger Body

Contact: Rob deCarvalho
Phone: (617) 495-3386
Email: rob@jsbach.harvard.edu

Units: Inches
Quantity: 2
Material: OFE Copper

Name of Piece: Sinter Fin
Name of File: ioffe\e:\users\rob\cell drawings\disposable_cell_121699
Name of Layer: cell heat exchanger

Tolerances: ± 0.005 unless stated

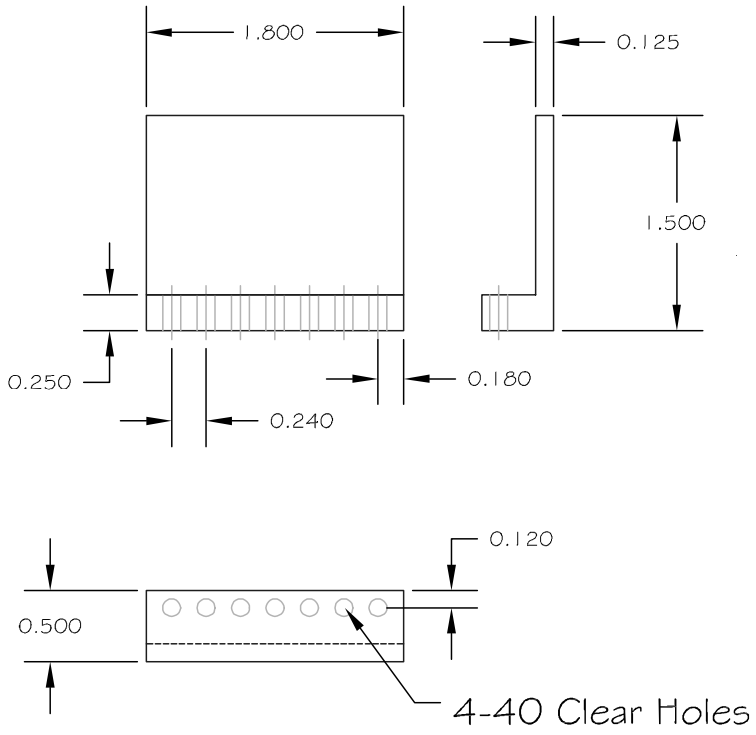

Figure 8.11: Heat Exchanger Fin

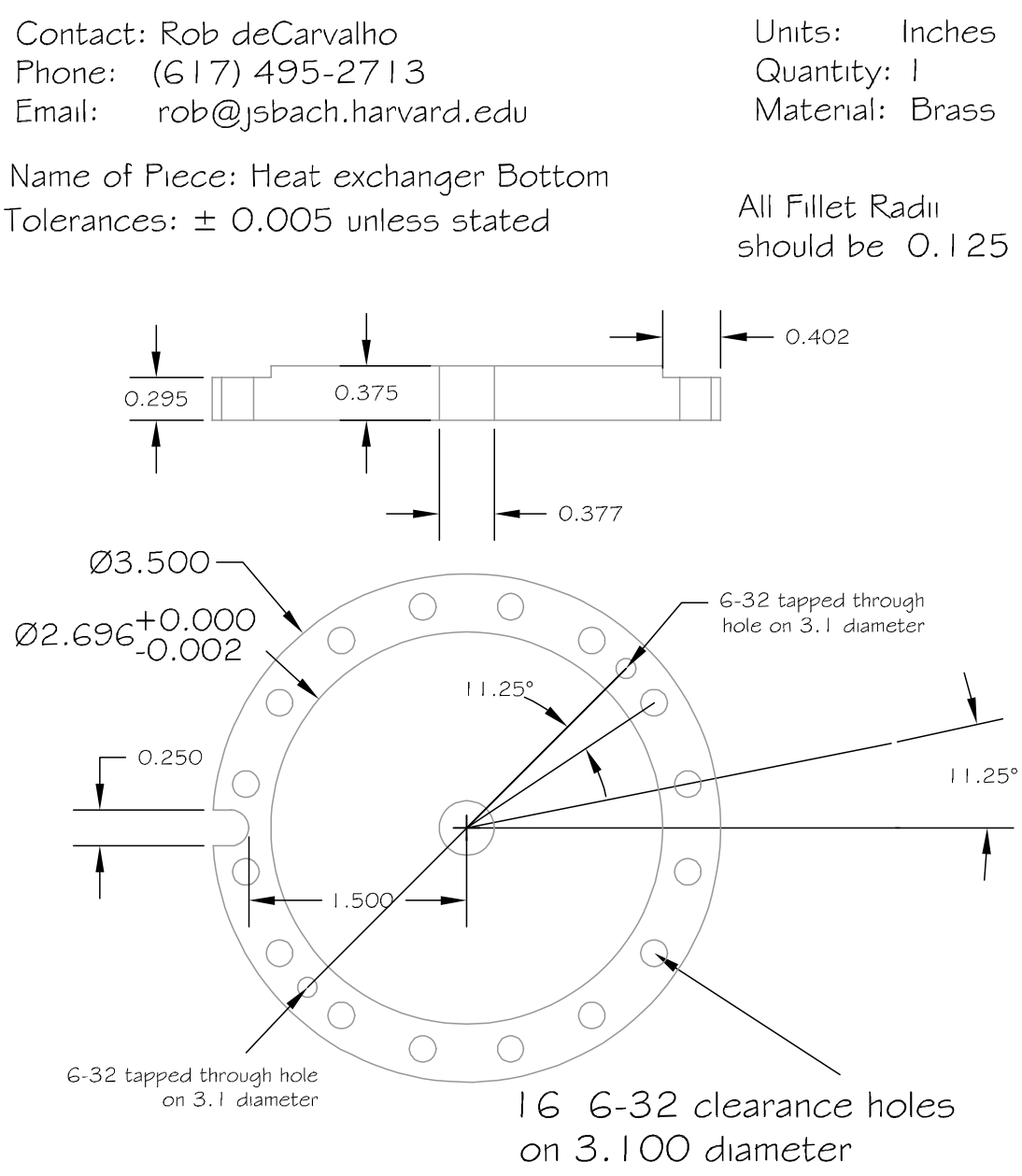

Figure 8.12: Heat Exchanger Lid

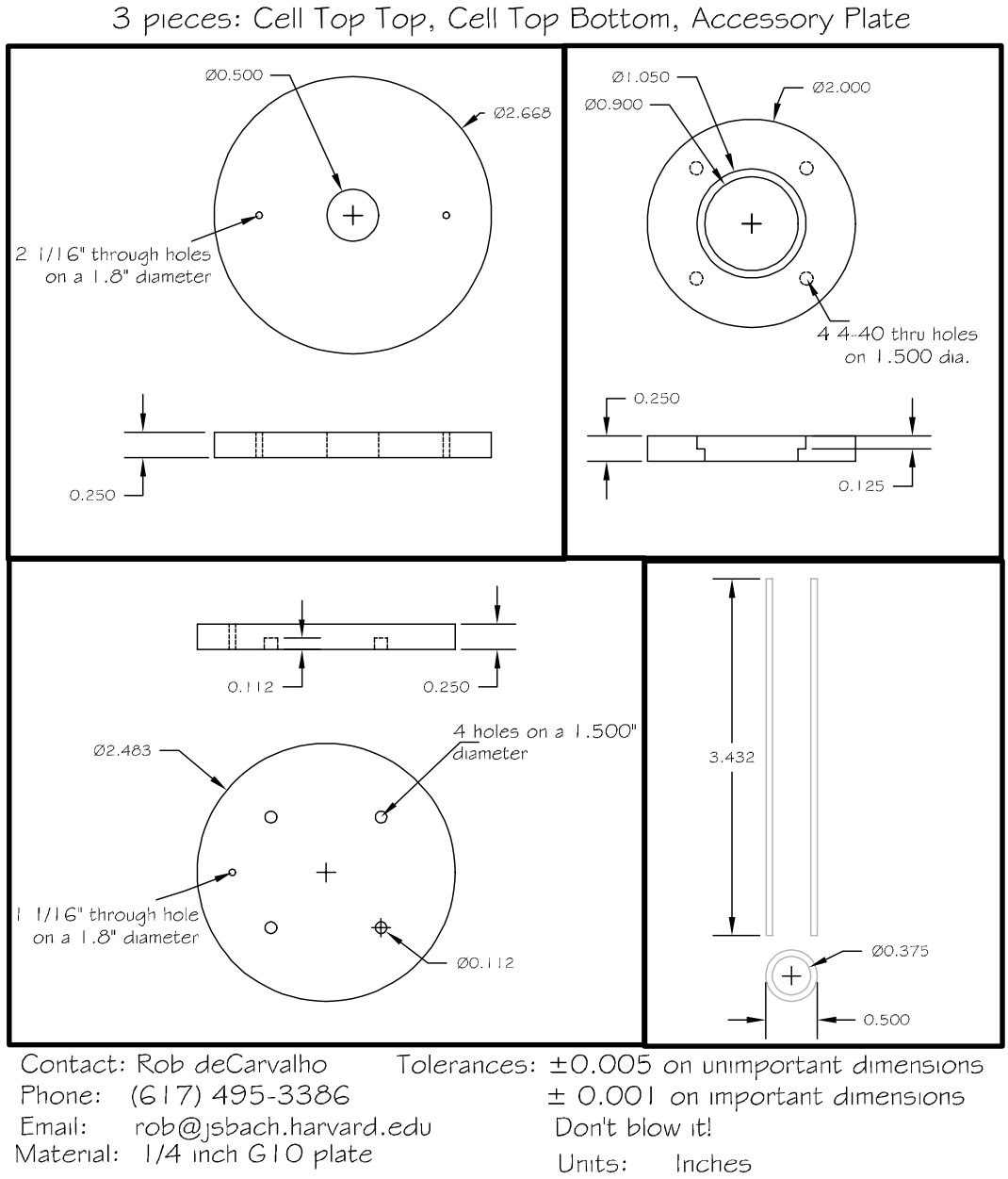

Figure 8.13: Cell Parts

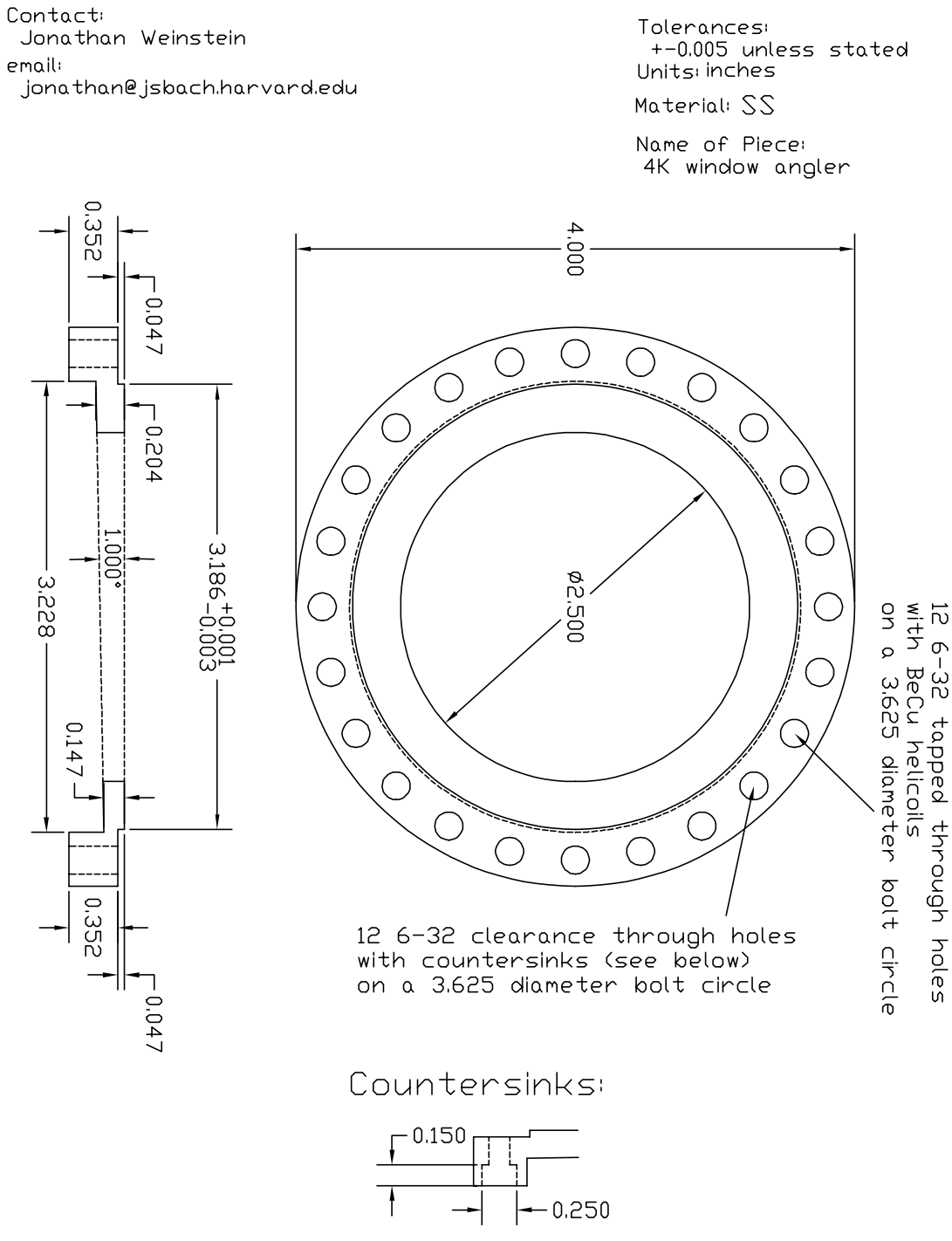

Figure 8.14: 4 K Window Angler

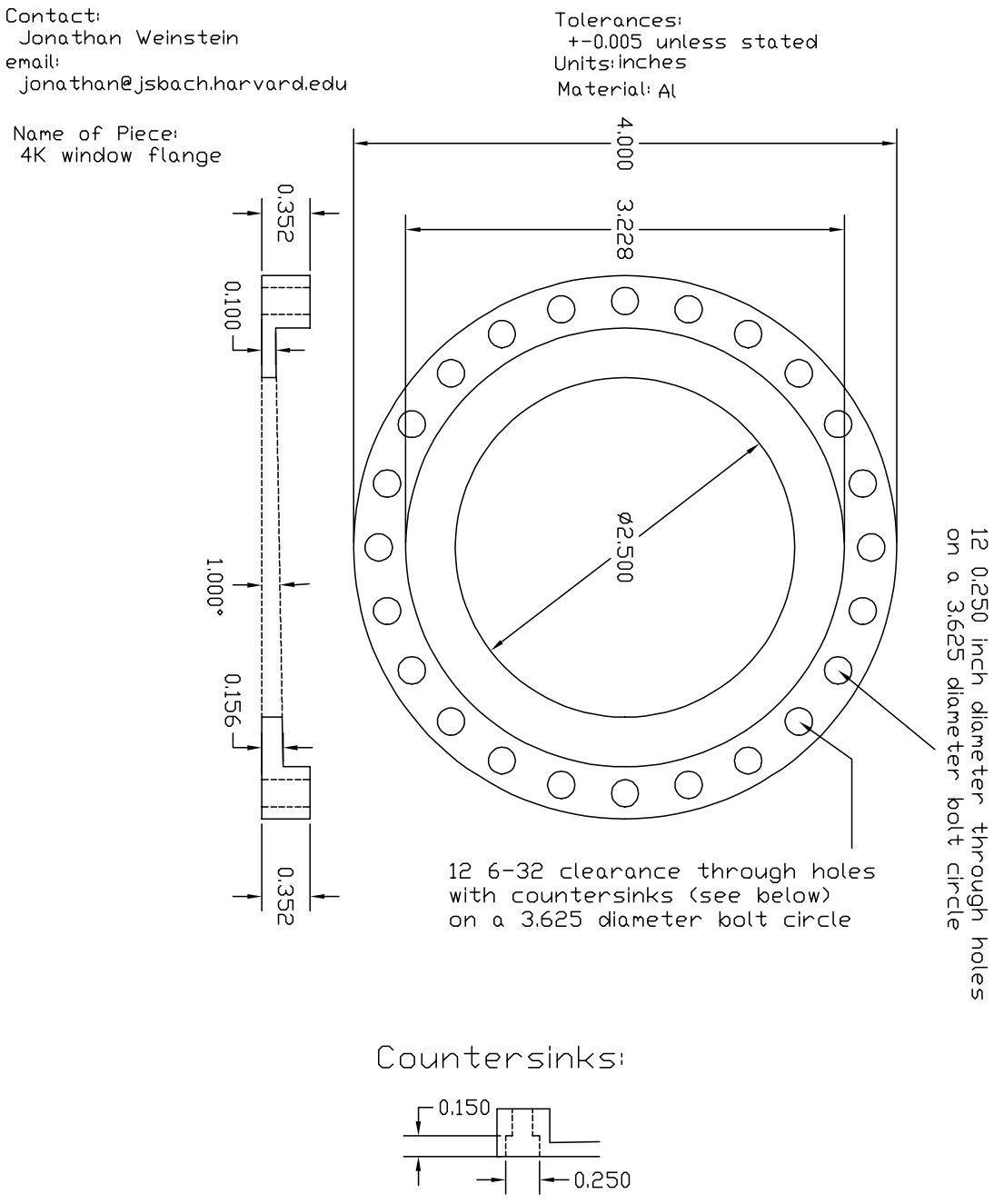

Figure 8.15: 4K Window Flange

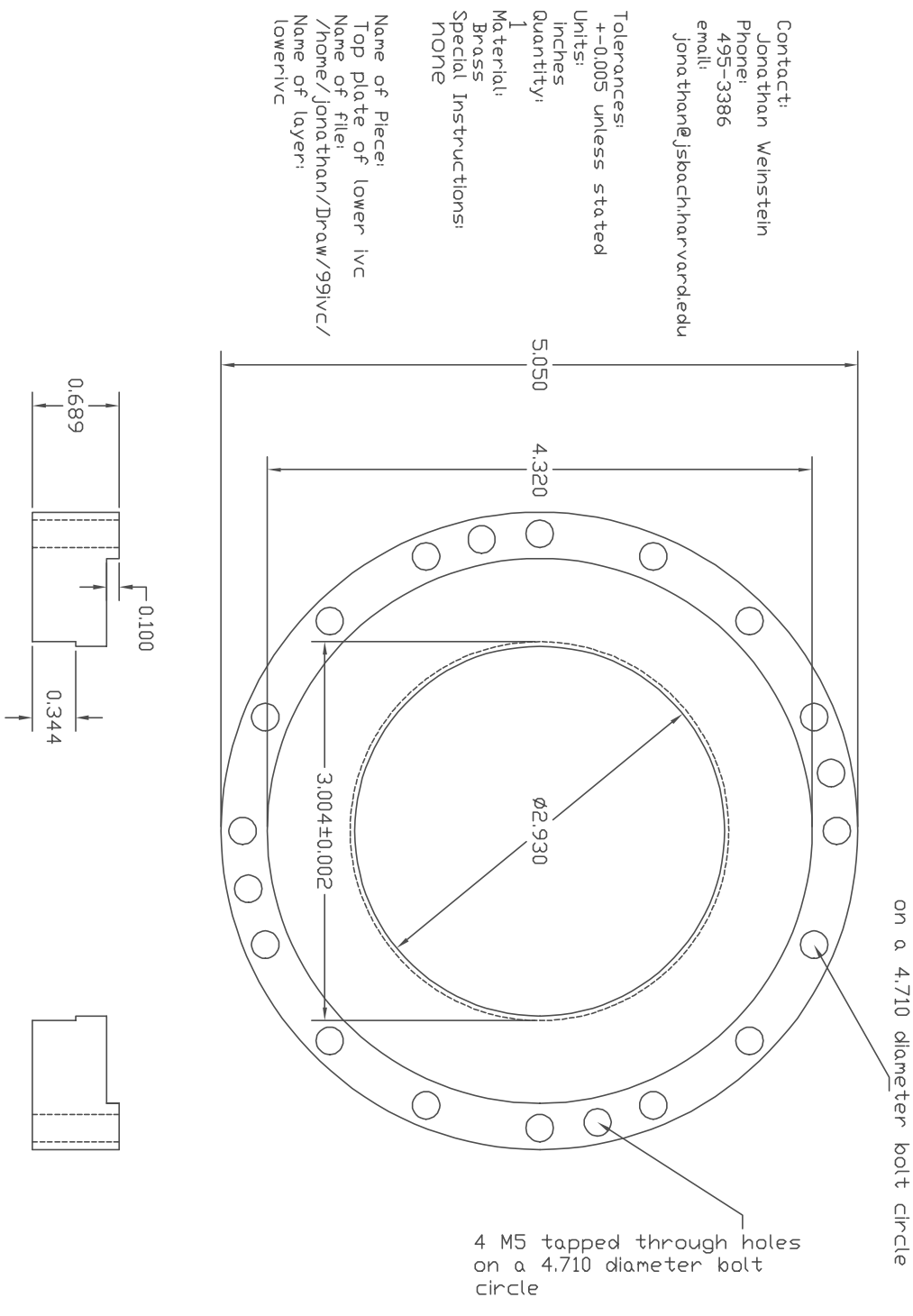

Figure 8.16: Top flange of lower IVC

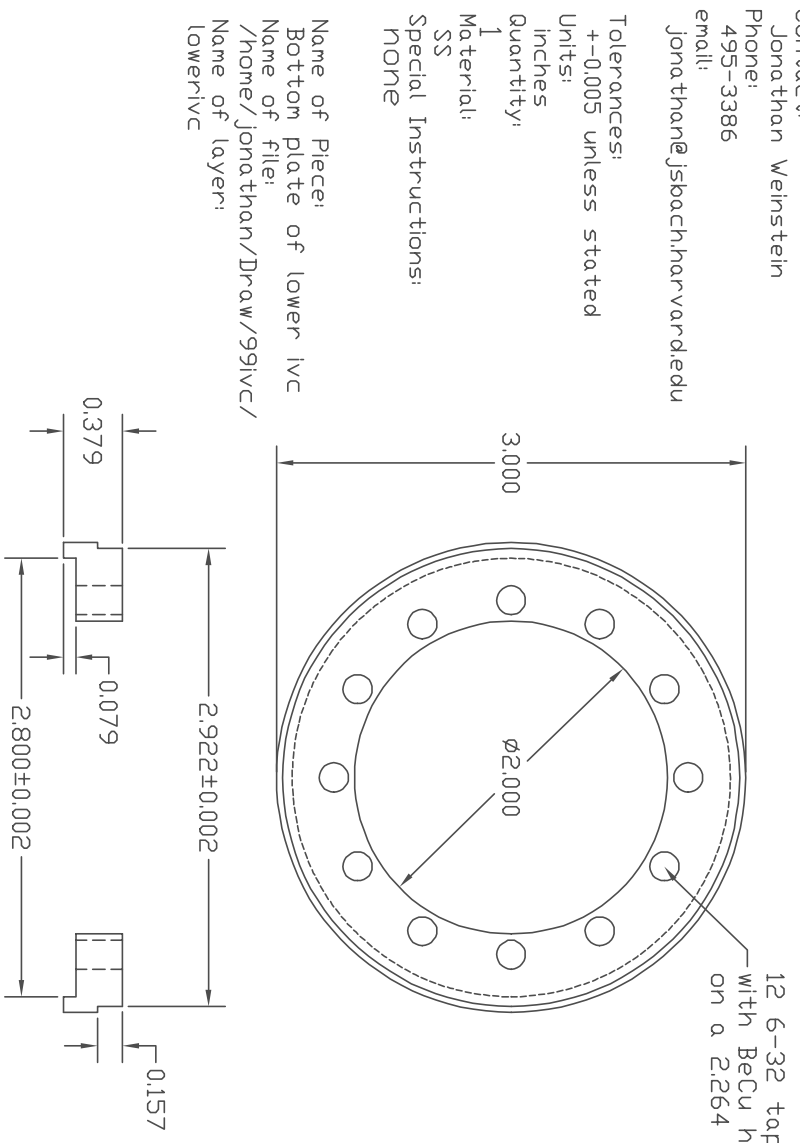

Figure 8.17: Bottom flange of lower IVC

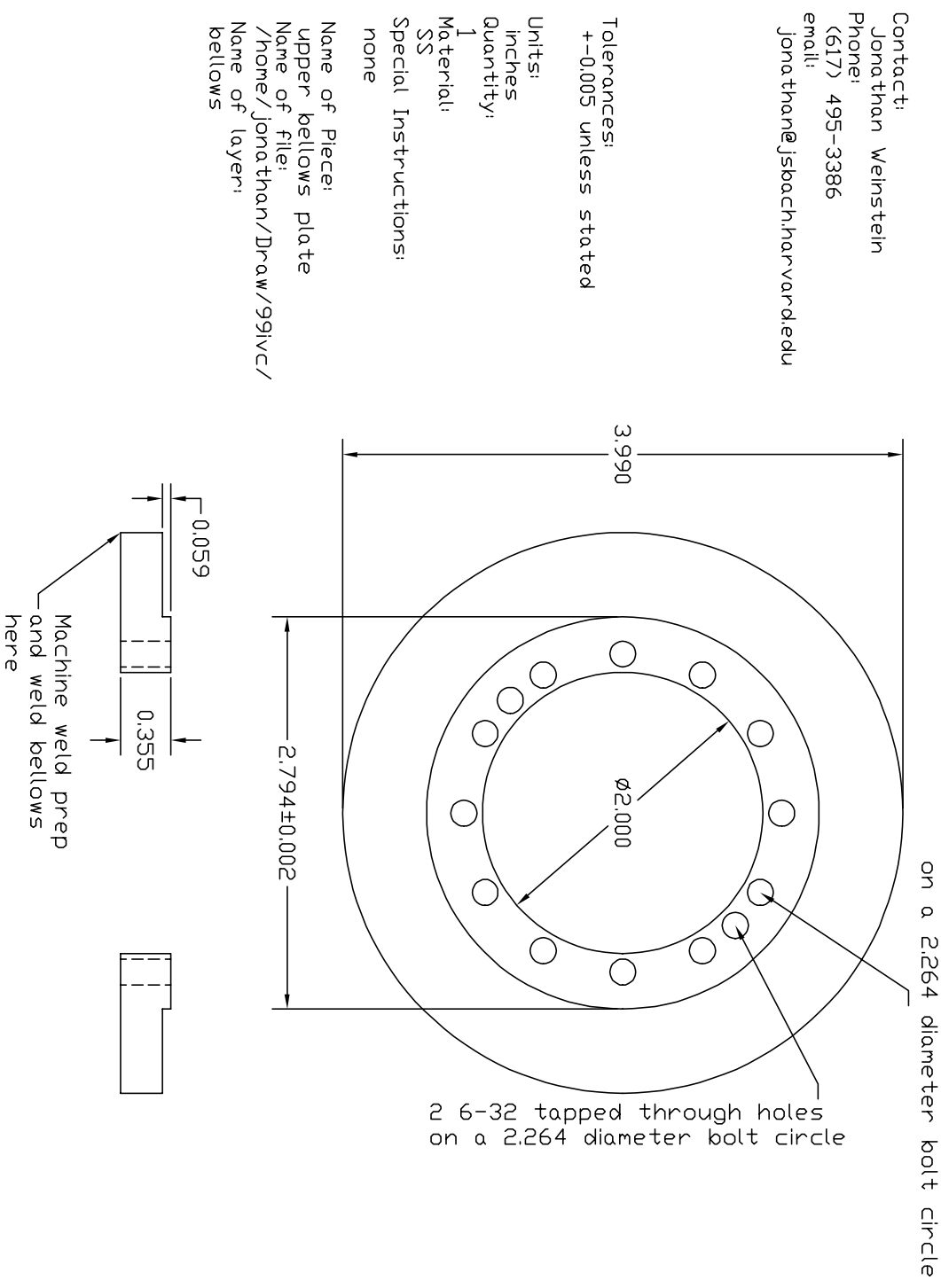

Figure 8.18: Upper bellows flange

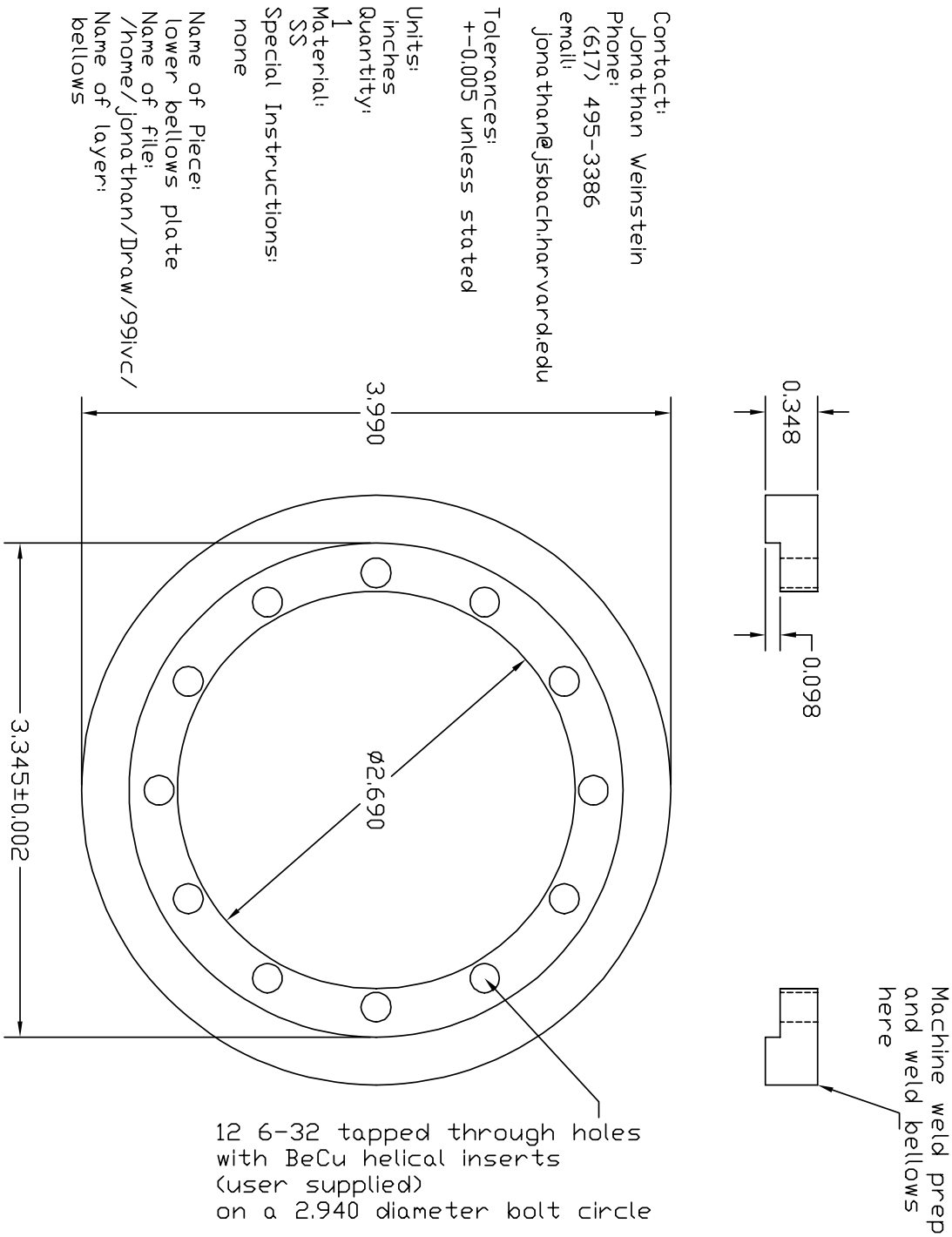

Figure 8.19: Lower bellows flange

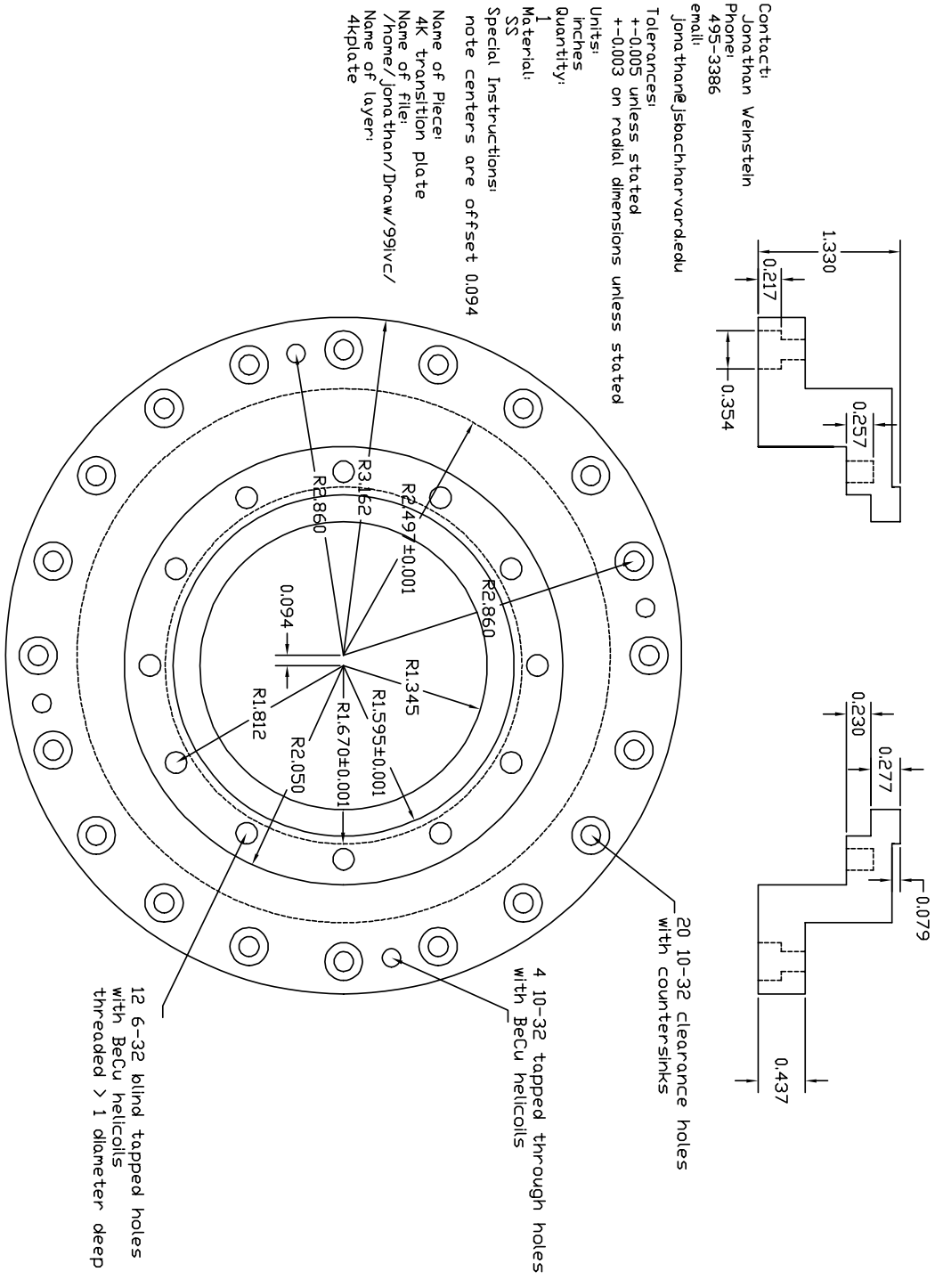

Figure 8.20: Bellows to Dewar 4K Transition Plate

Contact:
John Doyle
Phone:
495-3201
email:
doyle@physics.harvard.edu

Tolerances:
+-0.005 unless stated
Units:
inches

Special Instructions:
helicoils in blind taps

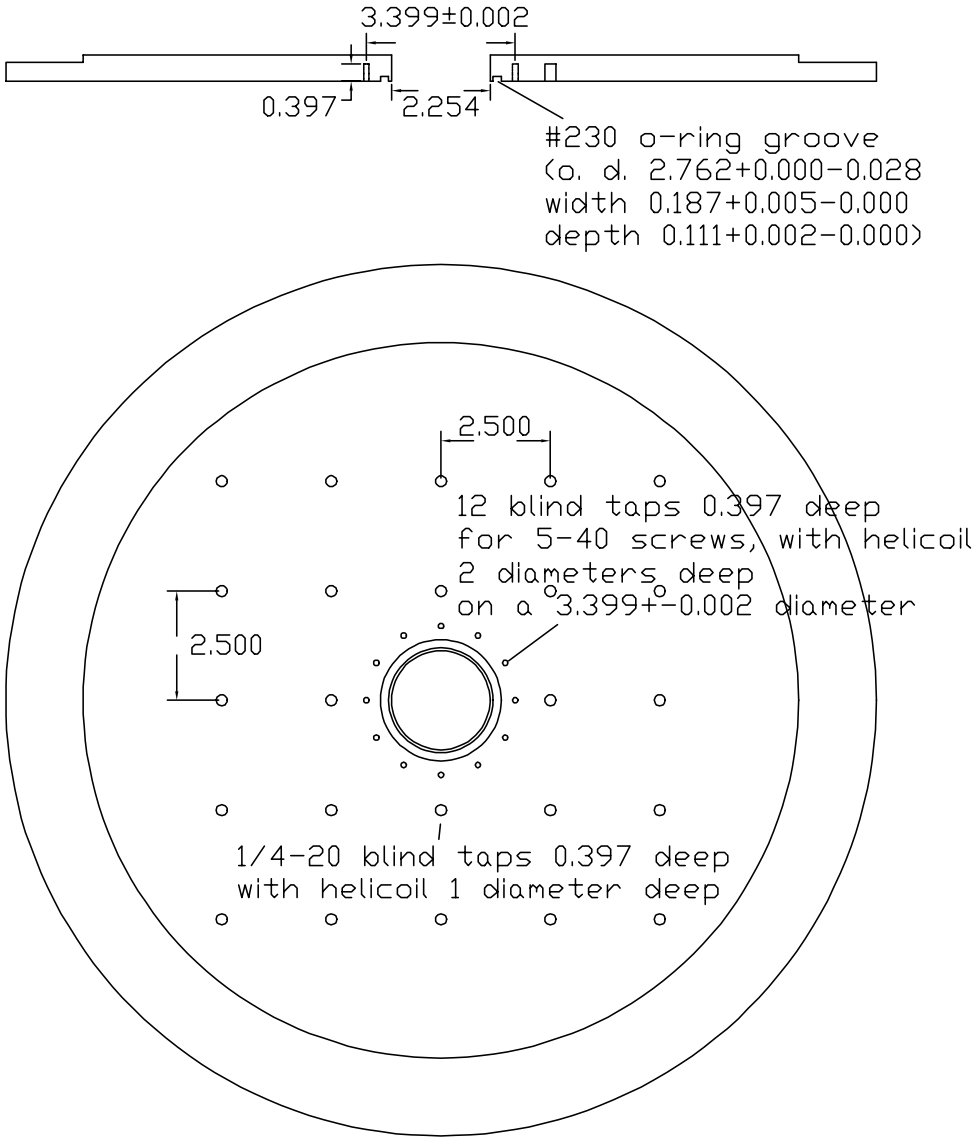

Figure 8.21: 300 K Plate

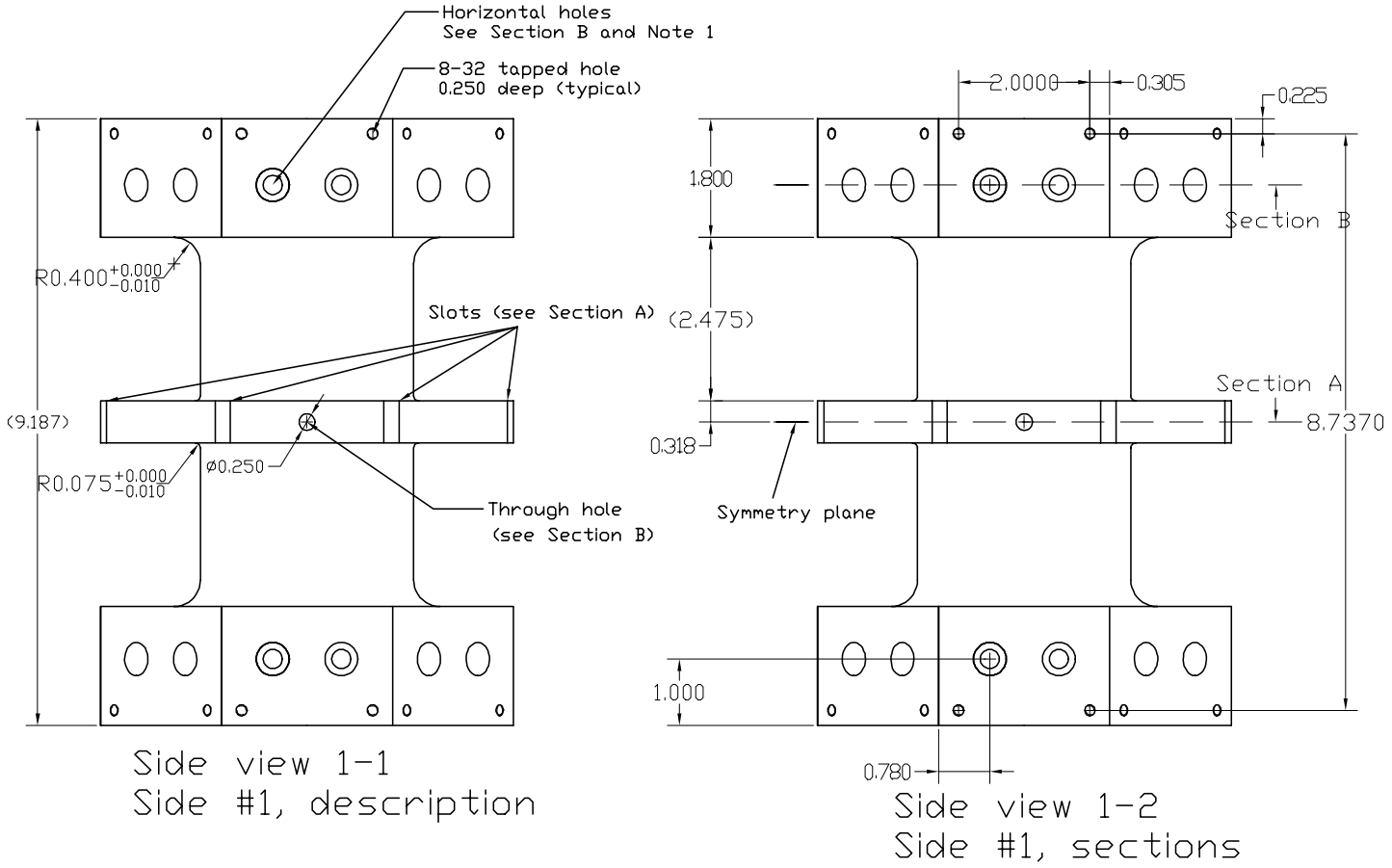

The part is up-down and left-right symmetrical.
Dimensions of holes and fillets are typical
Same views for sides #3,5,7

Figure 8.22: Magnet Side View

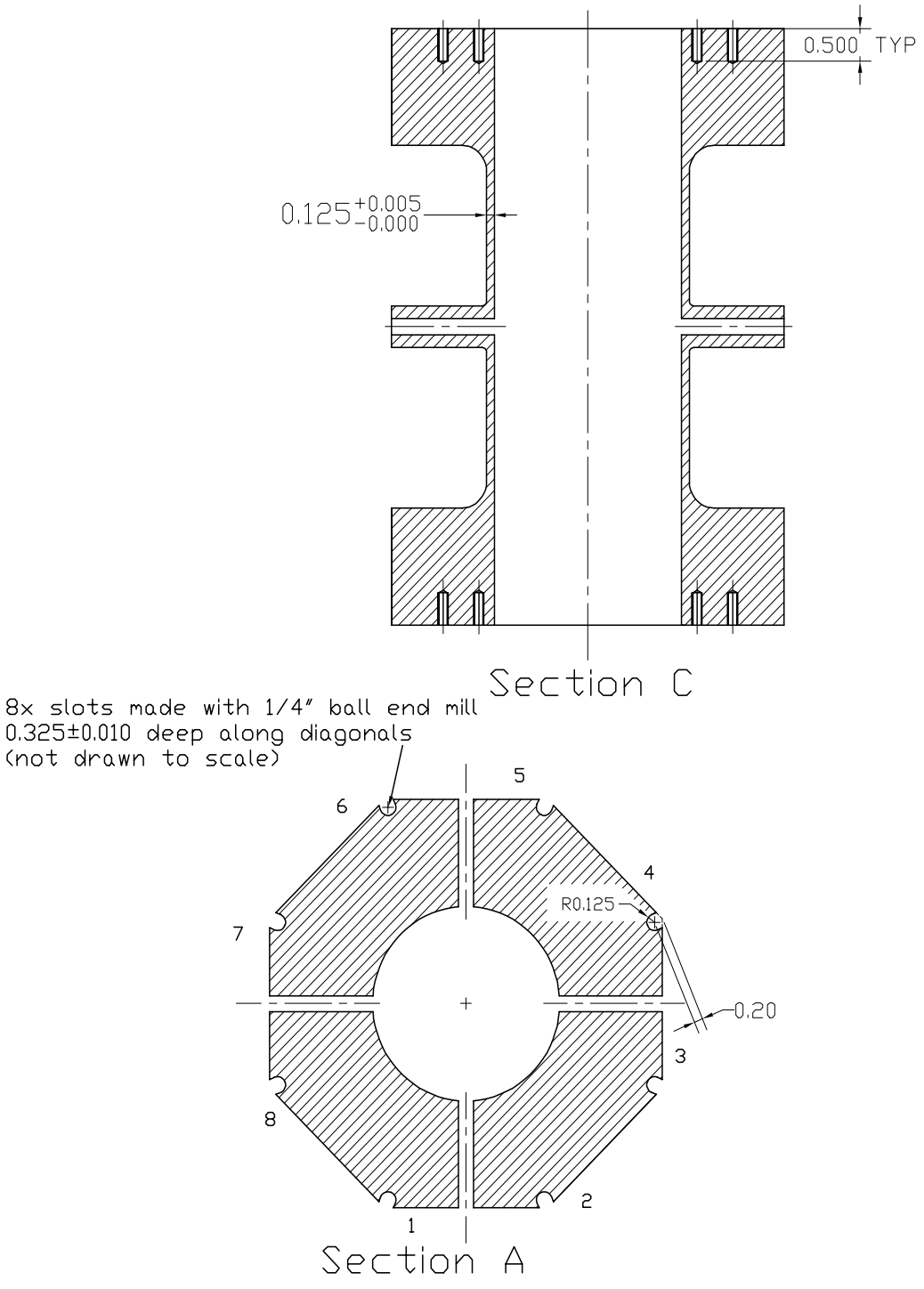

Figure 8.23: Magnet Sections A and C

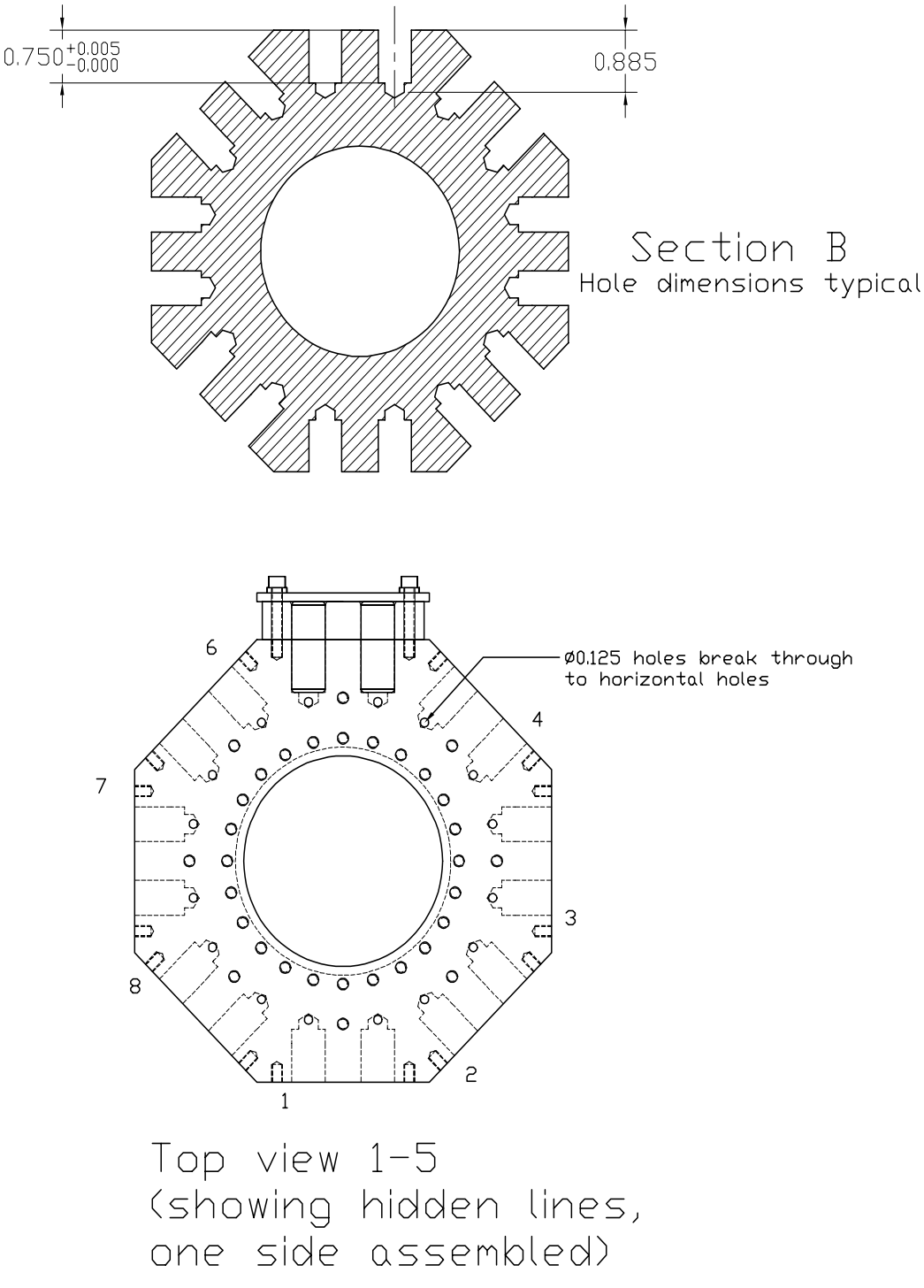

Figure 8.24: Magnet Top View and Section B

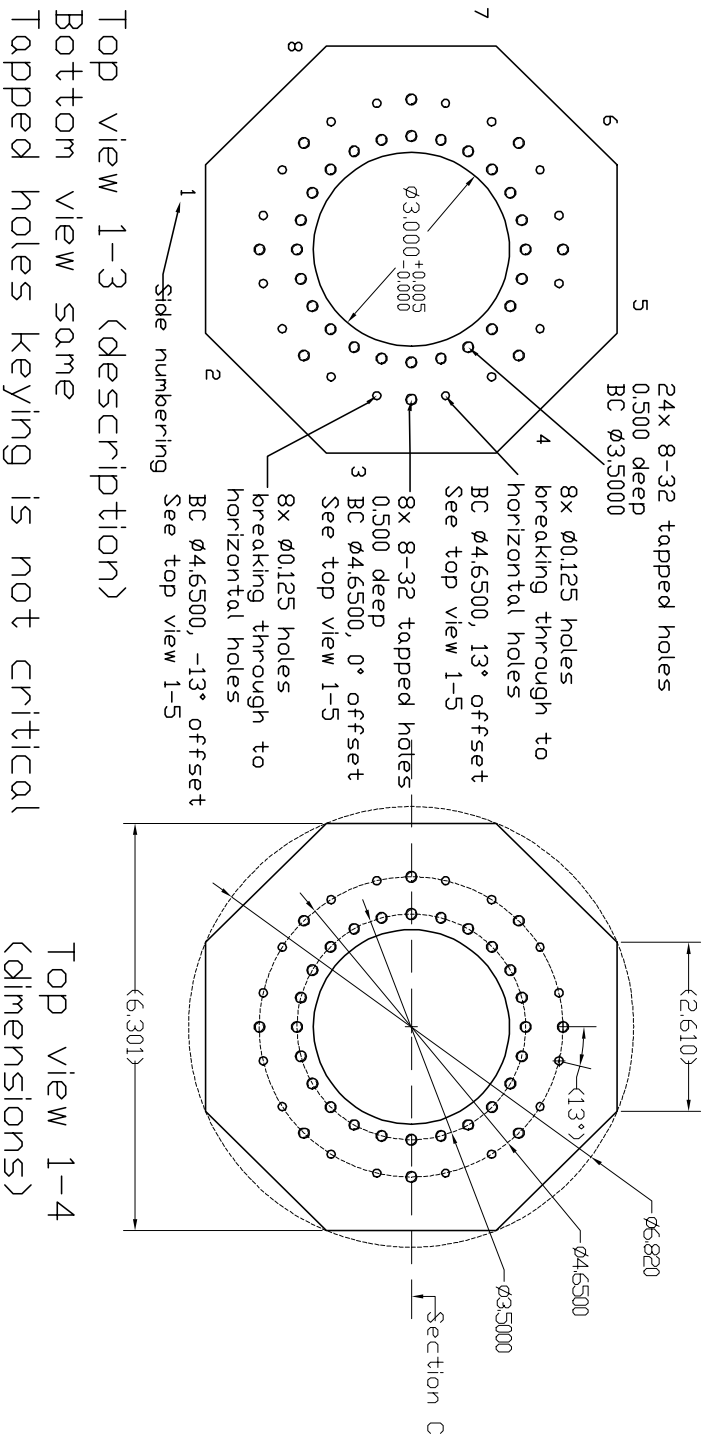

Figure 8.25: Magnet Top View

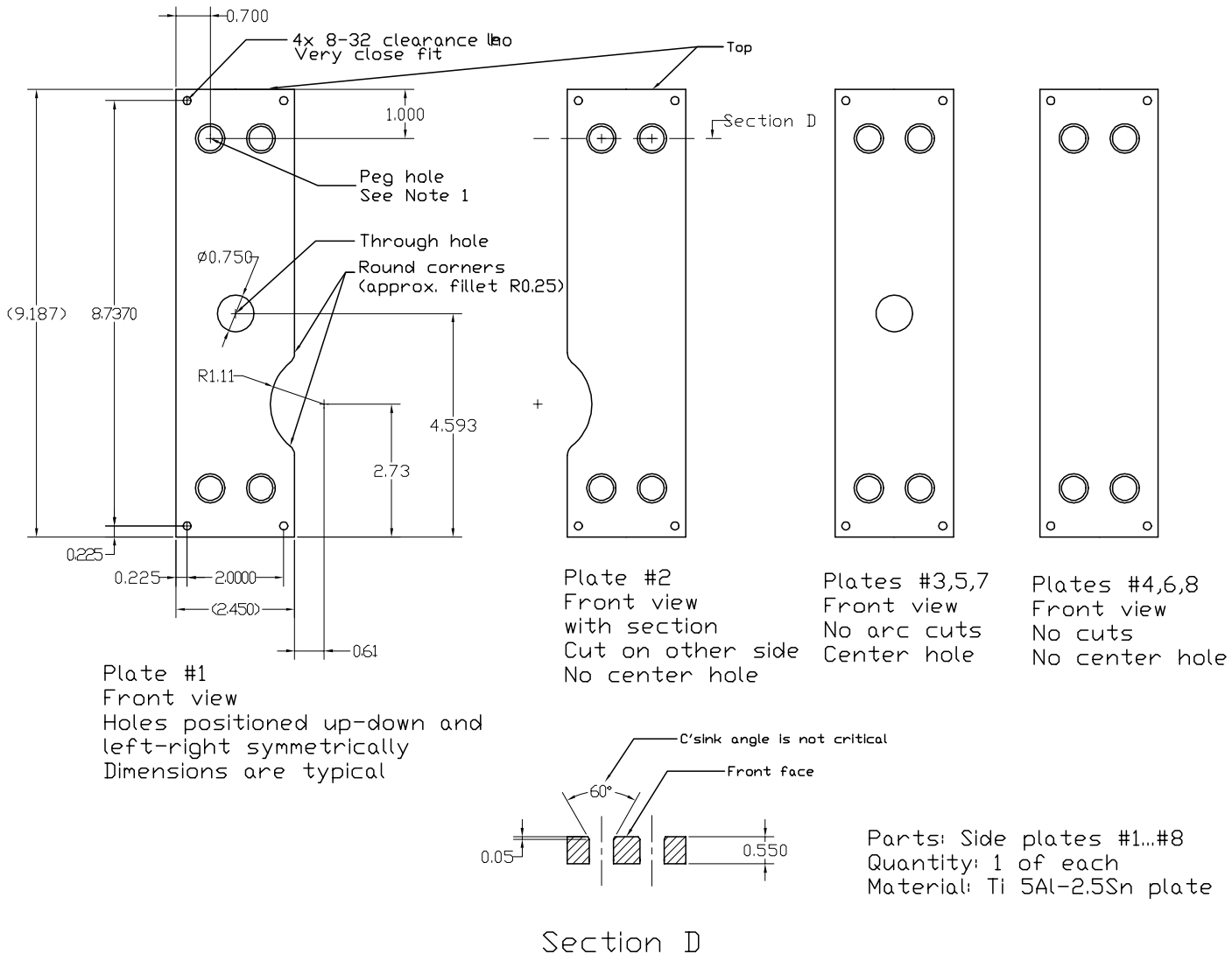

Figure 8.26: Magnet Side Plates

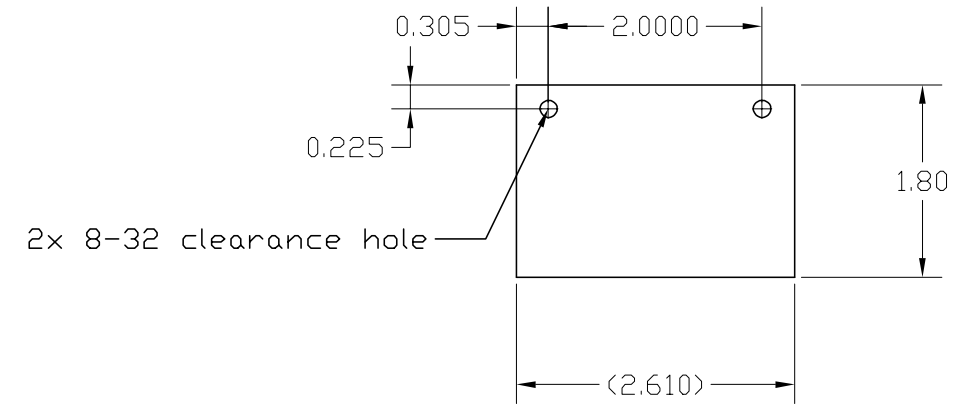

Plate is left-right symmetrical
Dimensions are typical

Part: Holding plate
Quantity: 16
Material: 1/8″ thick
Ti 5Al-2.5Sn sheet

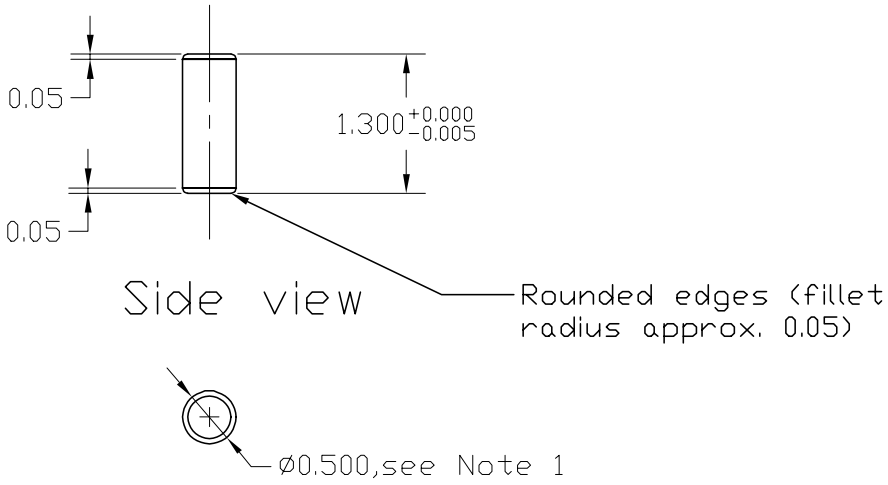

Part: Peg
Quantity: 32
Material: Ti 5Al-2.5Sn round bar about 0.500 diam. (see Note 1)

Figure 8.27: Magnet Pegs

Appendix C
Useful Experimental Information

C.1 Resistor calibration

The chip resistors we use for thermometry below $1\ K$ are all taken from a single batch we like to call the "MIT resistors." This name reflects the fact that they were calibrated at MIT a very long time ago by people and methods which remain mysterious to this author. We have not carefully calibrated this batch of resistors ourselves. However, the calibration curves we have for them give results consistent with a few NOR thermometry measurements taken in our lab to verify their behavior.

Using these calibration curves as well as the calibration curves for the manufacture-supplied thermometers mounted at various points on our dilution refrigerator, we obtain the following fits to the temperature vs. resistance curves. The functional form of these fits stems directly from the discussion of chip resistors found in the excellent book on low-temperature physics written by Pobell [25].

C.1.1 MIT Resistors

The MIT resistor calibration curve was fit for resistance values between roughly $2.2\ K\Omega$ and $6\ K\Omega$, or $0.15\ Kelvin$ and $0.9\ Kelvin$. In this range, the calibration curve

fits well to

$$\left[\frac{T}{K}\right] = 1.5369 \left[\ln\left(\frac{R}{0.6108K\Omega}\right)\right]^{-\frac{1}{0.3497}}.$$

We perform all thermometry using two-wire measurements. This causes the (often significant) resistance of the wires leading to the resistors to be included in all resistance measurements. It is important to subtract this lead resistance from any measurement to obtain the true resistance of the thermometer.

C.1.2 5 K Resistors

In our experiment, $5\ K\Omega$ resistors are mounted on the **1K pot** and the **still**. The calibration curves for these resistors span resistance values of roughly $6.2\ K\Omega$ to $16\ K\Omega$, or $0.75\ Kelvin$ to $9\ Kelvin$. In this range, the calibration curve fits well to

$$\left[\frac{T}{K}\right] = 1.0115 \left[\ln\left(\frac{R}{4.5484K\Omega}\right)\right]^{-\frac{1}{0.6603}}$$

C.1.3 2 K Resistors

In our experiment, $2\ K\Omega$ resistors are mounted on the **mixing chamber** and the **cold plate**. The calibration curves for these resistors span resistance values of roughly $3.4\ K\Omega$ to $10\ K\Omega$, or $0.2\ Kelvin$ to $2\ Kelvin$. In this range, the calibration curve fits well to

$$\left[\frac{T}{K}\right] = 9.2798 \left[\ln\left(\frac{R}{0.6646K\Omega}\right)\right]^{-\frac{1}{0.2549}}$$

C.1.4 1 K Resistors

In our experiment, a $1\ K\Omega$ resistor is mounted on the **mixing chamber**. The calibration curves for this resistors span resistance values of roughly $2\ K\Omega$ to $4\ K\Omega$, or $0.1\ Kelvin$ to $1\ Kelvin$. In this range, the calibration curve fits well to

$$\left[\frac{T}{K}\right] = 48.0724\left[\ln\left(\frac{R}{0.2424K\Omega}\right)\right]^{-\frac{1}{0.1613}}$$

C.2 Helium Vapor Pressure

The low temperature physics book written by Pobell [25] is an excellent source for the properties of liquid helium. From the general discussion on vapor pressure found in this book, the vapor pressure of a liquid scales like

$$P_{vap} = P_0 \exp\left[-\frac{L}{RT}\right]$$

where L is the latent heat of evaporation and R is the gas constant. This general formula can be applied to the case of liquid ^{4}He and ^{3}He to extrapolate their vapor pressure curves to temperatures below the range of feasible measurements. These extrapolations are performed by taking the 10 coldest vapor pressure values listed on pages 230 and 231 of Pobell [25] and doing a least squares fit to the functional form for the vapor pressure. The results of these fits can then be expressed in terms of density

rather than pressure. They are

$$\left[\frac{n}{cm^{-3}}\right]_{^3He} = \frac{3.54\times10^{21}}{\left[\frac{T}{K}\right]}\exp\left(-\frac{3.93}{\left[\frac{T}{K}\right]}\right)$$

$$\left[\frac{n}{cm^{-3}}\right]_{^4He} = \frac{3.233\times10^{22}}{\left[\frac{T}{K}\right]}\exp\left(-\frac{10.33}{\left[\frac{T}{K}\right]}\right)$$

It should be emphasized that these expressions are extrapolations and the density values they give are not necessarily a reflection of reality. However, since vapor pressure measurements do not exist for the lower temperatures achieved in our experimental cell, these extrapolations are a best guess at estimating the vapor pressures.

Appendix D
Atom Photon Interactions

D.1 Saturation Intensity

The saturation intensity is given by

$$I_{sat} = \frac{\hbar\omega_0^3\Gamma}{12\pi c^2\left(\hat{\mathbf{d}}\cdot\hat{\boldsymbol{\varepsilon}}\right)^2}$$

where ω_0 is the resonant frequency Γ is the natural lifetime, c is the speed of light and $\hat{\mathbf{d}}\cdot\hat{\boldsymbol{\varepsilon}}$ is the cosine of the angle between the polarization vector and dipole operator. If one assumes $\left(\hat{\mathbf{d}}\cdot\hat{\boldsymbol{\varepsilon}}\right)^2 = 1$, this can be rewritten as

$$\left[\frac{I_{sat}}{(mW/cm^2)}\right] = \frac{20.8}{\left[\frac{\tau}{s}\right]\left[\frac{\lambda}{nm}\right]^3}$$

where τ is the excited state lifetime and λ is the resonant wavelength. A transition is saturated when photons are scattered at a rate approaching one scattered photon per natural lifetime.

D.2 Photon Scattering Rate

The photon scattering rate is given by

$$\gamma = \frac{\Gamma}{2} \frac{\frac{I}{I_{sat}}}{1 + \left(\frac{2\Delta'}{\Gamma}\right)^2 + \frac{I}{I_{sat}}}$$

where $\Gamma = 1/\tau$ is the transition rate, I_{sat} is the saturation intensity, $\mathbf{k}$ is the optical wave vector and $\mathbf{v}$ is the atom velocity. The effective detuning is given by

$$\Delta' = [(\omega - \omega_0) - \mathbf{k} \cdot \mathbf{v}]$$

D.3 Optical Scattering Cross Section

The scattering cross section presented by a single atom to a stream of photons is given by

$$\sigma = \frac{3}{2\pi} \lambda_0^2 \frac{1 + \frac{I}{I_{sat}}}{1 + \left(\frac{2\Delta'}{\Gamma}\right)^2 + \frac{I}{I_{sat}}}$$

where λ_0 is the resonant wavelength, I_{sat} is the saturation intensity, $\mathbf{k}$ is the optical wave vector and $\mathbf{v}$ is the atom velocity. The effective detuning is given by

$$\Delta' = [(\omega - \omega_0) - \mathbf{k} \cdot \mathbf{v}]$$

D.4 Doppler Broadening

For a thermal ensemble of atoms at a temperature T, the normalized Doppler profile is given by

$$D(\nu, \nu_0) = \frac{1}{\sqrt{2\pi v_0^2}} \sqrt{\frac{mc^2}{k_B T}} \exp\left[-\frac{mc^2}{2k_B T} \left(\frac{\nu - \nu_0}{\nu_0} \right)^2 \right].$$

The full width at half max for this profile is given by

$$\left(\frac{\Delta\nu}{\nu_0} \right)^2 = 8 \ln(2) \left[\frac{k_B T}{mc^2} \right]$$

where ν is an arbitrary frequency of interest, ν_0 is the resonant frequency, $\Delta\nu$ is the FWHM of the Doppler profile, $k_B T$ is the approximate thermal energy, and mc^2 is the rest mass energy of the atom. This relationship can be inverted to obtain the temperature as a function of the Doppler width,

$$T = \frac{\lambda^2 (\Delta\nu)^2 m}{8 \ln(2) k_B}.$$

Plugging in actual numbers, we obtain the general formula

$$\left[\frac{T}{K} \right] = \left(2.168 \times 10^{-23} \right) \left[\frac{\lambda}{nm} \right]^2 \left[\frac{\Delta\nu}{Hz} \right]^2 \left[\frac{m}{a.m.u} \right]$$

where T is the atom temperature, λ is the resonant wavelength, $\Delta\nu$ is the FWHM Doppler width, m is the mass of the atom, and $a.m.u$ is the atomic mass unit.

For typical spectra taken in the laboratory, the FWHM is not obtained directly. Usually the spectra are fit to a Gaussian profile with three parameters. If we write this profile as

$$Spectrum = A \exp\left[-\left(\frac{\nu - a}{b} \right)^2 \right],$$

the FWHM can be extracted using the relation

$$\Delta\nu = b\sqrt{4\ln(2)} = 1.6651b.$$

Again, plugging in the numbers, we obtain

$$\left[\frac{T}{K}\right] = \left(6.011 \times 10^{-23}\right)\left[\frac{\lambda}{nm}\right]^2\left[\frac{b}{Hz}\right]^2\left[\frac{m}{a.m.u}\right]$$